“Remember to focus on virtues too, not just faults”
-*Kaan Williams*

THE MICROMECHANICS OF PHYLLOSILICATE-RICH FAULT ZONES: CASE STUDIES FROM THE MINAS FAULT ZONE, NOVA SCOTIA, CANADA AND THE SAN ANDREAS FAULT, CALIFORNIA, USA

by

Noah John Phillips

B.Sc. Honours Geological Sciences, University of British Columbia, 2012

A THESIS SUBMITTED IN PARTIAL FULFILLMENT OF THE REQUIREMENTS FOR THE DEGREE OF MASTER OF SCIENCE

in the Graduate Academic Unit of Earth Sciences

Supervisor: Joseph Clancy White, Ph.D., Earth Sciences

Examining Board: Karl Butler, Ph.D., Earth Sciences
Michael D. A. Thomas, Ph.D., Civil Engineering

This thesis is accepted by the
Dean of Graduate Studies

THE UNIVERSITY OF NEW BRUNSWICK
May, 2015

© Noah John Phillips, 2015

ABSTRACT

Phyllosilicate-rich transcurrent fault zones provide weak planes through the crust that can accommodate significant simple shear. They are often localized in fine-grained sedimentary units due to the low coefficients of friction for phyllosilicates and the increased efficiency of pressure solution within polyminerallic fine-grained units. Two phyllosilicate-rich fault zones are examined from field-scale down to TEM-scale to determine the predominant operating deformation mechanisms. XRD and electron microprobe of phyllosilicate phases has determined the crystal chemistry and dominant phyllosilicate phases at each location.

At the San Andreas Fault Observatory at Depth, cataclasis leads to a reduction in grain size until a critical effective grain size is obtained allowing for pressure solution processes to control deformation within phyllosilicate and quartz-rich gouges. Within the actively deforming zones, an effective grain size of 100nm is required to accommodate deformation of quartz by pressure solution. Enrichment in phyllosilicate concentration may occur due to solid species pressure solution depletion and/or growth of new phyllosilicate phases. With quartz actively deforming through pressure solution, or when phyllosilicates become significantly concentrated, deformation is controlled by the strength of the phyllosilicates, which have lower coefficients of friction (μ = 0.1-0.4) than predicted by Byerlee's law. Low friction clays (interlayered smectite and chlorite, vermiculite) have been observed in samples distal to the actively creeping zones.

Within the internal zone of the Minas fault zone exposed at Greville Bay, the Fountain Lake Gp rhyolite and the S-C domain of the Nuttby Fm. record crystal plastic deformation of quartz by sub-grain rotation recrystallization and grain boundary bulging

recrystallization. These features indicate higher metamorphic grades than the units to the north of them, which contain primary features and no evidence of crystal plasticity. Phyllosilicate crystallinity agrees with these observations, and chlorite geothermometry of the S-C domain indicates temperatures of 359 +/-12°C. The S-C domain, which has accommodated significant simple shear and contains high strain structures (*e.g.* shear bands and sheath folds), is deforming through pressure solution-accommodated creep within phyllosilicate-rich segments. Pressure solution-accommodated creep could accommodate strain rates up to ~$10^{-9}s^{-1}$ in the phyllosilicate-rich packages, where quartz aggregates exist with long axes ranging from 10-20μm surrounded by anastomosing phyllosilicate networks. The higher grade units may have been incorporated into the fault zone through the development of a positive flower structure in a region of transpression due to a change in strike of the fault from 82° to 68° as one moves to the west. A late brittle fault has formed a mesocataclasite in the Nuttby Fm. which has a "scaly" structure similar to those observed in accretionary wedge environments. Scaly fabrics accommodate shear through simultaneous slip on multiple surfaces which continually reorganize themselves.

Phyllosilicate-rich fault zones are consistently weaker than predicted by Byerlee's law at low strain rates due to concomitant deformation by pressure solution, frictional sliding along phyllosilicate foliae, and crystal plastic deformation of phyllosilicates. Crustal strength profiles of fine-grained phyllosilicate-rich rocks are substantially weaker when compared with traditional crustal strength profiles and could explain the weakness of many large transcurrent fault zones from shallow to middle crustal depths.

ACKNOWLEDGEMENTS

This thesis would not have been possible without enormous support from my supervisor, mentor, and friend, Dr. Joseph Clancy White. I will lean heavily on the framework of geological thought that he has helped me to lay down during my years here at UNB.

Thanks to my family, who have always been there for me, through all the ups-downs-sideways- and general excitement that comes through living. Mum and Dad, you have always encouraged me to pursue exciting paths in life, and I cannot thank you enough for that.

In addition I would like to acknowledge:

- NSERC, for funding this thesis through Dr. White
- The Microscopy and Microanalysis Facility at UNB, where the bulk of my data was collected. In particular, thanks to Louise Weaver for help and training on the TEM
- The SAFOD project leaders and core library technicians for providing samples for this project
- Jennifer Adam for field assistance along the MFZ

Thanks to everyone within the department of geology at UNB. You have all made my time here very enjoyable, and I hope to stay in touch with you in the years to come.

TABLE OF CONTENTS

ABSTRACT ii
ACKNOWLEDGEMENTS iiv
TABLE OF CONTENTS v
LIST OF FIGURES iix
LIST OF TABLES xii
LIST OF ABBREVIATIONS xiii
CHAPTER 1: INTRODUCTION AND OBJECTIVES 1
CHAPTER 2: REVIEW OF FAULT ZONE PROCESSES 3
2.1 Fault Zone Structure 3
2.2 How Geological Materials Deform 7
2.2.1 Categorizing deformation 8
2.2.2 Brittle fracture, frictional sliding and cataclastic flow 10
2.2.3 Dislocation glide, climb and creep 15
2.2.4 Nabarro-Herring creep and Coble creep 20
2.2.5 Superplastic creep 21
2.2.6 Dissolution-precipitation creep 21
2.3 Fault Zone Processes in the Crust 23
CHAPTER 3: METHODOLOGIES 28
3.1 Analysis of Microstructures 28
3.1.1 Preparation of polished thin sections 29
3.1.2 SEM 29
3.1.3 TEM sample preparation 29
3.1.4 TEM 30
3.2 Analysis of Phyllosilicates 30
3.2.1 Preparation of random powders for XRD 31
3.2.2 Preparation of oriented aggregate mounts for XRD 31
3.2.3 XRD of randomly oriented powders 33
3.2.4 X-Ray diffraction of oriented aggregate mount 33
3.2.5 Electron microprobe analysis of phyllosilicates 34
CHAPTER 4: THE MINAS FAULT ZONE 35
4.1 Introduction 35
4.1.1 Introduction to the Minas fault zone project 35

4.1.2 The Avalon zone 37
4.1.3 The Meguma zone 38
4.1.4 Original relationship between the Meguma and Avalon zones 38
4.1.5 The Maritimes basin 40
4.1.6 The Minas fault zone 41
4.2 Introduction to the Greville Bay Study Area 42
4.2.1 Location of the Greville Bay study area 42
4.2.2 Previous work at the Greville Bay study area 42
4.2.3 Primary lithologies of the Greville Bay study area 45
4.3 Field Observations of the Greville Bay Study Area 47
4.3.1 A natural cross-section through Greville Bay 47
4.3.2 Field observations of the Fountain Lake Group Rhyolite 49
4.3.3 Field observations of the S-C Domain of the Nuttby Formation: 49
4.3.4 Field observations of the Jeffers Group and Parrsboro Formations 53
4.3.5 Field observations of the Scaly Mesocataclasite – Nuttby Formation 55
4.3.6 Field observations of the Folded Carbonate Bearing Nuttby Formation 57
4.3.7 Interpretation of field observations 57
4.4 Microstructures of the Greville Bay Study Area 58
4.4.1 Introduction to the study of microstructures 58
4.4.2 Microstructures from the Fountain Lake Group rhyolite 58
4.4.3 Interpretation of microstructures – Fountain Lake Group rhyolite 60
4.4.4 Microstructures from the S-C domain – Nuttby Formation 61
4.4.5 Interpretation of microstructures from the S-C domain – Nuttby Formation 70
4.4.6 Microstructures from the "scaly"mesocataclasite – Nuttby Formation 72
4.4.7 Interpretation of microstructures from the "scaly"mesocataclasite – Nuttby Formation 76
4.4.8 Microstructures from the folded carbonate bearing phyllite – Nuttby Formation 80
4.4.8 Interpretation of microstructures from the folded carbonate bearing phyllite – Nuttby Formation 82
4.5 Metamorphic History of the Greville Bay Section of the Minas Fault Zone 82

4.5.1 Introduction to the study of metamorphism at Greville Bay 82
4.5.2 Macro to microstructural fabrics of samples taken from Greville Bay 83
4.5.3 XRD of oriented clay aggregates 84
4.5.4 Results of XRD 86
4.5.5 Microprobe results 87
4.5.6 Discussion and implications of results 97
4.6 Conclusions 100
CHAPTER 5: THE SAN ANDREAS FAULT OBSERVATORY AT DEPTH 103
5.1 Introduction 103
5.1.1 Introduction to the SAFOD project 103
5.1.2 Lithologies 106
5.1.3 Introduction to core segments 108
5.2 Methodology 109
5.3 Results 109
5.3.1 Microscopy 109
5.3.2 XRD of randomly oriented powders 116
5.3.3 XRD of oriented clay aggregates 116
5.4 Discussion 118
5.5 Conclusions 124
CHAPTER 6: DISCUSSION 127
6.1 A Comparison of the SAFOD and Minas Fault Zone Sites 127
6.2 Strength Profiles for Phyllosilicate-Rich Transcurrent Faults 128
6.2.1 Frictional sliding 128
6.2.2 Dissolution-precipitation creep 131
6.2.3 Crystal plasticity 134
6.2.4 Microphysical model and assumptions 136
6.2.5 Parameters used in calculations of strength profiles 137
6.2.6 Strength profiles for transcurrent fault zones 140
6.2.7 Implications of crustal strength profiles 144
6.3 Role of the Effective Grain Size on Strength 144
6.3.1 Role of the effective grain size at the SAFOD site 145
6.3.2 Role of the effective grain size at Greville Bay (S-C Domain) 148
6.3.3 Implications of effective grain size charts 151

6.4 A Note on Strain Rates 151
6.5 Weak faults? – Implications for fault zone behaviour 153
6.5.1 The heat-flow paradox 153
6.5.2 Frictional sliding on weak phases 156
6.5.3 Weakness as observed in this study 157
CHAPTER 7: CONCLUSIONS 159
REFERENCES 164
APPENDIX I: ELECTRON MICROPROBE RESULTS 182
APPENDIX II: THIN SECTION SCANS 193
APPENDIX III: XRD DATA FROM THE MINAS FAULT ZONE 210
CURRICULUM VITAE

LIST OF FIGURES

CHAPTER 2: REVIEW OF FAULT ZONE PROCESSES .....

2.1: Multidisciplinary approach to the study of faults 5

2.2: Structure of upper crustal, transcurrent fault zones 7

2.3: Constructing a Mohr failure envelope..... 12

2.4: Types of dislocations and dislocation multiplication 16

2.5: Cartoon of fault zone processes with depth 24

2.6: Strength of different materials with depth in the continental lithosphere 26

CHAPTER 3: METHODOLOGIES .....

3.1: Preparation of oriented clay aggregates..... 32

CHAPTER 4: THE MINAS FAULT ZONE .....

4.1: Major structural zones of the Appalachians..... 36

4.2: Location of the Minas fault zone and Cobequid fault..... 36

4.3: Meguma over Avalon seismic interpretation..... 40

4.4: Summary of geometry and kinetics from the Minas fault zone 44

4.5: Overview of the relationships between regional structures..... 44

4.6: Natural cross-section through Greville Bay 48

4.7: Mesoscopic structures from the Fountain Lake Gp..... 50

4.8: Mesoscopic structures from the S-C domain of the Nuttby Fm. 51

4.9: Mesoscopic structures from the Jeffers Gp and Parrsboro Fm.. 54

4.10: Mesoscopic structures from the 'scaly' mesocataclasite – Nuttby Fm.. ... 56

4.11: Photomicrographs of the Fountain Lake Group rhyolite..... 59

4.12: Comparative microstructures of the gouges within the Fountain Lake Group rhyolite 61

4.13: Photomicrographs of S-C Fabrics in the Nuttby Formation..... 63

4.14: SEM photomicrographs of S-C fabrics in the Nuttby Formation 64

4.15: SEM Photomicrographs of a dissolution seam Nuttby Formation..... 65

4.16: TEM Investigation of phyllosilicate-rich domain S-C domain, Nuttby Fm. 67

4.17: TEM images of coarse grained quartz-rich domain, Nuttby Fm..... 68

4.18: TEM images of fine-grained quartz-rich domain, Nuttby Fm. 69

4.19: Photomicrograph of the 'scaly' mesocataclasite – Nuttby Fm. 73

4.20: SEM Photomicrographs of the 'scaly' mesocataclasite, Nuttby Formation 74

4.21: TEM Photomicrographs of the fabric from the 'scaly' mesocataclasite, Nuttby Formation 75

4.22: TEM Photomicrographs of quartz precipitates, 'scaly' mesocataclasite, Nuttby Formation 77

4.23: TEM Photomicrographs of quartz vein material, 'scaly' mesocataclasite, Nuttby Formation 78

4.24: Microstructures from the folded carbonate bearing Nuttby Formation 81

4.25: Typical XRD plot from Greville Bay 86

4.26: Crystallinity data from the oriented clay aggregates 88

4.27: Crystal chemistry of phengites analyzed using the microprobe 91

4.28: Morphologies of chlorites analyzed using the microprobe 93

4.29: Crystal chemistry of chlorites analyzed using the microprobe 96

CHAPTER 5: THE SAN ANDREAS FAULT OBSERVATORY AT DEPTH .....

5.1: Location of the SAFOD site and sample intervals 104

5.2: Lithology of the SAFOD main bore hole 107

5.3: SEM Photomicrographs of sample E-14 110

5.4: Microstructures from sample E-16 110

5.5: Microstructures from sample G-12 112

5.6: Microstructures from sample G-23 114

5.7: Microstructures from sample G-42 115

5.8: XRD of oriented clay aggregates for the Salinian Block samples 119

5.9: XRD of oriented clay aggregates for the Great Valley Sequence samples 120

5.10: Effectiveness of pressure solution at the SAFOD site 125

5.11: Experimental data from the active segments of SAFOD core 125

CHAPTER 6: DISCUSSION .....

6.1: Changes in optimal fault zone orientation due to frictional properties ... 130

6.2: The effect of the coefficient of friction on shear resistance 130

6.3: Microphysical model for pressure solution-accommodated creep after Bos and Spiers (2002) 132

6.4: Frictional properties of phyllosilicates 139

6.5: Crustal strength profile for a transcurrent fault zone at fast deformation rates (10^{-8} and 10^{-10} s^{-1}) 141

6.6: Crustal strength profile for a transcurrent fault zone at slow deformation rates (10^{-12} and 10^{-14} s^{-1}) and a constant coefficient of friction (0.3) 142

6.7: Crustal strength profile for a transcurrent fault zone at slow deformation rates (10^{-12} and 10^{-14} s^{-1}) and an evolving coefficient of friction (0.1-0.3) 143

6.8: Effective grain size plot for the active portions of the SAFOD site 146

6.9: Effective grain size plot for the active portions of the SAFOD site 147

6.10: Effective grain size plot for the S-C domain of the Minas fault zone 149

6.11: Simplified view of the effective grain size plot for the S-C domain of the Minas fault zone 150

6.12: Width of the deforming volume necessary to accommodate displacement rates within a fault zone at a given shear strain rate 152

Map 1: Geology of Greville Bay .....

Map 2: Sample Locations for Greville Bay .....

Map 3: Sample Locations and Results for XRD at Greville Bay .....

LIST OF TABLES

CHAPTER 4: THE MINAS FAULT ZONE .....

4.1: Major stratigraphic subdivisions of the Maritimes Basin 40

4.2: Average chemical compositions of phengites in phyllites from the Minas fault zone 90

4.3: Average chemical compositions of chlorites in phyllites from the Minas fault zone 94

CHAPTER 5: THE SAN ANDREAS FAULT OBSERVATORY AT DEPTH .....

5.1: Reitveld analysis of randomly oriented XRD patterns 117

CHAPTER 6: DISCUSSION .....

6.1: Variables used in the calculation of crustal strength profiles 138

LIST OF ABBREVIATIONS

BDT – Brittle-Ductile Transition
BPT – Brittle-Plastic Transition
ChC – Chlorite Crystallinity
CIS – Chlorite Index Standard
CDZ – Central Deformation Zone
CPO – Crystallographic Preferred Orientation
CRSS – Critically Resolved Shear Stress
DFDP – Deep Fault Drilling Program
EDAX – Electron Dispersive X-Ray
EDS – Energy Dispersive X-Ray
EMPA – Electron Microprobe Elemental Analysis
FWHM – Full Width at Half Maximum
IC – Illite Crystallinity
JFAST – Japan Trench Fast Drilling Program
KI – Kubler Index
MBH – Main Bore Hole
MFZ – Minas Fault Zone
PIPS – Precision Ion Polishing System
SAF – San Andreas Fault
SAFOD – San Andreas Fault Observatory at Depth
SAR – Synthetic Aperture Radar
S-C - Schistosité et cisaillement
SDZ – Southern Deformation Zone
SEM – Scanning Electron Microscopy (or microscope)
SPD – Shape Preferred Orientation
TEM – Transmission Electron Microscopy (or microscope)
UNB – University of New Brunswick
***V*p** – Velocity of Primary Waves
***V*s** – Velocity of Secondary (Shear) Waves
WFSD – Wenchuan Earthquake Fault Scientific Drilling Project
XRD – X-Ray Diffraction

CHAPTER 1: INTRODUCTION AND OBJECTIVES

Crustal-scale transcurrent fault zones exert significant controls over the mechanical, seismological and hydrological properties of Earth's crust (Sibson, 1982, 1989; Caine et al., 1996; Townend and Zoback, 2000; Faulkner et al., 2008). These faults control the strength of the crust (as their frictional properties constrain the stresses able to accumulate in the crust), crustal-scale fluid flow, and the nucleation and propagation of earthquakes within the crust. In order to establish the structure of faults at depth, drilling programs of active faults and field studies of exhumed faults are undertaken (*e.g.* Sibson, 1977; Chester and Chester, 1998; Faulkner et al., 2003; Fagereng and Sibson, 2010; Zoback, 2010). These studies give insights into the mechanical properties of fault zones at depth.

A quartz-feldspar dominated upper crust is usually inferred when discussing or modelling strength profiles in the crust (Sibson, 1989; Kohlstedt et al., 1995); however, fault zones in the mid to upper crust are routinely composed of a low-permeability phyllosilicate-rich gouges (Sibson, 1977; Rutter et al., 1986; Chester and Chester, 1998; Ikari et al., 2009; Holdsworth et al., 2011). The properties of phyllosilicates differ greatly from quartz-feldspar mixtures (Carpenter et al., 2011; Ikari et al., 2011a; Tesei et al., 2012), and if fault zones largely control the strength of the upper crust, the deformation mechanisms within phyllosilicate-rich fault cores could control a large proportion of localized deformation within the upper crust.

This thesis examines two examples (Minas fault zone and San Andreas fault) of phyllosilicate-rich, crustal-scale, transcurrent fault zones with a primary objective of establishing the active deformation mechanisms. The mechanisms are in turn

incorporated into a comparison of fault behaviour at different depths and boundary conditions.

The thesis follows the following format. A review of fault zone processes is presented (Ch. 2), followed by an overview of the methodologies employed in this study (Ch. 3). Structures from an inactive and exhumed segment of the Minas fault zone, Nova Scotia, Canada, are examined from the macro-scale (field observations) to the micro-scale (electron microscopy) to determine the operating deformation mechanisms (Ch. 4). Crystal chemistry of phyllosilicates is used to determine the temperature and pressures of formation for these structures.

Chapter 5 comprises an analysis of five sections of core from the San Andreas Fault Observatory at Depth (SAFOD) drilling program, which intersected a creeping portion of the San Andeas fault at ~2.7km depth. Detailed X-Ray diffraction (XRD) to determine the composition of phyllosilicate phases, and microstructural observations to determine the deformation mechanisms operating are presented.

Similarities between the host lithologies and tectonic settings at the two sites allows for their comparison as phyllosilicate-rich fault zones intersected at different crustal levels. Models of fault strength with depth, the role of effective grain size at the two sites, and the relevance of this study to crustal-scale transcurrent fault zones are discussed (Ch. 6).

CHAPTER 2: REVIEW OF FAULT ZONE PROCESSES

2.1 Fault Zone Structure

Fault zones are complex. While a fault can be described as a planar discontinuity in a volume of rock across which there has been displacement, fault zones are composed of many anastomosing fault strands, where individual strands commonly link and splay (Caine et al., 1996; Faulkner et al., 2003; Wibberley et al., 2008 and references therein). The faults are hosted within heterogeneous, anisotropic, and discontinuous lithologies, where the physical properties of the host rocks can significantly change over short distances (Fagereng and Sibson, 2010; Faulkner et al., 2010). In addition, the deformation mechanisms operating within the fault both cause and respond to significant changes in the material properties of the fault zone, causing dramatic changes in fault zone rheology over geologic time (Sibson, 1977, 1989; Rowe et al., 2011; Rutter et al., 2013). This leads to complex time-dependent systems, where the deformation processes can change the physical properties of the host to such an extent that the deformation mechanism itself changes (Fagereng, 2013). Such overprinting can erase the complex history of deformation within a given locality (Kirkpatrick and Rowe, 2013).

The study of fault zones (like most geological phenomena) is further complicated by the fact that the processes are occurring at depth in the crust. Active faults can only be directly studied at the surface and through recovered drill core. Indirect images at depth can also be acquired using a variety of geophysical techniques (Bleibinhaus et al., 2007; Ellsworth and Malin, 2011). Drilling projects, such as the San Andreas Fault Observatory at Depth (SAFOD; Ch. 4), the Japan Trench Fast Drilling Program (JFAST), the Deep Fault Drilling Program (DFDP) in New Zealand, and the Wenchuan

earthquake Fault Scientific Drilling Project (WFSD) in China offer spatially limited (*i.e.* the diameter of the core) observations of active fault zones at moderate depths (up to ~3.5 km) (Zoback et al., 2010; Xue et al., 2013; Kirkpatrick et al., 2015). While they offer excellent direct observations to couple with geophysical imaging, the small sample size limits the study of the complexity of fault zones. In addition, the drilling fluid used for lubricating the drill bit can locally increase the fluid pressure, potentially inducing seismicity (Raleigh et al., 1976; Kim, 2013), making the drilling of locked fault segments unsafe. Drilling programs through active faults are therefore generally carried out in regions of fault creep (Zoback et al., 2010), or where rupture has recently occurred (Xue et al., 2013; Kirkpatrick et al., 2015). As such, the conditions immediately prior to fault rupture are rarely directly analyzed.

In order to study the processes that occur at depth in fault zones, field studies are carried out in exhumed fault zones (Sibson, 1977), where exhumation and erosion have exposed the inner workings of inactive, ancient faults (Ch. 3). Studies must be carefully completed, as younger deformation, occurring during exhumation may overprint the processes occurring at depth. Additionally, late faulting can juxtapose units that were deformed under unrelated conditions. Microstructural work on field samples is then coupled with geophysics, modelling, and experimental rock deformation (done at various temperatures, confining pressures, fluid pressures, and strain rates to simulate various conditions in the crust) with the goal of creating a model of active fault systems at depth (Fig 2.1; Di Toro et al. 2012).

Continental crustal-scale faults likely control the strength of the crust, as strength at shallower depths is largely limited by the frictional strength of faults (Faulkner et al., 2010). The permeability of crustal-scale faults keeps the pore pressures in the rest of the

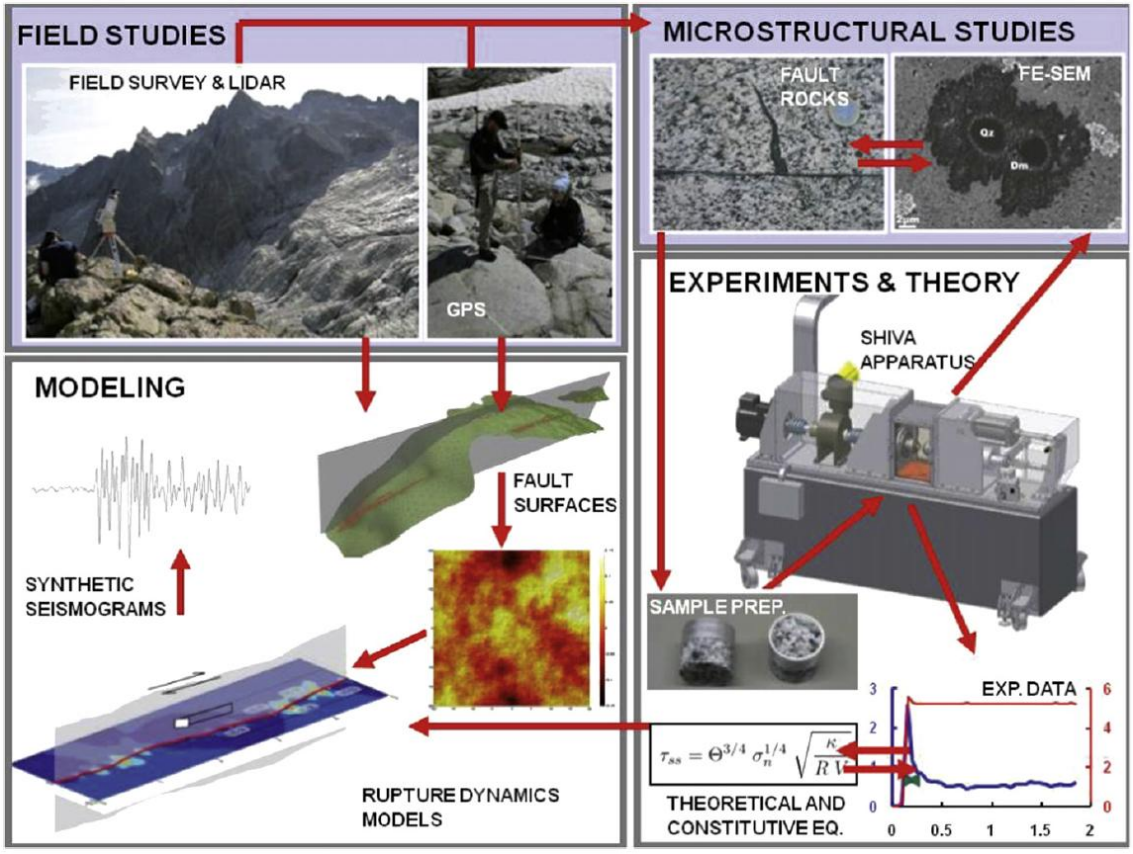

Figure 2.1: Multidisciplinary approach to the study of faults Field and microstructural studies are carried out and coupled with experimental data and theory to provide local data on faults. These are used in conjunction with modelling to create a geological model of faults. This geological model can then be coupled with geophysical data to better understand fault zone processes at depth (figure from Di Toro et al. 2012).

crust at approximately hydrostatic levels, helping to maintain crustal strength distal to fault zones (Townend and Zoback, 2000). An exception to this is in clastic continental margins and shale-rich mountain belts, where fluid pressures are commonly close to lithostatic pressure beyond a fluid-retention depth (2-4km; Suppe, 2014). The frictional strength and permeability of faults depends in large part on the material properties of faults and how they change over time. Field studies of fault zones offer insightful "snapshots" into fault zone properties, and allow one to begin to quantify and simulate these properties in the lab.

Despite the highly heterogeneous nature of fault zones, certain basic geometries seem to be consistently associated with crustal-scale faults. Most faults form a high-strain, low-permeability core, composed of fine-grained granular materials, surrounded by a fractured, high-permeability protolith known as the damage zone (Fig. 2.2; Chester and Logan, 1986; Chester and Chester, 1998; Wibberley et al., 2008; Faulkner et al., 2010). Mature fault zones tend to develop multiple cores, enclosing lenses of fractured protolith (Fig. 2.2b; Sibson, 1977; Faulkner et al., 2003). The deformational processes occurring within the core and damage zones are controlled by the material properties of the fault, temperature, confining pressure, pore fluid pressure, composition of the fluid present, and strain rate (Paterson and Wong, 2005). These vary greatly depending on location and depth in the crust.

Here, the processes and deformation mechanisms operating in fault zones at different levels in the crust are briefly discussed. General deformation mechanisms will be examined first, followed by their occurrence in faults from top to bottom.

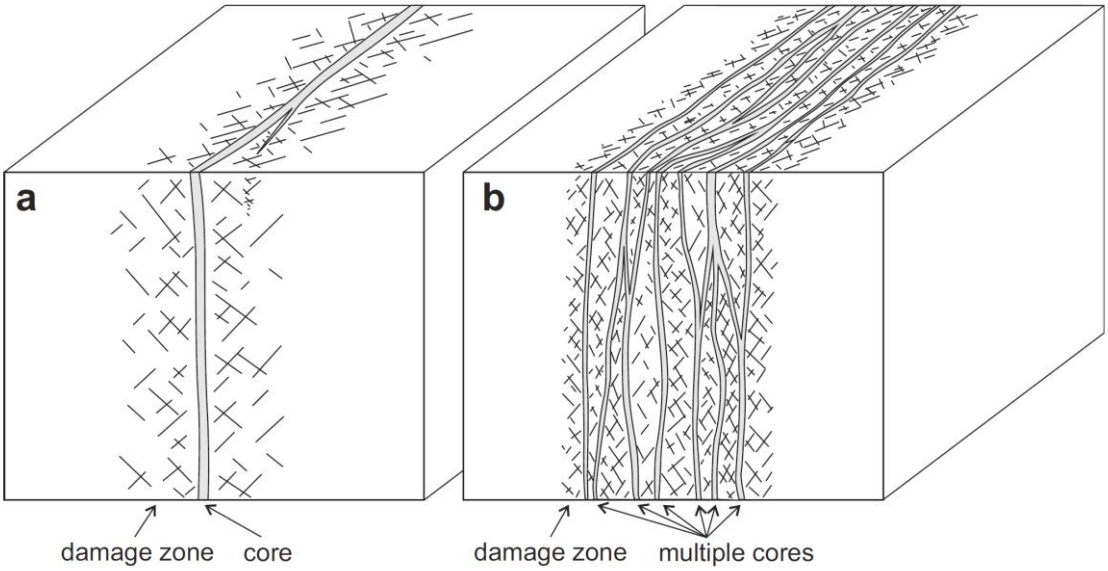

Figure 2.2: Structure of upper crustal, transcurrent fault zones **a)** A single high-high strain core surrounded by a fractured damaged zone based on field observations of the Punchbowl fault zone (Chester and Logan, 1986). **b)** Multiple fault core model, where anastomosing fault cores isolate variably fractured damage zones based on field observations of the Carboneras fault zone (Faulkner et al. 2003; figure from Faulkner et al. 2010).

2.2 How Geological Materials Deform

2.2.1 Categorizing deformation

There are several ways to examine how a rock deforms. One approach is to divide deformation by its flow unit of material displacement, *i.e.* the scale at which deformation occurs. Three categories of deformation mechanisms ensue that accommodate rocks and minerals deformation: diffusional flow, crystal plasticity, and granular flow (Rutter, 1986; Knipe, 1989; Paterson, 2013).

Diffusional flow has a flow unit at the atomic-scale, where deformation occurs by the movement of individual atoms or molecules. Included in diffusional flow is change of shape of materials through inter- or intra-crystalline diffusion, and viscous flow in amorphous materials. It also includes solution transfer processes (dissolution-precipitation) involving the change of shape of materials by transfer via a fluid phase (Paterson, 2013).

The flow units of intragranular flow are intracrystalline blocks or glide packets that slip over each other along specific crystallographic planes. These deformation mechanisms involve dislocations, and deformation occurs through crystal climb, glide, and creep (Knipe, 1989; Paterson, 2013).

Granular flow is the motion of individual grains, clastic fragments, or particles relative to one another, and typically occurs in soils and poorly cemented sedimentary rocks. Cataclastic flow in unconsolidated fault gouges would be included here, as would frictional sliding, and perhaps surprisingly, “superplastic” behaviour at high temperatures can be considered a form of granular flow from a mechanical perspective (Paterson, 2013).

Deformation can also be separated based on brittle and ductile processes. Brittle is used to describe gross fracturing (*i.e.* the formation of new surface area) on the scale of the whole body being discussed, with little internal deformation, due to loading beyond the elastic range (Paterson and Wong, 2005). Ductility, conversely, refers to the ability for materials to change shape without fracturing. It is important to note that these terms are scale dependent. For example a material that behaves in a ductile manner at a macro-scale may be deforming by distributed brittle deformation, which when viewed at the micro-scale, is clearly brittle (Paterson, 1958; Rutter, 1986). It is always important to note the scale of observation.

From the mechanistic standpoint, it is appropriate to discuss the change from brittle to viscous, or brittle to plastic deformation. In this sense, brittle refers to deformation mechanisms that involve granular flow, fracturing, and frictional sliding of materials, whereas plastic deformation refers to deformation via crystal plasticity (*i.e.* deformation by glide), and viscous refers to deformation by dislocation creep and diffusion (Rutter, 1986).

In general, in moving from shallow (low *P*-*T* conditions) to deeper (higher *P*-*T* conditions) crustal levels, behaviour becomes increasingly ductile (less brittle) at all scales. Theoretical, laboratory and observational studies all suggest that as pressure and temperature increase, deformation involves increasing amounts of crystal plasticity, diffusional flow, recrystallization, and flow of partially molten material (Kohlstedt et al., 1995). However, increasing the strain rate, or increasing the pore fluid pressure to near lithostatic pressures can cause reversion to brittle behaviour, including fracturing and cataclasis (Paterson and Wong, 2005).

Changes in the mode of failure depend on the material properties of the unit undergoing deformation, and can occur at different crustal levels within different geological materials. As such, there is no mappable surface in the crust across which a brittle-ductile transition occurs for all geological materials (Rutter, 1986), and should not be thought of synonymously with the seismic-aseismic transition, or a transition from brittle to plastic deformation. A brief overview of basic characteristics of deformation mechanisms in the crust will now be presented. Detailed accounts are contained in Lockner and Beeler (2002), Passchier and Trouw (2005), Paterson and Wong (2005), Karato (2012) and Paterson (2013), amongst others.

2.2.2 Brittle fracture, frictional sliding and cataclastic flow

Brittle fracture in experiment occurs in materials after loading beyond the elastic range, or after a brief period of ductility following elastic deformation (Paterson and Wong, 2005). Failure can either occur as a tensile fracture, oriented parallel to σ_1, or as shear fractures, where the fracture is typically oriented between 20° and 45° to σ_1. The relationship between fault orientation angle (θ), maximum compressive stress (σ_1), and minimum compressive stress (σ_3), follows directly from the expressions for normal stress (σ_n) and shear stress (τ) on a plane where

$$\tau = \frac{1}{2}(\sigma_1 - \sigma_3)\sin 2\theta \quad \text{and} \tag{1}$$

$$\sigma_n = \frac{1}{2}[(\sigma_1 + \sigma_3) - (\sigma_1 - \sigma_3)\cos 2\theta]. \tag{2}$$

Fluid pressures (P_f) act against the normal stress in all directions. Any load applied to a fluid will be countered by the pressure maintained by the fluid. As such σ_n can be replaced by the effective normal stress (σ_n') in the presence of fluid pressure, where

$$\sigma_n' = \sigma_n - P_f. \quad (3)$$

Shear fracture occurs when the shear stress on a plane reaches a critical value, which can be depicted as a Mohr failure envelope in τ versus σ_n space, and in ideal circumstances can be described by the Coulomb failure criterion

$$|\tau| = c + \mu_i \sigma_n \quad (4)$$

where μ_i is the coefficient of internal friction and c is cohesion (Fig. 2.3).

Brittle deviation from elastic behaviour first occurs by the growth of microcracks (or Griffith flaws), that exist in crystalline solids as open pores, contrasts in elastic properties of adjacent minerals, and grain boundaries. Shear failure will first occur along the most optimally oriented crack; however during propagation, local stresses at the crack tip contain a component of tension due to dilatancy within the sample that leads to the development of "wing" cracks as the crack tip propagates parallel to the σ_1 direction before the fracture toughness for shear failure is achieved. As the wing crack extends, stress intensity decreases and additional deviatoric stress must be applied to cause further crack growth (Lockner and Beeler, 2002). Microcracks elsewhere in the sample are activated in tension until bridging and coalescence of microcracks along a high shear stress plane causes failure.

Tensile fracture occurs when the tensile failure envelope (T_f) is reached, which in the crust occurs when there are extensional forces acting on a sample, or when fluid pressures generate effective tensile states. Deviatoric stresses ($\sigma_1 - \sigma_3$) must be low (generally $<4T_f$) or else the sample will fail by shear (Fig. 2.3).

A wide range of factors affecting the strength of rocks have been examined experimentally, leading to general statements on rock behaviour. Increasing the

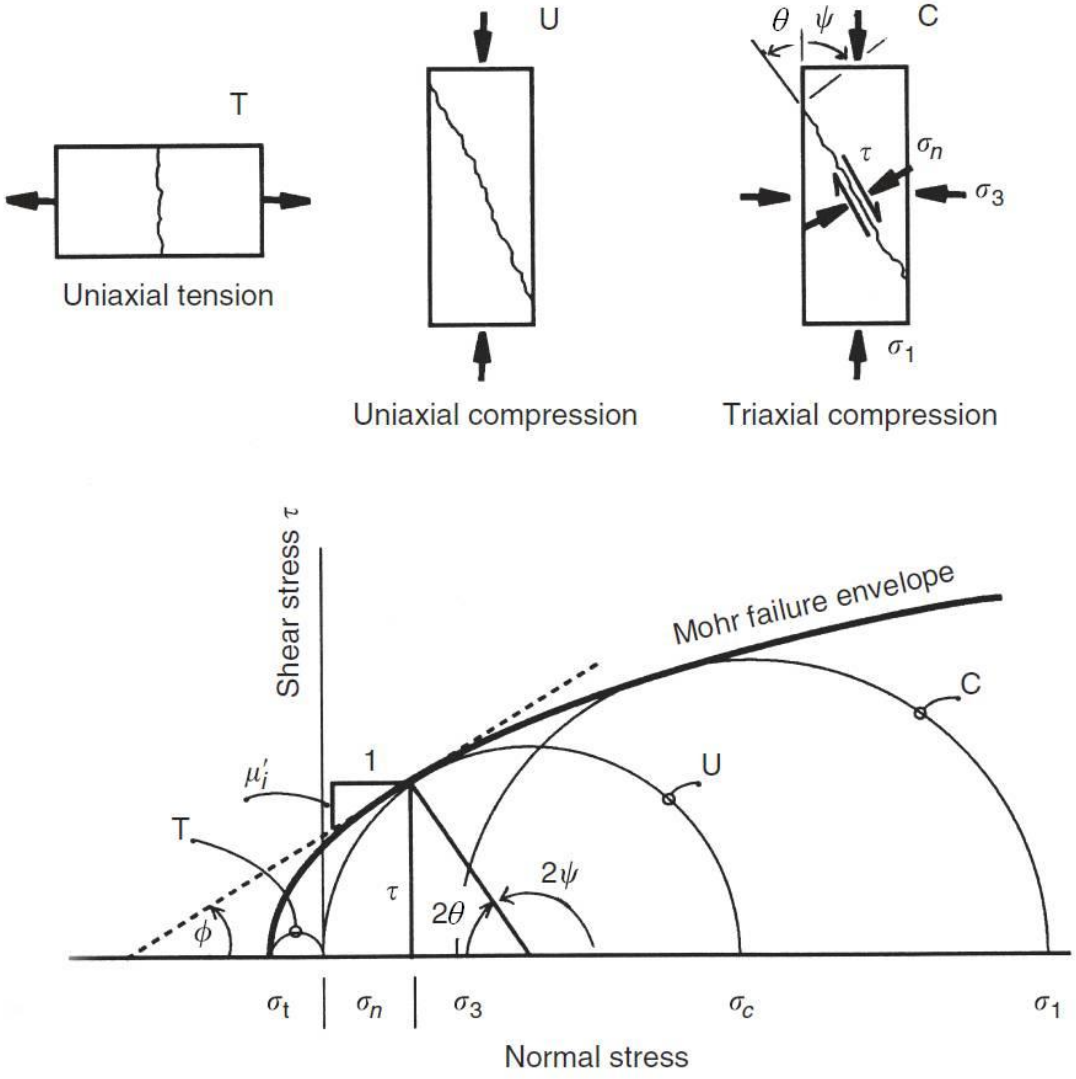

Figure 2.3: Constructing a Mohr failure envelope The three main experimental configurations for determining a Mohr failure envelope for a given sample, and an example of a Mohr failure diagram showing the geometric relationships with the experimental conditions labelled. (figure from Lockner and Beeler 2002).

confining pressure on a sample increases its strength by suppressing the growth of dilatant (tensile) microcracks, necessary for the development of a shear fracture (Lockner and Beeler, 2002). Pore fluid pressure lowers the effective normal stress within a rock, weakening it (Hubbert and Rubey, 1959). Increasing strain rate tends to increase the strength of rocks, due to the subcritical microcrack growth rate. At increased strain rate, there is less time for microcrack growth at specific stress states, allowing for a greater load to be applied to the sample before failure (Kranz, 1980). Increasing temperature reduces fracture strength by enhancing thermally activated mechanisms such as dislocation motion, diffusion, twinning, and the effects of water on grain boundary deformation mechanisms (Rutter and Mainprice, 1978; Hirth and Tullis, 1992).

Frictional sliding accounts for much of the movement along fractures in the lower crust (Beeler et al., 1996; Collettini et al., 2009). The resistance to frictional sliding is described by Amontons' law, where shear resistance to sliding along a surface (f_s) is directly proportional to the normal force (f_n) acting on it by

$$f_s = \mu_f f_n \tag{5}$$

where μ_f is the coefficient of friction. The applied forces are directly related to the stresses, which are described by the Coulomb relationship

$$\tau_c = \mu_f \sigma_n. \tag{6}$$

where τ_c is the shear strength, and σ_n is the normal stress acting on the plane at failure. For most geological materials the coefficient of friction is very weakly dependent on normal stresses. For coherent surfaces, the shear strength may not vanish at zero normal stress, so that

$$\tau_c = S_0 + \mu_f \sigma_n \quad (7)$$

where S_0 is an inherent shear strength similar to cohesion (Lockner and Beeler, 2002). In experimentation, the easiest ratio to measure is that of shear stress to normal stress which is referred to simply as friction (μ), and relates to the coefficient of friction by

$$\mu = \frac{\tau_c}{\sigma_n} = \frac{S_0}{\sigma_n} + \mu_f. \quad (8)$$

Byerlee (1978) compiled experimental results from a variety of rock types and found that at confining pressures less than ~5MPa (~200m depth) there is a wide variance in the frictional properties of rocks due to variance in surface roughness, while at confining pressures greater than ~5MPa the effect of surface roughness is diminished and friction is nearly independent of rock type. He proposed a piecewise linear function known as Byerlee's law where

$$\tau = 0.85\sigma_n \quad \text{where } 5 < \sigma_n < 200\text{MPa and} \quad (9)$$

$$\tau = 50\ MPa + 0.6\sigma_n \quad \text{where } 200 < \sigma_n < 1700\text{MPa.} \quad (10)$$

Significantly, Byerlee noted limitations in this approximation for sheet silicates (phyllosilicates). Montmorillonite and vermiculite in particular showed frictional values much lower than predicted by Eq. (9) and (10).

Bulk ductility can also occur through purely brittle processes in the form of cataclastic flow. The flow of whole grains, groups of grains, or rock fragments can accommodate significant distributed deformation in the lower crust through brittle fracture and frictional sliding of the grains past one another.

2.2.3 Dislocation glide, climb and creep

Materials can deform by intracrystalline deformation, by movement of defects through the crystal structure. Defects exist as line defects (*e.g.* edge dislocations and screw dislocations), point defects (*e.g.* vacancies, interstitials, or impurities), or surface defects (*e.g.* grain boundaries, twins, stacking faults, and cracks; Paterson, 2013).

Crystal dislocations are defined by a slip increment in a crystallographically defined direction (Burgers vector) along a crystallographic glide plane, together defining a glide system (Hirth and Lothe, 1982). Dislocations cannot end within a crystal; they can end at a crystal face, they can form loops (comprising segments of edge and screw dislocations), and they can form nodes with each other. When two dislocations of opposite signs (movements) meet, they annihilate each other. When they end at a crystal face, the remaining atoms are offset from their original configuration by the length of the Burgers vector (Hirth and Lothe, 1982).

The stress required for a dislocation to break apart and move an atomic unit within a glide plane is known as the critically resolved shear stress (CRSS). Dislocation movement allows for the plastic flow of crystals at stresses several orders of magnitude lower than that required to simultaneously break and restore all the interlayer bonds within a crystal through translation (Fig. 2.4a). This is because the breaking and reordering of bonds occurs at a "front" (*i.e.* the dislocation line itself) that moves over the plane on which translation is occurring, so that the breaking of bonds is only occurring at the front, lowering the stress that needs to be applied (Hirth and Lothe, 1982).

Line defects are confined to slip along a plane that contains both the Burgers vector and the dislocation line. Edge defects are confined to movement along a single

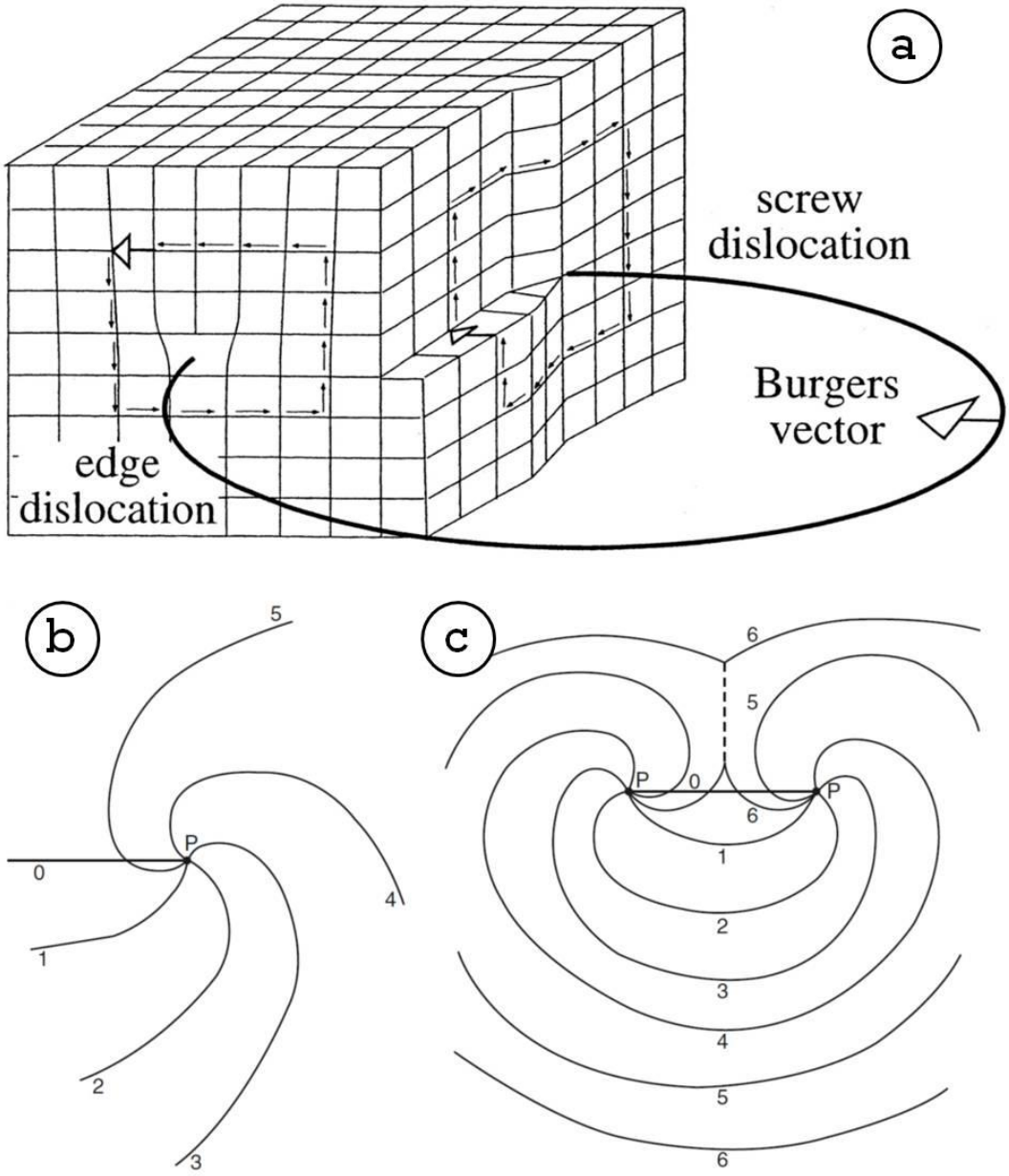

Figure 2.4: Types of dislocations and dislocation multiplication **a)** The two end members of dislocations (edge and screw), and their relationships to the Burgers vector. **b, c)** Two methods of increasing dislocation densities. In **b**, a dislocation is pinned on one end and increases in length as it spirals out. If the other end becomes pinned it can create a Frank-Read source (**c**) where dislocation loops can be repeatedly formed (figure from Paterson 2013).

glide plane, as the Burgers vector and dislocation line are perpendicular to one another, while screw dislocations are not restricted to a single plane as their dislocation line and Burgers vector are parallel to one another (Paterson, 2013).

In order to obtain appreciable strain by crystal plasticity within a crystal, dislocation densities must be very high. Ionic crystals of normal quality have dislocation densities around $10^{10}cm^{-2}$, while dislocation densities on the order of $10^{12}cm^{-2}$ are necessary to accommodate strain during plastic deformation (Paterson, 2013). Dislocation density can increase through multiplication by interacting with pinning sources (*e.g.* impurities, grain boundaries, other dislocations).

As dislocations progress through a crystal, they often become pinned by impurities or other dislocations. This leads to the formation of dislocation pile-ups or tangles, respectively. When one end of a dislocation is immobile the dislocation line will sweep circularly around the pinning point, and increase in length with every revolution around the source (Fig. 2.4b). If the mobile end of the dislocation also becomes pinned, a two-armed source is formed, known as a Frank-Read source (Frank and Read, 1950). The dislocation spirals out in two opposite directions simultaneously from the two pinning points, and when they meet, the ends annihilate creating a new dislocation loop (Fig. 2.4c). Spontaneously creating a dislocation loop within a crystal is unlikely; however, prismatic dislocation loops have been observed emanating from precipitates (*e.g.* fluid inclusions, impurities) when the internal stress is high (McLaren et al., 1983).

Increasing the dislocation density of a sample, through tangles and pile-ups, causes strain hardening within the crystal. In order to avoid this, dislocations must move out of their glide planes. Screw dislocations, because they are not restricted to one glide plane, can move into a new plane through cross-slip (Hirth and Lothe, 1982). This

requires that the dislocation move into a less favorable glide plane, and the critically resolved shear stress for movement on the new plane must be overcome to do this. Edge dislocations can only move into a new glide plane through climb, which involves the migration of vacancies to blocked sites of glide, allowing the dislocation to diffuse into another plane (Hirth and Lothe, 1982). The break (or step) formed by the movement of the dislocation into a new plane is known as a kink (movement within the glide plane) or a jog (movement perpendicular to the glide plane). Deformation can be thought of as glide dominated when the diffusion of vacancies is slow. When temperatures are high enough that climb accommodates dislocation movement readily, deformation is dominated by dislocation creep (climb and glide; Weertman, 1957).

When dislocation glide dominates deformation, high dislocation densities from tangles or "pile-ups" can lead to strain hardening, and ultimately, brittle failure (Knipe, 1989). Since crystals have a limited availability of glide systems, active slip systems are dependent on the orientation and magnitude of stress exerted on individual grains, and whether the critically resolved shear stress is exceeded for a given system. This creates inhomogeneous deformation within a given sample. Crystallographic preferred orientation (CPO), undulatory extinction, microkinks, and deformation lamellae are typical features indicating glide controlled slip (Knipe, 1989). Dynamic recrystallization (*i.e.* recrystallization under an imposed differential stresses) occurs through bulging recrystallization, where crystals with low dislocation density "bulge" into grains with high dislocation density along the bounds of crystals (Stipp et al., 2002).

At higher temperatures (*e.g.* when the homologous temperature, T_H, defined as $T/T_{melting}$, is greater than 0.4-0.5), dislocation climb controls deformation rate, and is referred to as dislocation creep (Weertman, 1957). Temperatures become high enough

for intracrystalline recovery; that is, dislocation re-organization into lower energy structures through annihilation and network formation. During this process a steady state dislocation density is approached for a given stress state (Hirth and Lothe, 1982). Dynamic recrystallization reorganizes grain boundaries through subgrain rotation at lower temperatures, and through grain boundary migration recrystallization as temperature increases (White, 1982; Hirth and Tullis, 1992; Stipp et al., 2002).

At high temperatures, when the differential stress becomes small, the rock will not be in a state of equilibrium, particularly if grain boundaries are highly irregular, which is common during grain boundary migration recrystallization. Static recrystallization may occur in the absence of differential stress, towards a lower internal energy configuration (with grains developing more polygonal grain boundaries; Passchier and Trouw, 2005).

For a steady-state strain rate during creep, a flow law can be derived. All flow laws are based on Orowan's equation (Orowan, 1934), which describes the shear strain rate ($\dot{\gamma}$) in terms of the Burgers vector (b), the average density of mobile dislocations (ρ_m), and the average velocity (v) as

$$\dot{\gamma} = b\rho_m v. \tag{11}$$

Dislocation creep is described using a power-law, where the function of stress is raised to the power n. For bulk-diffusion-controlled dislocation creep (also known as Weertman creep; Weertman, 1957), the 'natural' stress exponent derived is 3, and the flow law can be stated as

$$\dot{\gamma} = A_w \frac{\mu b D}{kT} (\sigma/\mu)^3 e^{(-\frac{H_L}{RT})} \tag{12}$$

where A_w is a material-dependent temperature constant, μ is the shear modulus, D is the constant for self diffusion, k is Boltzmann's constant, T is temperature, σ is the stress, H_L is the molar activation enthalpy for self-diffusion, and R is the gas constant.

2.2.4 Nabarro-Herring creep and Coble creep

Given sufficient temperature and time, diffusion itself can control the rate of creep. Coble creep *sensu stricto* accommodates strain by diffusion of atoms along the margins of crystals (boundary diffusion; Coble, 1963), where diffusion coefficients are typically enhanced compared with values in the lattice. Coble creep is described by the flow law

$$\dot{\gamma} = \frac{A_{CO}\mu V D_G W}{RTd^3}\left(\frac{\sigma}{\mu}\right)e^{(-\frac{H_L}{RT})} \tag{13}$$

where A_{CO} is a numerical factor primarily dependent on grain shape and boundary conditions, D_G describes the diffusion constant along grain boundaries, and W is the thickness of the grain boundary. Note the role of grain size (d) in Coble creep.

The diffusion of atoms through the body of the crystal (*i.e.* volume diffusion) can also control the rate of creep. This is known as Nabarro-Herring creep (Nabarro, 1948; Herring, 1950), and can be described using the flow law

$$\dot{\gamma} = \frac{A_{NH}\mu V D_V}{RTd^2}\left(\frac{\sigma}{\mu}\right)e^{(-\frac{H_L}{RT})} \tag{14}$$

where A_{NH} is a numerical factor primarily dependent on grain shape and boundary conditions, D_V is the diffusion constant for volume diffusion in a crystal.

Diffusional creep is strongly dependent on the grain size, where larger grain sizes make the process less efficient. The activation energy for boundary diffusion is less than for volume diffusion, which given the stronger inverse grain size dependence makes

Coble creep a more effective mechanism in the shallow crust. Nabarro-Herring creep is restricted to very high homologous temperatures, and/or to very coarse grain sizes.

2.2.5 Superplastic creep

Superplasticity refers to a material's ability to accommodate very high strains (ε>1000). The classical conditions required for superplasticity are high temperatures (T_H>0.5), a very small grain size (<10μm), and low stress and strain rates (Boullier and Gueguen, 1975). Modern studies, as reviewed by Langdon (2006), have extended the range of conditions under which superplastic behaviour can occur to include nanomaterials at lower homologous temperatures.

Superplastic creep can be accommodated by grain-boundary sliding, a phenomenon in which extreme bulk strain is achieved without substantial grain-scale distortion (Ashby and Verrall, 1973). Grain boundaries reorganize themselves through relative displacements accommodated by diffusion or dislocation movement (Gifkins, 1976). The difference between superplastic creep and granular flow is that diffusion is operating at a rate fast enough to prevent volume change within the sample (no porosity is created through the sliding process). It differs from Coble Creep in that individual grains are not changing shape (aspect-ratio) through diffusion; diffusion simply accommodates the sliding process between grains. Superplastic creep is highly dependent on grain size, and is proposed to occur after extreme grain size reduction, through dynamic recrystallization and/or cataclasis (Boullier and Gueguen, 1975; Hiraga et al., 2013).

2.2.6 Dissolution-precipitation creep

Dissolution-precipitation (or pressure solution) creep is a process in which a solid phase dissolves in a region of high stress, diffuses along a grain boundary interface

within a fluid, and is redeposited in a region of low stress (Rutter, 1983; Gratier et al., 1999; Renard et al., 2000). The fluid can exist as a thin continuous film, or as an island-channel structure along grain contacts (Rutter, 1983). The transfer process can be controlled by either the dissolution of the material, the transfer of the material, or the redeposition of the material (Niemeijer and Spiers, 2005). If the transfer process is rate-controlling, then it should follow the same form as Coble creep, except that the thickness of the grain boundary (W) will become the thickness of the intergranular fluid (δ), and the diffusional constant along the grain boundary (D_G) is exchanged for the molar volume (V_m), the molar concentration (c), and the diffusion constant (D_F) of the material in the fluid, so that

$$\dot{\gamma} = \frac{A_{FT}\mu {V_m}^2 c D_F \delta}{RTd^3}\left(\frac{\sigma}{\mu}\right) e^{\left(-\frac{H_L}{RT}\right)} \text{ (Paterson, 2013).} \quad (15)$$

If the reaction at the sources and sinks (grain boundaries) is the rate-limiting reaction, the equation becomes

$$\dot{\gamma} = \frac{A_R \mu b k}{RTd}\left(\frac{\sigma}{\mu}\right) e^{\left(-\frac{H_L}{RT}\right)} \quad (16)$$

where k is a rate coefficient. Here these equations are depicted so that the relationship between reaction rate, grain size, and rate-controlling mechanism can be viewed. Dissolution-precipitation creep will be more effective with decreasing grain size. Whether diffusion between source and sink or dissolution is the rate-controlling mechanism depends on local conditions (*e.g.* temperature, pressure, fluid composition).

Evidence for pressure solution in the rock record is recorded by stylolites, interpenetrative grains, crenulation cleavage, and truncated grains, fossils, or zoned crystals, each displaying dissolution. Reprecipitation is evidenced by newly grown grains in optic continuity with the relict grain and mineral growths in strain shadows.

The formation of a shape preferred orientation (SPO) without a crystallographic preferred orientation (CPO), deformation to high strains in the absence of dislocation movement and brittle fracture, and veining through reprecipitation of fluids can all be caused by dissolution-precipitation creep.

2.3 Fault Zone Processes in the Crust

With increasing depth in crust having a stable heat flow, temperature and pressure tend to increase linearly if no other thermal sources exist (*e.g.* plutonism, hydrothermal fluids). With increasing temperatures and pressures, deformation becomes increasingly ductile, whereas deformation mechanisms show increasing plasticity.

At shallow depths, pressure-dependent processes, including brittle fracture, cataclasis, frictional sliding, and cataclastic flow, control deformation (Fig. 2.5). The fault core, where the bulk of strain is accommodated, is primarily composed of gouge, cataclasites and ultracataclasites (Chester and Logan, 1986; Chester and Chester, 1998; Faulkner et al., 2010). Within the core, strain may be distributed relatively homogeneously, or discrete slip surfaces may accommodate a disproportionate amount of strain. Fault cores, because of their small grain size and relatively high phyllosilicate contents, are considered low permeability structures (Caine et al., 1996).

The damage zone, which surrounds the fault core, is characterized by fracturing. Fracture density (macro and micro) tends to decrease exponentially with distance from the fault core, and is related to the decay of stress away from a propagating fault tip (Mitchell and Faulkner, 2009). The maximum microfracture density is generally measured next to the fault core (Faulkner et al., 2010). Fault zone permeability is

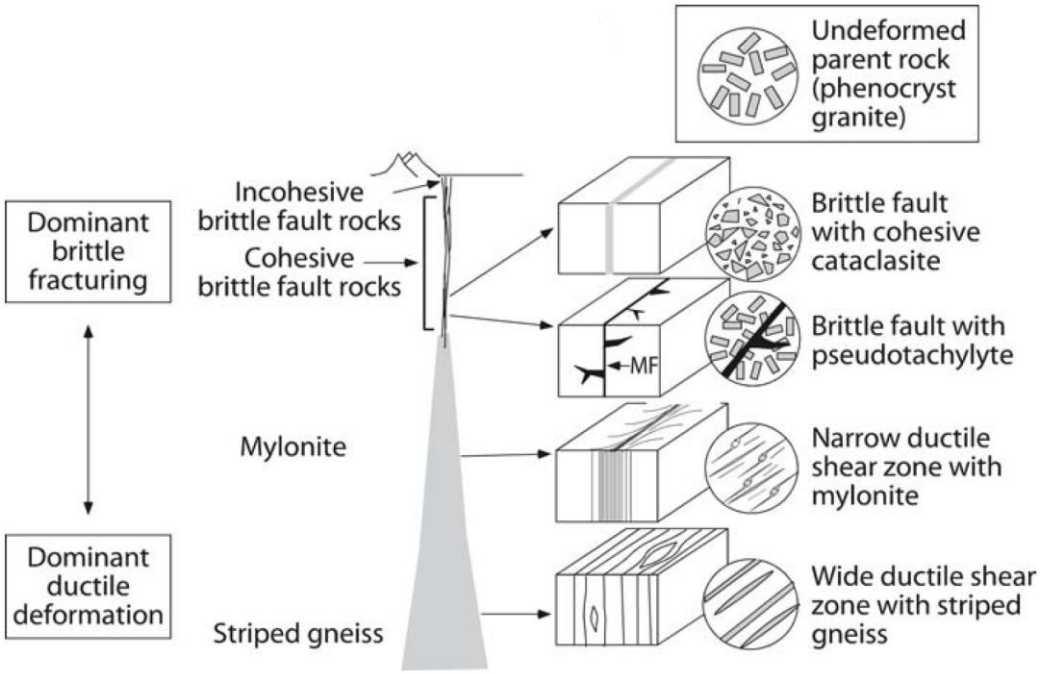

Figure 2.5: Cartoon of fault zone processes with depth With increasing depth in a transcurrent fault, processes become increasingly ductile and plastic as temperature and pressure increase. At shallow depths brittle fracture and frictional sliding dominate deformation, forming cataclasites and gouges as the dominant lithologies. Pseudotachylyte (frictionally generated melt during earthquake slip) can be found in seismogenic fault zones. Eventually temperatures and pressures become great enough to accommodate bulk ductility within the fault. Highly foliated mylonites become the dominant lithology at depth and attest to bulk ductility of the samples. At great depths where partial melting is an important process, gneisses are the dominant lithology within shear zones. (figure from Passchier and Trouw, 2005)

directly linked to fracture density; therefore, the core is often the least permeable feature in a fault, with the highest permeability immediate adjacent to it.

Pulverization is a special form of brittle fracture in damage zones characterized by a lack of shear in the brecciated material and a very small grain size (Wilson et al., 2005). They are inferred to form by a fast (potentially super-shear) propagating fracture due to quickly changing compressive and tensile stresses distal to the fracture front as the rupture passes (Reches and Dewers, 2005; Doan and Gary, 2009; Yuan et al., 2011). Experimentation has shown that a critical strain rate of ~150 s^{-1} must be achieved for pulverization to occur (Doan and Gary, 2009).

With increasing depth, deformation becomes increasingly distributed, and a change in failure mode occurs from localized faulting to distributed shear. The change in deformation mode is commonly known as the brittle-ductile transition (but see Rutter, 1986), while the change in dominant deformation mechanisms is known as the brittle-plastic transition (Rutter, 1986; Kohlstedt et al., 1995). A zone of semi-brittle deformation is anticipated to occur between the brittle-ductile and the brittle-plastic transition (Sibson, 1977; White and White, 1983; Kohlstedt et al., 1995). The macroscopic brittle-ductile transition of the crust bears the load of the upper crust, and most major earthquakes are thought to nucleate around this depth (Sibson, 1983).

Before the aforementioned brittle-ductile transition mylonites become the dominant lithology in shear zones (Fig. 2.5). Shear sense indicators are found throughout shear zones and include shear bands, porphyroclast systems, sigmoids, oblique foliation, fold asymmetry, and sheath folds (Passchier and Trouw, 2005).

A plot of the behaviour of some better understood geological materials with depth is provided in Fig. 2.6. Most crustal strength profiles are based on the behaviour of

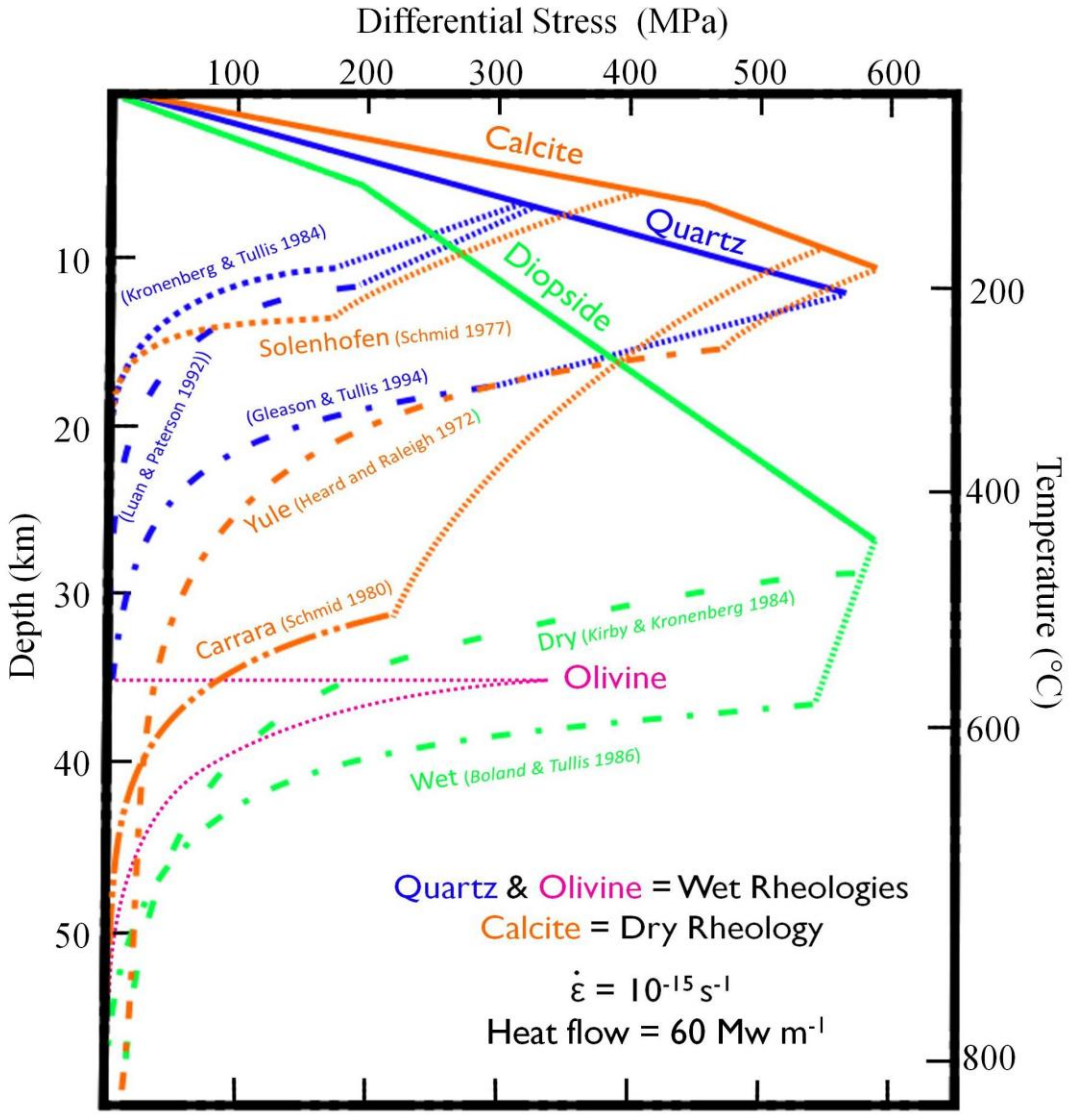

Figure 2.6: Strength of different materials with depth in the continental lithosphere Strength of various geological materials with depth in the crust after Kohlstedt et al. (1995). Solid lines represent brittle failure and frictional sliding, while curved dotted lines are plastic flow laws derived from the experiments cited. Calcite values are from three separate marbles (Carrara, Yule, and Solenhofen) traditionally used in experimentation. The stippled lines connecting the two deformation regimes represent the zone from the crustal-scale brittle-ductile transition (BDT) to the brittle-plastic transition (BPT). In this zone semi-brittle deformation is dominant and constitutive equations do not exist, with the exception of calcite, where Rutter (1986) showed that a power-law breakdown occurs through cataclastic flow. The brittle-ductile transition is the strongest part of the crust, and load is eventually transferred here by stress release in weaker portions of the crust (shallower and deeper). Large earthquakes nucleate when this strong portion of the crust eventually fails (Sibson, 1983). Flow laws for olivine are included at the transition from crust to mantle.

mono-mineralic quartz for the crust, while the mantle is modelled as olivine (Kohlstedt et al., 1995). This is a stark simplification from field observations of fault zones, where complex interplays between lithology, rheology and seismicity are found (Sibson, 1989; Rowe et al., 2011; White, 2012). Within faults, phyllosilicate-rich cores are common within the upper crust, and the rheology of these mixtures control the strength of the faults (Chester and Logan, 1986; Chester and Chester, 1998). Additionally processes such as pressure solution are not included in most crustal strength profiles, though the operation of this deformation mechanism could control deformation at a range of depths in the crust (Bos and Spiers, 2002; Niemeijer and Spiers, 2005; Imber et al., 2008). This thesis looks at two natural fault zones in an attempt to gain insights into the role of phyllosilicates in crustal-scale faults at different depths.

CHAPTER 3: METHODOLOGIES

3.1 Analysis of Microstructures

Understanding the processes that occur before, during, and after earthquakes at depth is hampered by our inability to directly observe them. Field work along strands of active faults allows us to study the effects of faults when they rupture the surface (Fenton et al., 2001); however, little insight is gained from these studies into the processes that cause earthquake propagation and initiation, which generally occurs at the brittle-ductile transition for quartzofeldspathic rocks (~10-20 km depth; Sibson, 1982; Kohlstedt et al., 1995). Drilling allows the study of active processes occurring at moderate depths (*e.g.* SAFOD at ~3 km, see chapter 4; Zoback et al., 2010; Holdsworth et al., 2011), but complications arising from high lithostatic pressures prevents deeper drilling, and the fear of rupturing an earthquake in locked segments though the pumping of drilling fluids prevents drilling into critically stressed active faults (Raleigh et al., 1976; Kim, 2013). Experimentation allows us to simulate various conditions, but the small sample sizes (cm-scale) does not mimic the complexity of anastomosing systems of varying rock types and morphologies observed in natural fault zones; additionally, the strain rates are generally several orders of magnitude higher than in nature (Paterson and Wong, 2005). Scaling relationships must be determined by comparing samples produced in the labs with natural samples from the field. Exhumed fault zones allow for direct observation of natural rocks subjected to the effects of fault motion at depth, and the study of these zones is therefore of paramount importance for understanding fault zone processes (Sibson, 1977; White and White, 1983; Faulkner et al., 2003; Fagereng and Sibson, 2010; Rowe et al., 2011). By studying the microstructures in these rocks and

comparing them to the structures formed during experimentation at varying temperatures and pressures, we can attempt to understand the processes in mature fault zones at depth.

3.1.1 Preparation of polished thin sections

Oriented thin sections were cut at the University of New Brunswick from field samples for the Minas fault zone and core from SAFOD. Polished thin sections were prepared for optical microscopy, microprobe, and SEM analysis. For SEM analysis, regions of interest were highlighted through optical microscopy.

3.1.2 SEM

A JEOL JSM6400 Digital SEM housed at the Microscopy and Microanalysis facility at the University of New Brunswick was used for SEM analysis. The microscope is equipped with Geller dPict digital image acquisition software, and an EDAX (Genesis) Energy Dispersive X-ray (EDS) Analyzer. Samples were carbon coated using an Edwards 306A carbon coater before observation in the microscope. Analysis was performed at an accelerating voltage of 15kV and a beam current of 1.5nA, with a working distance of 14mm. For EDS, collection time was 50 seconds per analysis point. Images were collected using Gatan Digital Micrograph.

3.1.3 TEM sample preparation

For samples analyzed by TEM, an additional doubly polished thin section was prepared and adhered to a glass slide using Crystalbond^{TM} thermo polymer adhesive. Copper slots (3mm) were adhered to the sample using epoxy in regions of interest determined by optical microscopy. Heating of the sample weakens the Crystalbond^{TM} and allows for the removal of the sample from the glass slide; the sample is then washed in acetone to remove any excess Crystalbond^{TM}. Copper slots are isolated using an X-Acto knife, and thinned in a Gatan Precision Ion Polishing System (PIPS) until a small

hole forms in the centre. The PIPS, which slowly thins the sample through ion milling using two argon ion guns at low tilt angles (4-5°) to the sample, creates a wedge shaped region of thinned material around the hole which meets the criterion of electron transparency (thickness is <200nm) for analysis by TEM.

3.1.4 TEM

Analytical (S)TEM was carried out using a JEOL 2011 scanning transmission electron microscope housed at the Microscopy and Microanalytical facility at the University of New Brunswick. The microscope is equipped with an EDAX Energy Dispersive X-ray system, and Gatan digital cameras. Analyses were performed at an accelerating voltage of 200kV. Images were collected using Gatan Digital Micrograph.

3.2 Analysis of Phyllosilicates

Understanding the micromechanics of deformation requires determination of the temperatures and pressures at which the rocks deformed, as decreasing temperature can often cause similar micromechanical effects as increasing strain rate (Paterson and Wong, 2005). Estimates of temperature and pressure determined from metamorphic mineral assemblages are often well constrained in the lower crust, whereas upper crustal (lower to sub-greenschist facies) processes are poorly understood. The slow reaction kinetics at low temperatures as well as the small grain size makes the study of these processes much more difficult than their higher *P-T* equivalents (Fagereng and Cooper, 2010). However, lower to sub-greenschist conditions are ubiquitous in the upper crust, and within the study of fault mechanics, understanding these rocks is of particular relevance to the study of accretionary complexes and brittle fault zones.

X-Ray diffraction (XRD) and electron microprobe were used to determine variations in phyllosilicate crystal chemistries and compositions. Both oriented aggregate mounts and random powders were prepared for XRD, while individually selected phyllosilicates were analyzed from polished thin sections using the electron microprobe.

3.2.1 Preparation of random powders for XRD

Samples were ground by hand for XRD to a size of 0.2mm. A portion of this powder was used for the analysis of randomly oriented powders, where crushed powder of the rock samples was loaded and compacted into a circular well in a plastic sample holder for analysis. The remainder was used to create oriented aggregate mounts.

3.2.2 Preparation of oriented aggregate mounts for XRD

Oriented aggregate mounts were prepared by separating the clay minerals from the silt particles following the procedure of Poppe et al. (2001). Five mL of powdered sample, 0.25g of dispersant (sodium hexametaphosphate), and ~20mL of distilled water were placed in centrifuge tubes (Fig. 3.1a,b). Tubes were placed in an ultrasonic bath for 2 minutes to ensure that the samples were dispersed. A centrifuge was then used to separate the clays from the silt (Fig. 3.1c). Run times were calculated using Stokes law. After each run the supernatant fluid was poured off into a beaker (Fig. 3.1d), and the centrifuge tube was cleaned and rinsed thoroughly. The supernatant was then returned to the centrifuge tube, was placed in the ultrasonic bath for 2 minutes, and was run again. This process was repeated until the supernatant fluid was reasonably clear (4-5 times).

A Millipore HA, 47-mm, 0.45-micron filtration device was used to create the oriented aggregate mount. The supernatant fluid was poured into the filtration device (Fig. 3.1e) which contains a vacuum pump on one side to pull the fluid through the filter paper. The

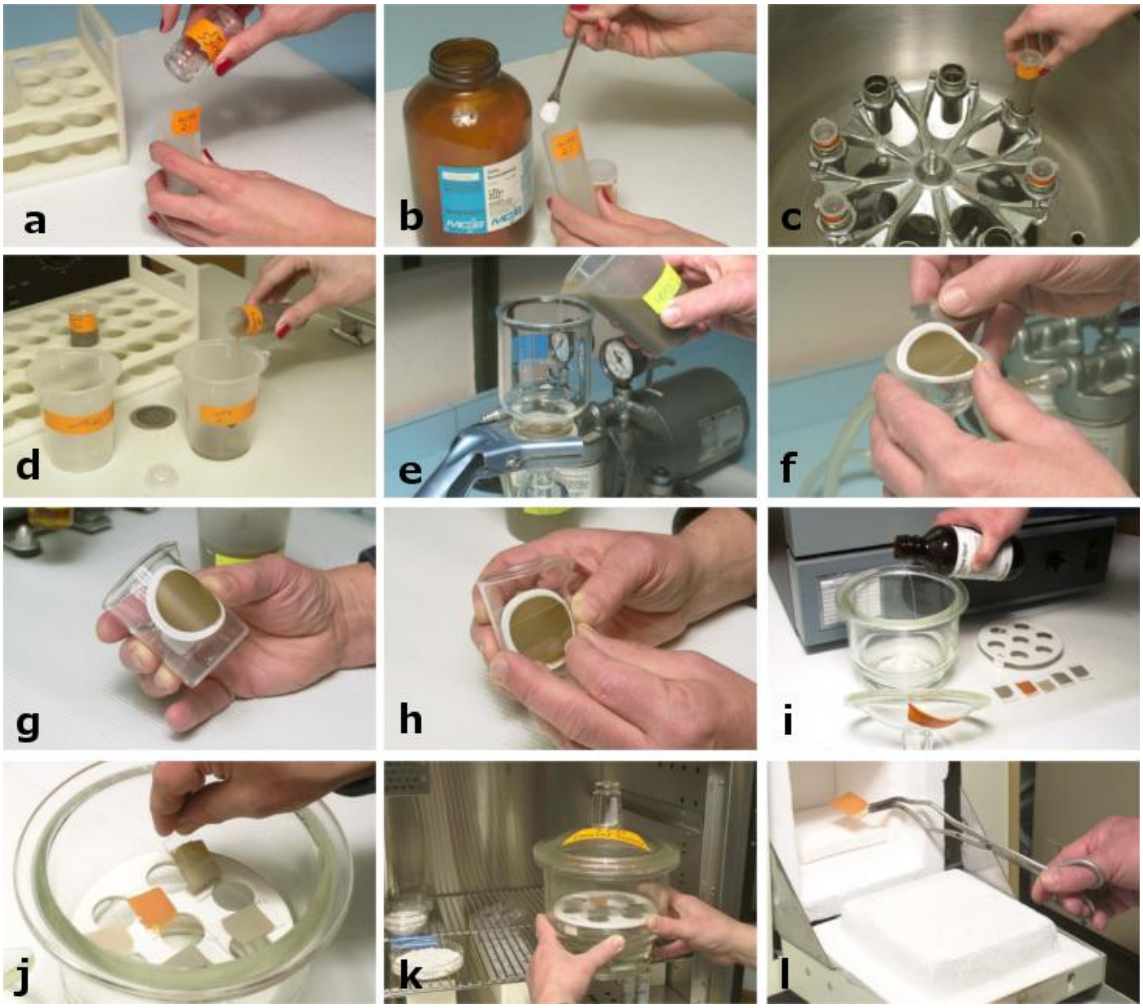

Figure 3.1: Preparation of oriented clay aggregates **a-b**) Sample, dispersant, and distilled water were placed in centrifuge tubes. An ultrasonic bath was used to mix samples. **c**) A centrifuge was then used to separate the clays from the silt. Run times were calculated using Stokes law. **d**) After each run the supernatant fluid was poured off into a beaker, and the centrifuge tubes were cleaned. The supernatant was then returned to the centrifuge tube, and the process was repeated until the supernatant fluid was reasonably clear (4-5 times). **e**) The supernatant fluid was poured into the filtration device which contains a vacuum pump on one side to pull the fluid through the filter paper. The clays adhere to the filter paper. **f**) The filter paper is then removed from the filtration device and **g**) is wrapped around a cylinder. **h**) With the membrane filter and clay film center-positioned near the glass slide, the filter paper with clay film is quickly, rolled across the slide to transfer the clay film to the slide. For glycolation (**i**), samples were placed on top of a holder above a small pool of ethylene glycol for a minimum of 24 hrs (**j,k**). For heat treatments (**l**) samples were placed in an oven for a minimum of 30 minutes.

clays adhere to the filter paper. The filter paper is then removed from the filtration device and is wrapped around a cylinder 2.5-5cm in diameter (Fig. 3.1f,g). With the membrane filter and clay film center-positioned near the glass slide, the filter paper with clay film is quickly, lightly, and smoothly rolled across the slide to transfer the clay film to the slide (Fig. 3.1h). Any hesitation or jerky motion during the transfer may cause rippling of the film and disrupt the preferred orientation. If this occurred the entire process was repeated. The slide is then given 24 hours to air dry before the first analysis.

3.2.3 XRD of randomly oriented powders

X-ray powder diffraction patterns for all samples were analyzed using a Bruker D8 Advance spectrometer. Finely crushed powder of the rock samples was loaded and compacted into a circular well in the plastic sample holder and placed on the sample stage with three reference points for sample height. The X-ray source was a sealed, 2.2 kW Cu X-ray tube, maintained at an operating current of 40 kV and 30 mA. Samples were scanned in the range of 2-90^{o} 2θ. A step size of 0.02^{o} and a step time of 1.0 sec were used during the measurements. The raw data obtained from the spectrometer was analyzed and refined by the program EVA (Bruker). Phase identification was made with a combination of windows-based programs Bruker EVA and MDI Jade.

3.2.4 X-Ray diffraction of oriented aggregate mount

Samples were analyzed using XRD under the same parameters as described above, but with a range of 2-35^{o} 2θ in order to achieve greater resolution of the clay mineral structure. Each oriented aggregate was analyzed three to four times: air dried, glycolated, heat treated to 400°C and if necessary heat treated to 550°C.

After having air dried for a minimum of 24 hours following preparation, the oriented aggregate mounts were analyzed for their first run. After each sample was

analyzed, samples were subjected to an ethelyne glycol treatment which causes any swelling clays to expand. Ethelyne glycol was poured into a desiccator to a depth of 1 cm (Fig. 3.1i). A shelf was placed over the ethelyne glycol on which the oriented aggregate mounts were placed (Fig. 3.1j). The samples were then covered and placed in an oven at 60°C for a minimum of 24 hours (Fig. 3.1k). Samples were taken out individually minutes before they were subjected to their second XRD analysis.

Once each sample was run glycolated, they were subjected to heat treatment (Fig. 3.1l). Heat treatments at various temperatures allow for clay mineral differentiation as they cause changes in crystal structure spacings and structure depending on species and temperature (Moore and Reynolds, 1997; Poppe et al., 2001). The first heat treatment was to 400°C. Samples were places in a tube oven pre-heated to 400°C for no less than 30 minutes. The samples were given 2 minutes to cool before their third analysis by XRD. For SAFOD samples, where a wider range of low-temperature clays are observed, a subsequent treatment to 550°C was performed.

3.2.5 Electron microprobe analysis of phyllosilicates

Major element chemical compositions of individually selected phyllosilicates were obtained using a JEOL JXA-733 Electron Microprobe with four 2-crystal spectrometers housed at the Microscopy and Microanalysis Facility at the University of New Brunswick. Standards used were jadeite (Na), clinopyroxene (Si, Ca), olivine (Mg), bytownite (Al), orthoclase (K), ilmenite (Ti), hematite (Fe), and bustamite (Mn). Formal references for standards, and reference analyses are found in Appendix 1. The microprobe was operated using an accelerating voltage of 15kV, and 30nA of current intensity. The measured intensity ratios for Al, Si, and Fe were recalibrated (post-acquisition) to a biotite standard.

CHAPTER 4: THE MINAS FAULT ZONE

4.1 Introduction

4.1.1 Introduction to the Minas fault zone project

The Appalachian orogen stretches from Alabama to Newfoundland within North America. The northern Appalachian orogen located within the Canadian provinces of New Brunswick, Nova Scotia, and Newfoundland is divided into five broad tectonic zones based on stratigraphic and structural contrasts (Williams, 1979; Hibbard et al., 2006). These are, from west to east, the Humber, Dunnage, Gander, Avalon, and Meguma zones (Fig. 4.1). The Humber zone is considered to be the edge of ancestral North America, while the other four zones are ribbon-shaped crustal blocks, composed of one or more terranes, that were accreted sequentially onto ancestral North America between the Late Ordovician and Early Carboniferous (van Staal et al., 2009). The Dunnage zone is peri-Laurentian, while Gander, Avalon, and Meguma are of Gondwanan affinity (van Staal et al., 2009). The accretion of each zone controlled an episode of orogenic activity within the northern Appalachians, namely: 1) the Taconic orogeny (~495-450Ma) in which oceanic terranes and arcs were accreted to the edge of ancestral North America along with Dashwoods forming the Dunnage zone, 2) the Salinic orogeny (430-422Ma) in which Ganderia was accreted to ancestral North America, 3) the Acadian orogeny (421-395Ma) in which Avalonia was accreted, and 4) the poorly understood and controversial (see below) Neoacadian orogeny (400-350Ma) in which Meguma was accreted against Avalonia.

The Minas fault zone defines the boundary between the Avalon and Meguma zones (Fig. 4.2). It is a series of anastomosing faults that record predominantly dextral

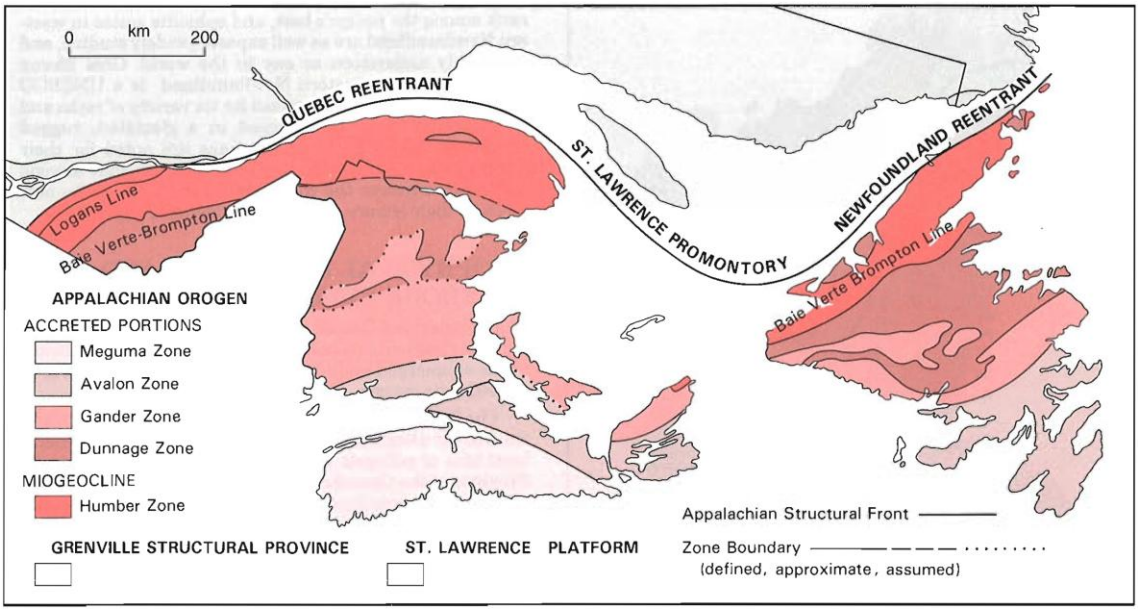

Figure 4.1: Major structural zones of the Appalachians The major zones of the Canadian Appalachians. The Avalon and Meguma zones are separated by the Minas fault zone. (Figure from Williams 1995)

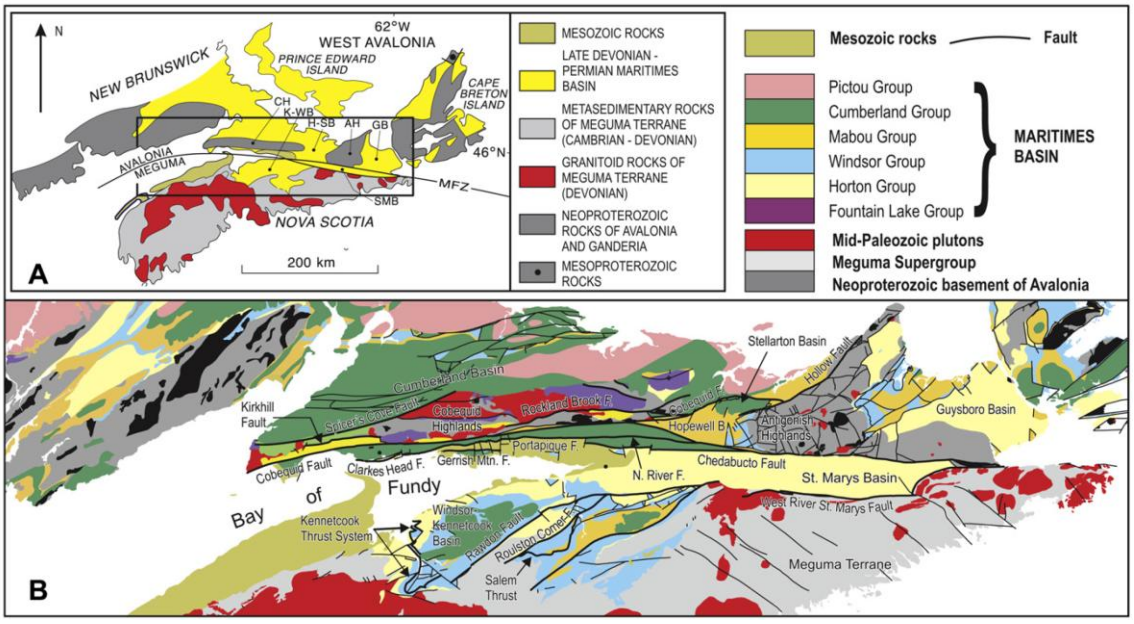

Figure 4.2: Location of the Minas fault zone and Cobequid fault **A)** General map of the Minas fault zone separating the Avalon zone to the north from the Meguma zone to the south. **B)** Overview of the major lithological groups of Nova Scotia (Keppie, 2000) and New Brunswick (New Brunswick Department of Energy and Resources, 2000) in the region of the Minas fault zone. (Figure taken from Murphy et al. 2011)

motion (Keppie, 1982; Mawer and White, 1987; MacInnes and White, 2004; Murphy et al., 2011). Centered along the Cobequid and Chedabucto faults, the Minas fault zone runs ~300 km in an E-W trend from Guysborough, Nova Scotia on the eastern coast to Cape Chignecto in northern Nova Scotia (Keppie, 1982; MacInnes and White, 2004; Murphy et al., 2011; Fig. 4.2). This study examines a phyllosilicate-rich segment of the Minas fault zone located along the Cobequid fault, at Greville Bay, Nova Scotia to elucidate the micromechanics of deformation within large transcurrent fault zones at depth. This study begins with an overview of the history of the Minas fault zone, then presents the findings from field work and subsequent micro-analytical work.

4.1.2 The Avalon zone

The Minas fault zone is bounded to the north-west by the Avalon zone (Fig. 4.2). The Avalon zone is primarily composed of fault bounded Neoproterozoic (635 – 570 Ma) juvenile arc-related volcanic belts with co-genetic plutonic rocks and sedimentary successions deposited in a variety of arc-related basins on the edge of Gondwana (Pe-Piper et al., 1989; Murphy, 2003). These are overlain by overstepping Cambrian - Early Ordovician shale-rich platformal successions. Mid-Cambrian (*c.* 475 Ma) bimodal volcanics were extruded sporadically and likely represent transtension just prior to rifting from Gondwana (van Staal et al., 2009). Early Silurian to early Devonian siliciclastic successions overlie all the latter lithologies (Hamilton and Murphy, 2004; Murphy et al., 2011).

Following a complicated and long lived Neoproterozoic history, paleomagnetic data and fossils indicate that Avalonia rested near or against the margin of Gondwana during the deposition of the Cambrian – early Ordovician platformal successions (van Staal et al., 2009). Similarities between Avalonian and Ganderian Cambrian to early

Ordovician sedimentary sequences have led some to believe they were contiguous with the Gondwanan margin; however, a wide range of geological arguments by Landing (1996) indicated that the two were unrelated terranes by the onset of the Paleozoic, which led Murphy et al. (2002) to propose an alternative position for Avalonia in proximity to Amazonia; in other words, close to Ganderia along the Gondwanan margin, but not connected (van Staal et al. 2009 and refs within).

4.1.3 The Meguma zone

Meguma, the most outboard of the five zones, is only exposed on land in southern Nova Scotia, to the south-west of the Minas fault zone. However, deep drilling and seismic surveys off the coast of Maine have traced the Meguma zone from the southernmost part of the Grand Banks of Newfoundland to southernmost Cape Cod (Hutchinson et al., 1988; Keen et al., 1991; Pe-Piper and Jansa, 1999). The oldest exposed rocks of the Meguma zone comprise a Cambrian – Early Ordovician turbiditic sandstone-shale sequence which was likely deposited on the continental rise next to Gondwana (van Staal et al., 2009). Rifting from Gondwana (approximately modern Morocco) deposited rift related bi-modal volcanics at ~440Ma disconformably over the sediments (van Staal et al., 2009).

4.1.4 Original relationship between the Meguma and Avalon zones

Two differing hypotheses on the original relationship between the Avalon and Meguma zones have emerged in the literature (Murphy et al., 2004). One considers Avalon and Meguma as two separate terranes, formed in different parts of Gondwana, which travelled separately with Iapetus and were accreted sequentially onto the Laurentian margin. The collision of Avalonia with Ganderia defines the Acadian Orogeny while the collision of Meguma with Avalonia is described as the Neo-Acadian

orogeny (van Staal et al., 2009). This hypothesis is based on markedly different Paleozoic stratigraphies within the two zones, and spatially restricted, voluminous, 395-390 Ma, S-type granitoids, which are consistent with a shallowly dipping Andean type subduction zone (Murphy et al., 1999; van Staal et al., 2009). A second hypothesis states that Meguma was deposited on Avalonian basement; the two travelled as a single tectonic unit, and were accreted together to the edge of Laurentia by the early Silurian during the Acadian orogeny (Keppie et al., 1997; Murphy et al., 2004). The lack of an intervening suture zone ophiolite, similarities between Nd isotope signatures in basement rocks from both zones, and detrital zircon populations are used to argue for this interpretation (Murphy et al., 2004).

Deep seismic studies off the coast of Maine show a minor Meguma thrust over Avalon relationship (Fig. 4.3), though the contact between the two zones has the character of a primarily transpressional continent-continent collision (Keen et al., 1991; Pe-Piper and Jansa, 1999). The interpretation of Pe-Piper and Jansa (1999) argues that suturing between the two zones occurred during the final convergence of Laurentia and Gondwana during the Alleghenian orogeny in the early Carboniferous, consistent with the interpretation of a Neo-Acadian orogeny.

Ambiguity in the original relationship between the Avalon and Meguma zones arises from intense Carboniferous deformation along the Minas fault zone associated with the Alleghenian orogeny which will be discussed in detail later. In addition the many episodes of compressional (thrusting, faulting) and extensional (basin formation) tectonics recorded along the Minas fault zone masks earlier phases of deformation.

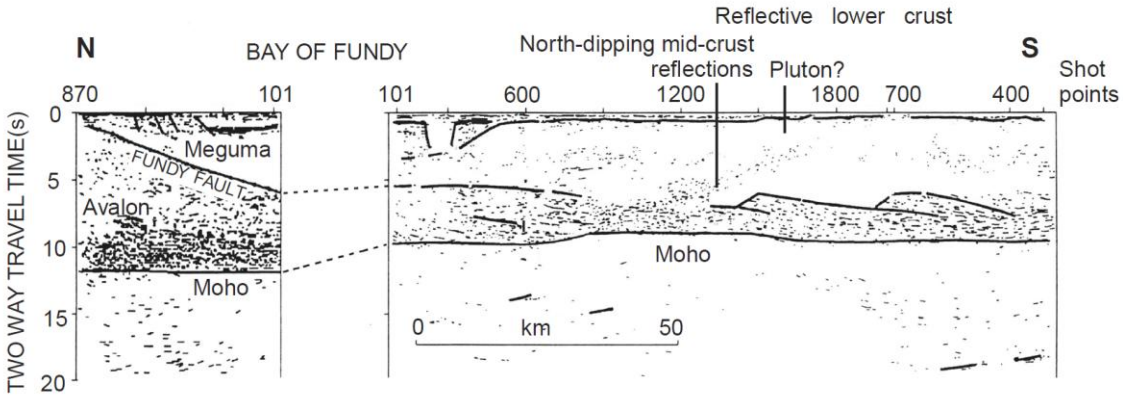

Fig. 4.3: Meguma over Avalon seismic interpretation Line drawing of deep-crustal seismic reflection lines across the Bay of Fundy – Southwest Scotian Shelf showing a Meguma thrust over Avalon relationship (Keen et al., 1991; Pe-Piper and Jansa, 1999).

Table 4.1: Major stratigraphic subdivisions of the Maritimes Basin

Group	Typical lithologies	Age Range
Pictou Gp	Red, non-marine clastic sedimentary rocks	Middle Pennsylvanian (Moscovian) to Lower Permian?
Cumberland Gp	Grey, coal-bearing, non-marine clastic sedimentary rocks	Lower Pennsylvanian (Bashkirian) to Middle Pennsylvanian (Moscovian)
Mabou Gp	Red, generally fine-grained lacustrine clastic sedimentary rocks, minor non-marine evaporates	Middle Mississippian (late Visean) to Upper Mississippian (Serpukhovian)
Windsor Gp	Marine to restricted limestones, evaporates and fine-grained red clastics	Middle Mississippian (Visean)
Horton Gp	Grey to red, mainly lacustrine to fluvial clastic sedimentary rocks	Upper Devonian to Lower Mississippian (Tournaisian)
Fountain Lake Gp	Bimodal volcanic and volcaniclastic rocks with associated mainly red, subaerial clastic sedimentary rocks	Upper Devonian

4.1.5 The Maritimes basin

The Maritimes basin is a large basin of primarily Carboniferous sediment fill that first opened during the Acadian orogeny, though the majority of sedimentation occurred during the Alleghenian orogeny, as clockwise rotation of Laurentia relative to Gondwana caused the opening of basins along releasing bends in major strike-slip faults (Murphy et al., 1999; Murphy, 2003). It covers much of the Maritime provinces of New Brunswick, Nova Scotia, Prince Edward Island, and Newfoundland (Calder, 1998). A nearly complete stratal sequence in Nova Scotia records continuous deposition up to 12 km thick during the Carboniferous. Basin inversion and unroofing in the early Permian marks the end of sedimentation in the basin, as Pangea was finally assembled and subsequently rifted again in the late Triassic (Durling and Marillier, 1993; Murphy et al., 2011).

The fill of the basin is complex, but in most areas a simple subdivision into six groups has been adopted (Table 4.1). These comprise nearly all of the rocks examined in the Greville Bay study area (with the exception of the Neoproterozoic Jeffers Gp).

4.1.6 The Minas fault zone

The Minas fault zone has been variously referred to as the Cobequid-Chedabucto fault zone (Webb, 1969), the Minas Geofracture (Keppie, 1982), the Cobequid-Chedabucto fault zone/system (Mawer and White, 1987), and the Minas fault zone/system (Gibbons et al., 1996; MacInnes and White, 2004; White, 2004; Murphy et al., 2011). While early motion along the Minas fault zone occurred in the late Devonian to early Carboniferous, it is well recognized that the majority of slip occurred in the late Carboniferous (Keppie, 1982; Murphy et al., 2011). Tracing stratigraphic subdivisions of the early Carboniferous Horton Group sediments on either side of the fault (Murphy

et al., 1995; Martel and Gibling, 1996), as well as Ordovician – Early Devonian volcanic and sedimentary rocks that were deposited in both the Avalon and Meguma zones, supports a minimum offset of ~150 km (Chandler et al., 1987; Murphy and Keppie, 1998).

4.2 Introduction to the Greville Bay Study Area

4.2.1 Location of the Greville Bay study area

The Greville Bay study area (Map 1) is located 26 km east of Parrsboro, Nova Scotia, Canada along route 209 (UTM: 374500E → 376500E). This study concentrates on a 2 km section of beach exposure where a wide exposure of the Minas fault zone crops out just south of Brookville, Nova Scotia. The study area is accessible by foot, via a short walk south from Brookville Rd.

4.2.2 Previous work at the Greville Bay study area

There have been four previous studies mapping this section of Greville Bay at various scales. The first comprehensive mapping project of the Minas fault zone in this locality was done by Donohoe and Wallace (1982) at a scale of 1:50 000 as part of a mapping program of the Cobequid Highlands through the Nova Scotia Department of Mines and Energy. The major lithologies of the Minas fault zone at Greville Bay were defined through this mapping project. In this locality they recognized that the Cobequid fault was hosted within the Nuttby Fm. of the Horton Gp (described as the Greville River Fm., but redefined as the Nuttby Fm. in later work by Pe-piper and Piper 2002) with various fault slices of Jeffers Gp, Fountain Lake Gp and Parrsboro Fm. (Pictou Gp) incorporated within a highly sheared and cataclasized fault gouge. Within this map, the

Minas fault zone is shown as a series of anastomosing faults, and is described as having a “lenticular nature” (Donohoe and Wallace, 1982).

A later regional (1:50 000) mapping project by Pe-piper and Piper (2005) also covered this section of Greville Bay; however, they simplified the lithologies into two categories: “sheared or cataclastic to mylonitic rocks” and “tectonic slices of Neoproterozoic igneous and metasedimentary rocks”.

Mawer and White (1987) made detailed observations of the various faults offsetting lithologies within the Greville Bay area. Both brittle (riedel shears, breccias, and gouges) and ductile (S-C fabrics, isoclinal folding, and sheath folds) fabrics were noted within the faults, with all but the latest generation of faults showing features consistent with dextral displacement (which are normal). Faults with major offsets are parallel to the main surface trace of the Minas fault zone, along Y Riedel shears, and are easily traced using various lithologies as markers. Riedel shears were shown to overprint ductile S-C fabrics.

While shear band foliation and S-C fabrics develop due to ductile deformation, and Riedel shear packages develop in brittle and semi-brittle regimes, Mawer and White (1987) argued that the orientations of the two groups of structures at Greville Bay shows that they serve the same kinematic purpose within their respective shear and fault zones (Mawer and White, 1987; MacInnes and White, 2004; Fig. 4.4). A similar conclusion was reached regarding S-C fabrics and shear bands; both form due to the same imposed kinematic boundary conditions and reflect strain softening (White et al., 1980). However, S-C bands formed early in the deformation of homogeneous rocks, ideally in an undeformed rock mass, while shear-band foliation develops late, and is caused by strain softening in strongly anisotropic rocks (Berthé et al., 1979; White et al., 1980).

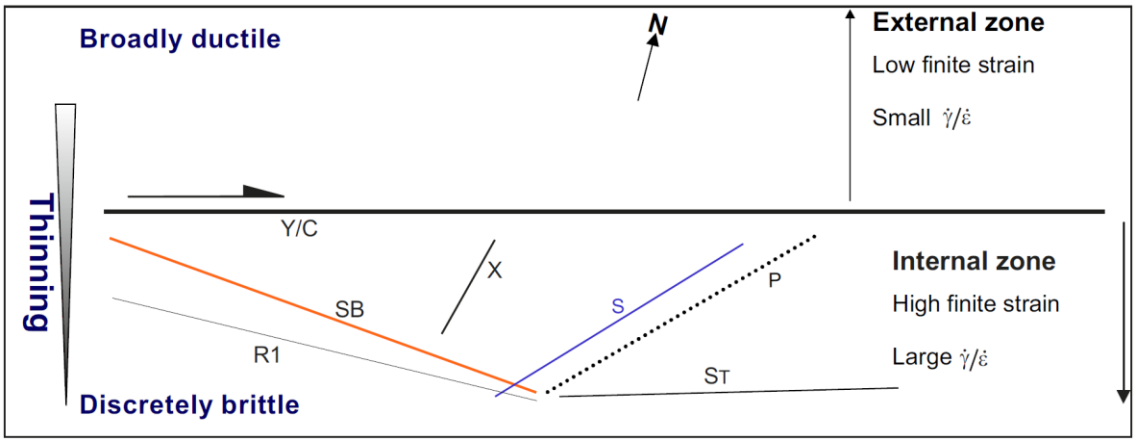

Figure 4.4: Summary of geometry and kinetics from the Minas fault zone Scale independent schematic representation of the orientations of the kinetic data taken from the Minas fault zone by MacInnes and White (2004).

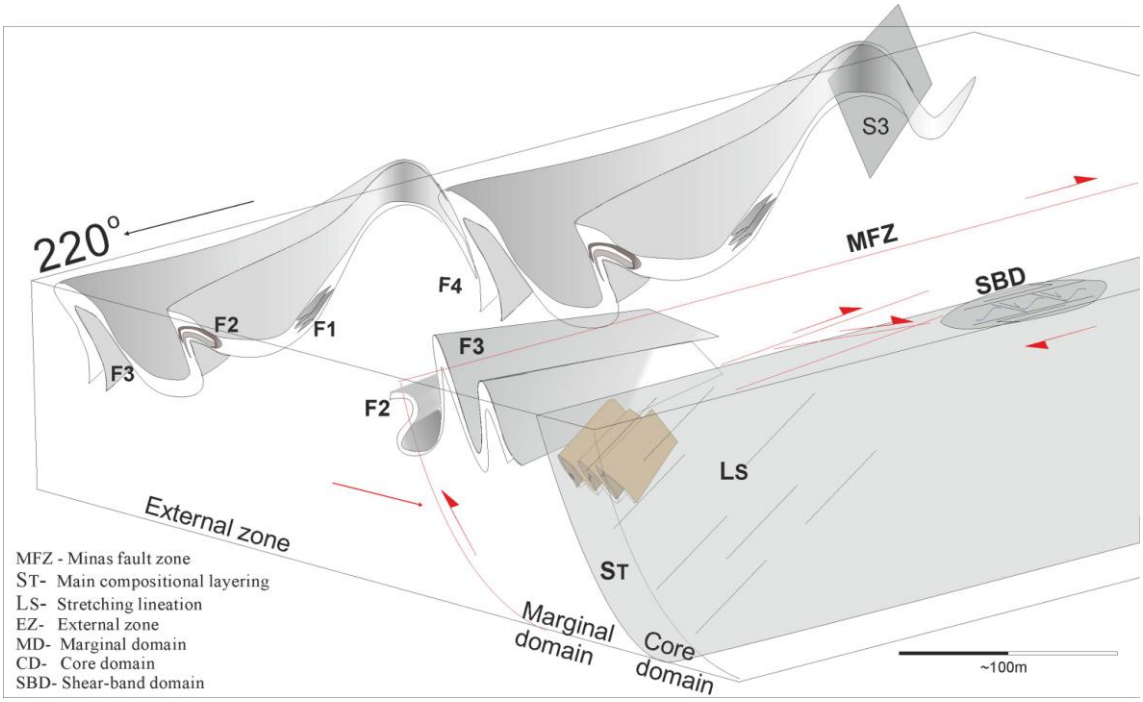

Figure 4.5: Overview of the relationships between regional structures The Greville Bay study area serves as the type locality for the processes occurring within the internal zone, in the marginal and core domains (MacInnes, 2005).

Structures found at a second study area, along the eastern margin of Nova Scotia in Chedabucto Bay, were consistent with dextral motion, indicating that the entire fault zone records primarily dextral displacement through the late Carboniferous (Mawer and White, 1987).

Detailed mapping of Greville Bay and Advocate Harbour was completed by MacInnes (2005) for her PhD thesis. Based on ~2500 structural measurements in the field, MacInnes was able to separate this large section of the Minas fault zone into two zones: an external zone and an internal zone. The zones exhibit similar and related kinematic histories (MacInnes and White, 2004); however, the external zone has accommodated significantly lower levels of finite strain allowing for the preservation of the sequence of deformation (Fig. 4.5). The internal zone, best exposed along the segment of Greville Bay studied here, accommodates primarily transcurrent motion. Evidence of early folding has largely been removed due to transposition, with fabrics being increasingly rotated into parallelism with the Minas fault zone trace with proximity to the core of the Minas fault zone (Fig. 4.5).

While a total offset of 150km has been identified along the Minas fault zone, there is at least a 20km offset within the units of the Greville Bay study area. Regional mapping by Donohoe and Wallace (1982), traced a distinctive rhyolite (Fountain Lake Gp) on either side of the fault zone and suggested a minimum offset of 20 km through dextral shearing.

4.2.3 Primary lithologies of the Greville Bay study area

The lithologies of the Greville Bay study area can be separated into four groups. From oldest to youngest these are: the Jeffers Gp, the Fountain Lake Gp, the Horton Gp (Nuttby Fm.), and the Cumberland Gp (Parrsboro Fm.).

The Jeffers Gp is a Neoproterozoic, green to grey volcanic unit, containing lithic tuffs, siltstone and agglomerate that has been altered by varying amounts of metamorphism and deformation (Donohoe and Wallace, 1982). Within the Greville Bay study area the Jeffers Gp crops out as a distinctive fault slice of light green, highly foliated phyllite (Map 1). Along its southern margin it is in fault contact with the black phyllite of the Nuttby Fm., while along its northern margin it is in fault contact with the sandstone of the Jeffers Gp. The phyllite is very fine-grained and is composed of chlorite, white-mica, alkali feldspar, albite, and plagioclase, with its distinctive colour coming from the high concentration of chlorite. Complex folding is seen within the unit.

The Fountain Lake Gp is a package of mid-Devonian bi-modal volcanic rocks, primarily composed of basaltic and rhyolitic flows (Donohoe and Wallace, 1982). Within the Greville Bay study area the Fountain Lake Gp is composed of a massive, to locally foliated, to intensely brecciated quartz-feldspar dominated rock, which has been interpreted as a rhyolite (Donohoe and Wallace, 1982; Mawer and White, 1987; MacInnes, 2005). The unit crops out as two distinct fault slices, offset by a dextral strike-slip fault along the southern margin of the study area (Map 1).

The Early Carboniferous Horton Gp (Nuttby Fm.) is the principal lithology of the Greville Bay study area. While the compositions and morphologies of the Nuttby Fm. within the fault zone are heterogeneous, the units all appear to be derived from the fine-grained sedimentary facies of the Nuttby Fm. found to the north of the fault zone. The fine-grained facies of the Nuttby Fm. is composed of a grey-black-purple argillite, siltstone, and fine sandstone (Pe-Piper and Piper, 2005). The compositions of Nuttby Fm. within the fault zone have been variously altered through the introduction of fluids and repeated transposition and differentiation of the units (MacInnes and White, 2004).

In recognition of the latter, the Nuttby Fm. is divided into three distinct domains within the fault zone: an S-C domain, a scaly mesocataclasite, and an isoclinally-folded carbonate-rich domain (Map 1).

The late Carboniferous Parrsboro Fm., which lies at the base of the Cumberland Gp, is a distinctive red to grey, wacke, siltstone, and shale dominated unit that locally contains red polymictic conglomerate (Donohoe and Wallace, 1982). It occurs as a thin fault slice within the study area, and is readily distinguishable based on its colour, coarser grain size and discernible primary features (graded bedding and cross bedding).

4.3 Field Observations of the Greville Bay Study Area

4.3.1 A natural cross-section through Greville Bay

A natural cross-section through the lithologies found at Greville Bay (Fig. 4.6) shows the relationships between the main units found in this segment of the fault zone. At the southern end, the Fountain Lake Gp rhyolite exists as a large sea stack (Fig. 4.6) and also crops out along the beach (Map 1). A brittle fault separates it from the sheared phyllite with S-C fabrics. Outboard to this are fault slices of Jeffers Gp and Parrsboro Fm. respectively which contain complex folds. These are bounded to the north by a brittle fault, which cuts through all lithologies. Where it passes through the Nuttby Fm., a thick package of mesocataclasite with a scaly fabric is developed. An isoclinally folded carbonate bearing variant of the Nuttby Fm. marks the most northern boundary of the fault zone. The field features of each unit below are now described from south to north (*i.e.* from the core of the fault to the periphery).

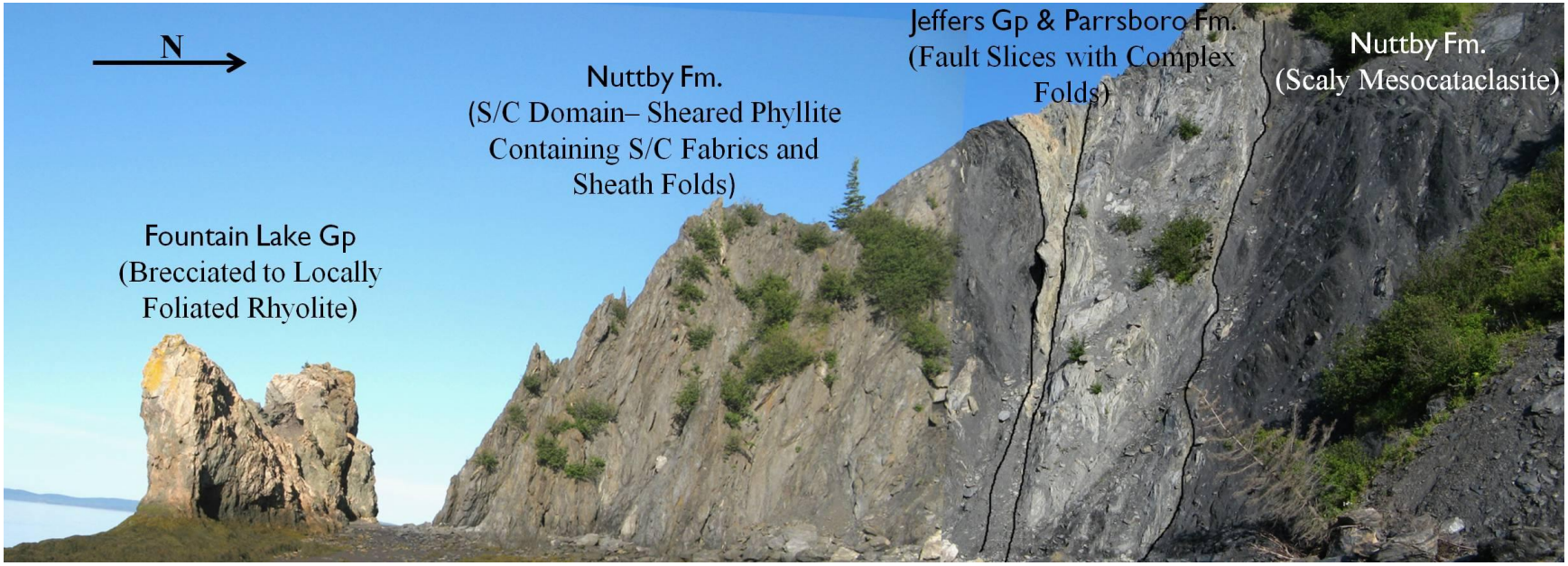

Figure 4.6: Natural cross-section through Greville Bay The basic units found within the Greville Bay study area. Each unit exists as a fault bounded slice. (The seastack composed of Fountain Lake Group rhyolite is known as Brookville Rock and is ~8m high).

4.3.2 Field observations of the Fountain Lake Group Rhyolite

The competent rhyolite block is massive to locally foliated and is not internally strained in the manner of the more incompetent phyllites of the Nuttby Fm. Discrete internal deformation, with high angle faulting and breccia zones occurs along the margins of the rhyolite block. Within breccia zones, the rhyolite is highly fractured and quartz (from silicic fluids) is seen to infill the fractures (Fig. 4.7b). High angle faults are oriented as expected for Riedel shears (R1 and Y) relative to the main fault zone trace (parallel to Y shears; Logan et al., 1992). The R1 Riedel shears, which strike at ~290°, exhibit dextral offsets and dip steeply (Fig. 4.7a). These Riedel shears have also been identified in the Nuttby Fm. to the north of the fault, and because they have been preserved (*i.e.* are not transposed into parallelism with the fault zone) are inferred to be representative of late brittle movement along the fault zone. The Riedel shears (both R1 and Y) contain thick (~3m) sections of grey foliated fault gouge (Fig. 4.7a). Thin seams of black gouge are found within the grey gouge close to the margins of the brecciated rhyolite.

The contact between the Fountain Lake Gp and the S-C domain of the Nuttby Fm. is defined by a high strain zone containing Riedel shears (Fig. 4.7c), and a cataclasite containing boudinaged fragments of Fountain Lake Group rhyolite. These features record dextral motion of the fault.

4.3.3 Field observations of the S-C Domain of the Nuttby Formation:

The S-C domain of the Nuttby formation consists primarily of black phyllites, with occasional green lenses within them (Fig. 4.8b). Structures attesting to bulk ductility are common within this unit. S-C shear band cleavage is pervasive, local sheath folds have been identified, and quartz veins have been boudinaged (Fig 4.8). As the

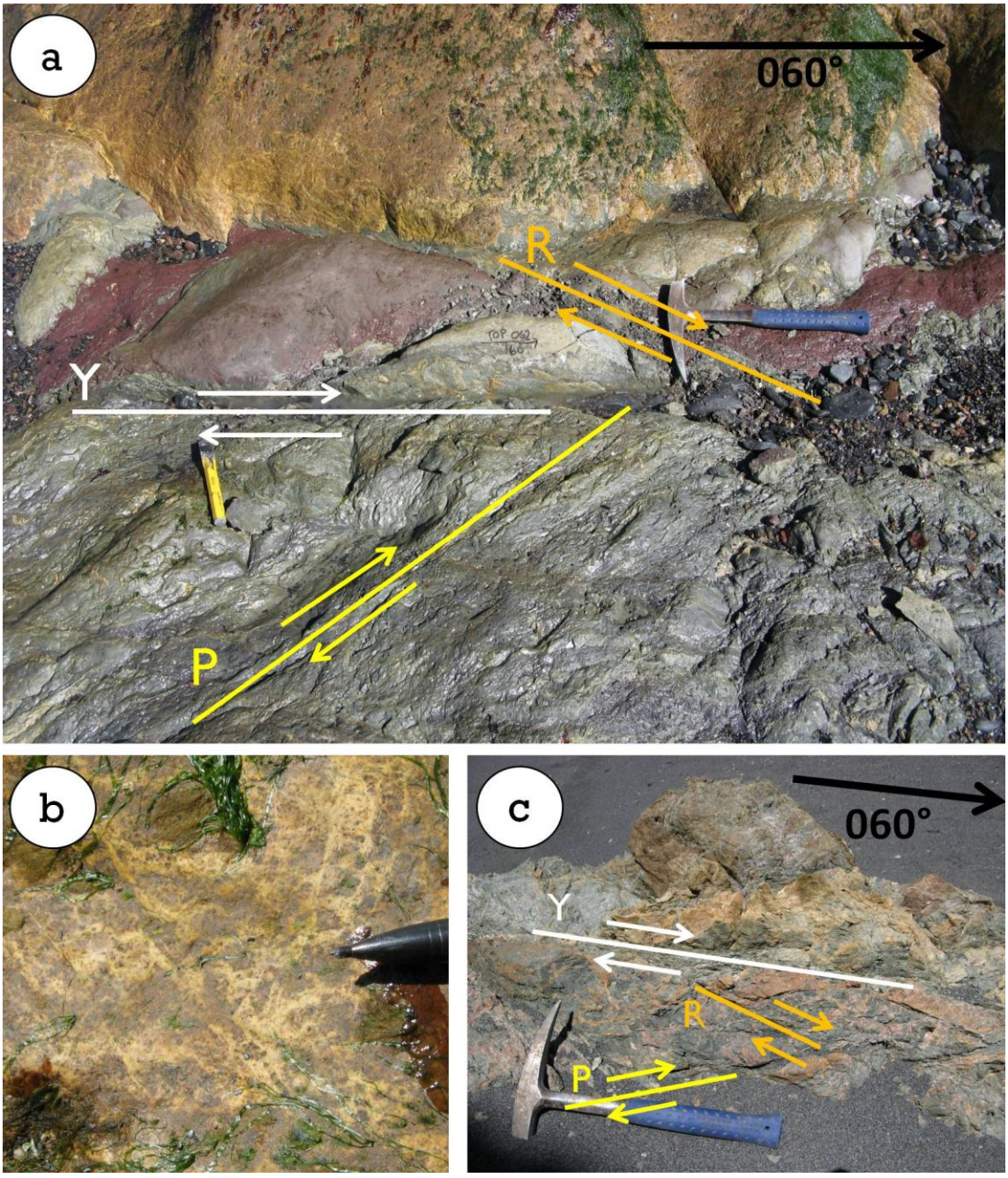

Figure 4.7: Mesoscopic structures from the Fountain Lake Gp Field photos from the Fountain Lake Gp rhyolite. **a)** Fault located within the brecciated Fountain Lake Gp. Brecciated rhyolite (tan unit at top) is offset by a gouge (purple and grey units) filled shear. Note the very fine black gouge unit located along the Y-shear. **b)** Close-up of brecciated rhyolite. Silicic fluids (tan) fill fractures formed within the purple rhyolite. **c)** Fault along the contact between the rhyolite and the S-C domain of the Nuttby Fm. to the north. (Hammer head = 20cm, Pencil lead = 7mm)

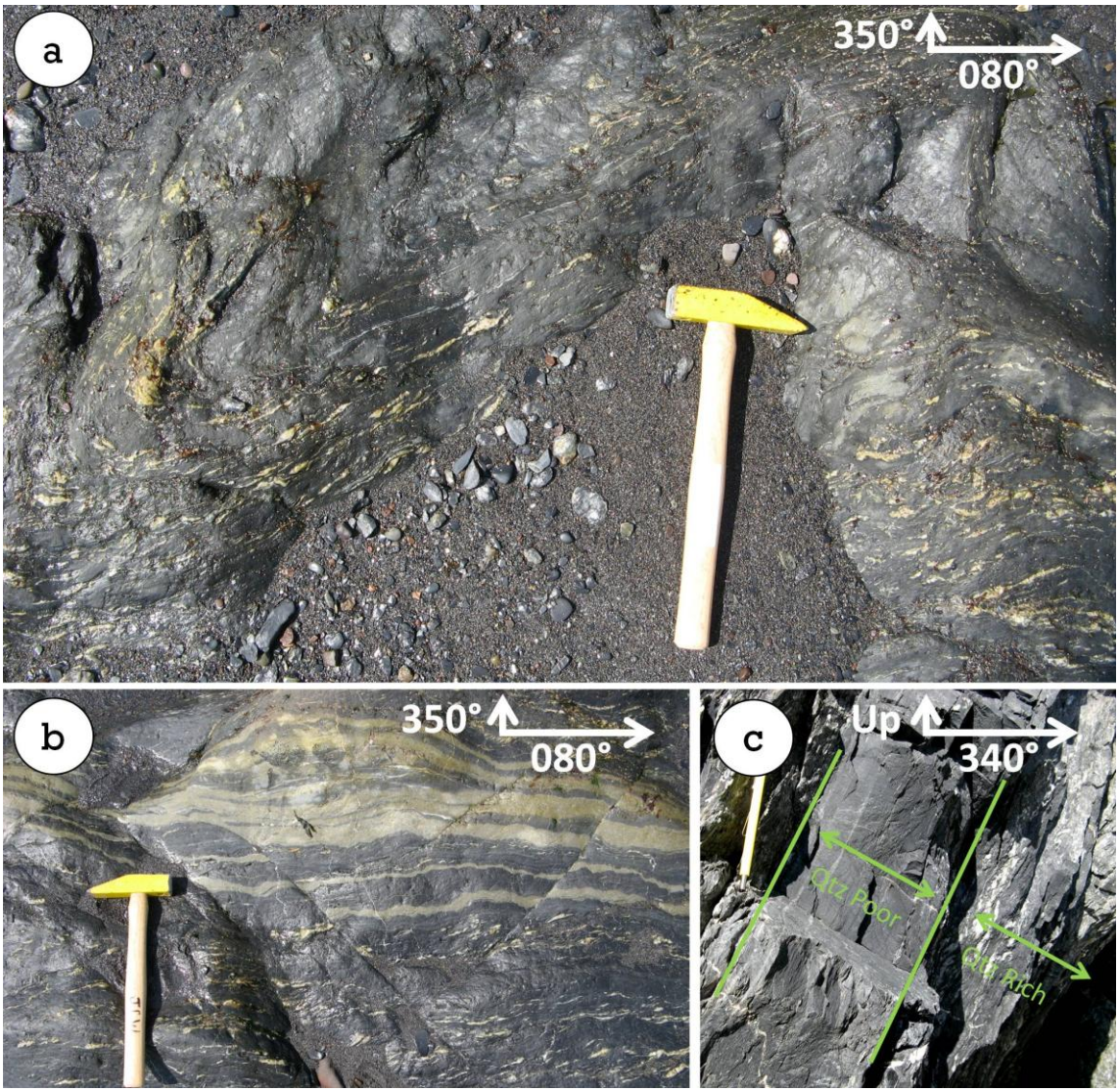

Figure 4.8: Mesoscopic structures from the S-C domain of the Nuttby Fm. Typical features of the S-C domain. Boudinaged quartz veins exist in a black phyllite (**a, b**). Local folds exist with axial planes approximately parallel to S plane orientations. Discontinuous lenses of quartz poor, chlorite-rich, light green phyllite exist within the unit (**b**). Looking at a vertical surface, one can see quartz vein poor and quartz vein-rich domains within the unit (**c**). (Hammer head = 15cm, Pen Magnet = 13cm)

contact with the rhyolite is approached, an increase in the intensity of deformation is observed. Extensional shear bands become increasingly common at a scale of 1-15cm (MacInnes, 2005).

The main compositional layering within the phyllite has been caused by transposition of the Nuttby formation. MacInnes (2005) identified at least three generations of progressive intrafolial folds (*i.e.* tight to isoclinal, syn-shear, overturned folds in ductile shear zones) in this unit, indicative of the cyclical nature of the transposition which repeatedly rotates pre-existing structural elements into parallelism by isoclinal folding. Late, open, low amplitude folds locally overprint the transposed foliation and intrafolial folds.

The majority of the unit (~90%) consists of a black phyllosilicate-rich phyllite containing 0-20% quartz (Fig. 4.8). Quartz exists within the phyllosilicate-rich phyllite as boudinaged veins in various degrees of transposition and as implosion breccias. The distribution of quartz is not homogeneous and rock volumes exist that contain no visible quartz (Fig. 4.8c). When quartz is absent, deformation becomes more difficult to see due to a lack of marker horizons. The other 10% of the unit is composed of quartz-rich material, which occurs as isolated horizons from 30cm to 2m in width, bounded on all sides by the phyllosilicate-rich phyllite. These samples contain up to 80-90% quartz, up to 10% feldspars, and ~10% chlorite. In hand sample quartz exists in layers ~5cm thick, with mm-scale chlorite horizons separating each layer. The chlorite horizons contain sub-horizontal slickenlines.

A brief overview of the orientations of the different structural fabrics will be discussed here; a full review is provided by MacInnes (2005). Where quartz and calcite are common, mineral stretching lineations have shallow to moderate SW plunges (28°

→ 218°). They are best developed in zones of high quartz content. In phyllosilicate-rich domains, crenulation of the transposed foliation is common, and commonly aligns with the stretching lineation seen in quartz-rich domains.

C-planes are oriented at 069° and dip 57°SE. They are defined by thin gouge zones, oriented phyllosilicates, and pressure solution cleavages. S-surfaces strike 044° and dip 57° SE. The boudinaged quartz veins typically are aligned with the S-planes, as are the crenulated micas. Shear bands are oriented at 095° and dip 57°S. They record dextral movement, and are recognized as they overprint and offset the transposed foliation. Shear bands are progressively rotated back into parallelism with the C-surfaces, and younger sets of shear bands overprint them.

4.3.4 Field observations of the Jeffers Group and Parrsboro Formations

Fault slices of the Jeffers Gp and Parrsbro Fm. respectively, are crossed when moving northward from the more interior S-C domain. These units have been considered together as their contact has experienced several generations of folding within the internal zone of the Greville Bay field area. While folding within the two units is intense, recognizable bedding planes can be seen in the green and red siltstones of the Parrsboro Fm. (Fig. 4.9), and the foliation of the Jeffers Gp has not been rotated into parallelism with the trace of the Minas fault zone indicating that the units have not experienced the same degree of transposition (or accommodation of shear strain) as units from the Nuttby Fm. Along coastal exposure, a steeply dipping fold hinge has been observed anastomosing down the cliff face (Fig. 4.9a). Thin section analysis shows that the sample is composed of quartz (50%), chlorite (25%), calcite (15%), muscovite (5%), and minor isotropic minerals (<5%). A very weak foliation is present, which follows the

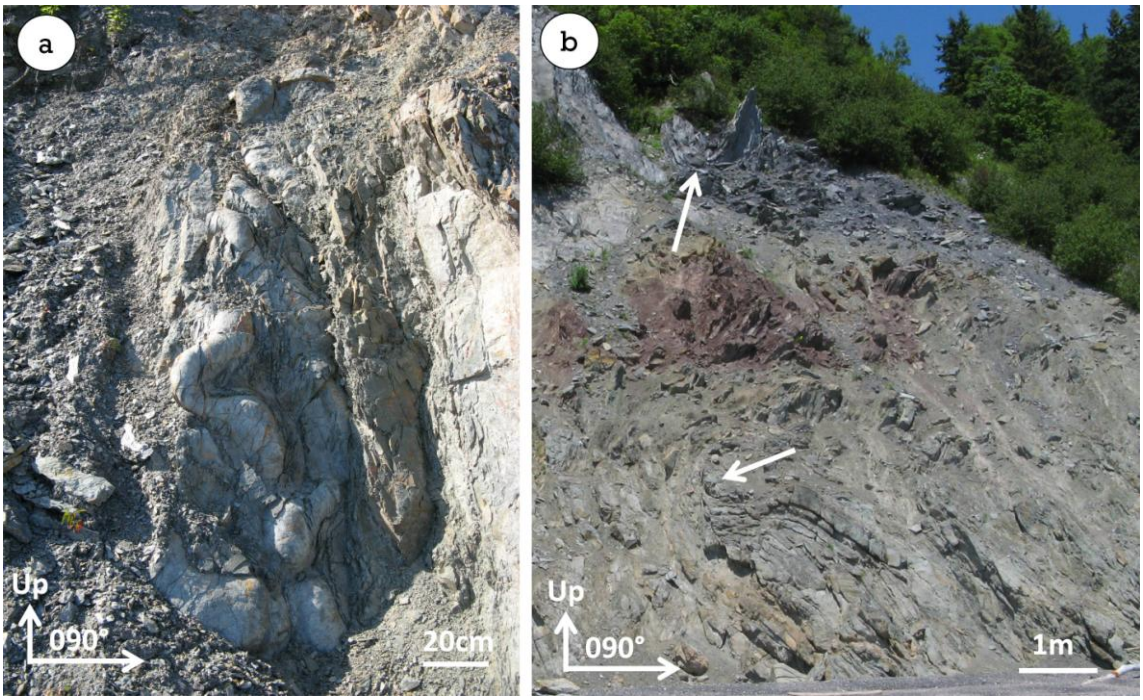

Figure 4.9: Mesoscopic structures from the Jeffers Gp and Parrsboro Fm. These units have accommodated far less simple shear than the Nuttby Fm. and have well preserved folds and primary features (graded bedding and cross bedding). The folds however are complex, with fold axes plunging in a wide range of orientations (**b**), as the fault slices have been affected by the simple shear of the internal zone and the regional folding of the external zone. The fold depicted in **a**, has an anastomosing fold axis which has been folded around isoclinally. This may be an artifact of soft sedimentary deformation preserved within the unit.

fold pattern. This is likely representative of bedding and it is possible that some of the complexity is preserved "soft sediment" deformation.

Where the units crop out in the marginal domain, folding is less intense, presumably due to the increased distance from the focus of shear deformation.

4.3.5 Field observations of the Scaly Mesocataclasite – Nuttby Formation

Outboard of the Jeffers Gp and Parrsboro Fm., a late fault cuts through all lithologies. The fault core is 1-2m in width where it cuts through the Jeffers Gp and Parrsboro Fm.; however, where it intersects the Nuttby Fm., the damage becomes more distributed (widens from 1-2m across to ~30m wide) and a "scaly" foliation develops within the core of the fault (Map 1). The fabric is anastomosing, forming trapezoidal phacoids from scales of 10's of cm's to sub cm-scale (Fig. 4.10). Phacoids can be broken apart into smaller and smaller sizes, and are always coated with very fine phyllosilicates (Fig. 4.10d), creating polished surfaces with slickenlines that can be rubbed off on your hands in a similar manner to graphite (however there is no graphite found within the samples; see Appendix 3). The slickenlines are tightly spaced, and within a given surface are parallel to one another. Angular to sub-rounded clasts of phyllite are commonly found entrained within the gouge matrix at a similar range of scales (Fig. 4.10b), and are seldom in contact with one another, making the gouge matrix supported. In addition to the clasts of phyllite, sub-rounded to rounded spheres of quartz carbonate vein material are entrained in the gouge (Fig. 4.10d). These are coated in polished clay surfaces, and are only identifiable as vein material by breaking them apart with a hammer.

Orientations of polished surfaces tends to mimic Riedel shear geometries; however, the orientation of Y-shears fluctuates from sub horizontal to sub vertical within

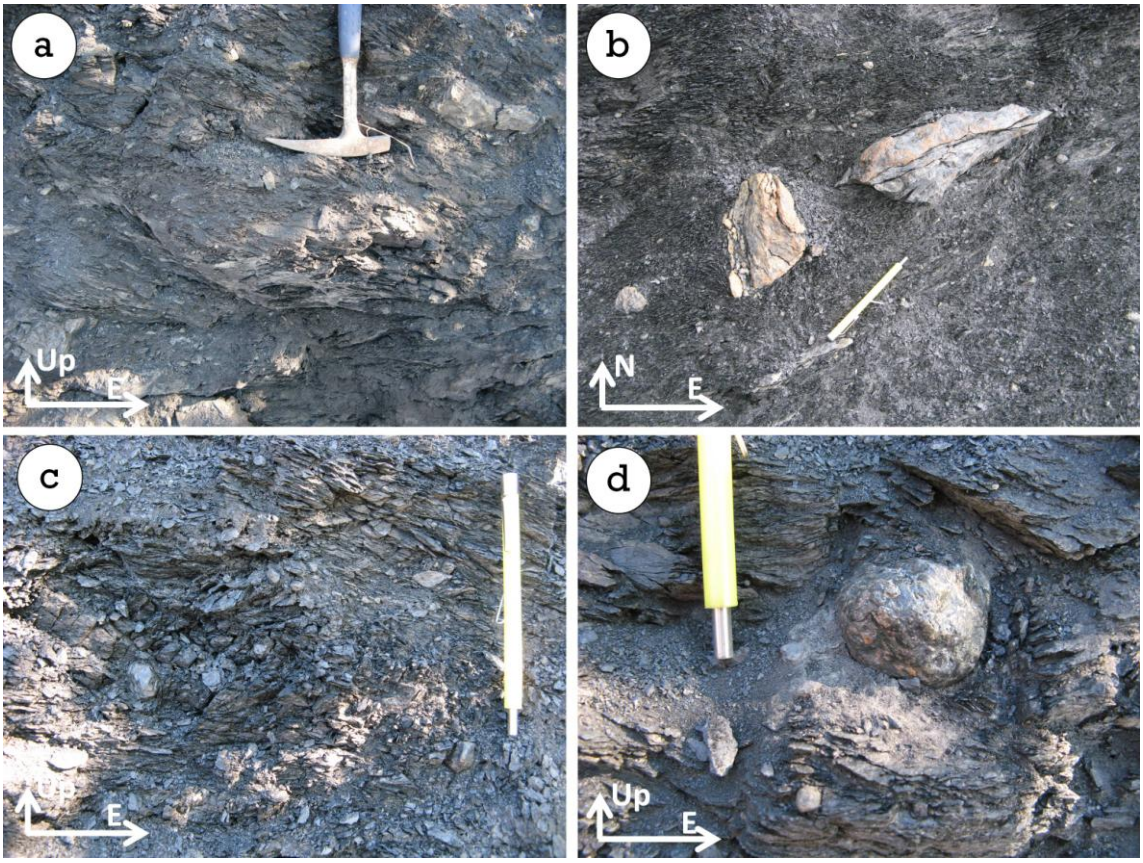

Figure 4.10: Mesoscopic structures from the 'scaly' mesocataclasite – Nuttby Fm. Field photos showing the anastomosing fabrics from the scaly mesocactaclasite. Individual phacoids are separated by polished surfaces containing densely spaced slickenlines. Angular clasts of wallrock (**a, b**) and rounded, polished quartz-carbonate veins (**c**, **d**) are found entrained in the gouge. (Hemmer head = 20cm, Pen magnet = 13cm)

the fault, while the bounding surfaces of the fault remain sub-vertical. Around larger clasts the foliations within the gouge form complex interference patterns.

4.3.6 Field observations of the Folded Carbonate Bearing Nuttby Formation

To the north of the latter brittle fault is a grey-black phyllite of the Nuttby Fm. These strata exhibit a lower level of deformation than the same unit (the S-C domain of the Nuttby Fm.) closer to the focus of deformation in the core domain. Isoclinal folds and steep, compositional layering characterize the deformation in the Nuttby Fm. The compositional layering does not strike parallel to the fault zone, indicating a lower degree of transposition.

4.3.7 Interpretation of field observations:

The S-C domain displays features indicative of bulk ductility including sheath folds, S-C fabrics, and extensional shear bands. Implosion breccias and multiple generations of veining are evidence of transient fluid pressures. Cyclic vein injection has led to local changes in bulk mineralogy, generally increasing the quartz content.

The rhyolite appears to behave as a large asperity within a weak fault, allowing for localization (and earthquake potential) along its margins (Chen and Sammis, 2003). The strength of the rhyolite compared with the weak phyllite, allows it to behave as a southern boundary for ductile deformation within the phyllite.

An intensification of deformation in the S-C domain of the Nuttby Fm. is evident as the resistant Fountain Lake Gp Rhyolite (Brookville Rock) is approached. This reflects the role that local boundary conditions have on the partitioning of deformation and emphasizes the heterogeneous nature of shear zones.

It is clear from the field observations that a significant proportion of the shear strain has been accommodated by faulted variants of the Nuttby Fm. In particular, the S-

C domain and the scaly mesocataclasite have accommodated significant fractions of shear displacement. In the following, observations of the microstructures from each of these units are presented in order to elucidate the operating deformation mechanisms.

4.4 Microstructures of the Greville Bay Study Area

4.4.1 Introduction to the study of microstructures

This section describes the microstructures within the units at Greville Bay to determine the operating deformation mechanisms (see section 3.1). A complex set of overprinting structures exists within the fault core (see section 4.3). Using optical microscopy, scanning electron microscopy (SEM), and transmission electron microscopy (TEM), the processes that produced these features are assessed.

4.4.2 Microstructures from the Fountain Lake Group rhyolite

Two morphologies of the Fountain Lake Gp rhyolite are examined: the brecciated rhyolite (Fig. 4.7b), and the grey and black gouges within shears offsetting the Fountain Lake Gp rhyolite (Fig. 4.7a). The brecciated rhyolite is formed primarily of quartz (85-90%), very fine-grained chlorite (~10%) and a minor component of feldspar (<5%; Fig. 4.11). Clasts of rhyolite exist at a variety of scales, though they tend to have been fractured to the mm to cm-scale. Individual clasts exhibit a shape preferred orientation (Fig. 4.11b), and have been rotated relative to one another indicating a level of shear during fracturing (Fig. 4.11c). Within larger clasts, crystal size is on the order of one micrometre, and is relatively consistent throughout the sample (Fig. 4.11c). Larger crystals of quartz within the sample have distinct undulose extinction (sub-grain walls), with a mean grain size of ~5 μm, and appear to be have undergone sub-grain rotation recrystallization.

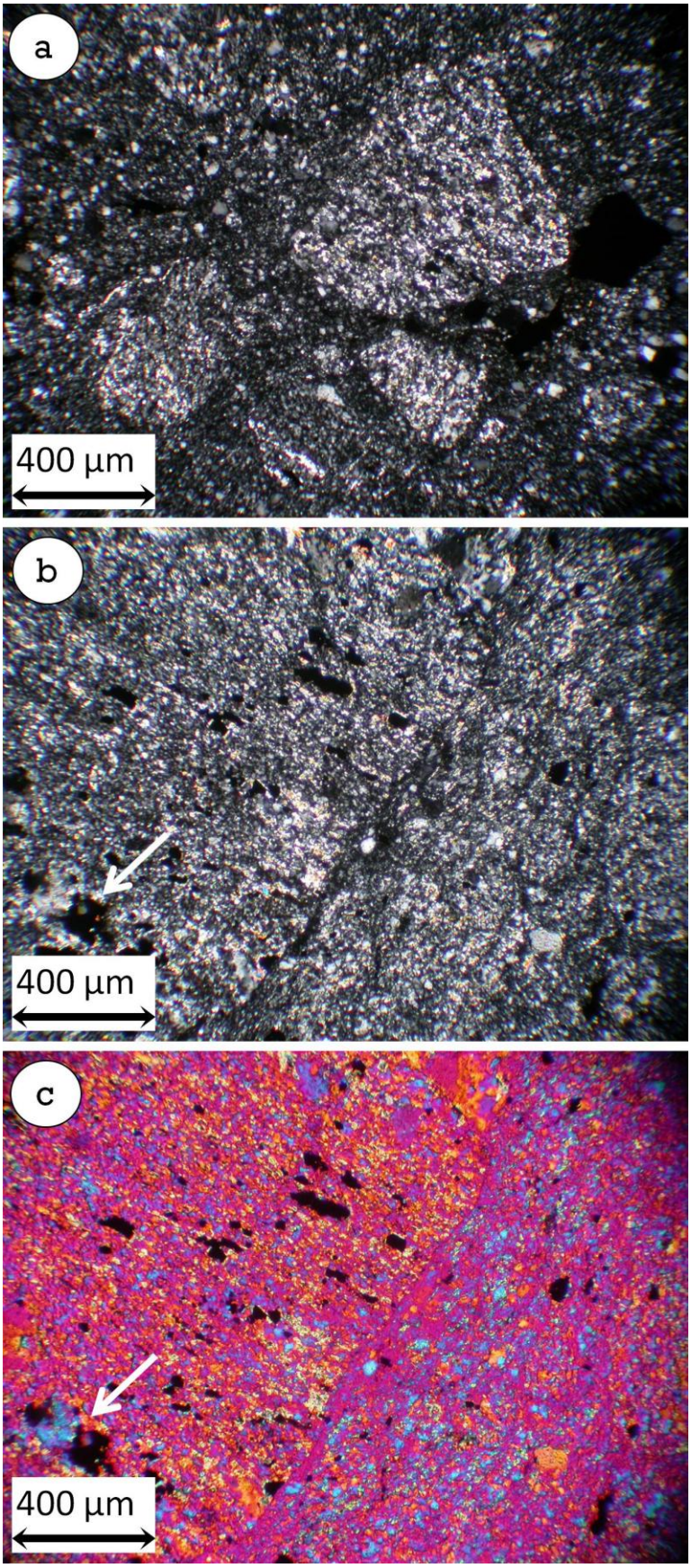

Figure 4.11: Photomicrographs of the Fountain Lake Group rhyolite Brecciated clasts of foliated rhyolite are seen within a matrix of fine-grained quartz (**a, b**). The rhyolite is composed of quartz (85-90%), chlorite (~10%) and a minor component of feldspar (<5%). The sample has a shape preferred orientation, and larger crystals appear to be deforming through sub-grain rotation recrystallization (arrow). Individual blocks of rhyolite have been rotated indicating a degree of shearing during brecciation (i.e.: the samples have not been fractured through the process of pulverization). This can be easily seen by inserting a Bertrand lens (**c**). Note that in **c** the two blocks show CPO's that are nearly perpendicular to one another.

The gouges (Fig. 4.7a) have a complex texture. Within the grey gouge an optically isotropic texture results from a structureless matrix (Fig. 4.12d). Laths of quartz-phyllosilicate-rich material extend in all directions (Fig. 4.12d). The black gouge clearly cuts the grey gouge and has a much finer grain size, unresolvable using optical microscopy.

SEM analysis of the gouges reveals quartz-rich and phyllosilicate-rich aggregates (Fig. 4.12e,f,g). The grey gouge is primarily quartz-rich, and shows evidence of fracturing (Fig. 4.12e). Fractures are filled with chlorite and pyrite indicative of high permeability due to fracturing (Fig. 4.12g). The black gouge has a higher phyllosilicate content and a strong foliation (Fig. 4.12f).

4.4.3 Interpretation of microstructures – Fountain Lake Group rhyolite

Three generations of deformation developed under distinctly contrasting conditions exist. The strong foliation and recrystallization within the rhyolite are indicative of temperatures on the order of 300°C or greater (Hirth and Tullis, 1992; Stipp et al., 2002). This is overprinted by brittle fracture, brecciation, and an influx of silica-bearing fluids precipitating quartz.

Within the gouge-rich shears (which overprint the brecciated rhyolite), the isotropic texture indicates higher strain rates along the margins of the brecciated rhyolite. This microstructure has been reproduced in higher strain rate experiments on phyllosilicate-rich fault gouges (Fig. 4.12b; Niemeijer and Spiers, 2005) indicating that higher strain rates have been reached by localizing the deforming volume along the edges of the shears. This is interpreted to be due to localization along the edge of a solid asperity (Chen and Sammis, 2003) within a unit deforming through bulk ductility (the S-C domain of the Nuttby Fm.).

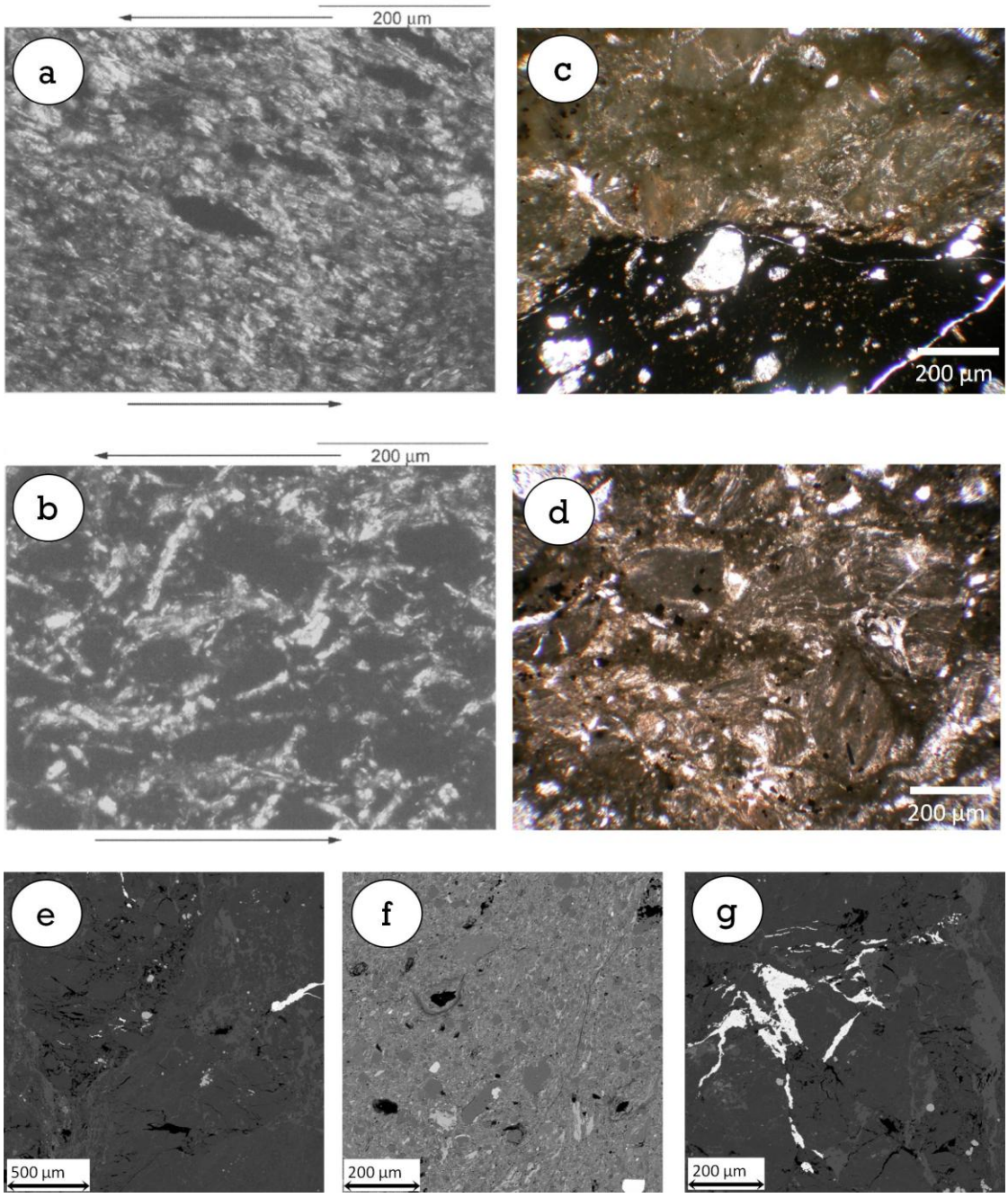

Figure 4.12: Comparative microstructures of the gouges within the Fountain Lake Group rhyolite Sample taken from the black and grey gouges in **Fig. 4.7a** along the Y shear. Figures **a** and **b** show microstructures from experiments carried out on phyllosilicate and halite mixtures at different strain rates (Niemeijer and Spiers, 2005). At low strain rates the sample takes on a highly foliated appearance (**a**), while at higher strain rates the microstructures become more isotropic with a structureless matrix (**b**). An isotropic microstructure is seen within the grey gouge (**c, d**). At SEM-scales, the grey gouge is more quartz-rich (**e, g**), and is highly fractured, with precipitates of pyrite (**g**) and chlorite forming along the seams, while the black seam is highly foliated and contains more chlorite and muscovite (**f**).

4.4.4 Microstructures from the S-C domain – Nuttby Formation

The S-C domain of the Nuttby Fm. is characterized by deformation features indicative of bulk ductility including S-C shear band cleavage, late shear bands, and sheath folds. In thin sections, minerals are aligned parallel to S-surfaces, while slip occurs parallel to C-surfaces or along shear band surfaces where present (Fig. 4.13). Chlorite is more concentrated along S-surfaces, while muscovite tends to align with C-surfaces (Fig. 4.14). Fabrics are disrupted where quartz-carbonate veins are present.

Quartz-carbonate veins exist in various phases of boudinage (Fig. 4.13a,b), with phyllosilicates enveloping the margins of blocks. Brittle fracture of the veins is not evident unless feldspars are present, and veins become isolated through movement along S and C-surfaces, local isoclinal folding, and concomitant recrystallization and dissolution of vein material (Fig. 4.13). Eventually vein material becomes completely entrained within the fine phyllosilicate-rich matrix (Fig. 4.13), forming pods of very fine, more quartz-rich phyllite. With increasing strain it is no longer possible to differentiate where vein material has been incorporated into the sample.

A tightly spaced (~150 μm) discontinuous cleavage exists parallel to S-surfaces, characterized by alternating light and dark seams (Fig. 4.13d). Dark seams parallel to S-planes show elevated concentrations of rutile, and apatite. Wavy dissolution seams exist along quartz veins, and also show elevated concentrations of rutile, phosphates, and precipitates of iron-silicates (Fig. 4.15).

TEM analysis of muscovite and chlorite from the fine-grained phyllosilicate-rich segments (Fig. 4.13d) shows well developed laths, with edge dislocations easily viewed from frequent lattice terminations within the crystal structure (Fig. 4.16). Phyllosilicates tend to be sub-parallel or at low angles to one another. Phyllosilicates envelope lenses

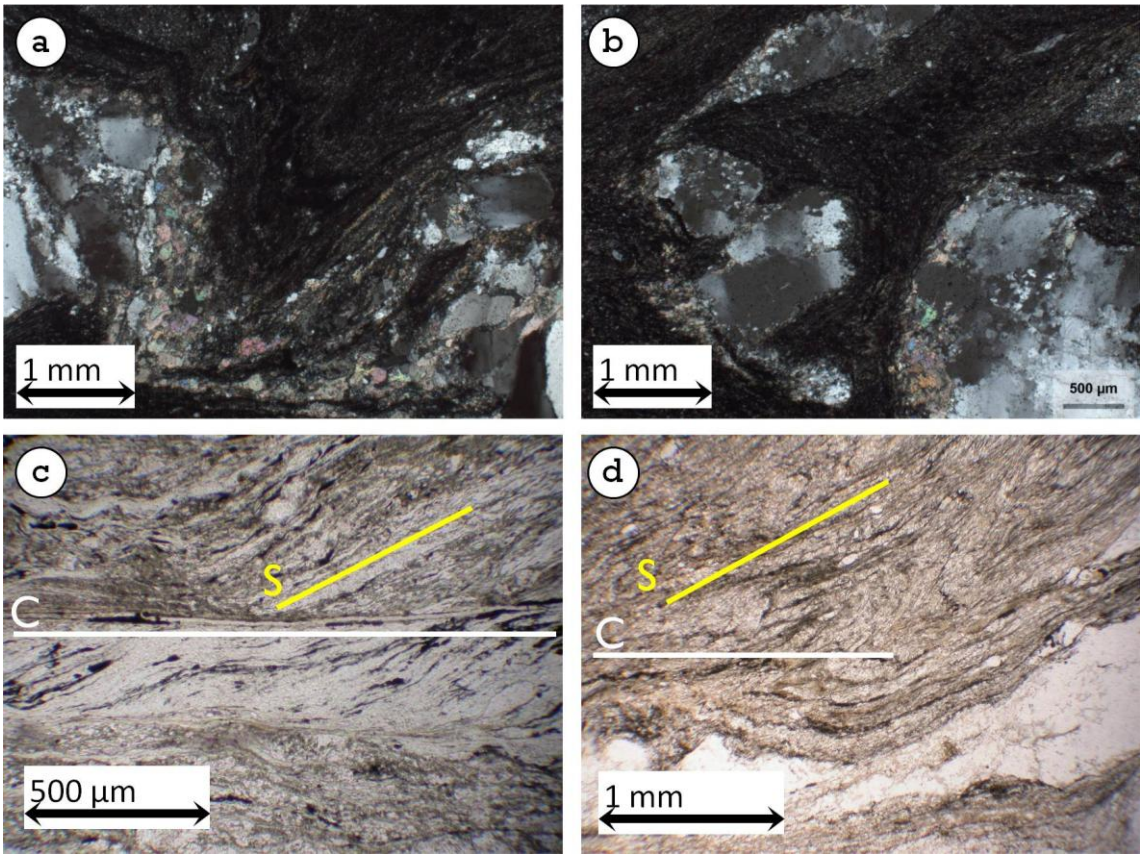

Figure 4.13: Photomicrographs of S-C Fabrics in the Nuttby Formation Fabrics within the S-C domain of the Nuttby Fm. S-C fabrics are well developed in areas of high phyllosilicate concentration (**c, d**). Fabrics are interrupted where quartz-carbonate veins are intersected (**a, b, d**). Veins undergo a process of boudinaging through slip along S and C-surfaces, as well as dissolution along vein margins before being integrated into the fine phyllosilicate matrix. Slip surfaces tend to run parallel to C-surfaces (**c**).

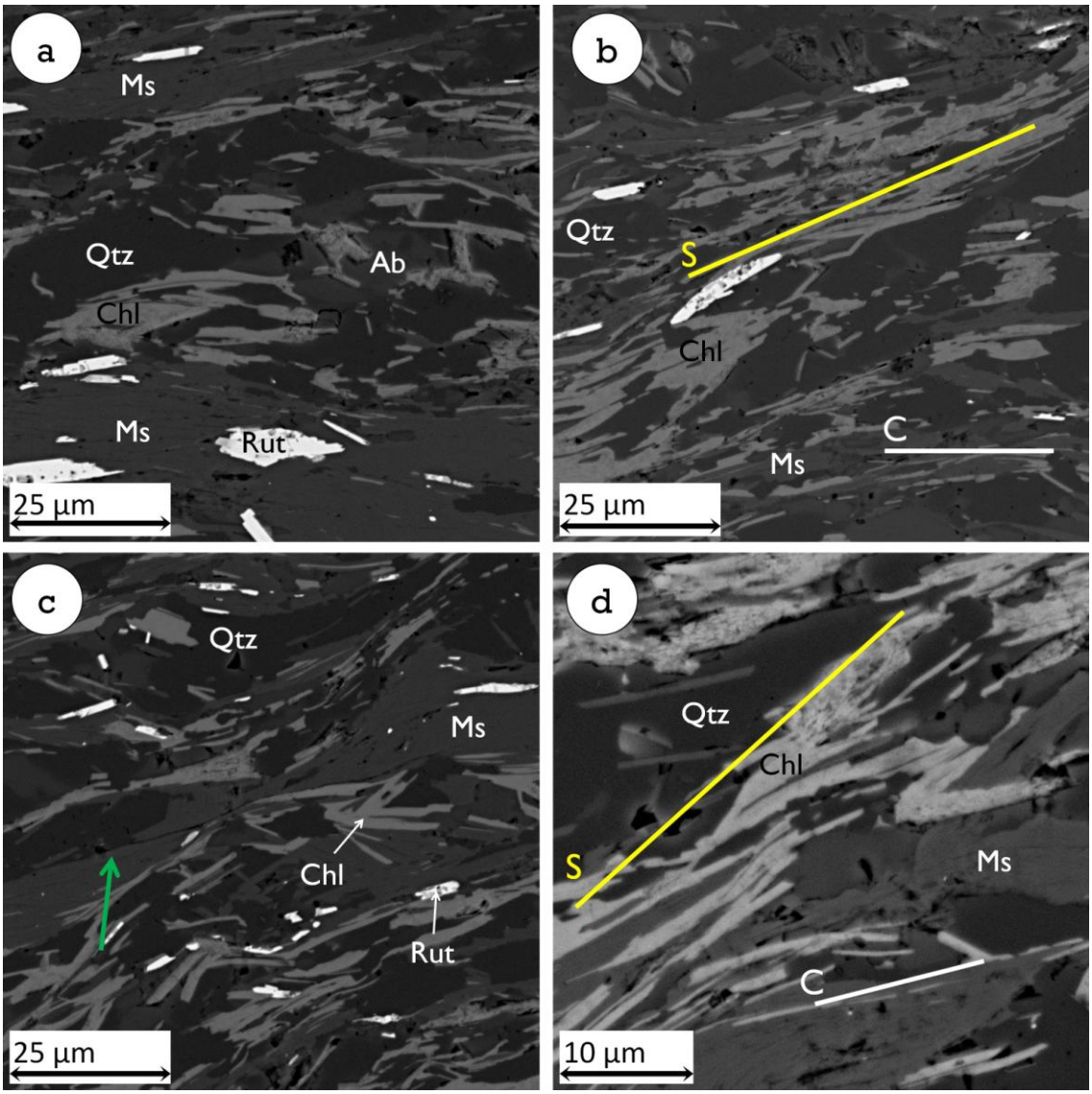

Figure 4.14: SEM photomicrographs of S-C fabrics in the Nuttby Formation Muscovite and chlorite envelop blocky aggregates of quartz and albite (**a, b**). Chlorite is more concentrated along S-planes (**b, d**) while muscovite is more concentrated along C-planes. Rutile is the most common accessory phase (**a, c**) while apatite is seen occasionally. Slip surfaces (green arrow, **c**) are most common parallel to C-surfaces.

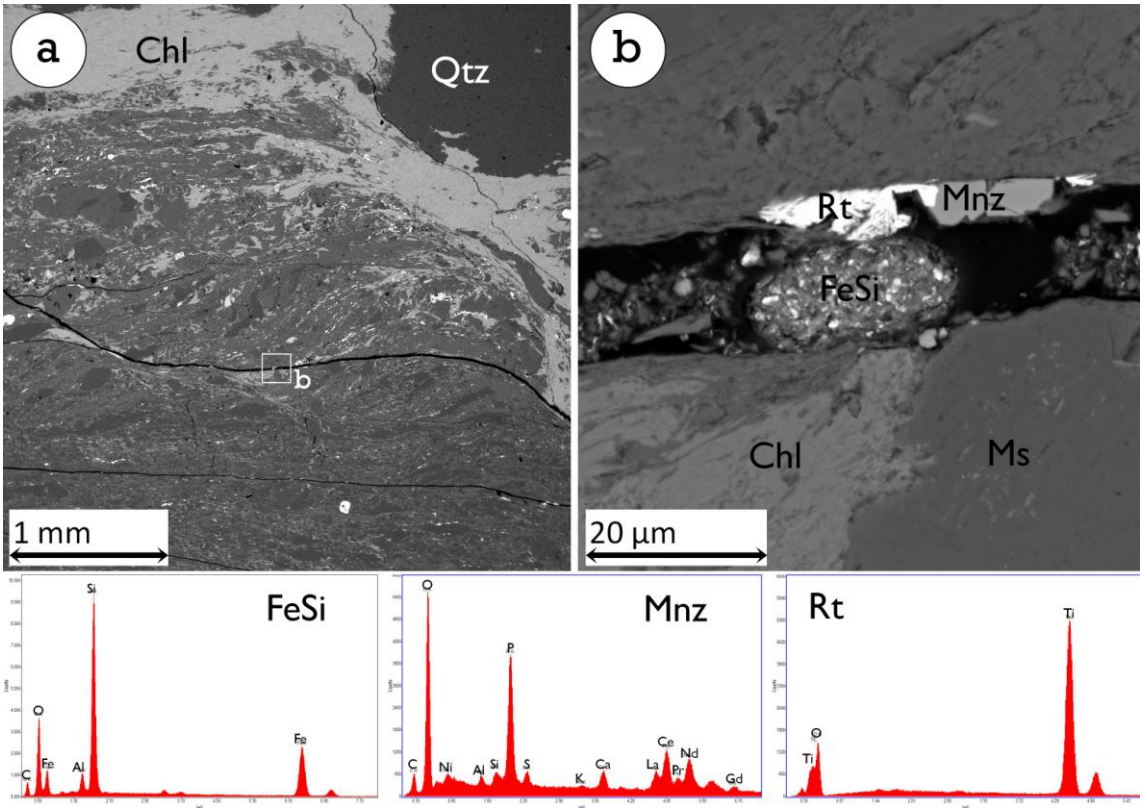

Figure 4.15: SEM Photomicrographs of a dissolution seam Nuttby Formation Thick dissolution seams occur along the edges of quartz veins (**a**). High concentrations of incompatible elements are found within the dissolution seams, and contain rutiles, phosphates (apatite and monazites), and precipitates of iron-silicates (**b**). Energy dispersive X-Ray analyses are shown for these phases.

10-20μm in width of quartz-albite, with dislocation free crystals forming locally along the margins of the lenses (Fig. 4.16b). Growth dislocations are commonly seen in the blocky quartz crystals forming along the margins of phyllosilicates (Fig. 4.16a). When slip surfaces are approached (as in Fig. 4.12c), the phyllosilicates are fractured (Fig. 4.16f), lattices are bent, and phyllosilicates form at high angles to one another.

Where quartz veins dominate the lithology, two primary morphologies exist, a coarser grained morphology and a finer grained morphology. Quartz grains have a high concentration of nanoscale fluid inclusions, and beam damage occurs quickly within the samples during TEM analysis, consistent with 'wet' quartz (*i.e.* a high hydroxyl content). Within the coarser grained quartz, deformation lamellae form perpendicular to the C foliation and undulose extinction occurs parallel to the deformation lamellae (Fig. 4.17a). Along the margins of the coarse grains, bands of fine, new grains exist, formed by grain boundary bulging recrystallization (Fig. 4.17a). This creates a core-and-mantle structure around the relict grains. TEM analysis shows a high concentration of dislocations within the coarser grained quartz (Fig. 4.17b, c). Sub grains (viewed in TEM) form better along grain margins due to an increase in strain (Fig. 4.17e). An increase in dislocation concentration and tangles are common in the presence of fluid inclusions and close to triple junctions (Fig. 4.17d). Dislocation-poor crystals can be seen bulging into dislocation-rich crystals.

The finer grained recrystallized quartz appears to be deforming by a combination of sub-grain rotation and grain boundary bulging (Fig. 4.18a). A weak foliation exists within the recrystallized quartz. TEM analysis shows a smaller dislocation density, due to the mobility of dislocations during glide. Grain boundaries are often irregular (Fig. 4.18b, c). Dislocation walls are seen creating arrays of sub-grains within crystals (Fig.

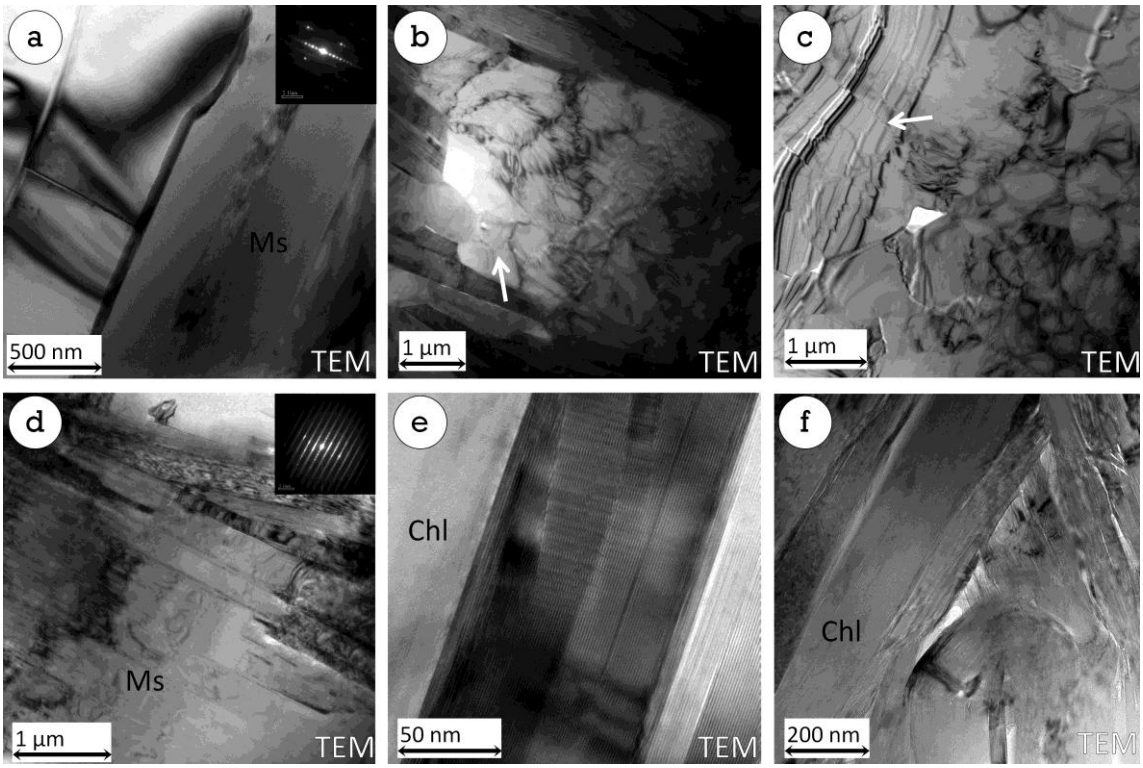

Figure 4.16: TEM Investigation of phyllosilicate-rich domain S-C domain, Nuttby Fm. Evidence of fluid precipitation is common in the form of growth dislocations (**a**), and late dislocation free aggregates of quartz (**b**). Late microcracking can be seen in quartz (**b**), albite, and chlorite (**c**). Muscovite (**d**) and chlorite (**e**) tends to form larger laths, however when a slip surface is approached as viewed in photomicrographs (see Fig. 4.12c) fracturing of the chlorites is common (**f**) indicating that the higher strain rate is no longer able to be accommodated by pressure solution and dislocation movement alone. Edge dislocations are seen in both muscovite and chlorite.

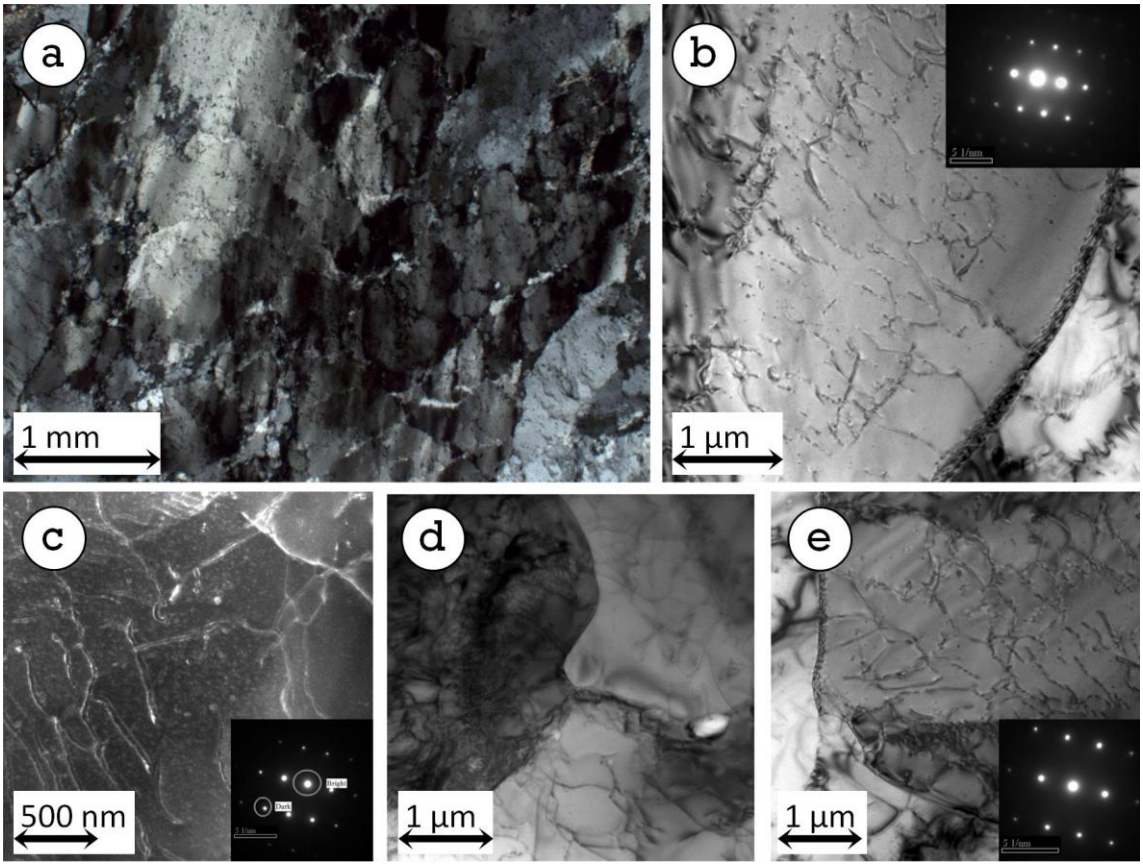

Figure 4.17: TEM images of coarse grained quartz-rich domain, Nuttby Fm. a) Undulose extinction and deformation lamellae are common in coarser segments of quartz. Recrystallization occurs through grain boundary bulging, creating a core-and-mantle structure around relict grains. **b, c)** Dislocation density is high when compared to the smaller recrystallized quartz grains. **d)** Grains with low dislocation density can be seen bulging into adjacent grains with higher dislocation densities. **e)** Sub-grains appear to form with more regularity along grain boundaries.

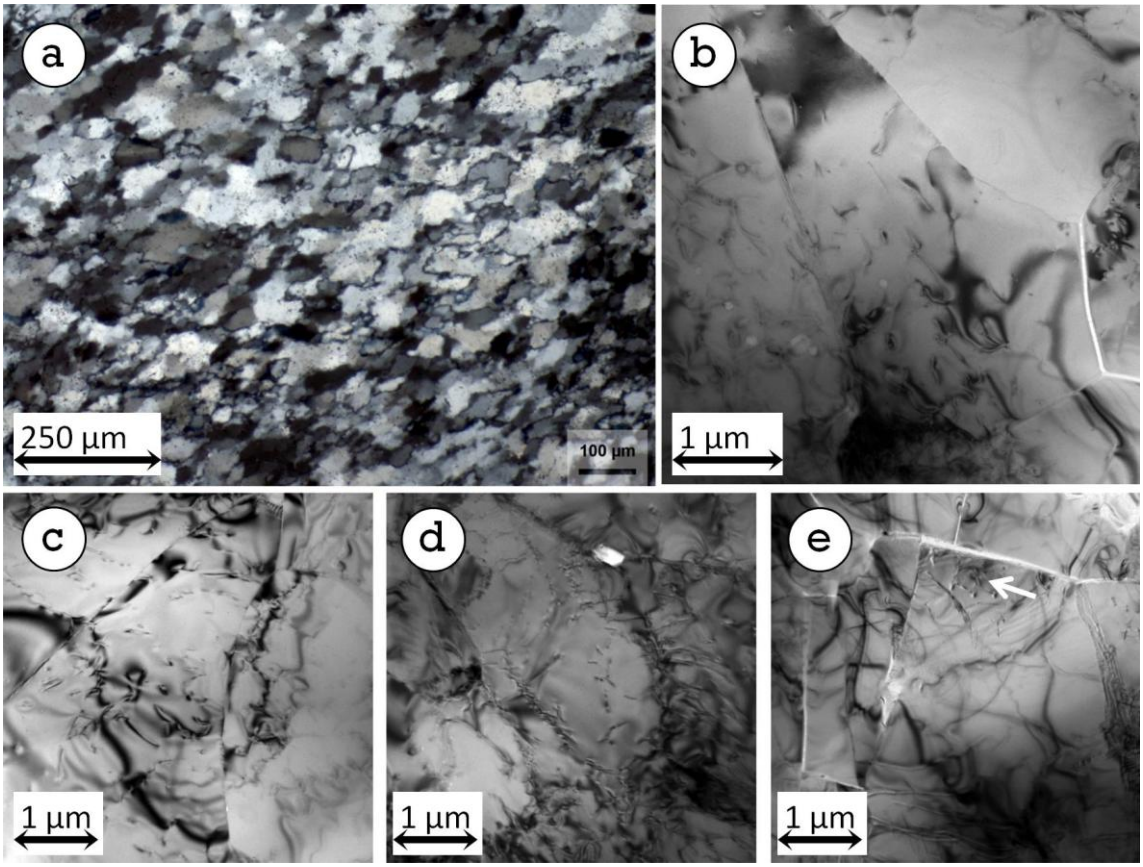

Figure 4.18: TEM images of fine-grained quartz-rich domain, Nuttby Fm. a) Recrystallization appears to occur by a combination of sub-grain rotation recrystallization and grain boundary bulging recrystallization. **b,c**) Grain boundaries are often irregular. **d)** Dislocation density tends to be lower than in the coarser segments, and sub grains are more common. **e)** Sub grains tend to form better along grain boundaries (arrow).

4.18d). Where grains are not completely recrystallized, subgrains can be seen forming in both the optical microscope and TEM.

Within the quartz-rich domains, late phyllosilicate-rich gouge horizons exist along C-planes, and contain well developed shear bands, mantled σ-quartz clasts, mica fish, and slip surfaces parallel to the C-planes (Passchier and Trouw, 2005). Fractured clasts of quartz are found within the phyllosilicate-rich gouge.

4.4.5 Interpretation of microstructures from the S-C domain – Nuttby Formation

A sequence of deformation exists in the microstructures of these rocks, indicating bulk ductility due to dislocation movement and dissolution-precipitation creep at high temperatures, overprinted by late frictional sliding along phyllosilicate-rich horizons at lower temperatures.

Many of the microstructures observed in the S-C domain are indicative of crystal plasticity. Edge dislocations are commonly seen in chlorite and muscovite, and dislocations are common within the quartz-rich domains. The formation of sub-grains attests to dislocation climb in quartz-rich segments (White, 1977). Crystal plasticity in quartz is considered to occur when temperatures are in excess of 300°C at geological strain rates (White, 1977; Hirth and Tullis, 1992; Stipp et al., 2002), though the presence of water is known to dramatically decrease the ductile yield strength of quartz and promotes crystal plasticity through hydrolytic weakening (Griggs, 1967; Kekulawala et al., 1978; McLaren et al., 1983; Jaoul et al., 1984; Kronenberg and Tullis, 1984; Paterson, 1989; Tullis and Yund, 1989). While the exact mechanism causing hydrolytic weakening to occur has not been elucidated, water is known to increase dislocation density (*i.e.* enhance dislocation multiplication), lower the nucleation energy of kinks and jogs, and accelerate the diffusion of oxygen and silicon through the quartz crystal

structure (Griggs, 1967; McLaren et al., 1983; Paterson, 1989). Samples show a high concentration of fluid inclusions, and beam damage during TEM analysis occurs quickly for quartz, indicating high intracrystalline water content (Ardell et al., 1974; Carter and Kohlstedt, 1981).

Pressure solution features are preserved as dissolution seams, tightly spaced disjunctive cleavage, growth dislocations within quartz precipitates along the margins of phyllosilicates, and dislocation-free domains of quartz at the corners of quartz aggregates (Figs. 4.13, 4.14, 4.15, 4.16). While dissolution seams tend to occur sub parallel to C-planes, and would accommodate primarily pure strain, the seams could provide pathways for fluids, assisting in dissolution-precipitation creep. There are strong similarities between the Minas fault zone microstructures and microstructures from experiments on halite-kaolinite mixtures by (Bos and Spiers, 2001, 2002) indicating that our samples could be deforming by frictional-viscous flow. In both cases quartz veins become progressively incorporated into the fine phyllosilicate matrix. In these experiments, S-C foliations only form when experiments are “wet”, under conditions favorable for pressure solution, and temperatures are too low for dislocation activity in halite or kaolinite. Shear strain in these experiments is accommodated by both dissolution and precipitation of halite with concomitant frictional sliding along phyllosilicate foliae.

Fractured phyllosilicates and visible slip surfaces along C-planes attest to discrete displacement occurring when deformation was no longer able to be accommodated by crystal plasticity. These phyllosilicate-rich horizons exist even within quartz units. The inclusion of fractured quartz in the fine, phyllosilicate matrix is consistent with late brittle fracture. The presence of hydrothermal fluids deposited

chlorite; once deposited, slip could easily occur here due to the lowered coefficient of friction along the chlorite horizons. The fact that they overprint the fabric of the recrystallized quartz indicates that they occurred later in the deformational sequence.

4.4.6 Microstructures from the "scaly"mesocataclasite – Nuttby Formation

Optical microscopy shows a clear mineral alignment in the fine grained matrix of the mesocataclasite (Fig. 4.19). SEM analysis of the gouge reveals a very fine, sub-micron-scale, clay-rich (chlorite and muscovite) composition which has been further confirmed by bulk powdered XRD, XRD of oriented clay aggregates, and microprobe analysis (see section 3.4). Larger (>10 μm) grains of quartz are found within the gouge (Fig. 4.20b). While the majority of the gouge appears to have a strongly developed foliation, indicative of bulk ductility (Fig. 4.20b), remnant quartz calcite vein material can be seen boudinaging through fracture and cataclasis (Fig. 4.20c,d). Once isolated, clays form sigmoidal flow patterns around sub-rounded quartz-calcite clasts.

TEM analysis of the gouge shows two primary orientations within the fine-grained phyllosilicates, one which parallels the primary foliation and the other which forms at an angle of ~50° to the primary foliation, forming a structure similar to S-C shear zone geometries, or Y and P Riedel shears (Fig. 4.21; Logan et al., 1992). Trapezoidal geometries can be seen forming down to the grain-scale (Fig.4.21a). Fracturing at the ends of individual phyllosilicates decreases the mean grain size. Average grain size is on the order of 100nm in length, with length to width aspect ratios of ~4.

Two morphologies of quartz exist within the gouge matrix. The first are single crystals of quartz, interpreted to be precipitates, with no visible dislocations. The second

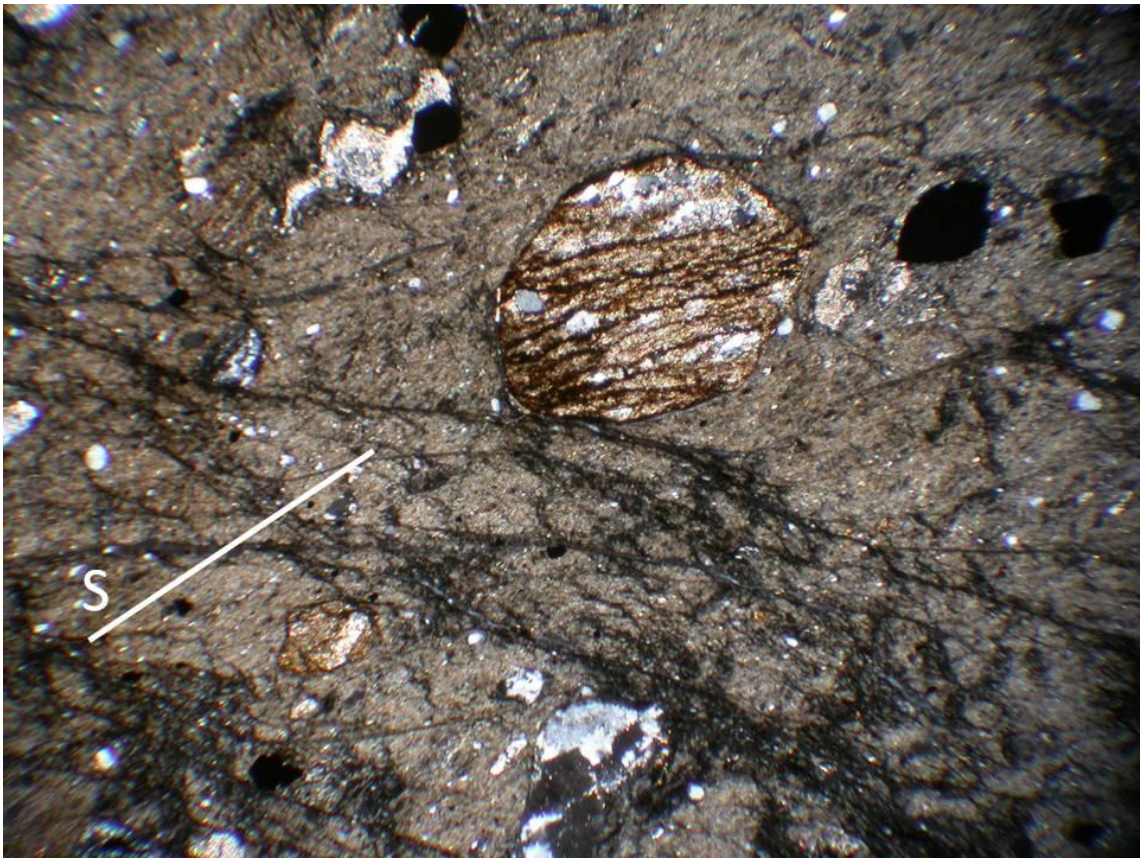

Figure 4.19: Photomicrograph of the 'scaly' mesocataclasite – Nuttby Fm. The gouge shows a strong mineral alignment (S). Clasts of rounded quartz carbonate veins, and rounded to angular clasts of wall rock from both sides of the fault are found entrained within the fine-grained matrix. (FOV = 2.4cm)

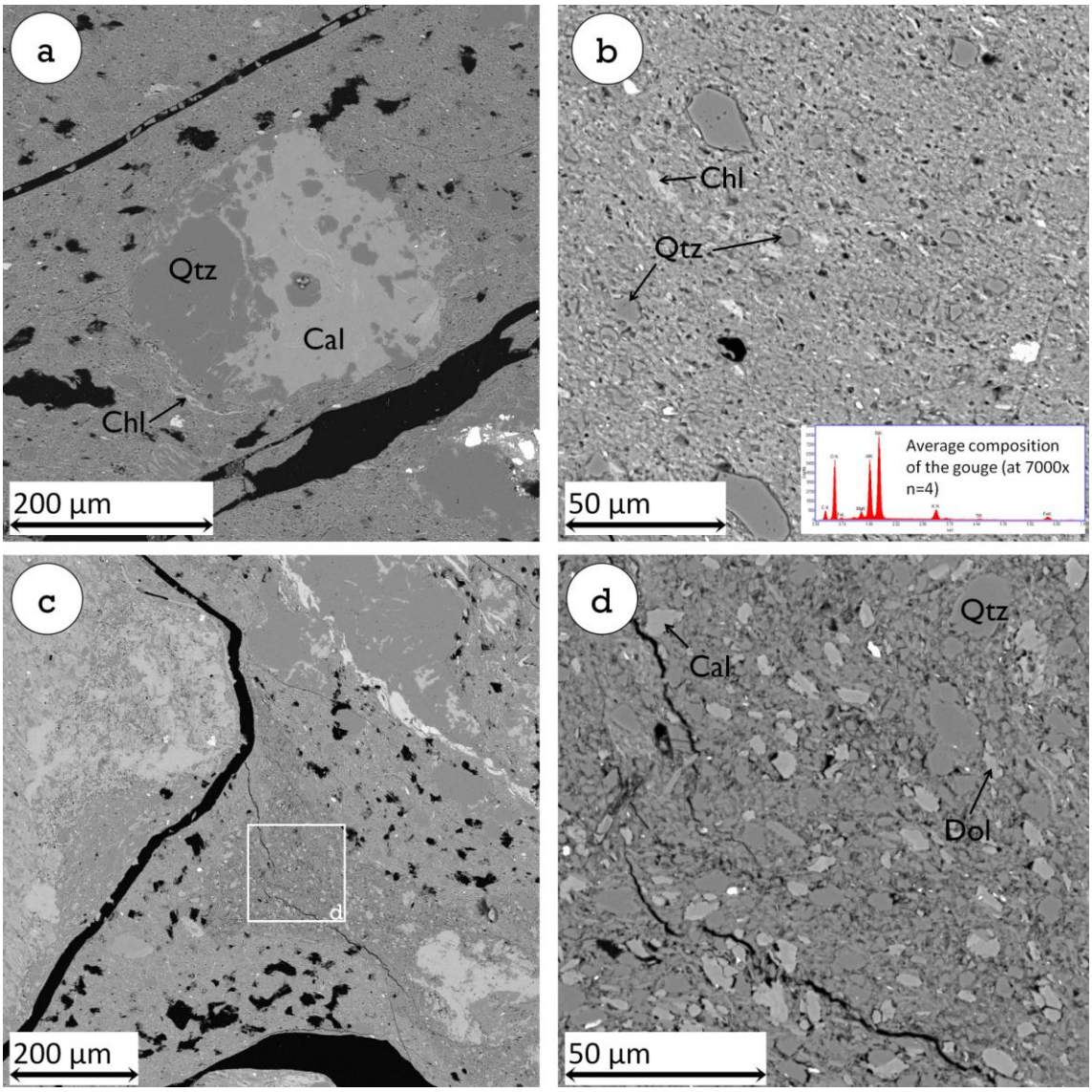

Figure 4.20: SEM Photomicrographs of the 'scaly' mesocataclasite, Nuttby Formation **a**) Clast of rounded quartz carbonate vein with sigmoidal pressure shadows. **b**) Well developed foliation within the gouges. The finest parts of the gouges are effectively mixtures of muscovite and chlorite. **c**) Brittle (cataclastic) fracture of a quartz-carbonate vein as it boudinages. **d**) Quartz-rich segments are clearly deforming through brittle fracture, indicating temperatures less than 300°C, or high strain rates.

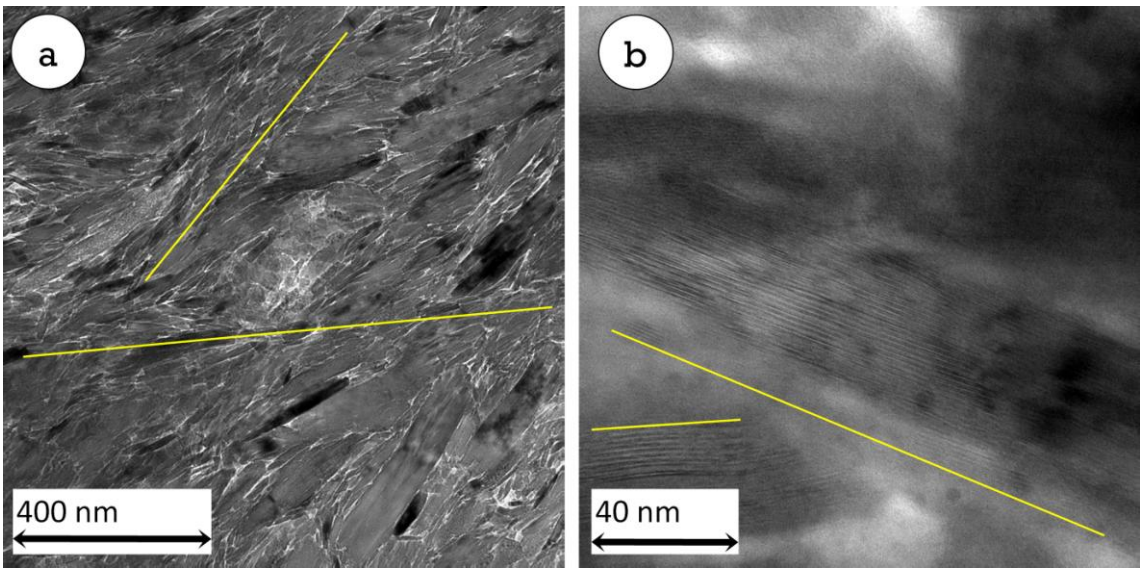

Figure 4.21: TEM Photomicrographs of the fabric from the 'scaly' mesocataclasite, Nuttby Formation TEM photomicrographs reveal two orientations within the phyllosilicate-rich portions of the gouge (**a, b**), which were unseen using SEM. The two foliations create trapezoidal geometries, similar to the foliation seen at the mesoscopic-scale. Individual chlorite and muscovite grains show examples of lattice terminations, and frequently stack on one another so that the ends of the phyllosilicates terminate along the sides of other phyllosilicates.

are large clasts composed of multiple crystals, interpreted to be vein material that has been reduced in size and rounded through chemo-mechanical attrition of vein fragments.

Along the margins of quartz precipitates, phyllosilicates are seen indenting into the quartz, creating a very fine (1-15 nm) film coating (Fig 4.22). The undulatory surface produced through this process is reminiscent of pressure solution seams (Fig. 4.22b). Overgrowths of quartz containing entrapped fluids are seen forming along the margins of individual quartz crystals. Dislocations are not seen within these precipitates, even when lattice fringes are bent allowing for the simultaneous observation of multiple crystallographic orientations (Fig. 4.22d).

Larger clasts of vein material contain abundant evidence of dislocations forming sub-grain walls (Fig. 4.23). Crystals form well developed triple junctions. Chlorine-rich fluid inclusions on the scale of 50-100nm are common. These clasts are similar in appearance and form to the quartz-rich segments observed in the S-C domain of the Nuttby Fm.

4.4.7 Interpretation of microstructures from the "scaly"mesocataclasite – Nuttby Formation

The intense reduction in grain size within the fine-grained phyllosilicate-rich gouge and the boudinaging of quartz-calcite vein material through cataclasis indicates that brittle processes are dominant within the scaly fabrics. However, evidence of concomitant dissolution-precipitation in the form of precipitated quartz with entrained phyllosilicates along their margins and fluid-rich overgrowths indicates that pressure solution is also in operation.

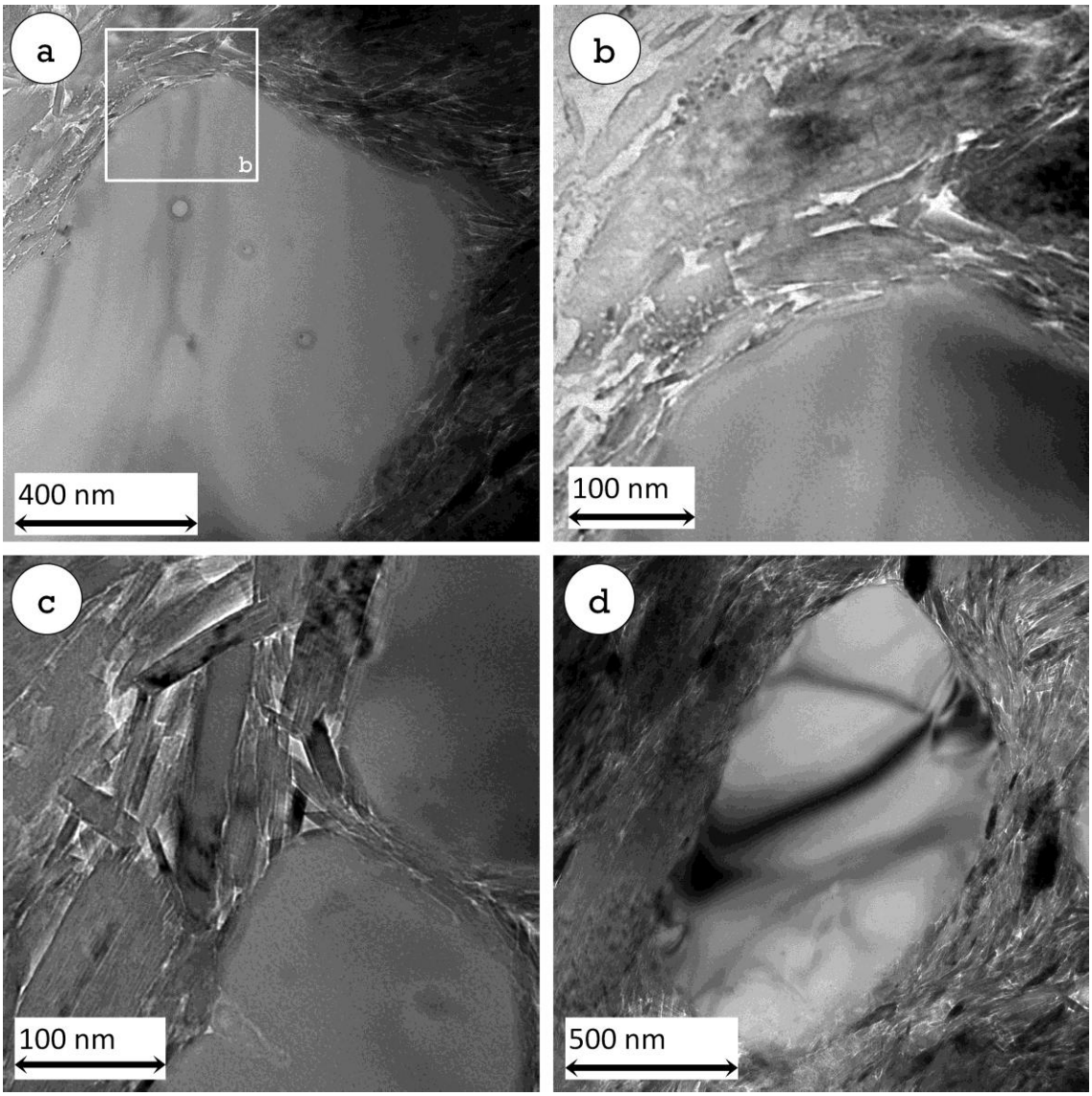

Figure 4.22: TEM Photomicrographs of quartz precipitates, 'scaly' mesocataclasite, Nuttby Formation In addition to vein quartz, sub-micron, dislocation free, precipitates of quartz exist within the phyllosilicate-rich gouge. Along the margins of the quartz clasts, phyllosilicates with widths on the nanometer-scale are seen indenting into the quartz clasts, creating an undulatory surface along the quartz precipitates similar to a pressure solution seam. While most easily seen in figures **a** and **b**, these nanocoatings exist on all the micron-scale quartz grains examined (**c**, **d**).

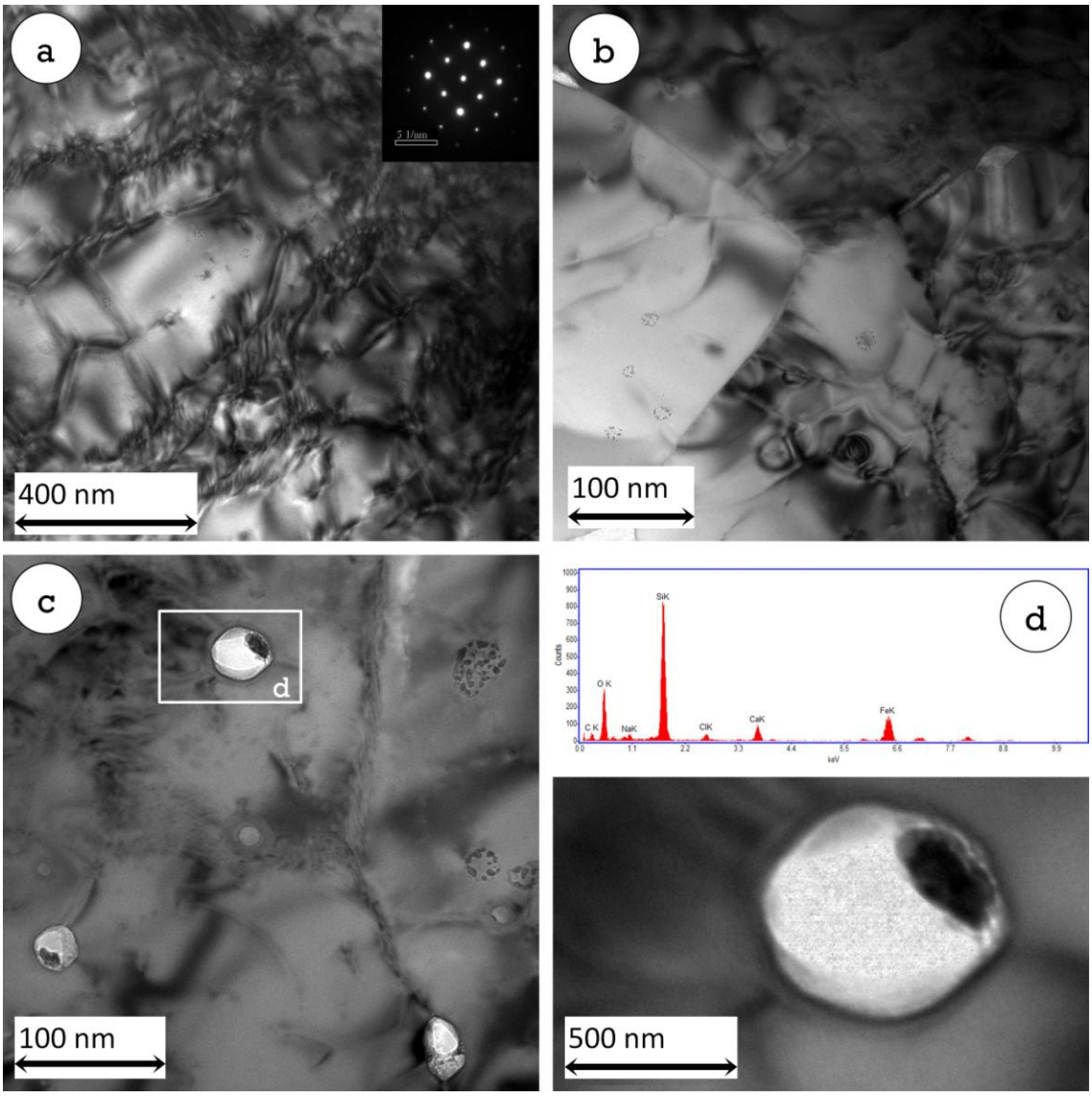

Figure 4.23: TEM Photomicrographs of quartz vein material, 'scaly' mesocataclasite, Nuttby Formation Vein quartz within the 'scaly' mesocataclasite shows many of the same attributes as the S-C domain of the Nuttby Formation. Dislocations and sub-grain walls are relatively common (**a**). Crystals tend to form well developed triple junctions (**b**), and small (5-20 nm), two-phase, chlorine-rich fluid inclusions are common (**c**, **d**). Dislocation tangles emanate from the fluid inclusions.

There is no agreement on how scaly fabrics form at the grain-scale. One hypothesis asserts a mechanical mechanism, in which rotation and realignment of existing mineral grains forms the observed fabrics (Lundberg and Moore, 1986). A second model favours reprecitation of neocrystallized thin clay coatings along the polished surfaces (Schleicher et al., 2009, 2010). Agar et al. (1989) and Prior and Behrmann (1990) discussed the possibility that scaly fabrics could be closely spaced rebound fractures, formed due to unloading of the material during excavation. This could be the case even here, as the decrease in confining pressure during the process of exhumation could have allowed for the formation of rebound fractures. However, detailed work by Labaume et al. (1997) and a detailed review of scaly fabrics in a variety of geological settings (Vannucchi et al., 2003) has found that these fabrics only form due to the alignment of phyllosilicates. The fabric itself can form from partings along aligned grains, or along fractures and pressure solution seams, but aligned platy minerals are a pre-requisite for forming scaly fabrics. The findings in this study are in agreement with these studies, with a distinguishable fabric visible through backscattered SEM, and a clear fabric within the fine gouges down to the nanometre-scale visible through TEM.

Scaly fabrics observed in active accretionary wedge drill cores develop within smectitic-clay-rich packages, and are interpreted to have formed in large part due to the frictional properties and weakness of low temperature phyllosilicates (*e.g.* smectites; Lundberg and Moore, 1986; Moore et al., 1986; Kameda et al., 2015; Kirkpatrick et al., 2015). In samples where scaly fabrics have been observed, clay contents are high; however, detailed XRD work by Schoonmaker (1986) revealed no correlation between scaly fabric development and sapponite or mixed-layer clay concentrations.

The samples examined here contain no mixed layer or smectitic clays (Appendix 3), and yet a scaly fabric exists. Smectitic clays are therefore not necessary in the formation of scaly fabrics in fault gouges, and the samples simply need to be weaker than the surrounding wall rock, have a high phyllosilicate content, velocity strengthening behaviour, and high fluid pressures promoting dilatancy within the samples. In these situations multiple slip surfaces can be accommodating slip simultaneously through continual re-organization of active surfaces during slip (Tarling and Rowe, 2015). TEM observations indicate that this occurs down to the grain-scale (Fig. 4.21).

4.4.8 Microstructures from the folded carbonate bearing phyllite – Nuttby Formation

The folded carbonate bearing phyllite has a strong foliation that has been isoclinally folded. Mineralogically, the primary difference is the extent of Fe-bearing dolomite within the sample (Fig. 4.24). Grain size is smaller than in any other sample, generally on the order of 1µm (Fig. 4.24a). Quartz and dolomite crystals have a blocky appearance, seeming to fill the voids between laths of phyllosilicates (Fig. 4.24a). Folding of the principal foliation is visible at the microscopic-scale (2-3cm), due to differences in carbonate concentration, forming light and dark bands (<0.1mm in width) within the sample. Tightly spaced (<1mm), foliation parallel, disjunctive, dissolution seams offset the compositional layering and veins. Pyrite aggregates form along the margins of calcite veins, and are particularly concentrated at the ends of boudinaged segments. Fluid inclusions are common in the presence of dislocations and along microcracks within the sample (Fig. 4.24b-d). Dislocation density is low, and intact veins show no evidence of recrystallization.

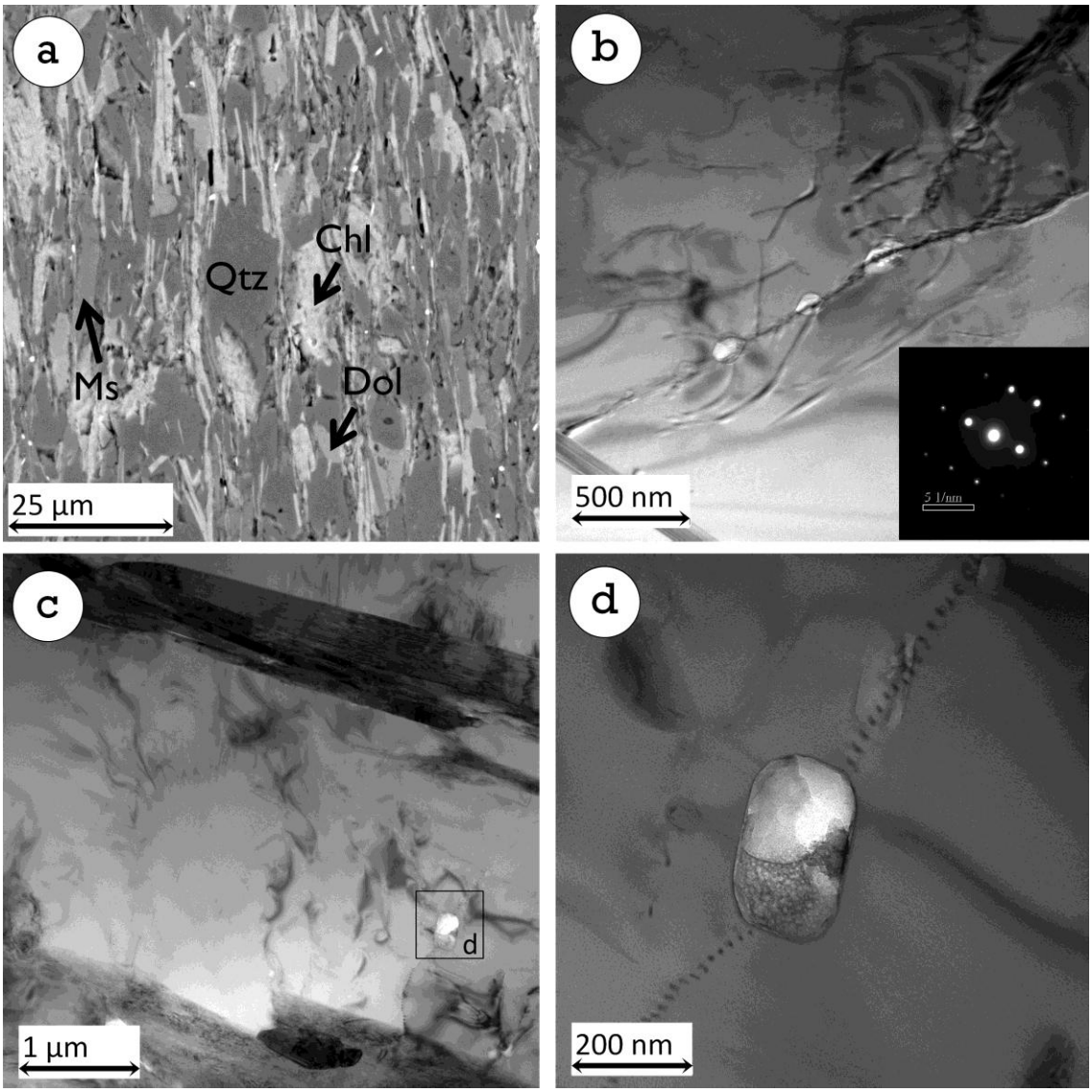

Figure 4.24: Microstructures from the folded carbonate bearing Nuttby Formation The unit has a strong foliation (**a**) that has been isoclinally folded. Quartz, muscovite, chlorite and Fe-bearing dolomite are the dominant phases present in this unit. Dislocation tangles are common in the presence of fluid inclusions (**b**). Three-phase fluid inclusions are seen forming along late microcracks in the quartz (**c, d**). Quartz tends to be blocky, with irregular grain boundaries filling voids between phyllosilicates (**a, c**).

4.4.8 Interpretation of microstructures from the folded carbonate bearing phyllite – Nuttby Formation

Evidence of dissolution-precipitation is evident in the form of tightly spaced dissolution seams, concentrated aggregates of incompatible material at the margins of veins, blocky aggregates of dislocation free quartz and dolomite, and an intensely reduced grain size. While the foliation is not parallel to the Minas fault zone (typical of units in the marginal domain, further from the focus of deformation), significant shear is preserved in the form of dissolution-precipitation and tight folds within the compositional layering. The lack of preservation of dislocation activity indicates lower temperatures than the units within the core domain.

4.5 Metamorphic History of the Greville Bay Section of the Minas Fault Zone

4.5.1 Introduction to the study of metamorphism at Greville Bay

In this section, new data that provide *P-T* constraints on the evolution of the Greville Bay study area are presented. While the structural complexity of the area and the overprinting brittle and ductile features at this site have been well studied (Mawer and White, 1987; MacInnes and White, 2004; MacInnes, 2005), the temperatures and pressures of deformation are poorly understood due to the fine-grained nature of the phyllitic host, and the large stability field for the mineral assemblages observed in these rocks (chlorite-muscovite-albite-quartz-+/- dolomite). In cases where brittle fabrics overprint ductile features, it is currently unknown whether these are due to variations in finite strain (MacInnes and White, 2004), or a decrease in temperature during exhumation. Using samples from across the fault zone, a multi- faceted study of phyllosilicate crystal chemistry (see section 3.2) is used to constrain the pressures and

temperatures under which these features formed, to complement microstructural observations.

Because the Greville Bay region of the Minas fault zone lacks equilibrated metamorphic mineral assemblages, techniques that have been developed specifically for low-grade metasedimentary rocks are utilized: 1) X-Ray Diffraction (XRD) of oriented clay mineral separates was used to determine the phyllosilicate phases present in fault rocks from the Minas fault zone, as well as illite and chlorite 'crystallinity' 2) Electron microprobe elemental analysis (EMPA) was used to determine phengite Si-content, Al^{IV} concentrations in chlorites for geothermometry, and variations in phyllosilicate crystal chemistry through the fault zone. Together these have been used to 1) constrain *P-T* conditions for the formation of the structural fabrics seen in Greville Bay, and 2) relate these conditions to the kinematic fabrics and deformation features seen at Greville Bay to better understand the processes in mature, transpressional fault zones at depth.

4.5.2 Macro to microstructural fabrics of samples taken from Greville Bay

Samples are all derived from the Nuttby Fm. Sample localities with overviews of the results are found in Map 3. For a full description of the fabrics from mesoscopic to TEM-scale refer to sections 4.3 and 4.4.

S-C Domain: S-C fabrics and shear bands are common features in the Nuttby Fm. south of the northern bounding fault which demarcates the internal zone from the marginal domain (MacInnes and White, 2004). Sheath folds are also found within this horizon. Within the core of the fault zone, deformation becomes more focussed as the contact with the Fountain Lake Group rhyolite is approached (Map 1; MacInnes and White, 2004). Shear bands become increasingly common toward the latter contact, ranging in

size from 1-15cm. Samples NJP-07-01, NJP-07-01A, and NJP-07-02 were taken from the S-C domain (from both quartz-rich and phyllosilicate-rich horizons).

Scaly Mesocataclasite: The northern boundary of the core of the Minas fault zone at this locality is a brittle fault that cuts all lithologies. Within the Nuttby Fm. this fault crops out as a wide (50-100m) well-indurated mesocataclasite (~80% gouge, 20% clasts) with a scaly fabric. Within the cataclasite sub-rounded clasts of quartz-calcite vein material are found from mm-scale to sizes of 10cm, and angular clasts of the phyllite from both sides of the fault are found entrained in the gouge. Due to the overprinting relationship of the fault, it is inferred to be a late feature; however, the fault did not simply reactivate pre-existing ductile fabrics or planes of weakness along the contacts between units, leading (MacInnes and White, 2004) to speculate that it is a "kinematic equivalent of the shear band domain under conditions of extreme work hardening". Whether this work hardening was caused by a decrease in temperature during crustal exhumation or a consequence of deformation being progressively accommodated in narrower volumes of rock (increase in strain rate) is unknown. Sample NJP-04-05 is from this unit.

Folded carbonate bearing phyllite: To the north (towards the external zone) of the fault the Nuttby Fm. contains a substantial component of Fe-bearing dolomite. Carbonate-rich seams from progressive accumulation of vein material during transposition provide horizons that display isoclinal folds on the cm-scale. The unit contains complex folds typical of the external zone that have been rotated due to interference from the internal zone of the fault. Sample NJP-08-02 is from this unit.

4.5.3 XRD of oriented clay aggregates

Oriented clay aggregates were prepared for 11 samples from Greville Bay. Clay mineral separation, and the preparation of oriented clay aggregates was performed using

the techniques of Poppe et al. (2001; see section 3.2.2). X-ray patterns were measured using the settings described in section 3.2.4. These settings are in accordance with the recommendations on sample preparation for crystallinity measurements laid out by Kisch (1991). Three sets of analyses were collected for each sample: one air dried for 24hrs, one glycolated for 24hrs, and one heat treated to 400 ^{o}C for 30 minutes (refer to Poppe et al. 2001 and section 3.2.4 for more detail).

After removing the background radiation, illite and chlorite crystallinity (IC and ChC respectively) were calculated from the raw data in Microsoft Excel. IC and ChC are defined by the measured width of the peak at half of its maximum height, referred to as the "full width at half maximum" (FWHM). Maxima were picked for the illite (001) and chlorite (002) peaks from the raw data, and the values of the upper and lower half maxima were then determined from the Excel spreadsheet. Crystallinity was calculated by subtracting the upper °2θ from the lower °2θ to determine the Δ°2θ CuKα. A raw data table is found in Appendix 3. While a "Chlorite Index Standard" (CIS) was not used (Warr and Rice, 1994; Potel et al., 2006; Fagereng and Cooper, 2010), raw data is reported as recommended by Kisch et al. (2004). A semi-quantitative calculation of temperature is not possible using this technique; however it is still possible to plot the data within a diagenesis, anchizone, and epizone plot as described by Kübler (1984).

Mineral identification was done by hand using the techniques described by Moore and Reynolds (1997), by plotting the data in Excel, overlaying air dried, glycolated, and heat treated samples and converting the peaks to crystal spacings in Angstroms using a spreadsheet (Fig. 4.25**)**.

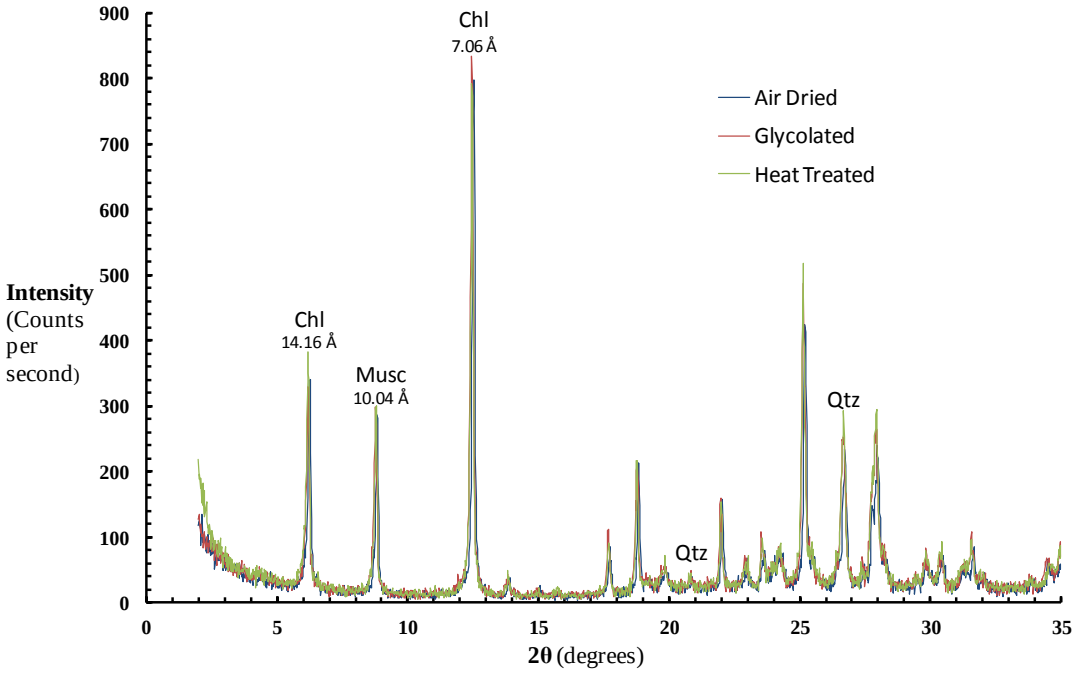

Figure 4.25: Typical XRD plot from Greville Bay Characteristic XRD plot from Greville Bay (sample NJP-07-06) showing well defined reflections for chlorite and muscovite. No low temperature phyllosilicates are found within any samples from Greville Bay. The additional XRD plots are found in Appendix 3.

4.5.4 Results of XRD

All samples show well developed, sharp peaks for the (001) and (002) reflections of muscovite and chlorite (Fig. 4.25). Glycolation and heat treatment did not affect the analyses indicating 1) that there are no expanding clays present in the samples and 2) that the clay mineralogy of the samples is stable up to temperatures of 400°C.

Samples from the Minas fault zone all record illite crystallinity (IC) (001) values between 0.10 and 0.15 $\Delta°2\theta$ CuKα and chlorite crystallinity (ChC) (002) values from 0.10-0.16 $\Delta°2\theta$ CuKα. These values are consistent with epizonal metamorphic grades. Based on the Kübler index (KI; Kübler, 1984), the epizone correlates with the introduction of lower-greenschist facies mineral assemblages assuming appropriate bulk chemistries (*i.e.* chloritoid).

When plotted against one another (Fig. 4.26), the samples plot in two distinct groups: a lower grade group that contains samples from the faulted Nuttby Fm. and the folded carbonate bearing phyllite north of the fault, and a higher grade group that lies on the limits of measurements for crystallinity and contains samples from the S-C domain of the Nuttby Fm. south of the fault. The low values for the KI are consistent with phengites being completely converted from the 1 M_d polytype to the 2 M_1 polytype in all samples, which has been observed to occur at KI values of 0.30 $\Delta°2\theta$ CuKα (Potel et al., 2006).

4.5.5 Microprobe results

Major element chemical compositions of individually selected chlorites and phengites were obtained using the methodology laid out in section 3.2.5.

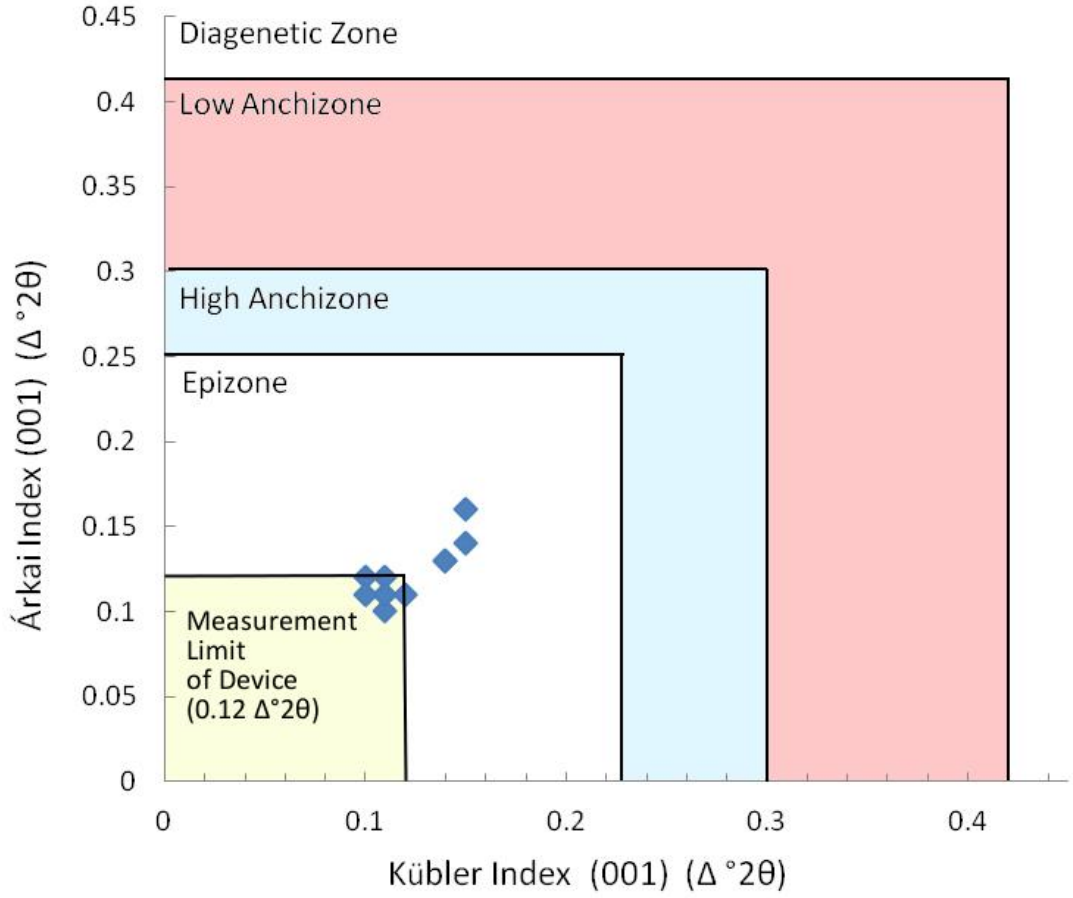

Figure 4.26: Crystallinity data from the oriented clay aggregates Crystallinity data from oriented clay aggregates of pelites from the Minas fault zone. Metapelite zone boundaries from Warr and Rice (1994). Note the two distinct groups of data: one higher grade set at the upper limits of crystallinity measurement, and one epizonal cluster.

Phengite:

Phengites were analyzed from four samples from the S-C bearing phyllite and the folded carbonaceous phyllite. No samples were analyzed from the north bounding fault as the intensely reduced grain size made clean (*i.e.* uncontaminated) analyses impossible. Average compositions of the K-white mica analyzed are presented in Table 4.2. Analyses are normalized to 11 oxygens under the assumption that all iron is ferrous. All analyses showing MnO % + TiO_2 % greater than 0.5% were rejected due to probable contamination (Vidal and Parra, 2000). Most analyses show distinguishable trends and relatively consistent data; however, the small grain size in NJP-08-02 has led to considerable scatter and the results from this sample are inconclusive. The average total interlayer charge (t.i.c. = K + Na +2Ca) for the other three samples is between 0.88 and 0.96, with most samples plotting near the muscovite end member (Figure 4.27a). Little substitution with phengite is observed, and while it appears there could be some substitution with pyrophyllite, a Si *v.* Al_{tot} plot (Figure 4.27b) shows little influence from pyrophyllite, and all samples plot in a small cluster at the muscovite end member. The relationship of Mg and Fe content in samples is considered to be a function of the bulk composition of the samples (Potel et al. 2006; Figure 4.27c), however, considerable scatter is seen in sample NJP-07-02. A (Mg + Fe) *v.* Si_{tot}. plot (Figure 4.27e) indicates that this may be due to minor chlorite contamination. On the basis of model calculations supposing various mixtures (Figure 4.27e), samples NJP-07-01 and NJP-07-01A show no contamination by quartz or chlorite (Potel et al., 2006). These two samples are used for Si-barometry.

Table 4.2: Average chemical compositions of phengite in phyllites from the Minas fault zone Calculated from electron microprobe analyses based on 11 oxygen per formula unit (see Appendix I for raw data)

Phengite								
Sample #	NJP-08-02		NJP-07-01		NJP-07-01A		NJP-07-02	
	n = 4	SD	*n = 13*	SD	*n = 11*	SD	*n = 11*	SD
SiO_2	47.36	5.52	46.65	1.53	46.97	2.36	44.34	3.22
TiO_2	1.00	1.51	0.29	0.26	0.17	0.04	0.45	0.27
Al_2O_3	30.21	5.07	37.15	1.00	37.14	2.56	34.56	4.52
FeO	4.55	2.73	1.97	0.81	1.14	0.20	4.56	4.58
MnO	0.02	0.01	0.01	0.01	0.01	0.01	0.02	0.03
MgO	1.70	1.05	0.09	0.15	0.42	0.04	1.98	2.77
CaO	0.10	0.05	0.16	0.27	0.38	0.71	0.04	0.02
Na_2O	0.61	0.22	1.41	1.18	1.37	0.74	0.96	1.68
K_2O	7.49	2.15	9.09	0.52	8.57	1.14	8.94	0.77
Total	93.03		96.80		96.19		95.84	
Si	3.22	0.29	3.04	0.06	3.06	0.13	2.97	0.11
Al	0.05	0.07	0.01	0.01	0.01	0.00	0.02	0.02
Ti	2.43	0.41	2.86	0.10	2.86	0.20	2.72	0.29
Fe^{2+}	0.26	0.16	0.11	0.04	0.06	0.01	0.27	0.30
Mn	0.00	0.00	0.00	0.00	0.00	0.00	0.00	0.00
Mg	0.17	0.11	0.01	0.01	0.04	0.00	0.21	0.32
Ca	0.01	0.00	0.01	0.02	0.03	0.05	0.00	0.00
Na	0.08	0.03	0.18	0.15	0.17	0.09	0.12	0.21
K	0.65	0.19	0.76	0.05	0.71	0.10	0.76	0.05

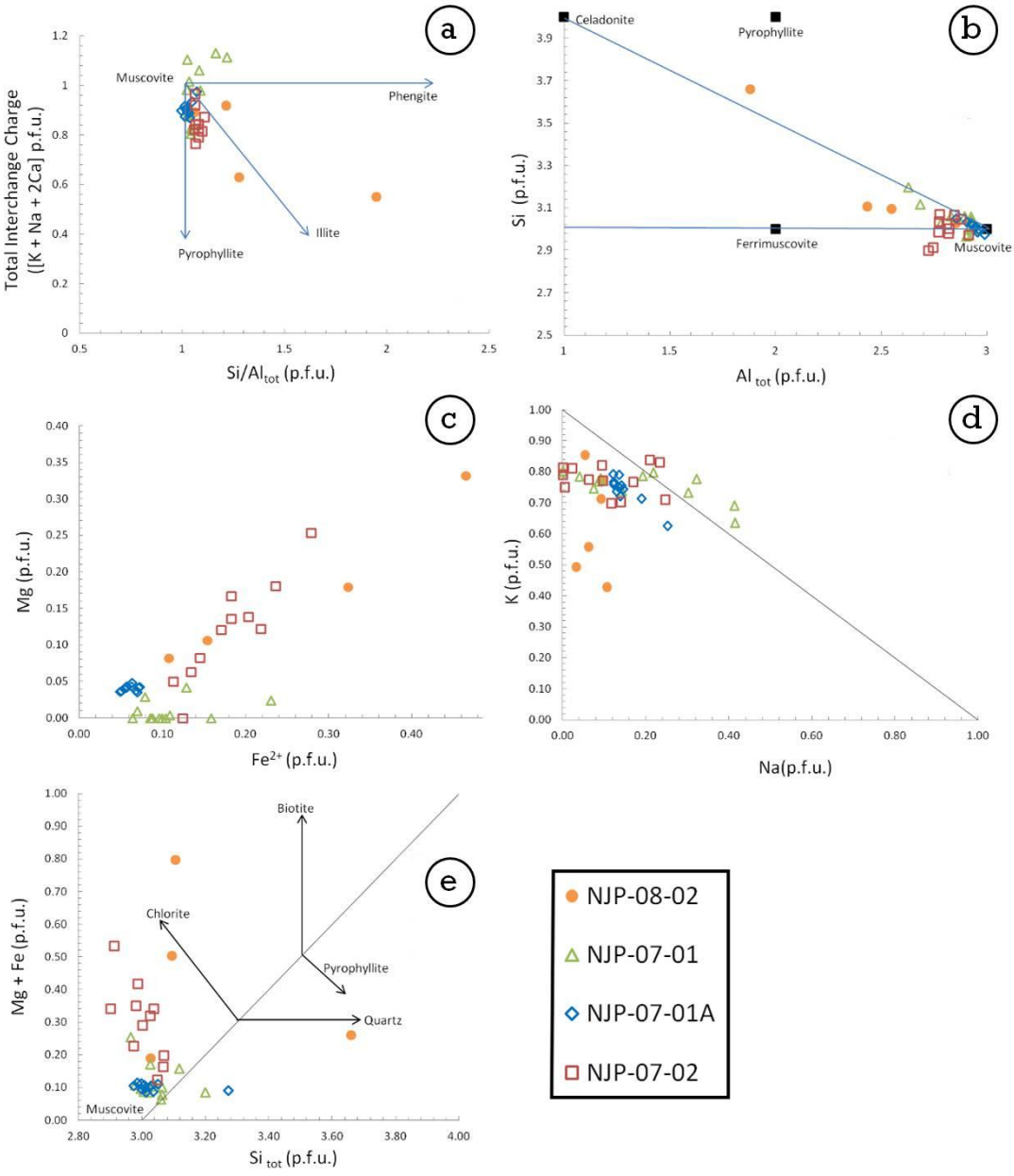

Figure 4.27: Crystal chemistry of phengites analyzed using the microprobe Crystal chemistry of phengites in pelites from the Minas fault zone. Plots of total interlayer charge, Si and Al (**a**, **b**) show most analyses plotting close to the pure muscovite end-member. Most samples plot in the muscovite, illite, paragonite field, with no Tschermak substitutions along the muscovite celadonite substitution line. Sample NJP-08-02 shows considerable scatter and results are likely contaminated due to the intensely reduced grain size. Samples are relatively low in Na (**d**), while evidence of non-Tschermak substitutions (**e**) exists in NJP-07-01 and NJP-07-02 between muscovite and chlorite.

Si values in K-white mica from the S-C domain are low (~3.0 for samples NJP-07-01 and NJP-07-01A). This is consistent with relatively pure muscovite (little substitution with celadonite or aluminoceladonite), and is indicative of low pressure, high temperature conditions (Massonne and Szpurka, 1997).

Chlorite

Chlorites were analyzed from five samples in order to determine the variations in crystal chemistry and for chlorite geothermometry. Morphologies of the chlorites analyzed are presented in Figure 4.28. Average compositions from 107 analyses (after the removal of analyses that did conform to chlorite crystal chemistries) are presented in Table 4.3. Compositions are normalized to 28 oxygens. In previous studies contamination from interlayered white micas and/or other phases is assumed if Σ(Ca + Na +K) is less than a certain value [<0.1 (Dalla et al., 1996); <0.2 (Potel et al., 2006), or if Σ (CaO + Na_2O +K_2O) < 0.5 wt% (Hillier and Velde, 1991). Here contamination is based on the criterion of Potel et al. (2006), as TEM studies have shown Σ (Ca + Na +K) to be greater than 0.10 in natural samples (Curtis et al., 1985). In the Minas fault zone samples, there is no contamination in hydrothermal chlorites associated with the shear from sample NJP-07-01A. However, the analyses of fine-grained chlorites from the other four samples show moderate contamination. NJP-08-02 and NJP-07-02 show Na and K contamination, NJP-07-01 Na contamination, and NJP-04-05 K contamination (Table 4.3). In spite of this, plots from all analyses reveal no deviations from ideal chlorite crystal chemistries, and the relatively low values of Σ (CaO + Na_2O +K_2O) (<1 p.f.u.) indicate that the contamination is not substantive enough to affect the interpretation of analyses.

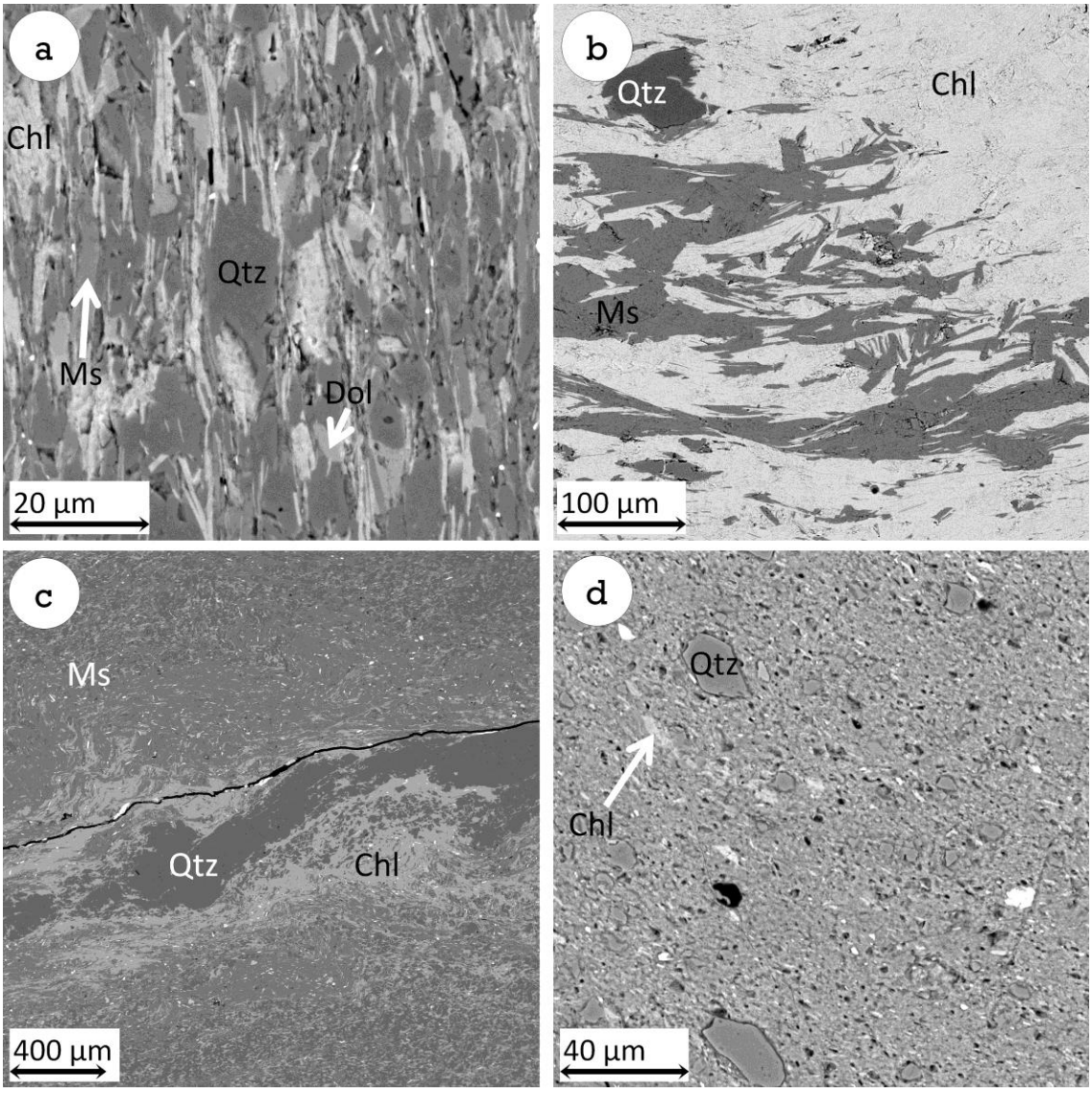

Figure 4.28: Morphologies of chlorites analyzed using the microprobe Characteristic morphologies of chlorites analyzed in this study. **a**) Chlorite within the folded carbonate bearing phyllite north of the fault. Samples from the S-C and shear band domain (**b** and **c**) have hydrothermal chlorites associated with quartz veining as well as chlorites (**c**) within the muscovite dominated host around the veins. Both were analyzed and no systematic differences between the two morphologies were found. From the mesocataclasite (**d**), chlorites were sampled from within the gouge as opposed to from the embedded clasts of phyllites. It is unknown whether these have been completely recrystallized during faulting therefore the temperatures recorded are a maximum.

Table 4.3: Average chemical compositions of chlorites in phyllites from the Minas fault zone Calculated from electron microprobe analyses based on 16 oxygen per formula unit. (See Appendix I for raw data)

Chlorite										
Sample #	NJP-08-02		NJP-07-01		NJP-07-01A		NJP-07-02		NJP-04-05	
	n = 11	SD	*n = 17*	SD	*n = 43*	SD	*n = 22*	SD	*n = 14*	SD
SiO_2	25.17	1.27	23.28	0.73	23.37	0.48	26.13	1.21	27.82	2.53
TiO_2	0.15	0.22	0.07	0.03	0.05	0.01	0.15	0.10	0.14	0.12
Al_2O_3	23.11	0.97	23.74	0.30	23.17	0.29	23.29	0.72	25.56	1.42
FeO	29.25	0.95	34.84	0.93	32.00	0.55	24.36	1.22	28.19	2.31
MnO	0.12	0.02	0.25	0.05	0.26	0.06	0.17	0.02	0.22	0.10
MgO	10.93	0.68	7.97	0.53	8.91	0.19	14.74	0.89	9.81	1.55
CaO	0.19	0.13	0.03	0.02	0.05	0.03	0.13	0.10	0.08	0.04
Na_2O	0.16	0.12	0.52	0.59	0.02	0.02	0.79	0.76	0.10	0.08
K_2O	0.35	0.17	0.09	0.16	0.02	0.07	0.53	0.44	0.79	0.48
Total	89.42	0.80	90.79		87.84		90.29		92.72	
Si	5.27	0.20	4.95	0.16	5.10	0.07	5.25	0.17	5.48	0.21
Al^{IV}	2.73	0.20	3.05	0.16	2.90	0.07	2.75	0.17	2.52	0.21
Al^{VI}	3.02	0.14	2.95	0.18	3.06	0.06	2.87	0.27	3.50	0.25
Ti	0.02	0.03	0.01	0.01	0.01	0.00	0.02	0.01	0.02	0.02
Fe^{3+}	0.12	0.10	0.04	0.07	0.09	0.05	0.07	0.12	0.45	0.20
Fe^{2+}	5.01	0.29	6.30	0.31	5.75	0.18	4.10	0.40	4.23	0.76
Mn	0.02	0.00	0.05	0.01	0.05	0.01	0.03	0.00	0.04	0.02
Mg	3.42	0.23	2.52	0.16	2.90	0.06	4.43	0.27	2.88	0.42
Ca	0.04	0.03	0.01	0.00	0.01	0.01	0.02	0.02	0.02	0.01
Na	0.13	0.10	0.42	0.48	0.01	0.02	0.63	0.53	0.08	0.06
K	0.19	0.09	0.05	0.09	0.01	0.04	0.30	0.22	0.39	0.24
X_{Fe} (Fe/Fe+Mg)	0.60	0.02	0.72	0.01	0.67	0.00	0.49	0.01	0.62	0.05
T (°C)	377	32	430	26	405	11	381	27	344	34
Al^{IV} *Zang & Fyfe*	2.50	0.21	2.72	0.17	2.61	0.07	2.62	0.18	2.28	0.26
T (°C) *Zang & Fyfe*	340	35	377	28	359	12	361	29	304	42

Chlorite analyses fall in a small group with an intermediate composition between chamosite and clinochlore when plotted in a Fe-Mg-Si diagram (Figure 4.29d). The plot of total interlayer cations *v.* total aluminum (Figure 4.29a) as well as the Si *v.* octahedral cations plot of Wiewióra and Weiss (1990) (Figure 4.29c) clearly show sudoitic substitutions between the chamosite-clinochlore intermediate composition and sudoite. Figure 4.29b shows that the Tschermak substitution plays an important role in the chlorites analyzed, while the divalent substitution shows little effect (Fe^{2+} for Mg^{2+}). These plots show that the main substitutions occurring in the chlorites analyzed are the Tschermak and tri-divalent substitutions.

Two temperatures were calculated using chlorite geothermometers. Using the chlorite geothermometer of Cathelineau (1988) mean temperatures ranging from 344 to 430°C were determined (Table 4.3). However, the Fe/Mg ratios in our samples (0.49-0.72) are substantially higher than those used by Cathelineau (1988) to calibrate the geothermometer. The Fe ↔ Mg substitution reflects changes in temperature, and in the oxygen and sulfur fugacities of the contemporaneous fluid. Zang and Fyfe (1995) revised the thermometer to accommodate the influence of Fe ↔ Mg substitutions on the content of Al^{iv}. As discussed in Frimmel (1997), this calibration seems to work better for chlorites with $X_{Fe} > 0.5$. In using this correction, temperatures from samples NJP-07-01, NJP-07-01A, and NJP-07-02, which all come from the S-C domain of the Nuttby Fm., fall within a smaller temperature range (359-377°C). The most robust of these temperatures is 359 +/- 12°C from the uncontaminated NJP-07-01A. The mesocataclasite records a temperature of 304 +/- 42°C while the folded carbonate bearing phyllite records temperatures of 340 +/- 35°C.

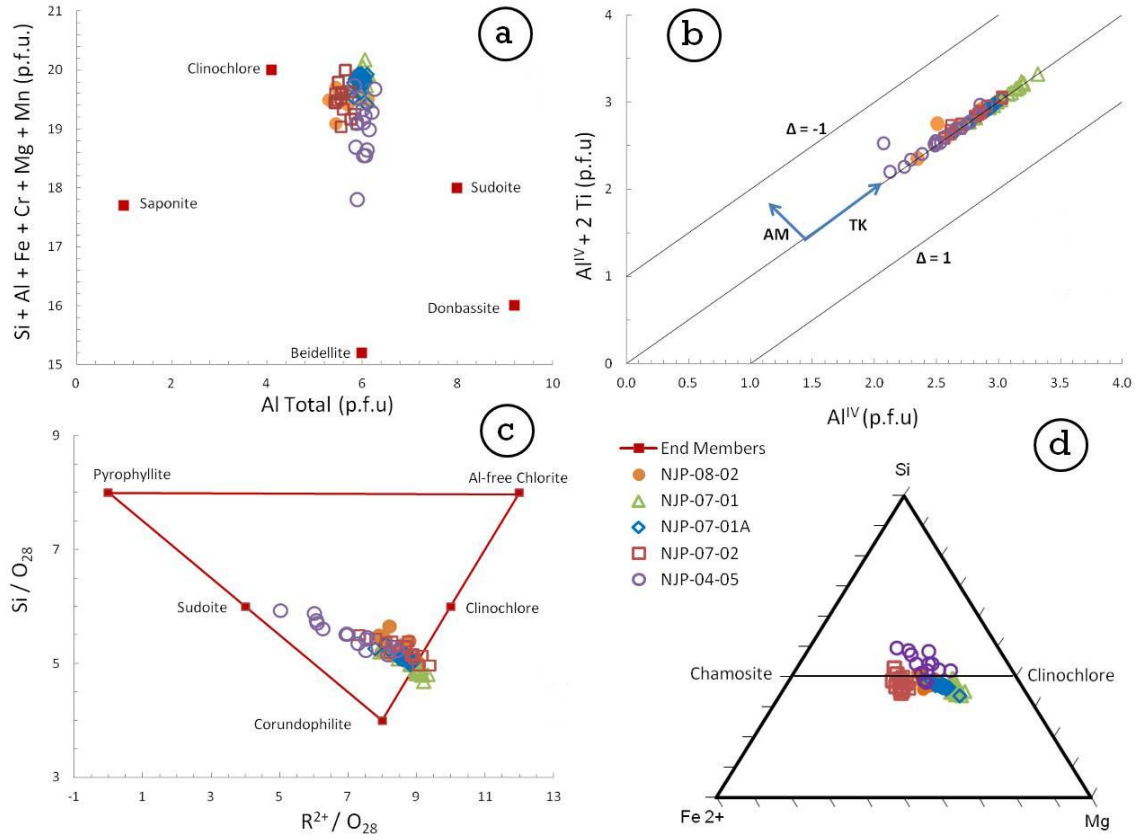

Figure 4.29: Crystal chemistry of chlorites analyzed using the microprobe Crystal chemistry of chlorites in pelites from the Minas fault zone. **a**) Plot of total non-interlayer cations *v.* total Al with end members based on Bailey (1988), (plot after Fagereng and Cooper 2010). **b**) Plot of Al^{VI} + 2Ti *v.* Al^{IV}. Arrows show TK (Tschermak) and AM (dioctahedral) substitution trends (plot after Potel et al. 2006). **c**) Chemical compositions of chlorite plotted in the R^{2+} - Si diagram of Wiewióra and Weiss (1990). R^{2+} represents the octahedral cations (Mg + Fe^{2+} + Mn^{2+}) The aluminum free chlorite is a fictive 14Å chlorite having a serpentine composition (Inoue et al., 2009). **d**) Si-Fe^{2+}-Mg triangular diagram showing all samples plotting in a small intermediate between clinochlore and chamosite.

Temperatures correlate well with crystallinity data: samples from within the northern fault and the folded carbonate-bearing phyllite to the north of the fault record lower temperatures than the ductile S-C domain to the south of the fault, with the late fault displaying the lowest temperatures (Map 3).

4.5.6 Discussion and implications of results

Samples plot in two clear groups for both temperature and "crystallinity" data, 1) a lower grade cluster that encompasses the north bounding fault and the folded carbonate bearing phyllite to the north of it, and 2) a higher grade cluster that encompasses samples from the S-C domain to the south of the fault (Map 3). The distinct offset of the northern bounding fault and the folded carbonate-bearing phyllite indicates that these fabrics are not simply the result of strain hardening within the fault, and represent later motion of the fault during exhumation.

Low Si values in phengites, consistent with purely muscovitic compositions within samples from the S-C domain indicate high geotherms within the Greville Bay region of the Minas fault zone. Several options exist for the high heat flow in this area including: 1) shear heating from movement along the fault, 2) heat from nearby plutons, 3) high heat flow from extensional pull-apart tectonics along the Minas fault zone, and 4) heat anomalies from hot deep crustal fluids migrating along the fault. Of these shear heating seems the most probable.

Shear heating from movement along faults is known to locally increase temperatures, and often causes a heat flow anomaly. Heat is argued to be transferred around fault zones through conduction at time scales greater than 10 000 years (Lachenbruch, 1980) and/or through heat transport by fluid advection (i.e.: the movement of thermal fluids through the crust; Scholz 2006). Hot springs (>8°C above

the ambient temperature) and cold springs (2 - 8°C above the ambient temperature) have been directly correlated with most major fault zones (Manga, 1998; Scholz, 2006). The widespread evidence of fluid circulation and significant fluid pressures at Greville Bay (veining, hydrothermal alteration in the form of precipitated chlorite and minor epidote phases, implosion breccias) indicates that fluid flow may have played an important role in the transport of heat generated within the fault zone. Post-depositional white micas from argillaceous sections of the White Rock Fm. to the south of the Minas Fault zone, and the Arsaig Gp further east along the fault zone record Ar-Ar ages of 322.6 +/- 2.1Ma, coeval with the Alleghenian orogeny. These ages were interpreted by Murphy and Collins (2008) to represent distributed fluid flow coeval with dextral shear along the fault zone. Within the St. Marys basin to the east of the Greville Bay study area, along the Cobequid fault, a steep temperature gradient (>35 °C/km) within the extensional sedimentary basin adjacent to the fault zone has been inferred by Abad et al. (2010) from similar clay mineral compositions (K-micas, chlorite and chlorite-mica stacks) and from b-cell dimensions of the K-white micas. Crystallinity reflected an increase in grade as the Chedabucto fault was approached, which correlates well with our higher grades observed within the fault core. Abad et al. (2010) interpreted this to be due to the enhanced permeability within fault zones allowing for fluids to flow along them (Sibson, 1989; Caine et al., 1996; Faulkner et al., 2010). However shear heating along the fault could also explain the increase in grade with proximity to the fault core.

Early Carboniferous plutons are widespread to the north of the Cobequid fault, including the Cape Chignecto Pluton (Rb-Sr isochron date of 338 Ma +/- 17; Ryan & Boehner 1990), the Moose River Pluton (342 +/- 5Ma; Pe-Piper et al. 1989), and the North River Pluton (Rb-Sr isochron date of 356Ma +/- 17; Pe-Piper et al. 1989) and

could be related to the elevated geotherms along the Minas fault zone. However the distance from our fault zone to the nearest pluton (Cape Chignecto) is ~4 km, and it is unlikely that the heat from the pluton affected our samples. Waldron et al. (1989) mapped deformation in the Cape Chignecto Pluton to the west of the Greville Bay study area, where the pluton was thrusted over the Fountain Lake Gp. Ductile fabrics, including recrystallization of quartz clasts and S-C fabrics within the thrusted pluton, and co-existing brittle fracturing of feldspars indicates greenschist facies conditions during deformation (300-400°C). The cooling time from emplacement of the pluton to these temperatures could occur within a period of two million years. Waldron et al. (1989) inferred that strike-slip motion on the Cobequid fault was directly related to this thrusting event due to a change in strike along the fault trace forming a restraining bend, causing transpression within Cape Chignecto. This movement is constrained to a time frame between 350 Ma (deposition of Horton Gp sediments) and 305 Ma (deposition of the overlapping Cumberland Gp). Donohoe and Wallace suggested that this event occurred at ~320 Ma based on correlative deformation across the fault zone. It seems likely that this event correlates with the 322 Ma ages of K-micas recorded by Murphy and Collins (2008), and could be related to one of our larger episodes of movement recorded at Greville Bay (the S-C domain?).

The ductile fabrics associated with the Minas fault zone are indicative of creep behaviour. Within actively creeping faults, such as the strand of the San Andreas fault in the region of Parkfield, elevated heat flow has been measured compared with the regional average (Williams et al., 2004). At 2.7km depth, a temperature of 120°C has been recorded. Assuming a surface temperature of 30°C, the geothermal gradient is on the order of 30°C/km. If we assume similar geotherms for the Minas fault zone at

Greville Bay, conditions for the formation of the ductile fabrics formed would be ~11km at 360°C. The brittle fault would have formed at ~9km at 300°C (maximum, as we are uncertain as to whether the chlorite analyzed here was precipitated during faulting, whether it is from the wallrock, or whether it was recrystallized during faulting).

An unresolved question is how do we juxtapose our two grades of rocks when the kinematic indicators all show dextral faulting? One hypothesis is that the boundary to the north of the S-C domain is a high angle thrust fault that has been later reactivated and overprinted by dextral slip. The thrust fault could be part of a larger scale positive flower structure formed due to a change in strike of the fault (from 082° to 068° over a distance of ~58 km; MacInnes 2005) as one progresses west . The higher grade rocks would then be a sliver that has become entrained in the fault zone.

The juxtaposition of different crustal levels also occurs elsewhere along the Minas fault zone. Dramatic juxtaposition of lower grade and upper crustal rocks occurs at Clarke Head, where Carboniferous sediments are found against metamorphic basement (Gibbons et al., 1996). The Clarke Head Megabreccia is a wide package of gouge-rich fault core which entrains large clasts of Carboniferous sedimentary rocks, as well as igneous and metamorphic basement that has been uplifted from temperatures of 700-860°C, and 750-950MPa (White, 2004).

4.6 Conclusions

- Microstructures from the Fountain Lake Group rhyolite are indicative of crystal plasticity in quartz. The S-C domain of the Nuttby formation shows features indicative of crystal plasticity within quartz-rich packages, while phyllosilicate-rich packages show features consistent with crystal plasticity in muscovite and chlorite and concomitant

pressure solution processes in quartz. Together these processes create a very fine-grained S-C structure, with increasing homogeneity with increased simple shear, and accommodate deformation within this unit. Crystal plasticity of quartz is not evident in the units north of the S-C domain, however tight folding and a very small grain size within the folded carbonate bearing phyllite is indicative of deformation accommodated by dissolution-precipitation. All features are overprinted by late brittle deformation.

- Chlorite geothermometry attests that the S-C domain of the Nuttby Fm. records higher temperatures (359 +/- 12°C) than the units to the north of it. These temperatures are well within the bounds for crystal plasticity for quartz, chlorite, and muscovite, but not for feldspar. Measurements of chlorite and muscovite crystallinity also show higher grades for the S-C domain of the Nuttby formation than for the mesocataclasite or for the folded carbonate bearing phyllite.
- Low silica content in white micas is indicative of high geotherms. The higher geotherms recorded in active fault zones such as the San Andreas fault (~30°C/km) could serve as a proxy for this locality and would indicate formation at ~11km for the S-C domain given a geothermal gradient of 30°/km.
- The Jeffers Gp and Parrsboro Fm. show primary features including bedding. These units have not experienced the same level of deformation as any other domain of the Nuttby Fm. Deformation has localized in the finest grained units.
- The boundary between the S-C domain and the units to the north is interpreted as a thrust fault (as part of a positive flower structure) incorporating a sliver of higher temperature and pressure fault rocks. This is consistent with a change in strike in the fault (curves to the south as you proceed to the west). The thrust has been overprinted by

late, dextral, motion along the Minas fault zone. Brittle faulting subsequently overprinted the ductile deformation found in the fault zone.

- Where a late brittle fault cuts through the fine-grained Nuttby Fm., a scaly mesocataclasite has formed. This unit contains mesoscopic features comparable to scaly fault zones found in accretionary prisms. Grain size has been reduced though cataclasis, and a clear fabric exists down to the TEM-scale. Microscopic clay coatings exist on quartz precipitates. These features have been formed in the absence of smectitic clays, and we postulate that the conditions for scaly fabric formation include a high concentration of phyllosilicates with low coefficients of friction and velocity strengthening behaviour, and high fluid pressures. Under these conditions shear accommodation occurs along multiple slip surfaces that continually reorganize themselves.

CHAPTER 5: THE SAN ANDREAS FAULT OBSERVATORY AT DEPTH

5.1 Introduction

5.1.1 Introduction to the SAFOD project

The San Andreas fault (SAF) is an over 1000 km long active fault zone extending to at least 15 km depth. Like many fault zones, the SAF is not a single fault surface, but an anastomosing system of linked faults and associated deformation features which range from several hundred meters to several kilometres in width (Streitz and Sherburne, 1980; Faulkner et al., 2010). Along the SAF, radar interferometry has shown that several segments undergo creep behaviour, while adjacent segments show little to no creep (Fig. 1b; Rosen et al., 1998). In order to study the processes causing creep in discreet sections and to directly observe an active fault at depth, the San Andreas Fault Observatory at Depth (SAFOD) drilling program was carried out in 3 phases between the summers of 2002 and 2007 across a creeping section of the SAF, ~11 kilometres north of Parkfield (Zoback et al., 2010). Phase III drilling produced 39.9 m of core in three runs, and crossed two actively deforming fault strands defined by deformed Phase II casing, and one major contact between the Salinian Terrane and the Great Valley Formation (Fig. 1a; Zoback et al., 2010). The fault zone was crossed at ~2.7 km depth and a local temperature of 120 °C was recorded (Zoback et al., 2010).

One of the primary objectives of the drilling program was to determine the cause of the San Andreas faults apparent weakness (Brune et al., 1969; Lachenbruch and Sass, 1980; Zoback et al., 2010). A principal stress orientation nearly perpendicular to the fault surface (Mount and Suppe, 1987, 1992; Hickman and Zoback, 2004) and the absence of a heat anomaly (Lachenbruch and Sass, 1980) point to a “weak fault within a

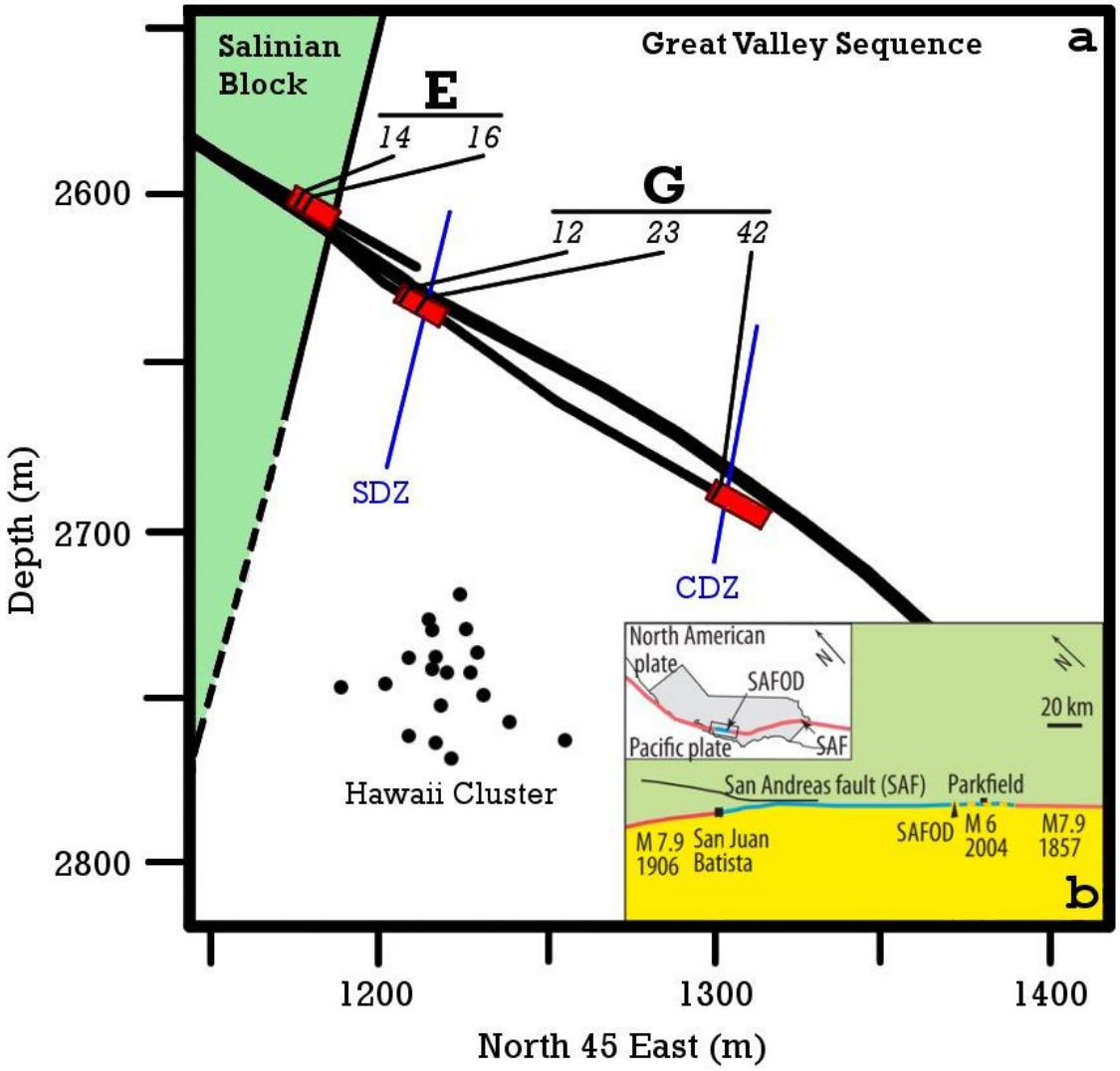

Figure 5.1: Location of the SAFOD site and sample intervals **a**) Profile of the phase 3 coring intervals (red squares) with respect to the main bore hole (MBH). Locations of the five intervals of core studied in this paper are marked within the coring intervals. Note the relative location of the southern and central deformation zones (SDZ and CDZ respectively) with respect to our studied samples. **b**) Map view of the San Andreas fault showing the creeping section (blue line) with the trace of the last two M_w 7.9 earthquakes within the locked section (red line; Gratier et al. 2011). The sliding rate is 28 mm/yr in the central part of the creeping section and decreases to 20 mm/yr at the SAFOD site (Titus et al., 2006; figure adapted from Gratier et al., 2011).

strong crust" model for the SAF, though the reason for the weakness is poorly understood. Two principal hypotheses have been proposed: 1) a frictional coefficient much lower than the crustal average of 0.6 within the fault zone due to favourable mineralogy, and 2) high pore fluid pressure lowering the effective stress and/or allowing for pressure solution creep and diffusive mass transfer to control deformation. Much of the recent analysis of SAFOD core has concentrated on the role of foliated clays in reducing the frictional coefficient of the fault gouge (Solum et al., 2006; Moore and Rymer, 2007; Carpenter et al., 2009, 2011; Schleicher et al., 2009, 2010; Holdsworth et al., 2011; Lockner et al., 2011; Hadizadeh et al., 2012; Janssen et al., 2012; Moore, 2014), while an absence of influxing fluids or gases, and a nearly constant *V*p /*V*s ratio during drilling has shifted the focus of discussion away from high pore pressure (Zoback et al., 2010). However, Wang (2011) has shown that the duration of direct measurements during drilling may not have been long enough to detect an influx of aqueous formation fluids, microstructural studies of the SAFOD core have shown pervasive evidence of pressure solution and diffusive mass transfer (Gratier et al., 2011; Holdsworth et al., 2011; Mittempergher et al., 2011; Hadizadeh et al., 2012; Richard et al., 2014), and a change in mud gas composition was recorded on either side of the fault core, indicating that the core acts as an impermeable seal (Wiersberg and Erzinger, 2008). High pore pressure may therefore still play an important role in the mechanics of the SAF.

Local earthquake rupture has been speculated to contribute to the long term weakening of creeping transcurrent faults. Çakir et al. (2012) analyzed SAR data from the North Anatolian fault, and showed creep following the 1999, M_w 7.4, Izmit earthquake, indicating that brittle processes during earthquake rupture can cause weakening and subsequent creep in fault zones. It has been suggested that the repeating

M_w 6.0 earthquakes in the Parkfield region contribute to the weakening processes that allow fault creep to occur at the SAFOD site (Gratier et al., 2011).

This component of the thesis comprises a microstructural study of five drill core pieces distal to the actively creeping zones (Fig. 5.1) and shows that foliated clays exist in discreet bands throughout the SAFOD core, that diffusive mass transfer is ubiquitous throughout the core, and how pressure solution-accommodated creep may be the most effective mechanism of deformation at the SAFOD site. While most investigations have concentrated on explaining the weakness of the creeping segments of the SAF relative to the "host lithology", these data demand that we ask why the SAF isn't weaker? Why do we see microseismicity surrounding the SAFOD site (Hawaii cluster, see Fig. 5.1) and why is the fault active only along two deformation zones?

5.1.2 Lithologies

Work on the mineralogy of cuttings from the main bore hole was performed by Bradbury et al. (2007) and Solum et al. (2006). They separated the main bore hole into six major lithologies based on the compositions of grain-mount thin-sections. From the top of the section to the bottom these are: 1) Quaternary and Tertiary sediments, 2) Salinian granite, 3) Salinian granodiorite, 4) feldspar-lithic arenite, 5) feldspar-lithic arenite +/- siltstone, and 6) siltstones, mudstones and shales (Fig. 5.2). A section of clay-rich alteration was documented between zones 4 and 5, while the main strands of the SAF were interpreted to intersect the main bore hole in the vicinity of the contact between zones 5 and 6 (Bradbury et al., 2007).

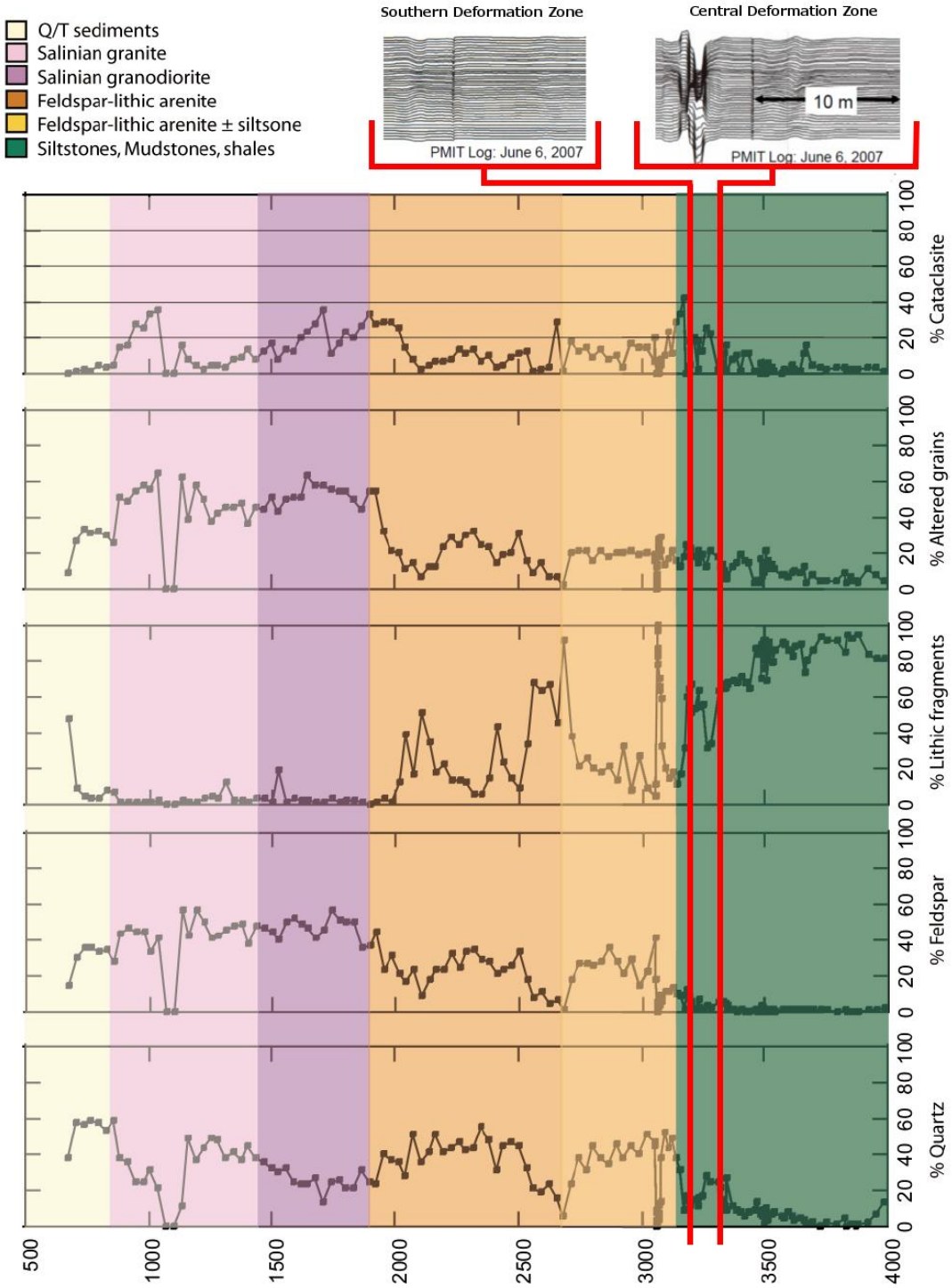

Figure 5.2: Lithology of the SAFOD main bore hole Lithologies of the main bore hole based on mineralogy of the cuttings (adapted from Bradbury et al. 2007). The SDZ and CDZ are shown in red with the accompanying casing deformation logs used to identify targets for phase 3 coring.

In the following year, Phase 3 side-track holes were drilled within 20m of the main borehole in the vicinity of the contact between zone 5 and 6, where the steel casing from the main bore hole had deformed due to deformation during the hiatus in drilling. This was accomplished in three runs: run E within the Salinian Block, and two runs labelled G, within the Great Valley Sequence (Fig. 5.1). Run E was separated into three units: a greenish-grey pebbly siltstone, a dark greyish black siltstone, and a greyish-red pebbly sandstone. The contact between the grey siltstone and pebbly sandstone is interpreted to be the contact between the Salinian Block and the Great Valley Sequence. Run G crossed two actively deforming strands of the SAF. The first segment which crosses the SDZ is composed of foliated siltstone-shale cataclasite, massive grayish-black shale, foliated fault gouge, and sheared siltstone and shale (SAFOD, 2010). The second segment crossing the CDZ is composed of sheared siltstone and sandstone, foliated fault gouge, sheared siltstone and mudstone, massive siltstone and very fine sandstone, sheared and fractured siltstone to very fine sandstone, sheared and fractured claystone, mudstone and siltstone, and sheared claystone and shale (SAFOD, 2010).

5.1.3 Introduction to core segments

Five segments of core were used for this microstructural study. From top to bottom these are: E14, E16, G12, G23, and G42 (Fig. 5.1). Based on the above classification scheme E14 is a dark grey siltstone, E16 is a reddish pebbly sandstone, G12 is a foliated siltstone-shale cataclasite, G23 is a foliated gouge, and G42 is a sheared and fractured siltstone. Photos of the core, and thin section scans are found in Appendix 2.

5.2 Methodology

The microstructural study was performed on five, 5 cm lengths of core from SAFOD (Fig. 5.1) using the techniques described in section 3.1. In order to establish phyllosilicate compositions, both randomly oriented powders and oriented clay aggregates were prepared and analyzed using XRD in order to record the diagnostic basal diffractions using the techniques described in section 3.2 (Poppe et al., 2001). Subsequent treatments of air drying, glycolation, heating to 400°C, and heating to 550°C between XRD analyses on the oriented clay aggregates shows the extent of d-spacing expansion or contraction, and enables the differentiation of clay minerals (Moore and Reynolds, 1997). Of particular interest in this study was the differentiation of mixed layer clays and smectites (*e.g.* montmorillonite and vermiculite).

5.3 Results

5.3.1 Microscopy

Samples E-14 and E-16 were collected from the Salinian Block and have previously been described as dark-greyish black siltstone and greyish-red pebbly sandstone respectively (SAFOD, 2010). Macroscopic analysis of E-14 is consistent with this interpretation (Fig. 5.3). Larger ~ 100 μm grains of albite and quartz are entrained in a fine-grained matrix of phyllosilicates. A weak foliation exists characterized by weakly aligned phyllosilicates. Pressure solution seams are prominent in SEM and are found throughout the sample along quartz-quartz interfaces (Fig. 5.3a), and along the margins of the phyllosilicates (Fig. 5.3b). Evidence of brittle fracturing is rare, though thin (~0.1 mm) veinlets are visible in the hand sample. Overall the sample is very weakly deformed and is likely representative of the protolith.

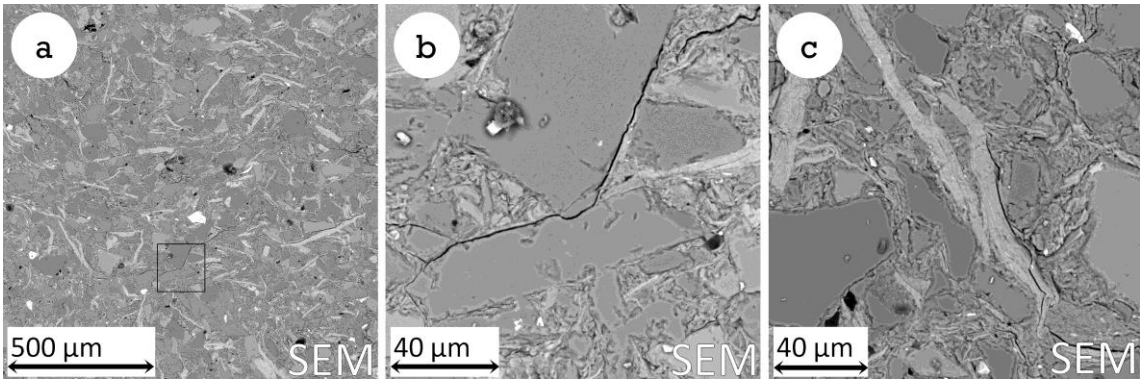

Figure 5.3: SEM photomicrographs of sample E-14 Dark greyish-black siltstone from the Salinian Block. **a**) Weakly foliated sample, with very little preferred orientation. Pressure solution seams exist, with dissolution at quartz-quartz interfaces (**b**), and along the margins of phyllosilicates (**c**).

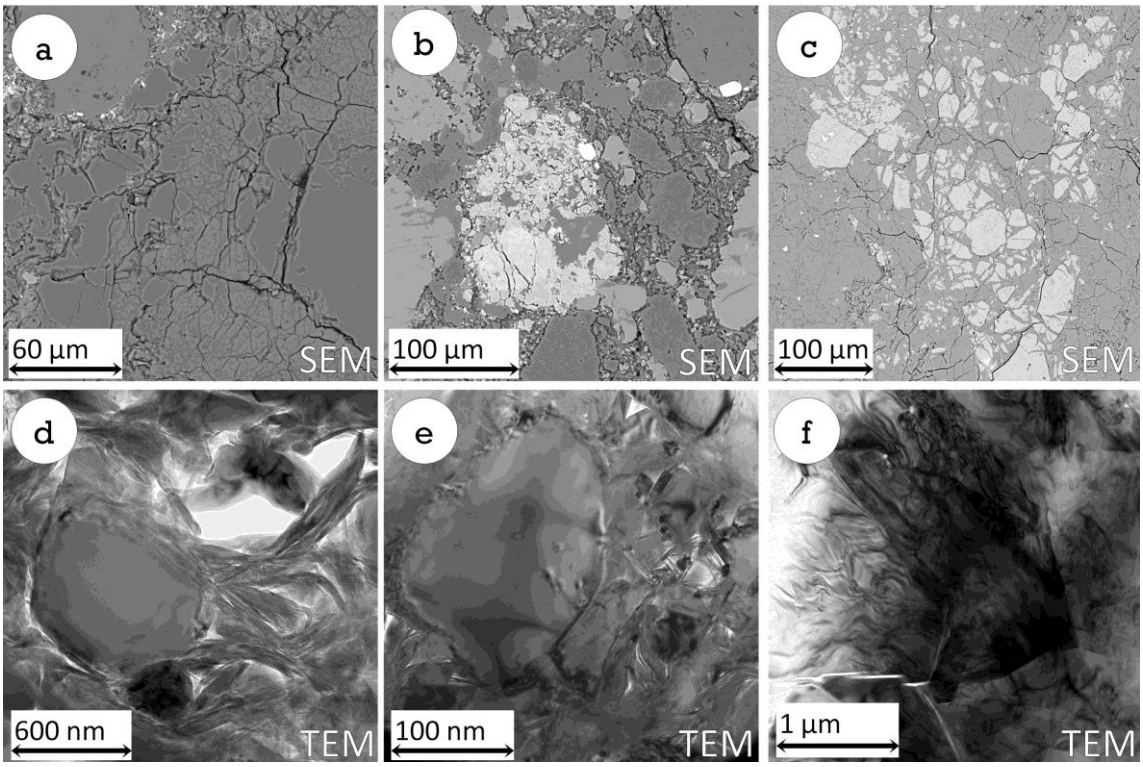

Figure 5.4: Microstructures from sample E-16 Lager clasts of quartz and feldspars are seen in a process of brecciation along seams of gouge (**a-c**). The gouge comprises much less of the sample than in the Great Valley Sequence samples. Fine-grained laumontite (zeolite) and chlorite (**d, e**) exist in the gouge coating fragments of framework silicates, with the majority of the framework silicates consisting of quartz (**e, f**).

Sample E-16, however, displays the gross composition of a granitic protocataclasite. Polymineralic clasts up to 2.5 mm in diameter are crosscut by dark, fine-grained seams containing gouge (Fig. 5.4). Brittle fracturing within larger grains is common and clasts often become entrained in the fine-grained gouges (Fig. 5.4a-c). The gouge is composed primarily of very fine-grained quartz (~10 nm; Fig. 5.4d-f), coated in a mixture of phyllosilicates and zeolites (laumontite and intercalated illite-vermiculite). Amorphous crystalline silica and secondary Fe-Ti oxides are common in the matrix. Large quartz grains exhibit undulose extinction and grain boundary migration recrystallization. Late-stage calcite veins cross cut the sample at a high angle to the gouge seams.

The three samples from the Great Valley Sequence are much more deformed than the Salinian Block samples. Sample G-12 displays several generations of foliated clataclasites with S-C geometry suggesting viscous flow (Fig. 5.5). Differentiating generations of cataclasis is facilitated by multiple generations of calcite and quartz veins. The veins, which occupy ~50 % of the sample in the oldest generations of cataclasites and do not exist in the youngest generation of cataclasites, are truncated by younger generations of gouge (Fig. 5.5a,b). Anastamosing arrays of dark, clay-rich gouge isolate clasts of previous generations of cataclasite with varying orientations of foliations indicating rotation during shear (Fig. 5.5b,d). This gouge can be seen injecting into cracks within larger clasts, a further indication of viscous flow (Fig. 5.5b). Pressure solution seams are ubiquitous and are especially evident in SEM (Fig. 5.5c,d). The curved surfaces of pressure solution seams attest the efficacy of fluid dissolution (Fig. 5.5c). Quartz is seen in TEM to form aggregates at a range of sizes, with the smallest (100 nm) related to solution transfer. Precipitates of pyrite are common (Fig. 5.5e). Chlorite coats grain boundary surfaces wherever it coexists with framework silicates.

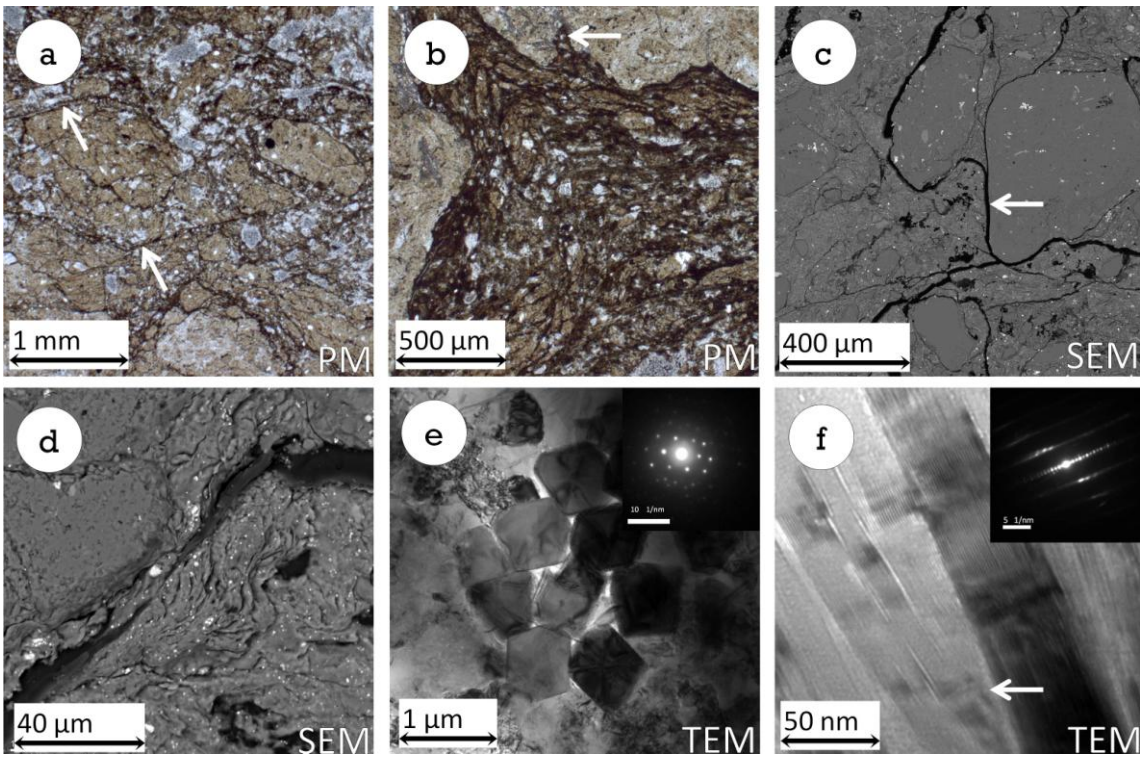

Figure 5.5: Microstructures from sample G-12 Gouge-rich sections offset clasts of cataclasite (**a**). Shears can be found cutting through both gouge and cataclasites. Gouge, where in abundance forms flow structures, and S-C geometries (**b**), and can be seen injecting into fractures within the cataclasite. Curved pressure solution seams attest to the efficacy o pressure solution within the samples (**c, d**). Aggregates of pyrite can be seen precipitating in the gouges at the TEM-scale (**e**), particularly along the curved pressure solution seams (**d**). Chlorite shows frequent lattice terminations (**f**).

These deform at the smallest grain-scale and where abundant, form good laths (Fig. 5.5f). In addition to chlorite, intercalated vermiculite and illite also exists in the sample.

Sample G-23 is a mesoclataclasite and has the highest phylosillicate content of any sample, exhibiting a well defined foliation from hand sample down to TEM analysis (Fig. 5.6). Like sample G-12, sample G-23 exhibits several generations of cataclasis, though the concentration of veinless dark black gouge is greater in sample G-23 (Fig. 5.6). The sample consists of a ~50/50 mix of gouge and clasts, which range in width from less than 0.1mm to ~2cm (Fig. 5.6a,b). Clasts, are composed of older generations of cataclasites and are cut by several generations of calcite veins (Fig. 5.6a). Shear planes and a schistose fabric are apparent throughout the sample and display a dextral shear sense. Significant aggregates of pyrite exist within the clasts (Fig. 5.6c,d), and nanocrystalline precipitates of silica are common (Fig. 5.6d,e). Where in abundance, chlorite shows evidence of kinking (Fig. 5.6f).

Sample G-42 is interpreted to be a sheared siltstone. Calcitic tension veins cross larger grains and macroscopic shears have a spacing of about 2.5 cm (Fig. 5.7a). Sheared regions are composed of a dark (Fig. 5.7b), fine-grained matrix containing very fine-grained quartz enveloped in phyllosilicates (Fig. 5.7c). Concentrations of deep red, insoluble material is found concentrated at the margins of larger clasts of the protolith (Fig.5.7b). Phyllosilicates envelop quartz grains and dissolution of quartz is evident where it is in contact with other quartz grains (interpenetrative grains; Fig. 5.7e,f). Phyllosilicates are composed of illite, chlorite, and corrensite (intercalated montmorillonite and chlorite).

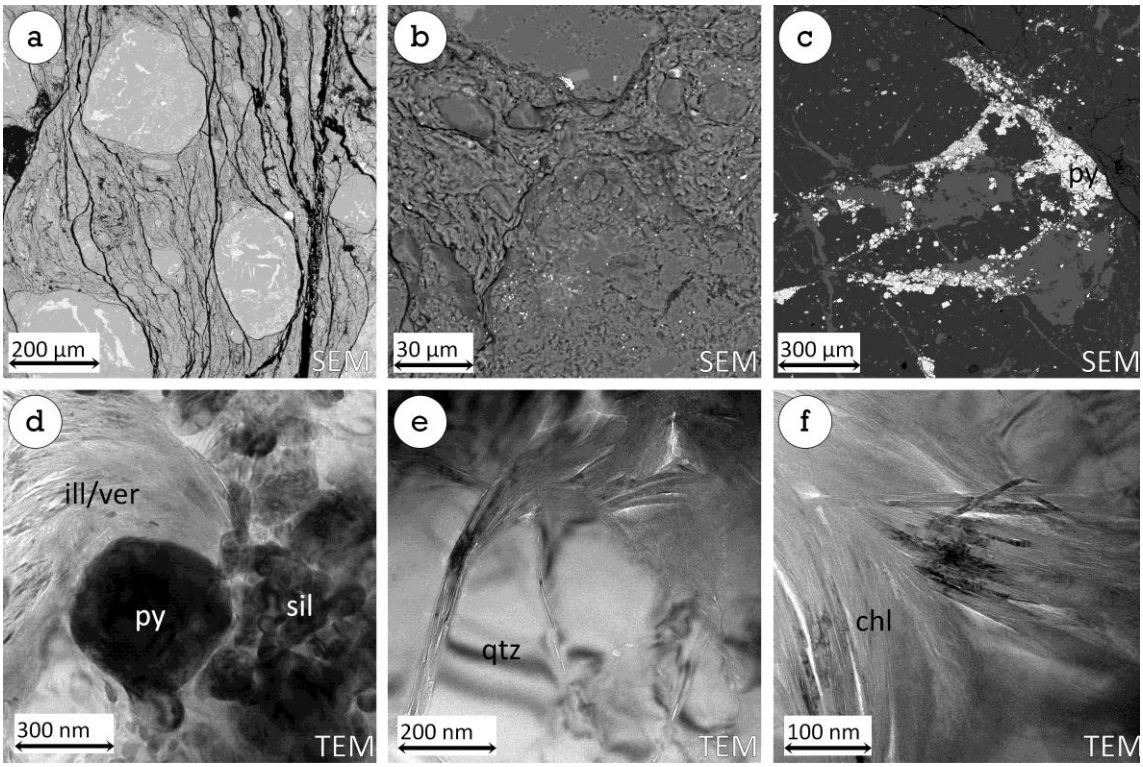

Figure 5.6: Microstructures from sample G-23 Sample G-23 contains the highest proportion of phyllosilicates from any of the samples, and contains the highest proportion of gouge. Within the gouges anastomosing pressure solution seams are ubiquitous, and encircle clasts of older cataclasite (**a**). The gouges show flow structures (**b**). Significant aggregates of pyrite exist in the older cataclasites (**c**). TEM photomicrographs show pyrite and nanocrystalline silica precipitating in the gouges (**d**). Intercalated illite-vermiculite and chlorite are seen enveloping all framework silicates (**d, e**). Where in abundance, chlorite shows evidence of kinking (**f**).

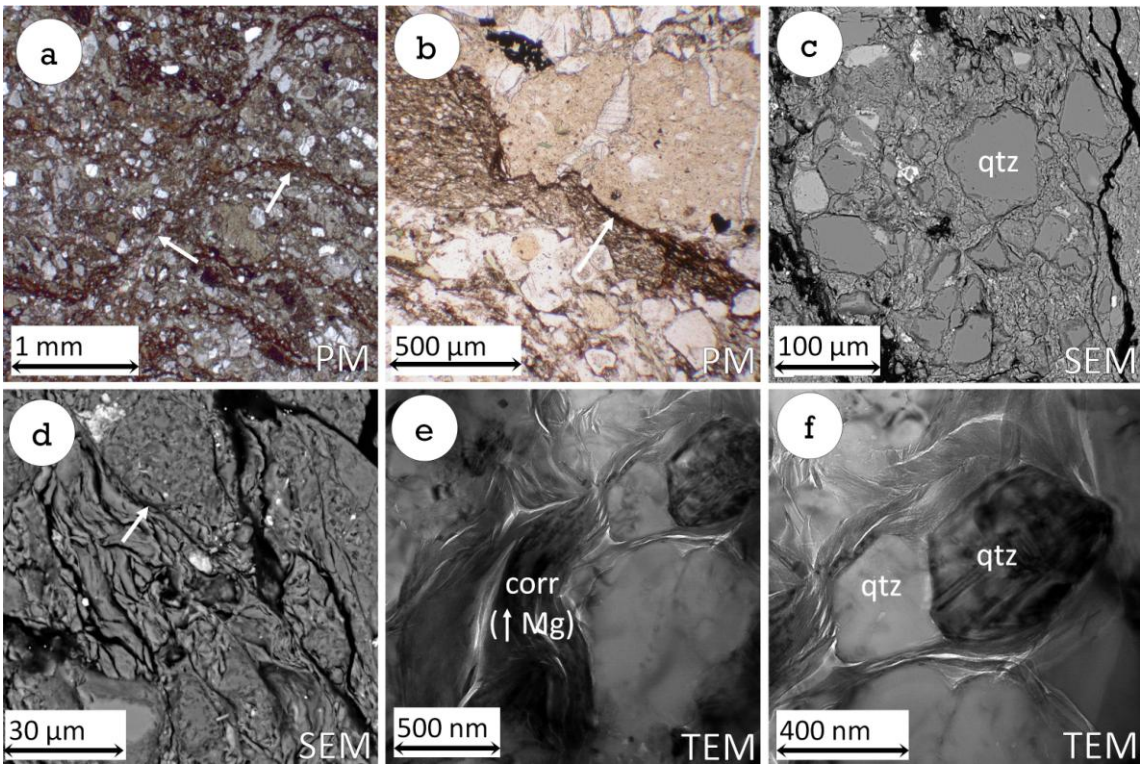

Figure 5.7: Microstructures from sample G-42 (PM = optical photomicrograph; SEM = scanning electron microscopy; TEM = transmission electron microscopy) **a**) Dark seams of fine-grained gouge cut through the sample, with concentrations forming along the edges of cataclasite (**b**). Within the larger clasts of cataclasite, calcitic tension veins cut through the clasts (**b**). The gouges contain clasts of quartz ranging from 10-100µm, surrounded by a fine-grained gouge matrix (**c**). Slip surfaces can be found within the gouge matrix (**d**). TEM photomicrographs of the gouge reveals smectitic Mg-rich phyllosilicates (corrensite), coating interpenetrative quartz grains (**e, f**).

5.3.2 XRD of randomly oriented powders

XRD of randomly oriented powders gives an approximate bulk mineralogy for all samples. Limitations of this technique include the fact that the detection limit in multi-component samples is approximately 2%, and that samples which contain more than four components are difficult to analyze using a Reitveld analysis. Because of these limitations, oriented clay aggregates were used to determine minor clay phases and clay mineralogy of each sample. Using the randomly oriented powders, the relative proportions of clay minerals in each sample can be obtained by combining the results from the phyllosilicates used in the Reitveld analysis (Table 5.1).

5.3.3 XRD of oriented clay aggregates

Analysis of XRD of oriented clay aggregates was done using raw data patterns plotted in Excel. Air dried, glycolated, and heat treated results were overlain in order to easily recognise the mineral transitions with each treatment. 2θ spacings were converted to angstroms using a chart which uses a Kα weighted mean, using the equation below:

$$[2*(K\alpha\ 1) + (K\alpha\ 2)]/3 \quad . \qquad (17)$$

This equation gives Kα 1 more weight due to its greater intensity relative to Kα 2 (Poppe et al., 2001).

Sample E14 shows a substantial illite component compared with other samples (Fig. 5.8a). Minor interstratified illite/chlorite was identified based on the width of the (001) reflection peaks of chlorite, which range from 13.94Å to 12.28Å, much lower than the typical values of 14.2Å values of pure chlorite (Fig. 5.8a).

Sample E16 contains a mixture of laumontite, intercalated illite and vermiculite, and illite (Fig. 5.8b). The interstratified illite-vermiculite is identified based on the d-spacing contraction during heating. The (001) peak of di-octahedral vermiculite

Table 5.1: Reitveld analysis of randomly oriented XRD patterns Mineral percentages of SAFOD samples from Reitveld analysis of randomly oriented XRD patterns. Also plotted is the total phyllosilicate content (Tot Phy) from each sample and the distance to the nearest active zone (Distance to AZ). Mineral abbreviations after Kretz (1983). (Qtz – quartz, Ab – Albite, Mc – Microcline, Cal – Calcite, Chl – Chlorite, Ms – Muscovite, Bt – Biotite, Phg – Phengite, Lmt – Laumontite, Tot Phy – Total phyllosilicate content [Phg+Bt+Ms+Chl])

	Qtz	Ab	Mc	Cal	Chl	Ms	Bt	Phg	Lmt	Tot Phy	Distance to AZ
E-14	28	42.3	7.7	-	14.4	2.1	5.6	-	-	**22.1**	**52m to SDZ**
E-16	42	37	20	-	<1	-	-	-	1.3	**<1**	**50m to SDZ**
G-12	88.1	-	-	-	<1	4.4	-	3.6	3.9	**8-9**	**10m to SDZ**
G-23	69.2	3.9	-	6.3	<1	11.2	-	9.4	-	**20.5-21.5**	**4m to SDZ**
G-42	64.6	14	-	12.3	4.8	-	4.3	-	-	**9.1**	**0.6m to CDZ**

collapses to 12Å after heating to 400°C, and collapses further to ~11Å after heating to 550°C (Fig. 5.8b; Douglas, 1989). Laumontite was found in the sample. Its characteristic peaks at 9.52Å and 6.88Å, and the fact that the crystal structure collapses upon heating allowed for its identification (Fig. 5.8b; Poppe et al., 2001).

Sample G12 has a larger quartz content than other samples, indicating that there is either a larger microcrystalline silica component, or that the sample has a much smaller clay component, making the separation of clays more difficult (Fig. 5.9a). Two phases of clays were identified, chlorite and interstratified illite-vermiculite (Fig. 5.9a).

Sample G23 by comparison contains more interstratified illite-vermiculite than sample G12 or E16 within the clay separate (Fig. 5.9b). The quartz content is less than in sample G12.

Sample G42 is the only sample to contain smectitic clays (Fig. 5.9c). The unglycolated spacing, showing a peak at 28.89Å, expands to 30.9Å upon glycolation of the sample. As is expected with smectites, the peak is destroyed upon heat treatment, as most smectitic clays desiccate between 125°C and 150°C (Frey and Robinson, 1999).

5.4 Discussion

Three primary deformation mechanisms are in operation within the SAFOD core. In areas in which gouge development is low, brecciation and catalasis are observed. Once the grain size has been sufficiently reduced and a thick enough seam of gouge develops, pressure solution dominates the internal deformation of the gouge. Slip surfaces which propagate through both the gouge and the host material show that frictional sliding also accommodates some of the deformation. The coupling of these processes has been observed before. Renard et al. (1999) noted that if an episode of

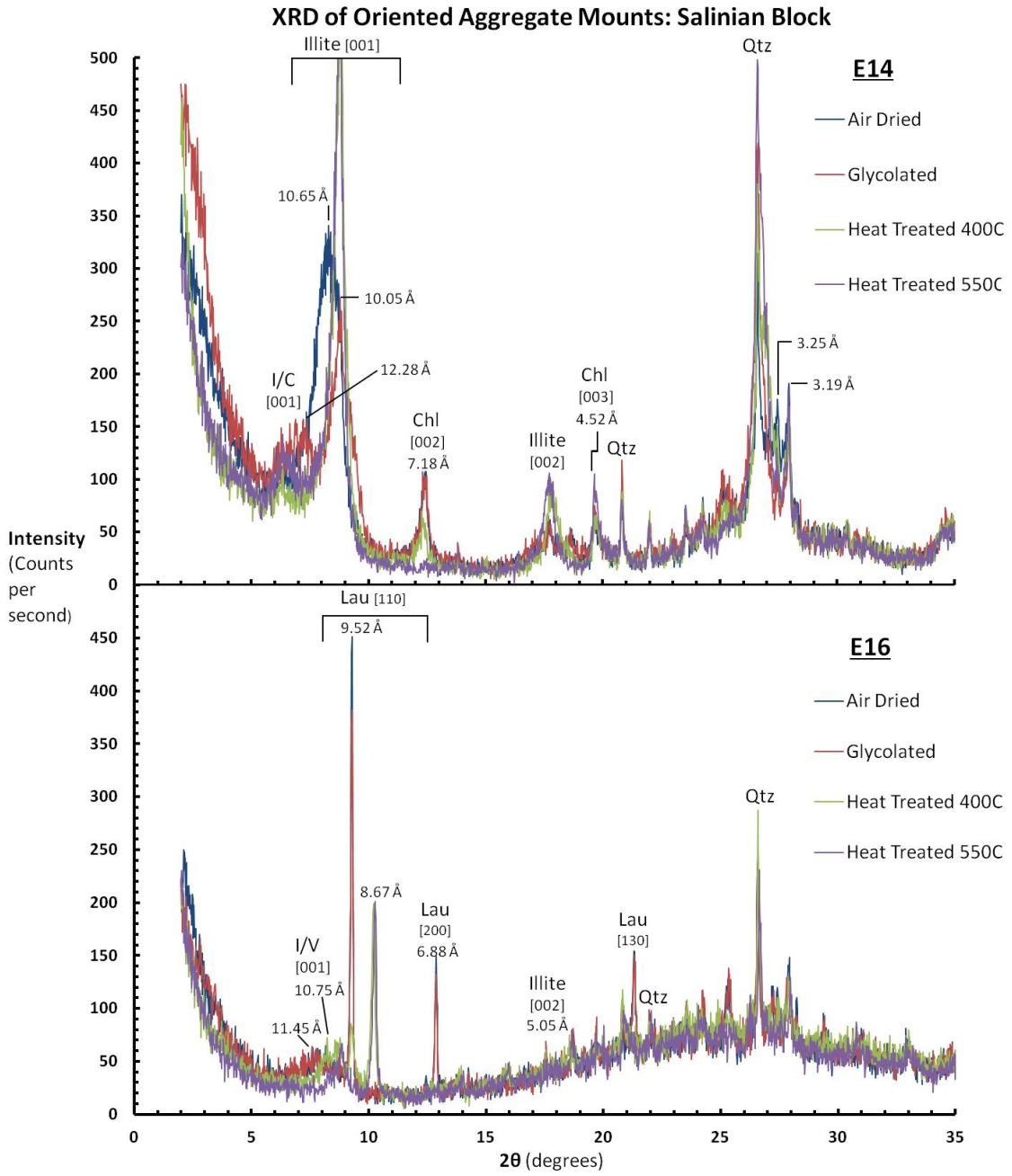

Figure 5.8: XRD of oriented clay aggregates for the Salinian Block samples Sample E14 shows substantial illite and chlorite while sample E16 is the only sample to contain laumontite, a calcium-rich zeolite.(I/C = intercalated illite-chlorite; I/V = intercalated illite-vermiculite; Lau = laumontite; Chl = Chlorite)

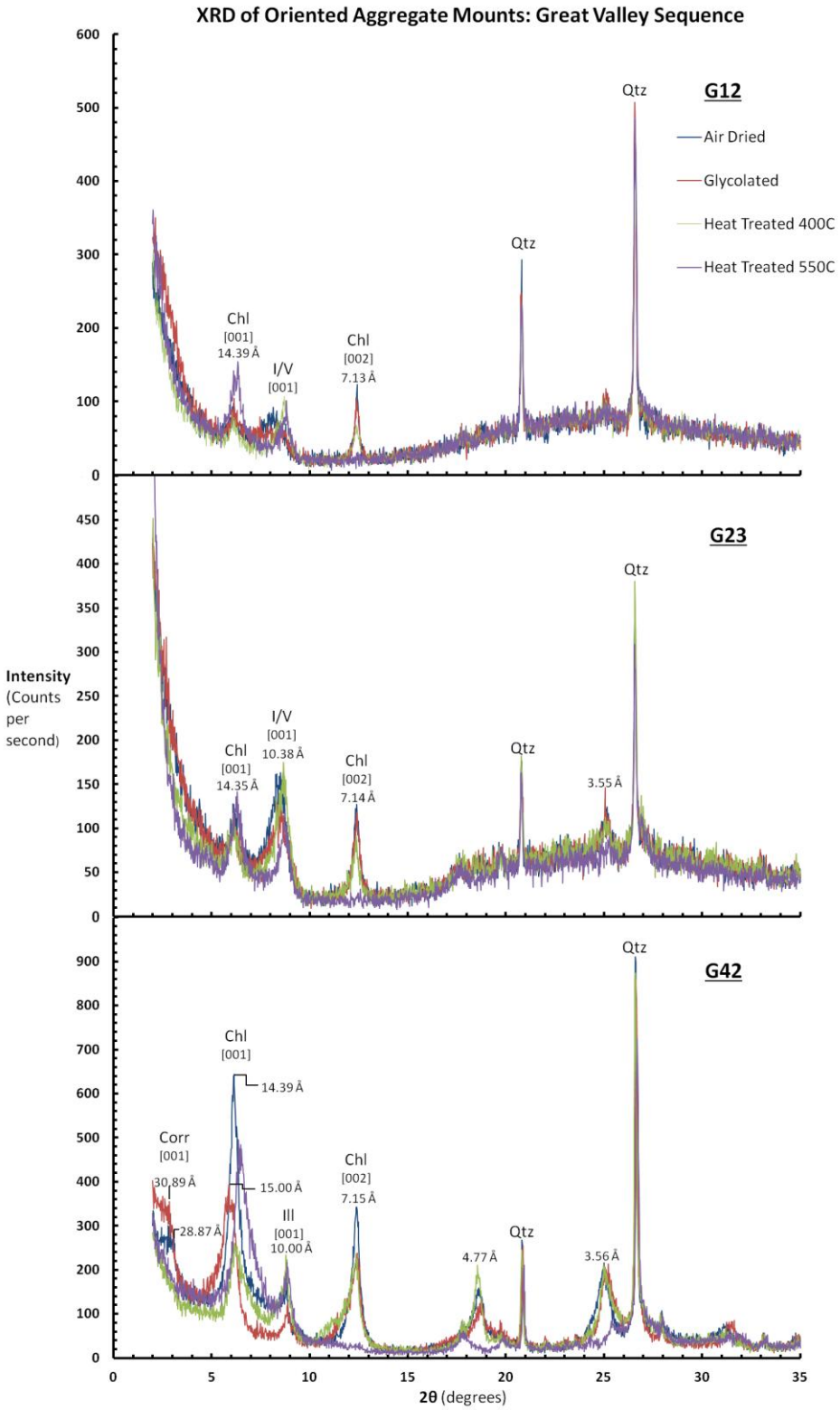

Figure 5.9: XRD of oriented clay aggregates for the Great Valley Sequence samples All samples contain chlorite (Chl) and illite (Ill), while sample G42 is the only sample to contain corrensite (Corr), an interlayered Mg-rich smectite and chlorite. Samples G12 and G23 contain intercalated illite and vermiculite (I/V). (Qtz = quartz)

brittle deformation reduces the grain size of a rock, the distance for diffusion in the grain contacts is lowered and the effectiveness of pressure solution is enhanced.

The gouges are enriched in phyllosilicates. This could arise by passive concentration of phyllosilicates due to soluble species pressure solution depletion (Gratier et al. 2011) or through growth of new phyllosilicates within the gouge (Schleicher et al., 2010; Holdsworth et al., 2011). It is uncertain whether this enrichment would promote pressure solution processes in the samples or inhibit them. One argument is that the increased concentration of phyllosilicates would inhibit sealing of soluble materials by getting trapped along the margins of soluble materials, keeping diffusive paths along solution seams open, and promoting continued deformation by pressure solution (Niemeijer and Spiers, 2005; Gratier et al., 2011). Alternatively, if phyllosilicates coat quartz clasts, precipitation on the pore surface area is hindered from a loss of pore surface area. The pore fluid becomes sufficiently supersaturated in silica that the concentration gradient between the contact and the pore can disappear, removing the driving force for dissolution and decreasing the rate of pressure solution (Renard et al., 1999). The observations herein show numerous pressure solution pathways in the form of pressure solution seams, with an increasing concentration of seams in the more gouge-rich samples, indicating that the driving force for dissolution has not been hampered with increasing phyllosilicate content. This is in agreement with observations from compaction experiments showing an increase in pressure solution processes with an increase in wet phyllosilicate content (Rutter and Wanten, 2000). Likewise, in a series of experiments where convex halite and silica lenses were pressed over silica plates in brine, applying a film of Na-montmorillonite to the silica interface was found to increase the rate of pressure solution by five times (Hickman and Evans, 1995).

A question central to understanding gouge deformation at SAFOD is how much of the deformation can be accommodated by pressure solution alone? Gratier et al. (2011) calculated the diffusive distance required for the strain rates observed (3.3 x $10^{-10}s^{-1}$ for a 1m shear zone accommodating the 20mm/yr displacement; 1.1 x $10^{-9}s^{-1}$ for a 3m wide shear zone). Calculations were based on equations from laboratory indentation experiments, using the derived equation:

$$\dot{\varepsilon} = \Delta d/d\Delta t = 8DwcV_s(e^{\frac{3\Delta\delta_n V_S}{RT}} - 1)/d^3, \quad (18)$$

where c is the solubility of the diffusing solid, V_s is the molar volume of the stressed solid, R is the gas constant, T is the temperature, D is the diffusion constant along the stressed interface, w is the thickness of the trapped fluid phase along which diffusion occurs, t is the time and $\Delta\delta_n$ is the driving stress, the difference between normal stress on dissolution surface and the fluid pressure in the vein (Gratier et al., 2009, 2011). The maximum diffusive distances required for the conditions at the SAFOD site range from 90-125 μm for quartz, to 350-500μm for feldspar (Gratier et al., 2011). Given that most of the SAFOD gouges contain an abundance of quartz, 90-125μm appears to be an appropriate diffusive distance. It is important to note that the indenter experiments from which this equation, and these results have been derived deal with the dissolution-precipitation kinetics of a single material (*i.e.* quartz, calcite, or feldspar), and that the interface at a quartz-feldspar contact, or more applicably for our samples a quartz-phyllosilicate contact may be substantially different than those calculated from these experiments.

Within gouge packages, observations suggest diffusive distances are much less than 100μm, with macroscopic pressure solution seams at intervals of 25μm or less, and

average grain sizes less than 1μm within the gouge supported matrices (Figs. 5.9, 5.10). How then is there any strength in these samples? If pressure solution is operative, the entire section of core should be moving at different rates along small phyllosilicate-rich seams.

One possible resolution would require progressively more silica removal from this open system through pressure solution (bulk chemistry of the gouges does not equal bulk chemistry of the host). Sufficient quartz removal eventually destroys its efficacy as a load-bearing network, and the stresses at quartz-mica interfaces are not substantial enough to promote dissolution. Alternatively, the reduction in quartz could eventually lead to a situation where there is physically not enough quartz to accommodate creep by pressure solution processes alone. Once this point is reached frictional sliding along the phyllosilicate-rich seams becomes operative (Niemeijer and Spiers, 2005). Pre-existing pressure solution interfaces could serve as easy slip horizons. Gouge thickness is known to affect the frictional properties of the material studied, and with increasing thickness, gouges are weaker and show greater strain hardening (Ikari et al., 2011b). Deformation then may localize in gouge zones of greatest widths, explaining why deformation is concentrated along the CDZ and SDZ which are much wider than the seams studied here. Thicker gouge packages could also cut off fluid circulation, leading to locally high fluid pressures through compartmentalization (Caine et al., 1996). The increase in pore fluid pressure at thicker gouge packages would lower the effective stress, and promote slip.

Samples from the actively sliding zones at the SAFOD site have even higher concentrations of phyllosilicates than the samples studied here, with up to 65% phyllosilicate content (Bradbury et al., 2011; French et al., 2014). At low sliding

velocities these samples show velocity strengthening behaviour and are weak (μ = 0.14-0.21) compared with rocks outside the active zones (μ = 0.25-0.65), with values generally decreasing with proximity to the actively deforming zones (Fig. 5.11; Carpenter et al., 2011; Lockner et al., 2011). It is important to note that in these experiments, natural samples from the SAFOD site are ground into homogeneous powders with a grain size of <150μm. The samples in this study show seams of gouge cutting through older generations of healed, vein-rich cataclasite. Homogenizing these samples into a gouge paste removes the complexity observed, and it is suggested that the frictional properties of the samples in the damage zone are likely much closer to the properties observed in the active segments than these experiments suggest. While smectitic clays were only found in sample G42, intercalated vermiculite and chlorite was found in all other samples with the exception of E14. Vermiculite is also known to have a very low coefficient of friction, which in some experiments is lower than montmorillonite (Byerlee, 1978). The main difference between active samples and our inactive samples is the thickness of the gouge seams.

At higher velocities samples from the active zones show velocity weakening behaviour, comparable to other high-velocity experiments in other gouge types (Di Toro et al., 2011; French et al., 2014), making the propagation of an earthquake nucleated elsewhere (*e.g.* the M_w 7.0 Parkfield event) through the creeping zone possible (Noda and Lapusta, 2013).

5.5 Conclusions

- Microstructural observations show a sequence of deformation mechanisms in operation. In order for pressure solution to be an effective deformation mechanism, it

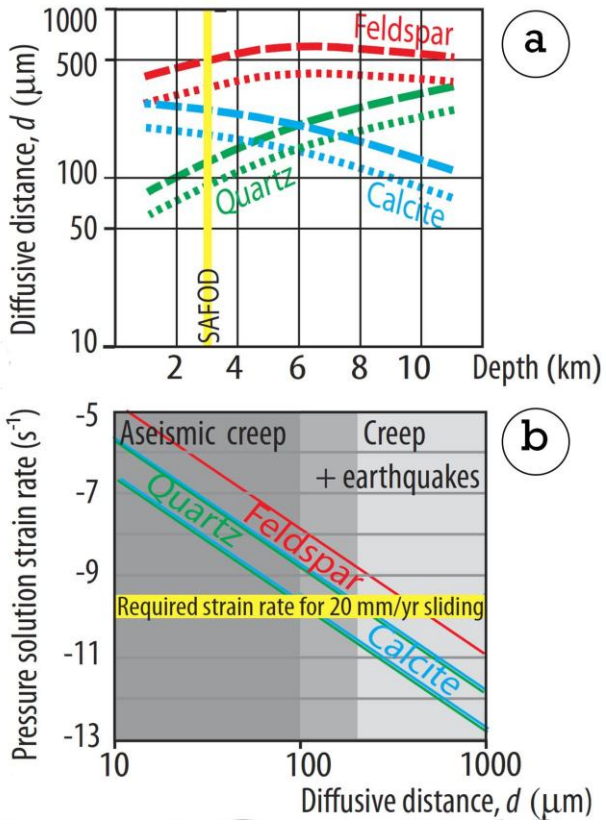

Figure 5.10: Effectiveness of pressure solution at the SAFOD site Calculations of the effectiveness of pressure solution at the SAFOD site by Gratier *et al.* (2011). **a**) For known strain rates ($3.3 \times 10^{-1}s^{-1}$ – dotted line; $1.1 \times 10^{-9}s^{-1}$ – solid line) the required diffusive distances for quartz, feldspar, and calcite are shown. **b**) Pressure solution strain rate versus diffusive distance for quartz calcite and feldspar through the crust. Strain rates at the SAFOD site are in the yellow bar.

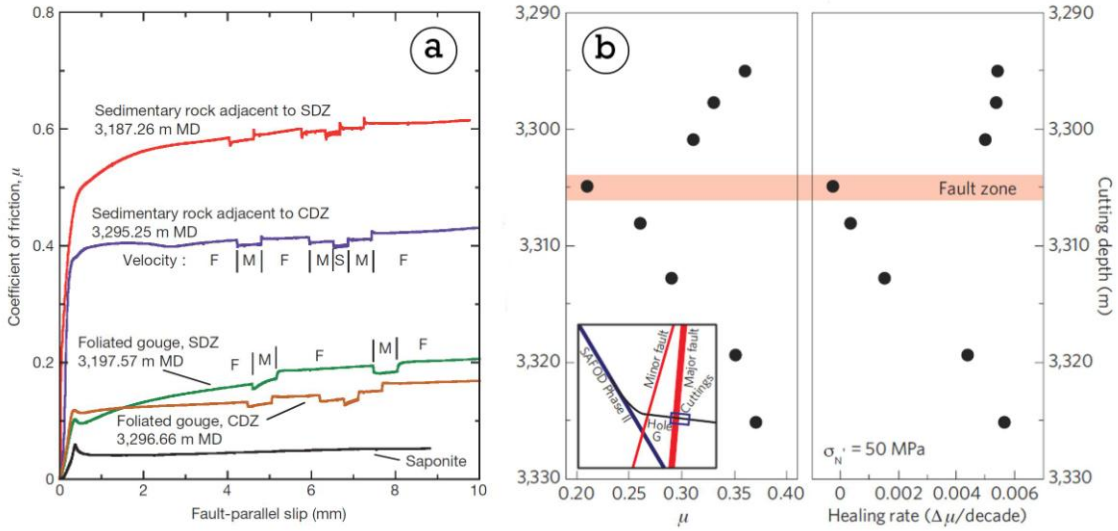

Figure 5.11: Experimental data from the active segments of SAFOD core Experimental data from **a)** Lockner et al. (2011) and **b)** Carpenter et al. (2011) of frictional strength from the SAFOD core. In their analyses, the foliated gouges from the active segments (CDZ and SDZ) show much lower coeffiecients of friction than the inactive segments studied here. However, samples have been crushed into a homogenous gouge, removing the complexity of the structures (see text for detail).

must be precluded by grain size reduction through brittle fracture and cataclasis. Once operational, brittle fracture, cataclasis, and pressure solution are operating coevally. Late frictional sliding is observed within gouge-rich cores.

- Phyllosilicates with low coefficients of friction (vermiculite and montmorillonite) are observed in all samples with the exception of E14.
- The primary difference between the active segments and the segments studied here is the thickness of the gouge packages. Thicker packages can more easily maintain high fluid pressures, and are more likely to form an interconnected weak plane through the crust.
- Deformation has been localized in the fine-grained phyllosilicate-rich siltstones, close to the contact with the coarser grained sandstones, due to the increased effectiveness of pressure solution in fine grained, phyllosilicate bearing units.

CHAPTER 6: DISCUSSION

6.1 A Comparison of the SAFOD and Minas Fault Zone Sites

While the Minas fault zone is a paleo-fault zone, and the San Andreas fault is active, the similarities between host lithologies and tectonic settings at the two localities studied allows their comparison as phyllosilicate-rich fault zones at different crustal levels. Both are complex, mature, fault zone segments hosted in fine-grained sedimentary lithologies, where several deformation mechanisms are observed to be operating simultaneously. The ductile fabrics associated with the S-C domain of the Minas fault zone are indicative of a creeping fault, in analogy with the actively creeping SAFOD site but at greater depth.

Deformation within both fault zones is distributed. At SAFOD, a 200m wide "damage zone" (Fig. 5.1; Holdsworth et al., 2011) surrounds two actively creeping zones 1-2m in width separated by ~100m. This study has identified numerous generations of healed gouges and veining within the "damage zone", indicating cyclical periods of activity (Figs. 5.8-5.10). Within the S-C domain of the Minas fault zone, a 50-100m wide package exhibiting bulk ductility is observed (Figs. 4.13-4.18). The widths are comparable as transcurrent fault zones tend not to widen with depth until high amphibolite to granulite facies conditions are reached (Sibson, 1983).

At the SAFOD site, where deformation is occurring at lower temperatures (~120°C; Zoback et al., 2010), brittle fracture and cataclasis are observed to be operating coevally with pressure solution processes. Within the S-C domain of the Minas fault zone, where recorded temperatures are higher (~360°C), pressure solution and crystal plasticity are seen operating in conjunction. These observations attest to changes in

deformation mechanisms with increasing depth in phyllosilicate-rich transcurrent fault zones, while the presence of pressure solution processes at both sites attests to the efficacy of pressure solution over a wide range of geological conditions (Rutter, 1974, 1983; Wheeler, 1992).

6.2 Strength Profiles for Phyllosilicate-Rich Transcurrent Faults

Fault strength is anticipated to vary with depth for a phyllosilicate-rich transcurrent fault and will be dependent on the operating deformation mechanisms. The effectiveness of the various deformation mechanisms with depth, including dilation and frictional sliding, dissolution-precipitation creep, and crystal-plastic flow will be examined. These deformation mechanisms will be in turn integrated into the model of Niemeijer and Spiers (2005) for pressure solution-accommodated creep and applied to the San Andreas Fault Observatory at Depth (SAFOD) site and to the S-C fabrics at Greville Bay in the Minas fault zone.

6.2.1 Frictional sliding

Following Sibson (1974), the frictional strength of a transcurrent fault is taken as linear in reflection of Byerlee's law (Byerlee, 1978). Failure will occur when

$$\tau > \tau_f = \mu\sigma_n \tag{19}$$

where τ is the applied shear stress, τ_f is the frictional shear resistance, μ is the coefficient of friction, and σ_n is the normal stress across the fault. This applies for faults with or without well developed cores of granular material. By substituting in the principal stresses from equations (1) and (2) the strength relationship becomes

$$(\sigma_1 - \sigma_3)\sin 2\theta = \mu[(\sigma_1 + \sigma_3) - (\sigma_1 - \sigma_3)\cos 2\theta]. \tag{20}$$

Following Sibson (1974) we now define $R(\theta)$ as the differential stress ratio, σ_1/σ_3, for which failure will occur at fault angle θ, *i.e.* $R(\theta) = \sigma_1/\sigma_3\ (\theta)$. From equation (20) we find

$$R = [\sin 2\theta + \mu(\cos 2\theta + 1)]/[\sin 2\theta + \mu(\cos 2\theta - 1)]. \quad (21)$$

Differentiating equation (21) and setting $dR/d\theta = 0$ yields

$$R' = R(\theta_f) = [-(1+\mu^2) - \mu]^2 \quad \text{and} \quad (22)$$

$$\theta_f = \tfrac{1}{2}\tan^{-1} 1/\mu \quad (23)$$

where θ_f is the fault angle generated by the minimum value R' required to produce faulting (Sibson, 1974). If we apply this to Andersonian faulting end members (Anderson, 1905), each type of fault (normal, reverse, or transcurrent) will have an ideal orientation for failure, where the lowest possible differential stress causes failure. For this analysis an assumption will be made that the strike-slip faults examined exhibit the conditions

$$\sigma_2 = \tfrac{1}{2}(\sigma_1 + \sigma_3) \quad \text{and that} \quad (24)$$

$$\sigma_v' = \sigma_2 = \rho g z * (1 - \lambda) \quad (25)$$

where ρ is crustal density, g is the effect of gravity, z is the depth in the crust and λ is the pore fluid factor (ratio of pore fluid pressure to lithostatic pressure). Under these assumptions the equation for shear stress at failure (1) can be rewritten in terms of R' giving

$$\tau = \frac{\sigma_v'(R'-1)}{R'+1} * \sin 2\theta_f. \quad (26)$$

Figure 6.1 shows the variation in the value of R' and θ_f for varying coefficients of friction. Note how the angle of failure changes from 45° for a fault where $\mu = 1$ to

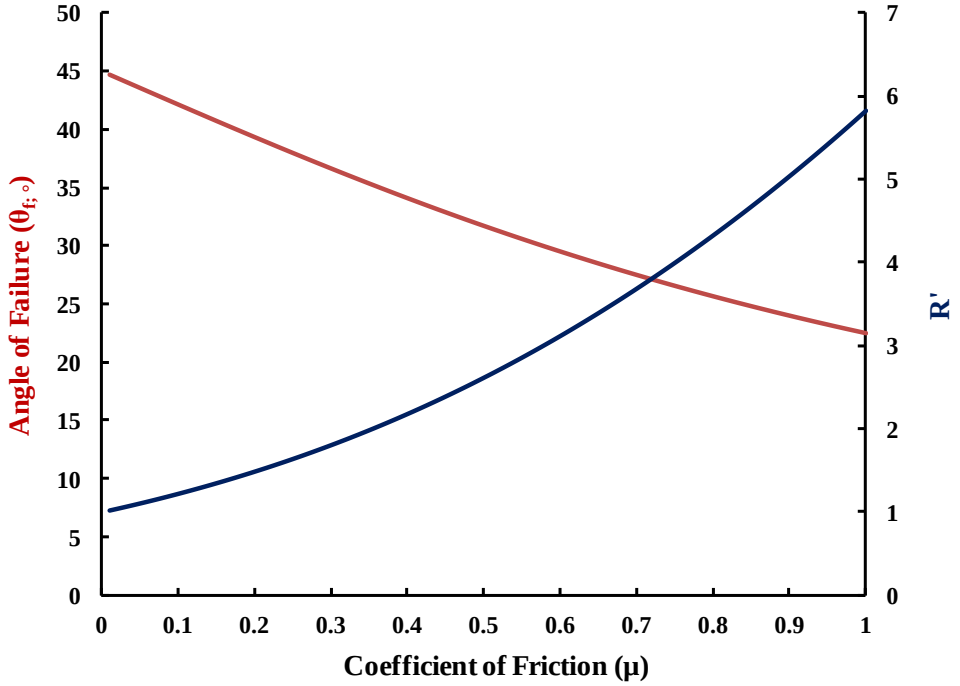

Figure 6.1: Changes in optimal fault zone orientation due to frictional properties Change in the angle of failure (θ_f) and the parameter R' (see text) due to changes in the coefficient of friction, μ (after Sibson 1974).

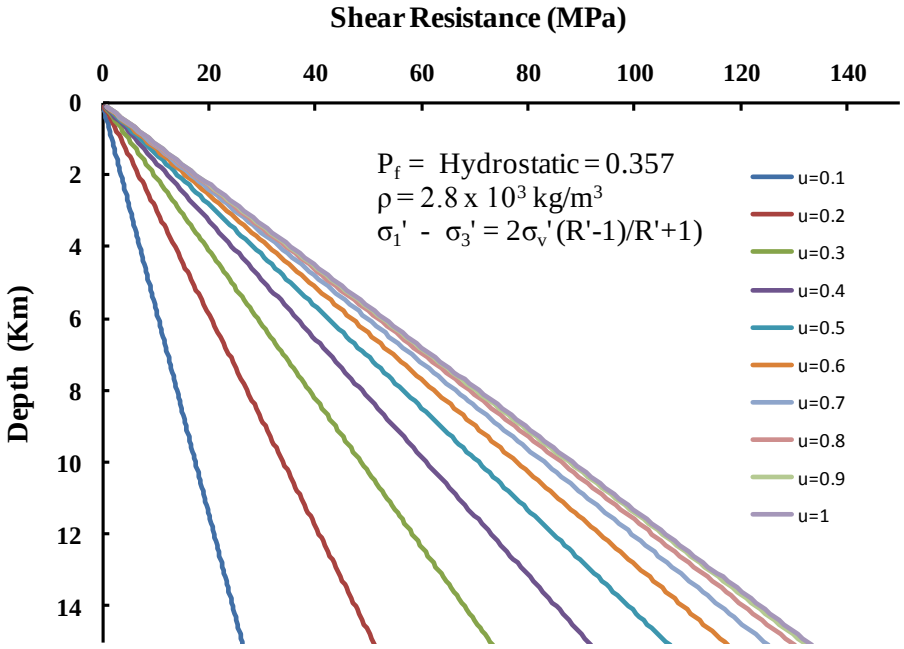

Figure 6.2: The effect of the coefficient of friction on shear resistance The effect of the coeffeicient of friction (μ) on the shear resistance of a transcurrent fault assuming hydrostatic pore fluid pressures, stress orientations consistent with andersonian faulting and an average crustal density of 2.8 x 10^3kg/m^3 (after Sibson 1974).

22.5° if $\mu = 0$. Assuming an ideal angle for sliding, and pore fluid pressures at hydrostatic conditions (λ = 0.357), shear resistance (Fig. 6.2) is strongly dependent on the coefficient of friction. If the coefficient of friction in nature for various phyllosilicates is as variable as experimentation demonstrates (Byerlee, 1978; Ikari et al., 2009, 2011a; Behnsen and Faulkner, 2012), the evolution of phyllosilicate content and composition will significantly affect the frictional properties of faults.

6.2.2 Dissolution-precipitation creep

To avoid ambiguity in terminology, "pressure solution" describes the process of dissolution and reprecipitation, "dissolution-precipitation creep" describes the ability for a material to accommodate strain through pressure solution, and "pressure solution-accommodated creep" describes the ability for a material to accommodate strain by combined processes of pressure solution, frictional sliding, and crystal plasticity.

Pressure solution also plays a role in the deformation of phyllosilicate-rich fault zones. Dissolution can occur within aggregates of quartz, or along boudinaged quartz carbonate veins at regions of high stress, with diffusion along island-channel structures or an interconnected film along phyllosilicate foliae, and re-precipitation at regions of low stress (Fig. 6.3; Bos and Spiers 2001; Bos and Spiers 2002; Niemeijer and Spiers 2005; Jefferies et al. 2006; Rowe et al. 2011).

The rate of pressure solution can either be controlled by the rate of dissolution, the rate of diffusion, or the rate of reprecipitation, though in geological environments the rate of reprecipitation does not contribute to shear strength (Renard et al., 1997; Gratier et al., 2009). Microphysical models presented by Bos and Spiers (2001; 2002) and Niemeijer and Spiers (2005) of pressure solution within phyllosilicate-rich fault rocks predict a region of deformation controlled by dissolution-precipitation creep within the

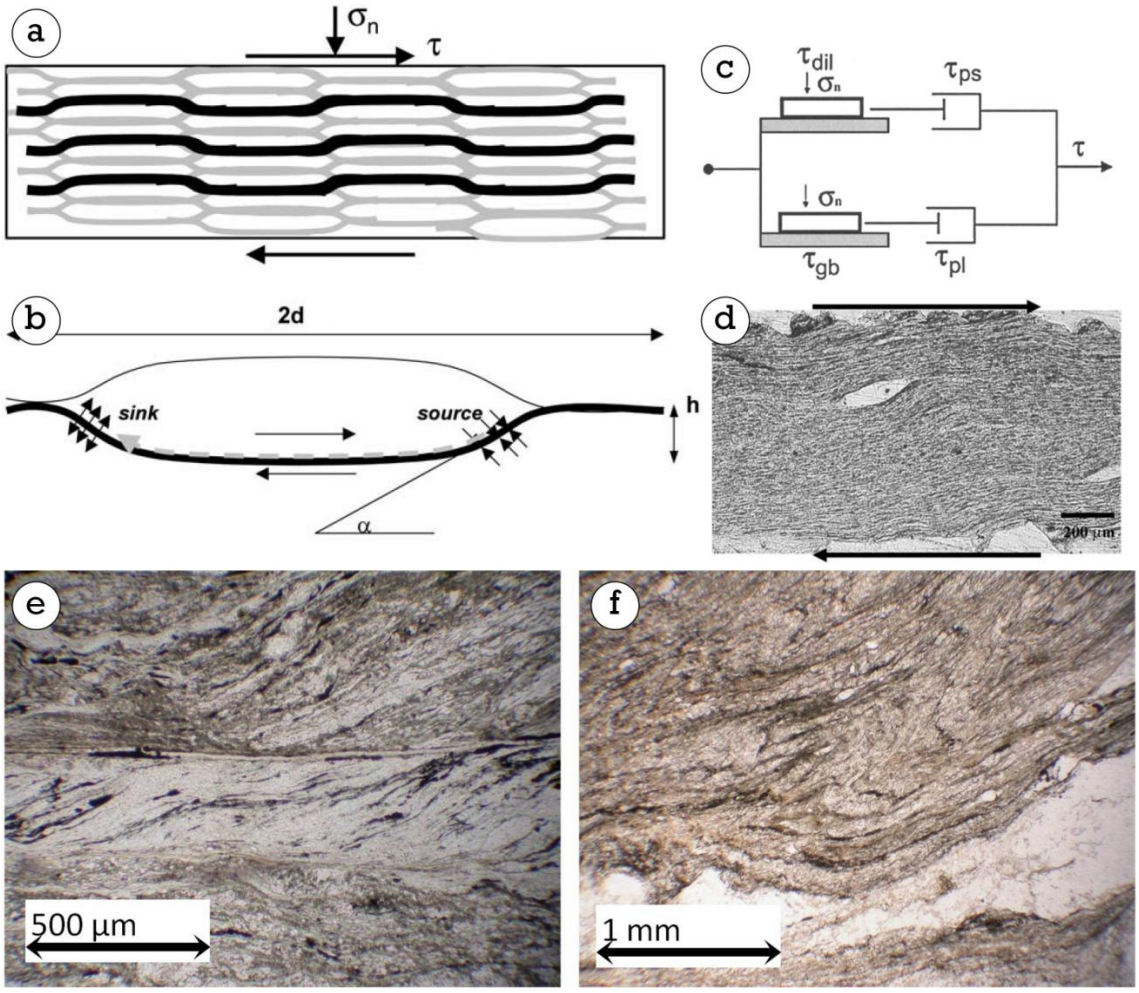

Figure 6.3: Microphysical model for pressure solution-accommodated creep after Bos and Spiers (2002) **a)** The model requires an anastomosing phyllosilicate-rich matrix isolating elongate grains of a soluble solid, with the presence of a fluid phase. **b)** Frictional (or plastic) sliding along the phyllosilicate foliae creates regions of high and low stress within the soluble solid. Regions of high stress become sites of dissolution (sources) and regions of low stress become areas of precipitation (sinks). The long axis of the soluble grains has a length of *d*. **c**) A mechanical analogue diagram can be created for the process where the shear stress of the system is equal to the sum of the shear input of dilation along the foliation (τ_{dil}), pressure solution of the solid (τ_{ps}), frictional sliding along the anastomosing phyllosilicates (τ_{gb}), and plastic flow in the phyllosilicates (τ_{pl}). **d)** A typical microstructure produced at high strains when pressure solution is operative which the microphysical model is based on. Grain size becomes increasingly fine-grained and homogeneous with progressive shear. **e, f)** Photomicrographs of samples from the S-C domain at the Minas fault zone where pressure solution-accommodated creep is occurring. (**a, b, d** are taken from Bos & Spiers 2002; **c** is taken from Niemeijer & Spiers 2005).

quartz phases and concurrent frictional sliding within interconnected phyllosilicate networks (Fig. 6.3). Through high strain experiments on kaolinite-halite, and muscovite-halite mixtures, three deformational regimes were identified: 1) a low velocity regime where deformation is controlled by frictional or plastic sliding on the foliation of interconnected phyllosilicates, 2) an intermediate velocity regime where the strength of the gouge is determined by accommodation through pressure solution and frictional sliding on the phyllosilicate foliae, and 3) a high velocity regime in which pressure solution is too slow to accommodate geometric incompatibilities so that dilation occurs (Bos and Spiers, 2002). Within regime 2, a microstructure emerged, comprising elongated clasts of halite embedded in a fine-grained kaolinite matrix (Bos and Spiers, 2001). With increasing strain, halite grain sizes decreased and became progressively incorporated in the fine-grained phyllosilicate matrix, creating an increasingly homogeneous fabric and a well defined foliation with S-C geometries (Fig. 6.3d). A mechanical analogue was proposed for deformation within regime 1 and 2, where the shear strength of the gouge is determined by the combined shear resistance from frictional sliding on the phyllosilicate foliae, pressure solution in the halite, and dilation on the phyllosilicate foliae (Bos and Spiers, 2002). Niemeijer and Spiers (2005) then incorporated plastic flow of phyllosilicates into the model, creating the mechanical analogue diagram seen in Figure 6.3c. Crustal strength profiles based on these models were developed for different faulting regimes. It was found that for a transcurrent fault and a fixed strain rate of $10^{-11}s^{-1}$, diffusion-controlled pressure solution-accommodated creep operated from 3-8km for a grain size of 25μm (Bos and Spiers, 2002), and that dissolution-controlled pressure solution-accommodated creep operated from 4-7km at a strain rate of $10^{-10}s^{-1}$ for a grain size of 50μm (Niemeijer and Spiers, 2005).

Bos and Spiers (2002) calculated the shear stress contributions from diffusion-controlled and dissolution-controlled precipitation creep for phyllosilicate bearing rocks. For diffusion-controlled pressure solution

$$\tau_d = \frac{\rho_s RT d^3}{B^3 \rho_f D \delta C_s \Omega_s} \dot{\gamma}, \tag{27}$$

where ρ_s is the molar density of the solid, R is the gas constant, T is temperature, d is the grain size, B is the aspect ratio of the grains, ρ_f is the molar density of the fluid, D the diffusion coefficient, δ the thickness of the fluid phase, C_s is the molar solubility of the solid, Ω_s is the molar volume of the solid and $\dot{\gamma}$ is the strain rate. For dissolution-controlled pressure solution

$$\tau_s = \frac{RTd}{B^2 k_s \Omega_s} \dot{\gamma}, \tag{28}$$

where k_s is a phenomenological rate coefficient. The relative effectiveness of each of these mechanisms is highly dependent on strain rate, grain size, and temperature, causing the rate-controlling mechanism to vary as a function of local conditions.

6.2.3 Crystal plasticity

Crystal plasticity will become the dominating deformation mechanism at sufficiently high temperatures, with crystal plasticity along the basal (001) plane in phyllosilicates replacing frictional sliding along phyllosilicate foliae, and crystal plastic flow of quartz replacing the dissolution-precipitation creep of quartz.

For quartz, the flow law of Luan and Paterson (1992) developed for quartzite will be used in the analyses presented. This quartz flow law was derived from experiments on synthetic quartz aggregates, formed by hot pressing natural quartz powder, impure silica, and high-purity silicic acid to create aggregates with water

contents comparable to natural quartzites. The flow law is comparable to that of Gleason and Tullis (1995), and is commonly used in strength profiles of the crust (Fig. 2.6). Rewritten for the case of simple shear the flow law takes the form

$$\dot{\gamma} = 3^{(n+1)/2} A \tau^n e^{-Q/(RT)} \tag{29}$$

where n and A are geometrical constants, and Q is the activation energy. Solving for τ results in

$$\tau_{qtz} = \left(\frac{\dot{\gamma}}{3^{\frac{n+1}{2}} A e^{-\frac{-Q}{RT}}} \right)^{\left(\frac{1}{n}\right)}. \tag{30}$$

Flow laws have been developed for basal (001) slip in biotite (Kronenberg et al., 1990) and for muscovite (Mares and Kronenberg, 1993). These experimentally derived flow laws determined (at varying temperatures, pressures, strain rates and orientations) the critical resolved shear stresses required to activate plastic flow. Experimental data were fit to both exponential and power law relationships between stress and strain rate. Here the exponential relationship will be considered, consistent with lattice resistance (*i.e.* Peierls) models of glide (Peierls, 1940; Kronenberg et al., 1990), which takes the form

$$\dot{\varepsilon} = C e^{(\alpha \sigma_d)} e^{-Q/(RT)}. \tag{31}$$

C and α are constants determined from experimentation, and σ_d is the differential stress ($\sigma_1 - \sigma_3$). Rearranging the equation and solving for simple shear (Niemeijer and Spiers, 2005) results in

$$\tau_{pl} = \frac{1}{\alpha} \log((\sqrt{3}\,\dot{\gamma}_{pl})/(C e^{-\frac{-Q}{RT}})). \tag{32}$$

Within quartz-phyllosilicate mixtures $\dot{\gamma}_{pl}$ will equal $\dot{\gamma}/R_{phy}$, where $\dot{\gamma}$ is the bulk shear strain rate and R_{phy} is the ratio of phyllosilicate foliae to total gouge thickness.

6.2.4 Microphysical model and assumptions

Crustal strength profiles have been created using the microphysical model of Niemeijer and Spiers (2005), adapted to the conditions observed at the San Andreas Fault Observatory at Depth and for the S-C fabrics observed within the Minas fault zone at Greville Bay. The crustal strength profiles are created by plotting the shear stress at failure for dilation, the shear stress for pressure solution-accommodated creep, and the shear stresses at failure for quartz and phyllosilicate plasticity. The shear stress for pressure solution-accommodated creep takes the form

$$\tau_{PSAC} = \{(\tau_{gb})^{-m} + (\tau_{pl})^{-m})\}^{-1/m} + \{(\tau_{ps})^{-n} + (\tau_{dil})^{-n})\}^{-1/n} \quad (33)$$

where τ_{gb} is the behaviour of frictional sliding along the phyllosilicate foliae following

$$\tau_{gb} = \mu\sigma_n, \quad (34)$$

τ_{pl} is the critically resolved shear stress for plastic sliding along the basal plane of phyllosilicates from equation (32), τ_{ps} is the rate-controlling mechanism for dissolution-precipitation creep of quartz (either τ_d from equation (27) or τ_s from equation (28)), τ_{dil} is the dilational strength of the rock which will equal the shear stress of failure from equation (26), and *m* and *n* are exponents used to reproduce the sharp transition from dilational strength to the strength of pressure solution-accommodated creep seen in experimentation. A value of 20 for *m* and *n* fits the experimental data well (Niemeijer and Spiers, 2005).

Strength profiles (Figs. 6.5-6.7) are constructed under the following assumptions: 1) If $\tau_{dil} < \tau_{PSAC}$, then the strength profile will follow that of τ_{dil}. 2) Once pressure solution-accommodated creep is initiated ($\tau_{dil} > \tau_{PSAC}$) it will dominate until the flow law for quartz is intersected. 3) Pressure solution-accommodated creep will be activated

when the shear stress of the rate-controlling mechanism (the higher value out of τ_d or τ_s) is achieved.

6.2.5 Parameters used in calculations of strength profiles

Table 5.1 shows the values for the variables used in the calculation of shear stresses at failure for the different deformation mechanisms. For the models developed in the next sections a geothermal gradient of 30°C/km with a surface temperature of 30°C, a pore fluid factor, λ, of 0.357, and a crustal density of 2.8x 10^3kg/m^3 have been assumed. Strength profiles are modelled for strain rates of 10^{-8}, 10^{-10}, 10^{-12}, and 10^{-14}s^{-1}, and are plotted on two separate charts, one for slow strain rates (10^{-12} and 10^{-14}s^{-1}), and one for fast strain rates (10^{-8} and 10^{-10}s^{-1}). An additional slow strain rate chart has been added for the presence of smectite at shallow crustal levels (see below).

For the coefficient of friction of the phyllosilicate horizons, a value of 0.3 is used which approximates most phyllosilicate phases (chlorite, kaolinite, lizardite, pyrophyllite, phlogopite, and biotite); however certain phases show lower coefficients of friction (talc = 0.2, montmorillonite = 0.1), and some higher (illite = 0.4, and muscovite = 0.4; Fig. 6.4). This becomes important in the analysis of SAFOD samples at slow strain rates, where coefficients of friction less than 0.1 have been measured in the creeping gouges due to the presence of smectitic phases (Carpenter et al., 2011; Lockner et al., 2011). Smectitic phases are only stable up to temperatures of ~120°C, after which they convert to a Mg-rich chlorite (Frey and Robinson, 1999). An additional low strain rate chart has been provided where the coefficient of friction for the phyllosilicates changes linearly from 0.1 to 0.3 over a temperature range from 100 to 150°C.

The strength profiles are constructed assuming optimal orientations of stresses for Andersonian faulting in a transcurrent setting for the given coefficient of friction.

Table 6.1: Variables used in the calculation of crustal strength profiles

GENERAL TERMS			
Symbol	***Explanation***	***Value/Equation***	***Reference***
z	Depth (m)	-	-
Geo	Geothermal Gradient (°C/km)	3.00E+01	-
ρ	Density of the Crust (kg/m^3)	2.80E+03	-
g	Gravity (m^2/s)	9.81	-
λ	Pore Fluid Factor (Hydrostatic)	0.357	*Sibson 1974*
DIFFUSION CONTROLLED PRESSURE SOLUTION (*Bos & Spiers 2002*) $\tau_d = (\rho_s R T d^3)/(B^3 \rho_f D \delta C_s \Omega_s)\dot{\gamma}$			
Symbol	***Explanation***	***Value/Equation***	***Reference***
ρ_s	Density of the Solid (kg/m^3)	2.65E+03	*Gratier 2009*
R	Gas Constant (J/mol*K)	8.31446	-
T	Temperature (K)	*Geo* *z+30+273.15	-
d	Grain Size (m)	2.50E-05	-
B	Aspect Ratio	4	-
ρ_f	Density of the Fluid Phase (kg/m^3)	1.00E+03	-
D	Diffusion Coefficient (m^2/s)	1.00E-09	*Gratier 2009*
δ	Thickness of the Fluid Phase (m)	6.00E-10	*Gratier 2009*
C_s	Molar Solubility of the Solid (mol/m^3)	(10^[-1107/T-0.0254])*1000	*Rimstidt 1997*
Ω_s	Molar Volume of the Solid (m^3/mol)	2.20E-05	*Gratier 2009*
$\dot{\gamma}$	Shear Strain Rate (1/s)	*Varied*	-
DISSOLUTION CONTROLLED PRESSURE SOLUTION (*Bos & Spiers 2002*) $\tau_s = (RTd)/(B^2 k_s \Omega_s)\dot{\gamma}$			
Symbol	***Explanation***	***Value/Equation***	***Reference***
k_s	Rate Coefficient for Dissolution (1/s)	10^(1.174-(0.002028*T)-(4158/T))	*Rimstidt & Barnes 1980*
FLOW LAW FOR QUARTZ (*Luan & Paterson 1992*) $\tau_{qtz} = \left(\frac{\dot{\gamma}}{3^{\frac{n+1}{2}} A e^{\frac{-Q}{RT}}}\right)^{\left(\frac{1}{n}\right)}$			
Symbol	***Explanation***	***Value/Equation***	***Reference***
A	Experimental Coefficient	1.80E-18	*Luan & Paterson 1992*
Q	Activation Energy (J/mol)	150000	*Luan & Paterson 1992*
n	Experimental Coefficient	2.3	*Luan & Paterson 1992*
FLOW LAW FOR PHYLLOSILICATES (*Kronenberg 1990*) $\tau_{pl} = \frac{1}{\alpha}\log((\sqrt{3} * \dot{\gamma}_{pl})/(C e^{\frac{-Q}{RT}}))$			
Symbol	***Explanation***	***Value/Equation***	***Reference***
α	Constant From Experimentation (MPa)	0.41	*Kronenberg 1990*
$\dot{\gamma}_{pl}$	Shear strain in the phyllosilicate foliae (1/s)	$\dot{\gamma}$ /0.1	*Kronenberg 1990*
C	Constant From Experimentation (1/s)	4.60E-06	*Kronenberg 1990*
Q	Activation Energy (J/mol)	86000	*Kronenberg 1990*

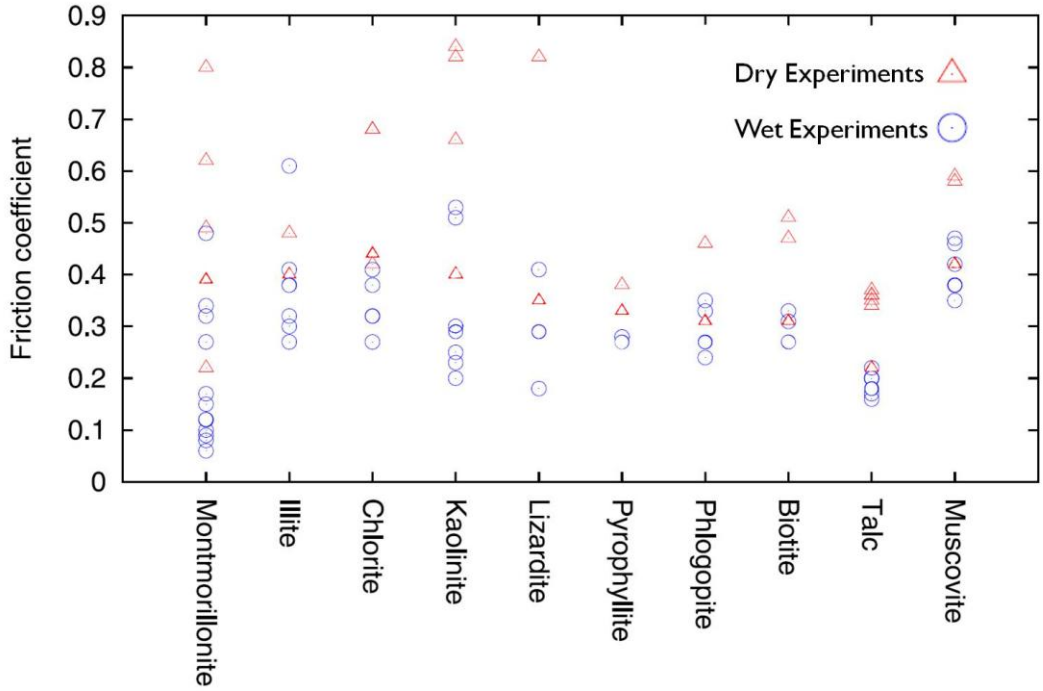

Figure 6.4: Frictional properties of phyllosilicates The range of coefficients of friction (μ) for various phyllosilicate phases under dry and wet conditions determined by experimentation. Note the anomalously low values for montmorillonite (<0.1 when wet) and that the bulk of phases fall within a range from 0.3-0.4. (taken from Behnsen & Faulkner 2012; references for experiments are found within)

This follows the assumption that the stress state near a fault will rotate to an optimal orientation with proximity to a fault.

6.2.6 Strength profiles for transcurrent fault zones

Within the strength profiles, different regimes exist depending on the dominant inputs from our mechanical analogue for pressure solution-accommodated creep, as predicted by Bos and Spiers (2002) and Niemeijer and Spiers (2005). The transition between each regime is abrupt. The dominant inputs for each curve have been labelled.

At faster geological strain rates ($10^{-8}s^{-1}$ and $10^{-10}s^{-1}$), diffusion is the rate-controlling mechanism for pressure solution in quartz. At $10^{-8}s^{-1}$ the rate of diffusion is too slow for deformation by pressure solution-accommodated creep, and the strength profile follows that for dilation and frictional sliding until the flow law for quartz is reached (Fig. 6.5). At a strain rate of $10^{-10}s^{-1}$ diffusion-controlled pressure solution-accommodated creep controls deformation from depths of ~7 to 17km.

At slower geological strain rates ($10^{-12}s^{-1}$ and $10^{-14}s^{-1}$), dissolution is the rate-controlling mechanism. When the coefficient of friction for phyllosilicate phases is consistently 0.3, pressure solution-accommodated creep dominates deformation starting at very shallow depths (3km for strain rates of 10^{-12} and at 1km for strain rates of $10^{-14}s^{-1}$; Fig. 6.6). At strain rates of $10^{-14}s^{-1}$, plastic flow of the phyllosilicate phases occurs at ~2.3km depth, and for $10^{-12}s^{-1}$ at 3.1 km depth.

For slow deformation rates where the coefficient of friction along phyllosilicate phases changes with depth from a smectitic value (0.1) to the value of chlorite (0.3), a region of deformation occurs where strength is primarily controlled by frictional sliding along the phyllosilicates, before it becomes controlled by crystal plasticity within the phyllosilicate phase (Fig. 6.7).

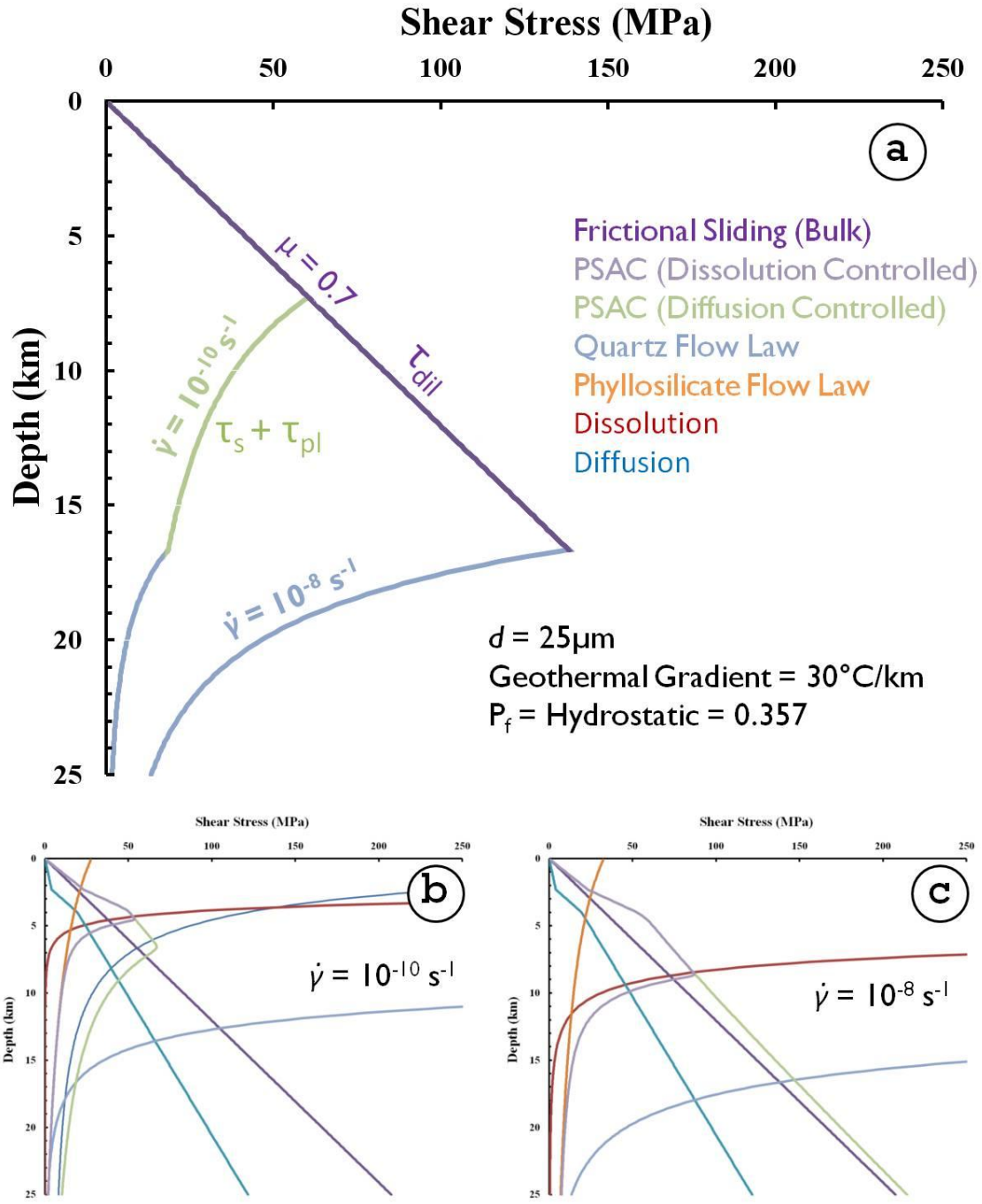

Figure 6.5: Crustal strength profile for a transcurrent fault zone at fast deformation rates (10^{-8} and 10^{-10} s^{-1}) **a)** The final strength profiles for the conditions examined. At strain rates faster than $10^{-12}s^{-1}$, pressure solution is not an effective deformation mechanism as the rates of diffusion are too slow. At a strain rate of $10^{-10}s^{-1}$ diffusion-controlled pressure solution-accommodated creep operates from 7-17km depth. **b, c)** Strength profiles for each of shear inputs into the calculation of pressure solution-accommodated creep, as well as the curves for dissolution and diffusion-controlled pressure solution-accommodated creep.

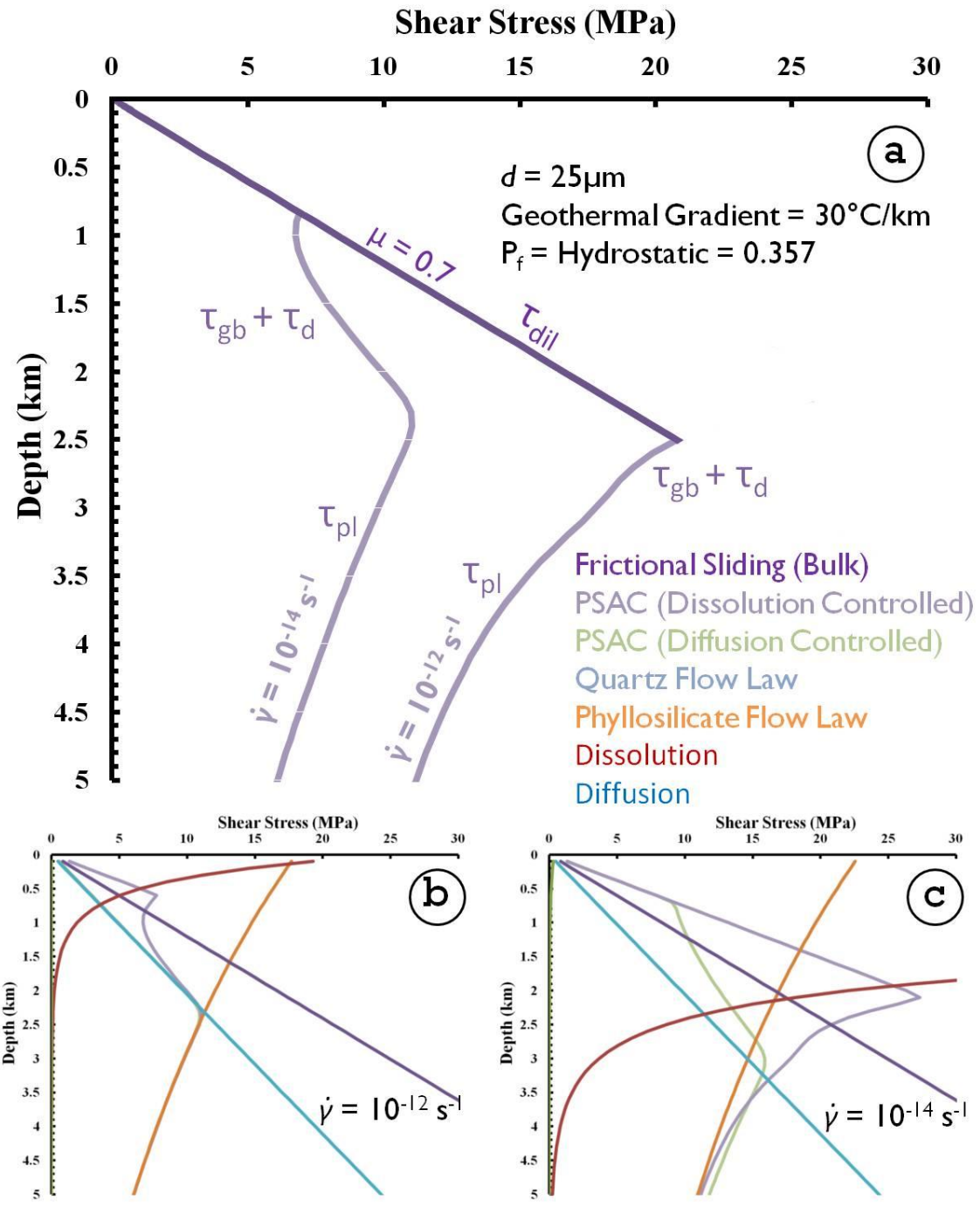

Figure 6.6: Crustal strength profile for a transcurrent fault zone at slow deformation rates (10^{-12} and 10^{-14} s^{-1}) and a constant coefficient of friction (0.3) a) The final strength profiles for the conditions examined. At low strain rates pressure solution is dissolution-controlled and becomes effective at shallow depths. The strength is only briefly controlled by pressure solution before it is controlled by plastic of the phyllosilicates. **b, c)** Strength profiles for each of shear inputs into the calculation of pressure solution-accommodated creep, as well as the curves for dissolution and diffusion-controlled pressure solution-accommodated creep.

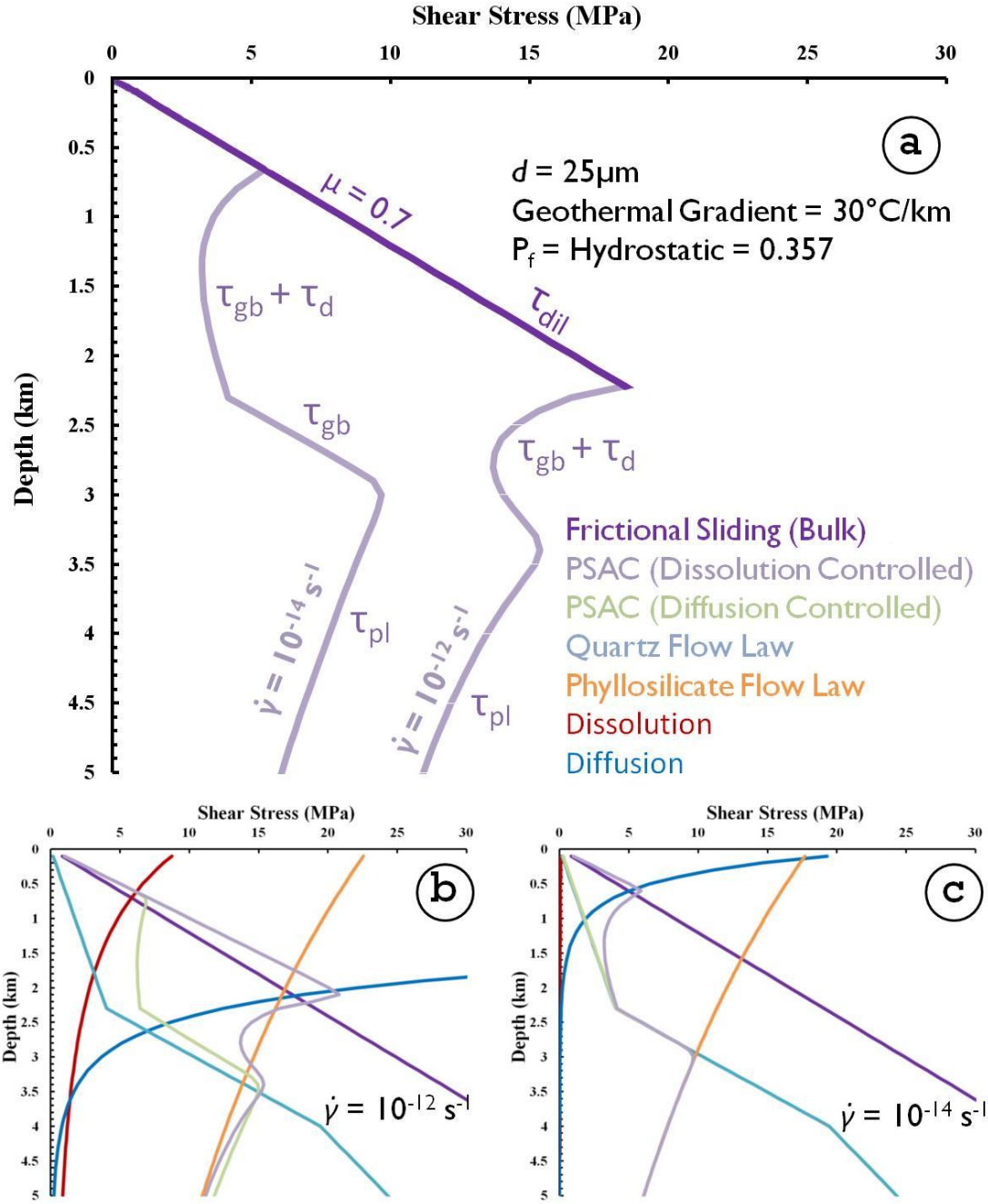

Figure 6.7: Crustal strength profile for a transcurrent fault zone at slow deformation rates (10^{-12} and 10^{-14} s^{-1}) and an evolving coefficient of friction (0.1-0.3) In these curves the coefficient of friction for the phyllosilicate phase linearly evolves from a smectitic value (0.1) up to 100°C to the value for chlorite (0.3) by 150°C. **a)** The final strength profiles for the conditions examined. As in the previous graph pressure solution is dissolution-controlled and strength is only briefly controlled by pressure solution before it is controlled by sliding within the phyllosilicate phases. **b, c)** Strength profiles for each of the shear inputs into the calculation of pressure solution-accommodated creep, as well as the curves for dissolution and diffusion-controlled pressure solution-accommodated creep.

6.2.7 Implications of crustal strength profiles

Given a grain size of 25μm, at fast geological strain rates (>$10^{-8}s^{-1}$), pressure solution is not an effective mechanism in phyllosilicate-rich transcurrent faults, and strength is comparable to the classical crustal strength profiles of Kohlstedt (1995). At intermediate strain rates (10^{-10}) a region of diffusion-controlled pressure solution-accommodated creep occurs between ~7 and 17km depth. Varying the coefficient of friction of phyllosilicates (0.1-0.4) does not affect these results.

At slow deformation rates, dissolution is the rate-controlling mechanism and pressure solution is much more effective at shallower depths (starting at <1km for strain rates of 10^{-14} and 2-2.5km depth at strain rates of 10^{-12}). The strength of faults is controlled by the frictional properties of phyllosilicates by 3km depth.

6.3 Role of the Effective Grain Size on Strength

The efficacy of dissolution precipitation creep is highly dependent on the effective grain size, which will depend on the spacing of permeable networks (*e.g.* fractures, grain boundaries that can accommodate an intergranular fluid, pressure solution seams, stylolites). Crustal strength profiles, while useful at depicting the overall behaviour of the crust, do not show the interrelationship of different processes at a given location in a fault zone. For example, the poorly understood process of fault healing (commonly thought to involve hydrothermal precipitation and deposition of silica; Xue et al. 2013) will increase the effective grain size and reintroduce silica to a system, while disaggregation occurring through cataclasis and brecciation will decrease the effective grain size. These processes are known to occur cyclically within fault zones (Sibson, 1992). The deposition of hydrothermal minerals will decrease the proportion of

phyllosilicate phases in the gouge, increasing its coefficient of friction (Tembe et al., 2010). With increasing diffusive distance, silica can be removed from a system through pressure solution, increasing the phyllosilicate content of a system. To examine these competing processes, plots of effective grain size against shear stress were made for the SAFOD site and for the S-C domain at the Greville Bay section of the Minas fault zone.

6.3.1 Role of the effective grain size at the SAFOD site

Figure 6.8 shows an effective grain size plot for the SAFOD site at a strain rate of $10^{-10}s^{-1}$, as estimated based on a 1-3m shear zone accommodating 10mm/yr of slip. The local temperature is 120°C (Zoback et al., 2010), and assuming hydrostatic fluid pressures, $\sigma_v = 47.7$MPa at 2.7km depth. The shear stresses at failure are plotted assuming $\sigma_v{}' = \sigma_2 = \sigma_3$, and a cohesionless fault gouge. These serve as maxima; if $\sigma_3 < \sigma_2 = \sigma_v{}'$, the shear stress at failure would be less than the values calculated. An optimally oriented fault (θ = 27.5°) with a coefficient of friction of 0.1 will fail at shear stresses of 5MPa, while using the values of the principal stress orientation distal to the fault zone (θ=70°; Hickman & Zoback 2004) gives a shear stress at failure of 6.6MPa.

For this strain rate, dissolution is the rate-controlling mechanism for dissolution precipitation creep as it requires a smaller grain size in order to accommodate deformation (Fig. 6.8). Grain sizes between 100nm and 1μm are needed to initiate dissolution-controlled precipitation creep. If a sample has a larger effective grain size than the rate-controlling mechanism for dissolution precipitation creep, pressure solution will not be an effective deformation mechanism.

The effect of varying strain rate under the same conditions is shown in Figure 6.9. For faster geological strain rates ($10^{-8}s^{-1}$ and $10^{-10}s^{-1}$), dissolution is the rate-controlling mechanism, while at slower rates ($10^{-12}s^{-1}$ and $10^{-14}s^{-1}$) diffusion controls the

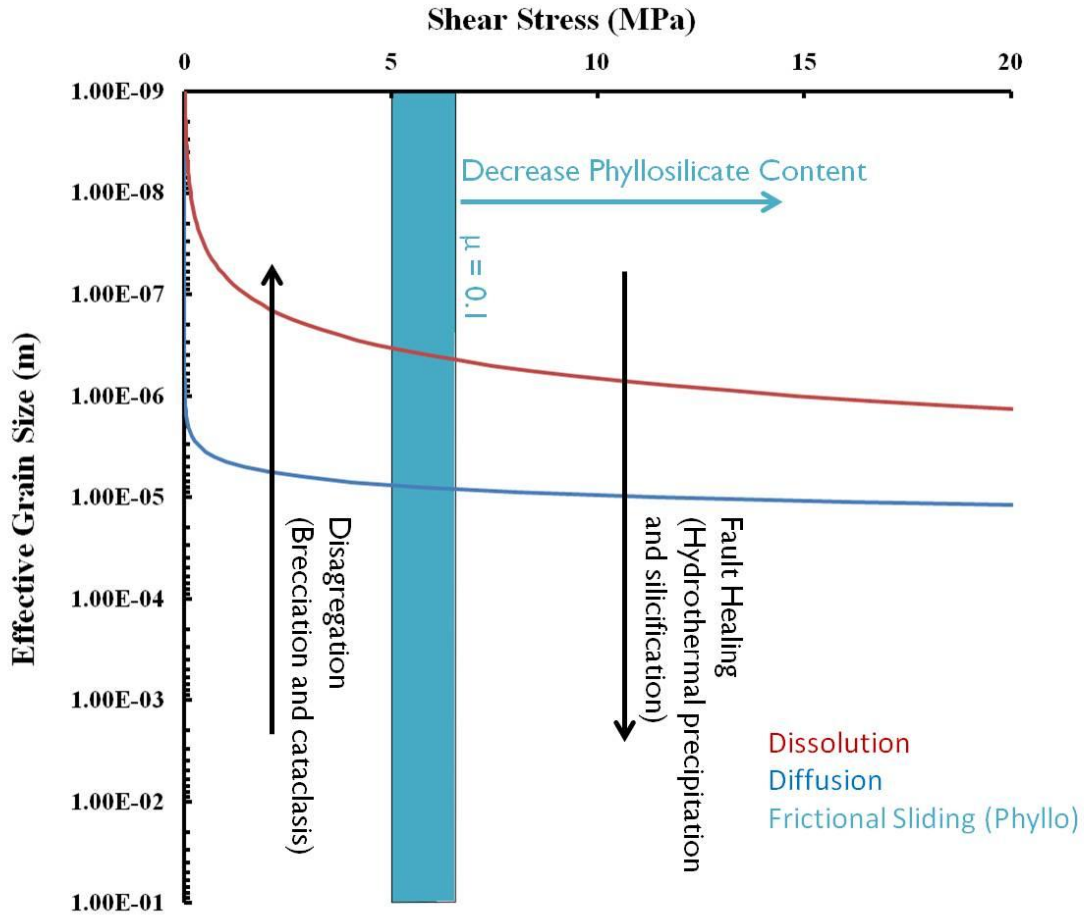

Figure 6.8: Effective grain size plot for the active portions of the SAFOD site Stress curves for pressure solution (dissolution and diffusion-controlled) are plotted against the effective grain size (d) at a strain rate of $10^{-10}s^{-1}$ under hydrostatic conditions at 2.7km depth and a local temperature of 120°C. The shear stress at failure for frictional sliding in the gouge is plotted (blue rectangle) assuming no cohesion and fault zone orientations ranging from 27.5° to σ_1 to 70° to σ_1. Disaggregation of the samples can initiate pressure solution, while fault healing will stop the process. The critical grain size is ~250μm, and pressure solution processes are dissolution-controlled.

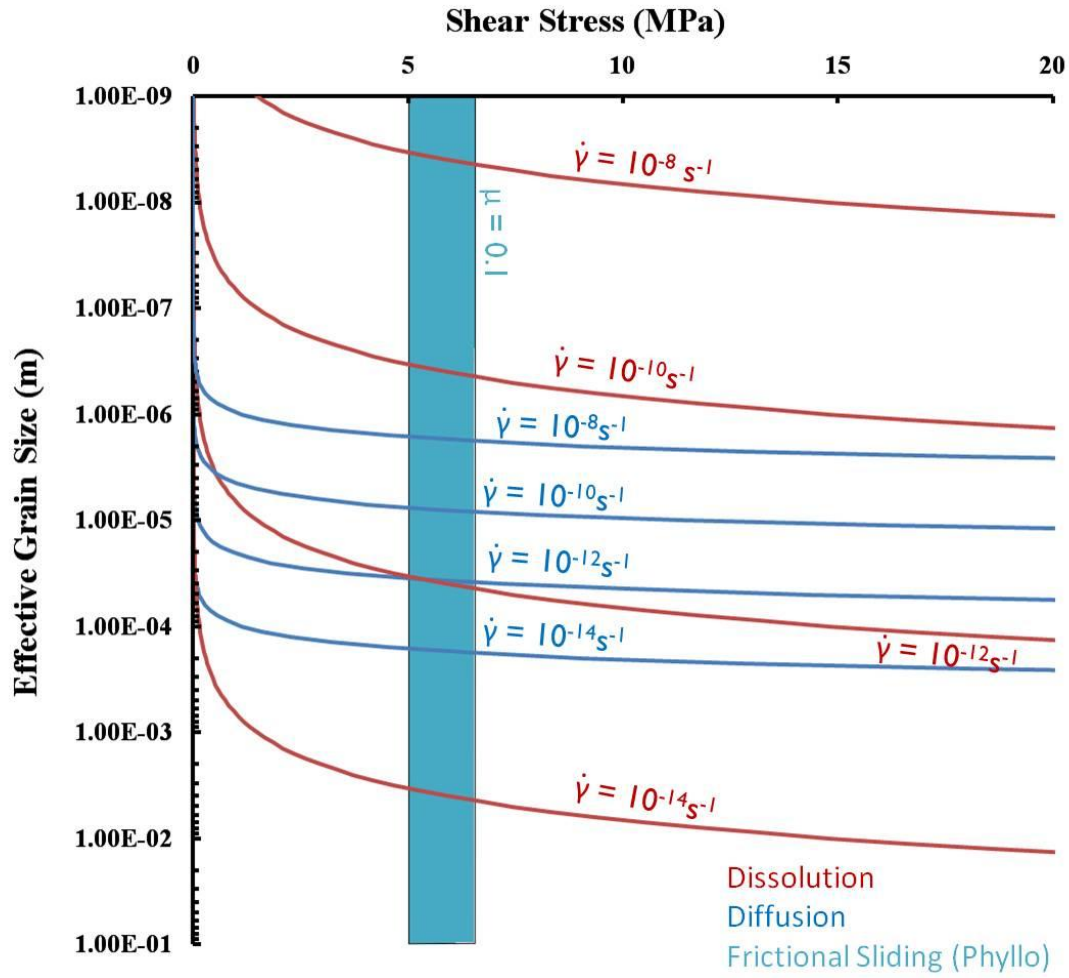

Figure 6.9: Effective grain size plot for the active portions of the SAFOD site Stress curves for pressure solution (dissolution and diffusion-controlled) are plotted against the effective grain size (*d*) at various strain rates under hydrostatic conditions at 2.7km depth and a local temperature of 120°C. The shear stress at failure for frictional sliding in the gouge is plotted (blue rectangle) assuming no cohesion and fault zone orientations ranging from 27.5° to σ_1 to 70° to σ_1. Note that pressure solution changes from dissolution-controlled at fast strain rates ($>10^{-12}s^{-1}$) to diffusion-controlled at lower strain rates.

efficacy of pressure solution. The maximum grain sizes that would enable pressure solution to be the primary accommodation mechanism range from 1-15nm for deformation at $10^{-8}s^{-1}$, to 100-250μm at a strain rate of $10^{-14}s^{-1}$.

In order that pressure solution-accommodated creep occurs at the SAFOD site, given a strain rate of $10^{-10}s^{-1}$, effective grain sizes must be less than 1μm. This is only possible within the finest grained gouges. However, the diagrams also demonstrate that slower strain rates ($10^{-14}s^{-1}$) can be accommodated with effective grain sizes between 100 and 250 μm.

6.3.2 Role of the effective grain size at Greville Bay (S-C Domain)

The same principles can be applied to the S-C fabrics at Greville Bay. Assuming hydrostatic pore fluid pressures, a geothermal gradient of 30°C/km, optimally oriented faults (stresses), and a local temperature of 360°C (see section 4.5), it is possible to determine the critical effective grain size for initiating pressure solution processes in the quartz packages.

At the higher temperatures of formation for the S-C fabrics, diffusion is consistently the rate-controlling mechanism for pressure solution, and maximum critical grain sizes to accommodate pressure solution range from 4.5-10μm for a strain rate of $10^{-8}s^{-1}$, to 300μm-1mm for a strain rate of $10^{-14}s^{-1}$ (Fig. 6.10).

It is important to note that deformation of phyllosilicates through dislocation glide along the basal (001) planes has a very low critical resolved shear stress at these temperatures, and is more effective than frictional sliding. In addition, the strength of quartz is very low at slow deformation rates, and at strain rates less than $10^{-12}s^{-1}$, plastic flow of quartz will be the dominant deformation mechanism (Fig. 6.10).

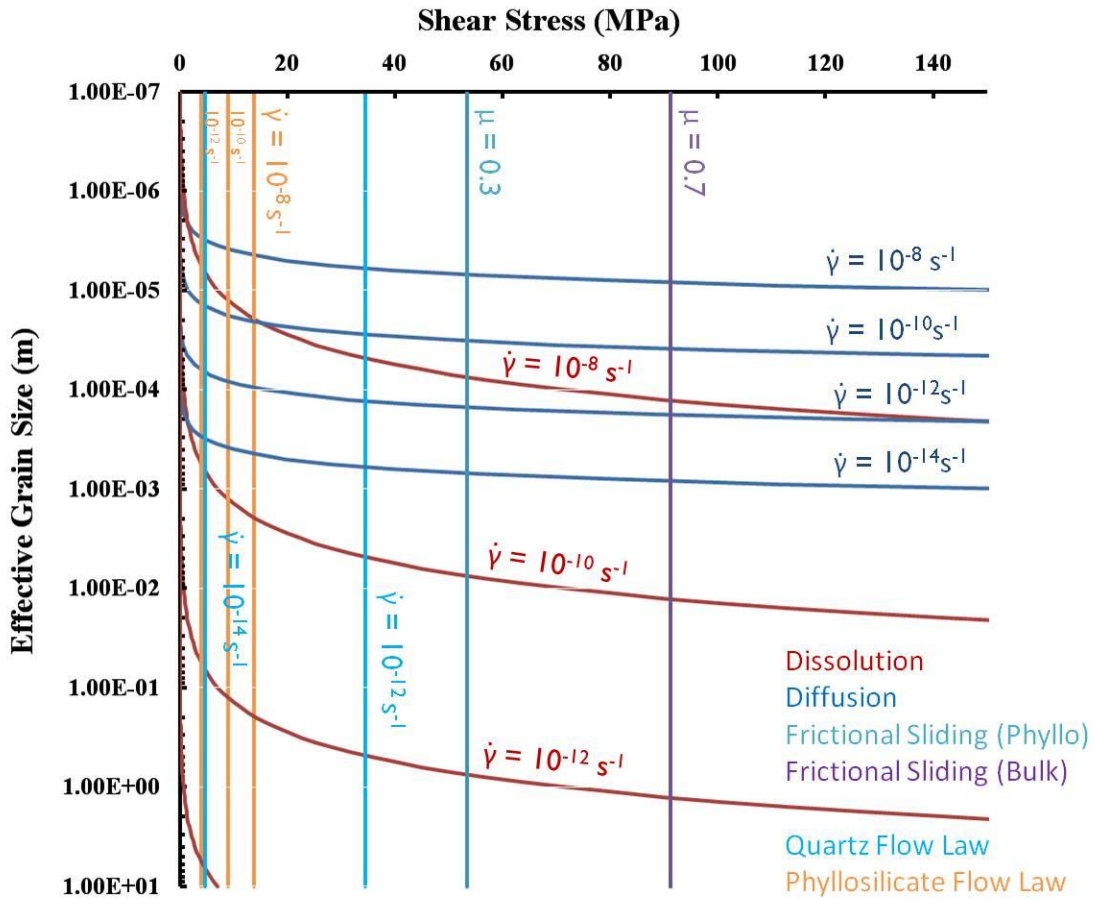

Figure 6.10: Effective grain size plot for the S-C domain of the Minas fault zone Stress curves for pressure solution (dissolution and diffusion-controlled) are plotted against the effective grain size (*d*) at various strain rates under hydrostatic conditions at 11km depth and a local temperature of 360°C with an ideal fault zone orientation to σ_1. Pressure solution is diffusion-controlled at these depths, and the frictional properties of the phyllosilicates holds no bearing as plasticity in the phyllosilicates is easily activated. At low strain rates crystal plastic flow of quartz is easily activated, while at higher strain rates pressure solution can be activated when the effective grain size is less than 5μm ($10^{-8}s^{-1}$) to less than 44.7μm ($10^{-10}s^{-1}$).

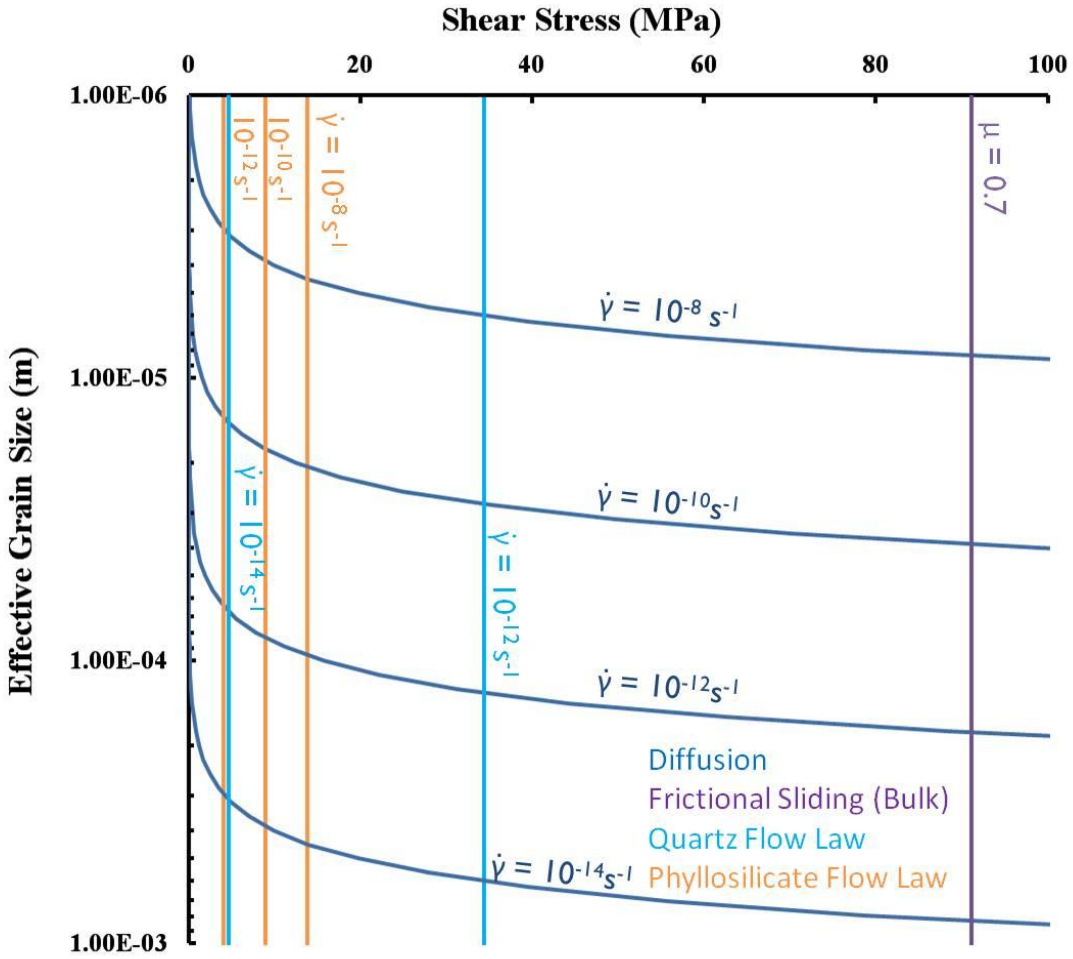

Figure 6.11: Simplified view of the effective grain size plot for the S-C domain of the Minas fault zone Stress curves for pressure solution (dissolution and diffusion-controlled) are plotted against the effective grain size (*d*) at various strain rates under hydrostatic conditions at 11km depth and a local temperature of 360°C with an ideal fault zone orientation to σ_1. Pressure solution is diffusion-controlled at these depths, and the frictional properties of the phyllosilicates holds no bearing as plasticity in the phyllosilicates is easily activated. At low strain rates crystal plastic flow of quartz is easily activated, while at higher strain rates pressure solution can be activated when the effective grain size is less than 5µm ($10^{-8}s^{-1}$) to less than 44.7µm ($10^{-10}s^{-1}$).

6.3.3 Implications of effective grain size charts

Plotting effective grain size against shear stress shows the critical grain size necessary for pressure solution to be an effective deformation mechanism at a given site. Within the core at SAFOD, where a strain rate of $10^{-10}s^{-1}$ is observed, grain sizes less than 100nm are needed to initiate dissolution-controlled creep. At grain sizes smaller than this strength will be controlled by the frictional properties of the phyllosilicate phases. Fault healing can increase the effective grain size in the active fault making pressure solution unfavorable.

Within the damage zone, pressure solution can be initiated through disaggregation down to a critical grain size. For a strain rate of 10^{-14} the maximum effective grain size needed is 250μm.

Within the S-C fabrics at Greville Bay, diffusion is the rate limiting reaction for pressure solution. To accommodate deformation at $10^{-8}s^{-1}$ effective grain sizes less than 5μm are required, at $10^{-12}s^{-1}$ effective grain size must be less than 100μm. By $10^{-14}s^{-1}$ quartz strength is controlled by crystal plastic deformation.

6.4 A Note on Strain Rates

Strength profiles and effective grain size plots have been constructed for various strain rates in the crust. Within creeping segments, strain rate depends on the displacement rate of the fault zone and the width over which displacement is being accommodated (Fig. 6.12). It is important to note that in actively deforming fault zones, the strain rate can be variable across the fault, so that the displacement rate recorded along a fault zone may be accommodated by multiple parallel strands operating at different shear strain rates. For a simple example, consider a fault zone accommodating

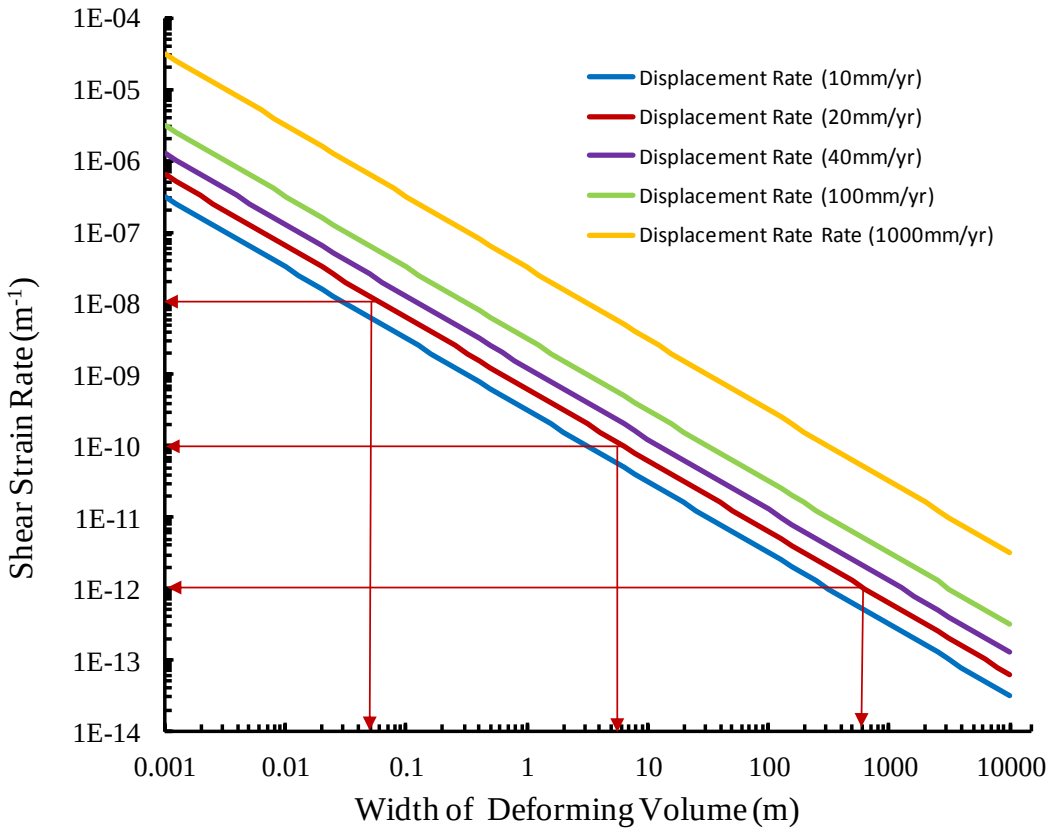

Figure 6.12: Width of the deforming volume necessary to accommodate displacement rates within a fault zone at a given shear strain rate Plots of the width of a deforming volume needed to accommodate given shear strain rates for a given yearly displacement across a fault zone. Arrows show the necessary widths to accommodate 20mm/yr of slip at strain rates used in the calculation of strength profiles in this section. Note the change from centimetre-scale widths at a strain rate of $10^{-8}s^{-1}$ to hundreds of metres at $10^{-12}s^{-1}$.

40mm/yr of slip, with a quickly deforming fault core, and a slowly deforming damage zone. The fault core could be accommodating 20mm/yr of slip at a strain rate of $10^{-8}s^{-1}$ over a width of ~5cm, while the damage zone could also be accommodating 20mm/yr of slip at a strain rate of $10^{-12}s^{-1}$ over a width of 500m to obtain the total 40mm/yr of displacement along the fault zone (Fig. 6.12). Additionally, strain rate can be transient, with fault segments locking due to fault healing, or increasing in strain rate due to brittle fracture following a seismic event (Çakir et al., 2012). It is important not to assume steady-state strain rates in highly heterogeneous fault zones.

6.5 Weak faults? – Implications for fault zone behaviour

6.5.1 The heat-flow paradox

Within the San Andreas fault low geothermal gradients have been recorded on either side of the fault (Brune et al., 1969; Lachenbruch and Sass, 1980; Sass et al., 1997; Williams et al., 2004), with a principal stress orientation nearly perpendicular to the fault (Mount and Suppe, 1987, 1992; Hickman and Zoback, 2004). This observation, known as the "heat-flow paradox", led Lachenbruch and Sass (1980) to assume a low shear strength (< 20MPa) for the San Andreas fault, and to the development of a weak fault in a strong crust model for the San Andreas fault (Mount and Suppe, 1987; Townend and Zoback, 2000; Imber et al., 2008; Zoback et al., 2010).

The model, while widely cited and referred to, is contentious and has been a long standing source of debate in the geological community. Elevated regional deviatoric stresses measured within 1km of the active fault (Zoback et al., 1987; Hickman and Zoback, 2004) seem inconsistent with a weak fault, and more consistent with the values expected for a strong fault (Scholz, 2000). Several authors (Rice, 1992; Tembe et al.,

2009; Lockner et al., 2011) have invoked a mechanical description of the stress state in the fault, where the region outside the fault zone is in a critical state of stress for thrust failure, while the fault core itself is critically stressed for strike-slip failure (Fig. 6.13). In these analyses, the core is considered to be a soft ductile layer in a harder surrounding which experiences higher internal stresses than the surrounding material (Rice, 1992). The stresses inside and outside the fault are linked by traction on the fault surface (Fig. 6.13). Rice (1992) used the model to explain fault weakness due to elevated pore fluid pressures within the fault core, where both the core and outside region exhibited Byerlee coefficients of friction (~0.7). Following the drilling program at SAFOD, Tembe et al. (2009) and Lockner et al. (2011) modified the analysis, removing the condition of elevated pore fluid pressure, instead using the model to explain the measured low coefficients of friction of the fault core within an elevated regional stress state (Fig. 6.13). In these analyses, however, it is unclear how tensile fracturing, visible in core from SAFOD in this study and by Mittempergher et al. (2011) may occur, since the analyses assume cohesionless faults.

The stress orientations themselves are also contentious, with θ values ranging from 25-90° depending on the parameters for inversion of focal mechanisms (see Hardebeck and Michael, 2004 and refs within); several studies have postulated that σ_1 rotates into a more optimal orientation with proximity to the fault core (Scholz, 2000, 2006; Hardebeck and Michael, 2004 and refs within).

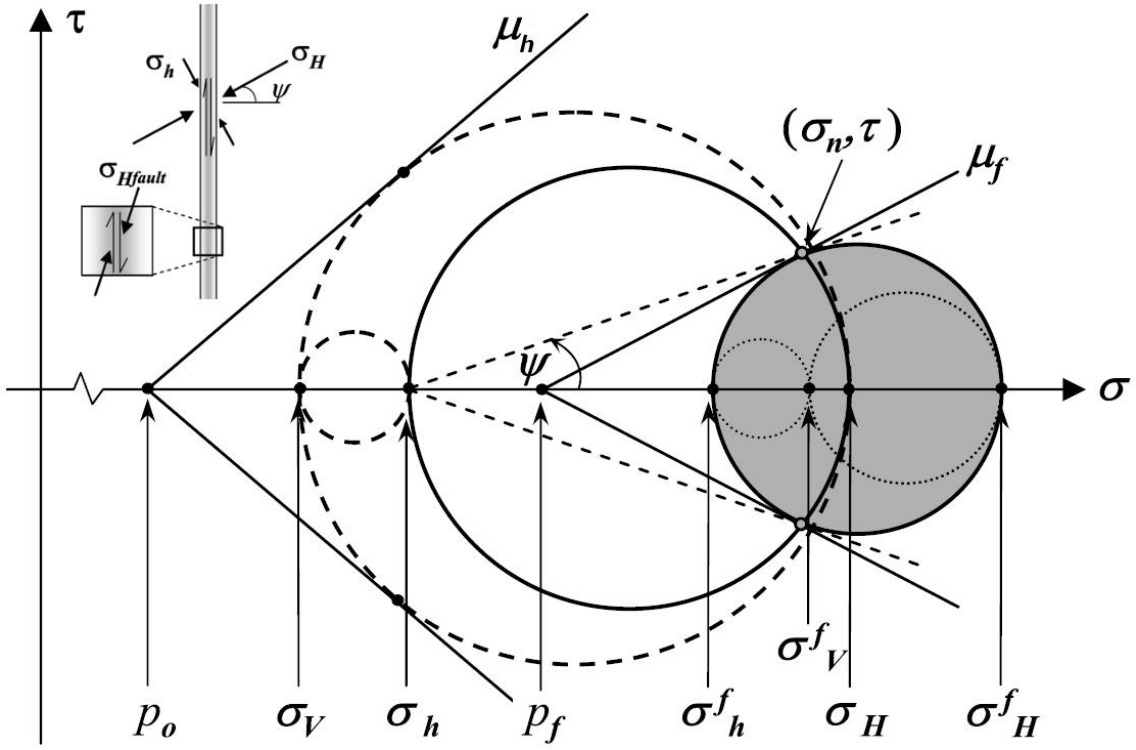

Figure 6.13: Analyses for a simultaneously critically stressed host rock (thrust failure) and fault core (strike-slip failure) The Rice model for a critically stressed host rock (thrust failure) and fault core (strike-slip failure) linked by traction along the fault interface (Rice, 1992). This model was used to explain higher pore fluid pressures in the fault core (Rice, 1992) where the coefficient of friction for both the host (μ_h) and the fault (μ_f) was 0.7. The model was subsequently modified by Tembe et al. (2009) and Lockner et al. (2011) for low fault friction (μ_f=0.1-0.2), within a region of elevated deviatoric stress with Byerlee coefficients of friction (μ_h=0.6-0.7). Pore pressures and stresses are assumed to vary continuously with distance from the fault core between the two stress states shown. Figure modified from Rice (1992) and Tembe et al. (2009).

Ambiguity also arises in measurements used for the heat-flow paradox itself. Heat flow measurements from deep drilling programs penetrating the active fault show elevated geotherms [91mW/m^2 at SAFOD (Williams et al., 2004) and 90mW/m^2 at Cajon pass (Sass et al., 1992)] compared with the regional average of 68-74mW/m^2 calculated from shallow boreholes (generally ~250m in depth) used to argue for the lack of a heat flow anomaly (Lachenbruch and Sass, 1980; Sass et al., 1997; Scholz, 2006).

Additionally, the heat-flow paradox assumes that heat is transported by conduction alone, and that advective heat transfer from fluid flow is not substantial enough to remove a heat flow anomaly (Lachenbruch and Sass, 1980). Models based on topographic driven groundwater flow appear to confirm this hypothesis within certain sections of the San Andreas fault (the Mojave section shows a good correlation while the Parkfield section shows inconclusive results; Saffer et al., 2003); though the models are unable to account for transient advective heat transport following an earthquake due to an increase in permeability and fluid flow from fracturing (Sibson, 1989), which could substantially alter the heat signature and permeability networks (Scholz, 2006).

6.5.2 Frictional sliding on weak phases

Upon the apparent discovery of talc in the cuttings from the main borehole (Moore and Rymer, 2007), weak phases in the actively creeping zones were used to explain the heat-flow paradox in the Parkfield area. When drill core was eventually examined, however, no talc was found (Ch. 4; Holdsworth et al., 2011; Mittempergher et al., 2011; Hadizadeh et al., 2012), shifting the conversation to the presence of concentrated smectitic clays within the actively creeping zones (Carpenter et al., 2011; Lockner et al., 2011). Smectitic clays are only stable up to temperatures of ~120°C, and

are therefore unable to explain the weakness of the San Andreas fault to greater depths (Frey and Robinson, 1999; Holdsworth et al., 2011).

6.5.3 Weakness as observed in this study

Observations in this study of the ductile S-C fabrics in the Minas fault zone, where phyllosilicate-rich lithologies are deforming through a combination of crystal plasticity and pressure solution, and contain a high percentage of chlorite and muscovite, could explain the weakness at greater depths. In addition the pressure solution processes observed in this study and by others in core from the SAFOD site (Gratier et al., 2011; Holdsworth et al., 2011; Mittempergher et al., 2011; Richard et al., 2014) indicate that pressure solution processes are active at the SAFOD site and operate at a range of depths in phyllosilicate-rich fault zones.

The strength profiles modelled in this study indicate substantial weakening within phyllosilicate-rich fault cores once a critical effective grain size has been ascertained due to concomitant pressure solution processes and frictional sliding on phyllosilicate phases with low (~0.3) coefficients of friction (Figs. 6.5-6.11). Strength and strain rate are viewed as transient processes, dependent on rates of fault healing, disaggregation, and changes in bulk rock composition as shown in plots of effective grain size (Fig. 6.8).

The relative weakness of fault zones located within fine grained sedimentary hosts may be explained by weak low-temperature clays at shallow crustal levels. At depth, once low-temperature clays have been converted to chlorite, phyllosilicate-rich fault zones likely have similar frictional characteristics to chlorite (~0.3). With progressive grain size reduction, pressure solution processes become increasingly effective within fault zones, and faster strain rates may be accommodated by combined

pressure solution processes in quartz and frictional sliding along the phyllosilicate foliae. Crystal plasticity within phyllosilicate foliae becomes operative once a given depth has been ascertained, further weakening the fault zone.

These observations do not impose a weakness on all faults, or across the entire San Andreas fault, as the pre-requisite for weakness here is a high percentage of phyllosilicates within the host lithology. Weakness is therefore implied in sections of transcurrent fault zones hosted within fine-grained sedimentary facies.

CHAPTER 7: CONCLUSIONS

Phyllosilicate-rich fault zones provide weak planes through the crust across which significant shear can be accommodated. Within the two fault zones examined, deformation has been focussed in fine-grained siltstones close to the contact with coarser sandstones (SAFOD) or volcanic units (Minas fault zone). While a decreasing grain size is known to increase the fracture strength of materials (Paterson and Wong, 2005), the weakening effects of phyllosilicates and increased efficiency of pressure solution within fine-grained samples leads to localization within these units.

At slow strain rates (*i.e.* creeping fault zones), deformation can be accommodated by a combination of processes (*e.g.* pressure solution, frictional sliding, crystal plasticity) with the strength of the material being determined primarily by the rate limiting mechanism(s). For pressure solution to be operative at a given strain rate, a critical effective grain size must be achieved, which can be calculated by plotting effective grain size *v.* strength at a specific temperature and confining pressure. When pressure solution is operative there is significant weakening when compared with Byerlee strength profiles (Byerlee, 1978; Niemeijer and Spiers, 2005). Phyllosilicates are weak compared with Byerlee coefficients of friction and show velocity strengthening behaviour (Byerlee, 1978; Ikari et al., 2011a, 2011b; Behnsen and Faulkner, 2012).

At very fast strain rates, phyllosilicate-rich fault zones show velocity weakening behaviour (Di Toro et al., 2011; French et al., 2014) indicating that an earthquake nucleated elsewhere may propagate through the creeping segment of the fault zone (Noda and Lapusta, 2013); however, geological evidence of seismicity is quickly overprinted by sub-seismic processes (Kirkpatrick and Rowe, 2013). Brittle fracture

through seismic processes and a sudden influx of fluids could lead to weakening and creep behaviour in locked segments following a seismic event (Gratier et al., 2011; Çakir et al., 2012).

At the San Andreas fault low geotherms have led many authors to invoke a weak fault in a strong crust model to explain the lack of heat flow from shear heating (Lachenbruch, 1980; Lachenbruch and Sass, 1980; Carpenter et al., 2011; Wang, 2011). Analysis of core from the SAFOD drilling program has focussed primarily on the role of foliated clays in reducing the coefficient of friction along the fault, while an absence of influxing fluids during drilling has moved the conversation away from suprahydrostatic fluid pressures. The microstructural study of core distal to the actively creeping zones presented here has shown that there is a sequence of deformation in effect. Thin veinlets of young gouge cut through older generations of healed cataclasites. Brittle fracture leads to a reduction of effective grain size in the cataclasites and the formation of gouge seams. Once a thick enough package of gouge exists and a critical effective grain size has been reached for the entrained fragments, pressure solution becomes operative. The gouge then forms S-C structures and can be seen injecting into cracks within the healed cataclasites. Enrichment in phyllosilicates can be achieved in the gouges through solid species pressure solution depletion, or through the growth of new phyllosilicate phases.

For a strain rate of $10^{-10}s^{-1}$ to be achieved through pressure solution, a critical effective grain size of ~100nm must be achieved for quartz within the two creeping segments. Grain size reduction can occur through fracturing and cataclastic flow, while fault zone healing through the deposition of hydrothermal minerals can cause an increase in effective grain size. These processes can occur cyclically and explain the generations of cataclasites observed within SAFOD core.

When pressure solution is operative in the core, the strength of quartz is greatly reduced and the strength of the fault is controlled by the frictional properties of phyllosilicates. At very shallow depths, the low friction coefficient for phyllosilicates controls fault zone weakness, while at greater depths it is controlled by crystal plasticity along the phyllosilicate foliae.

Within the Minas fault zone, at the Greville Bay study area, the S-C domain of the Nuttby Fm. shows features indicative of crystal plasticity within muscovite and chlorite. Quartz, where it exists in large packages shows evidence of concomitant grain boundary migration recrystallization and sub-grain rotation recrystallization. Within the phyllosilicate-rich packages, quartz is deforming by pressure solution as evidenced by growth dislocations and dislocation free precipitates. Chlorite geothermometry indicates that these deformation mechanisms are operating at 359+/-12°C.

Microstructures in the Fountain Lake Gp. rhyolite are also indicative of crystal plasticity, with a clear crystallographic preferred orientation and evidence of sub-grain rotation recrystallization in larger clasts of rhyolite.

An effective grain size plot for the S-C domain indicates that quartz plasticity only occurs at very low strain rates (10^{-12}-$10^{-14}s^{-1}$), while higher strain rates can be accommodated through pressure solution-accommodated creep when effective grain sizes are less than ~45µm ($10^{-10}s^{-1}$) and 5µm ($10^{-8}s^{-1}$). Within phyllosilicate packages, quartz aggregates on the order of 10-20µm are surrounded by phyllosilicate phases indicating that pressure solution-accommodated creep causes significant weakening at this site up to strain rates of ~$10^{-9}s^{-1}$.

Phyllosilicate crystallinity and chlorite geothermometry attest that the S-C domain reached deeper crustal levels than the other domains of the Nuttby Fm. to the

north of it. This is interpreted to be due to a region of transpression at Greville Bay due to a change in strike in the fault zone (from 082° to 68° as one moves west) forming a positive flower structure. The steep reverse faults have been reactivated as strike slip faults erasing the vertical kinetic history.

The units to the north of the S-C domain do not show evidence of crystal plasticity and often preserve primary features. A fine-grained carbonaceous phyllite has been tightly folded and appears to be deforming through pressure solution-accommodated creep. The foliation has not been rotated into parallelism with the main trace of the Cobequid fault indicating that it has experienced less simple shear than the other units.

A late brittle fault cuts through all the units and is ~1-2m in width. When it intersects the fine-grained Nuttby Fm., a mesocataclasite with a scaly fabric has formed. The microstructures examined indicate the existence of a foliation down to TEM-scale, and that grain size reduction has occurred by brittle processes. This fabric, commonly observed in accretionary wedge drilling projects, has often been attributed to a high concentration of smectitic clays (Lundberg and Moore, 1986; Moore et al., 1986; Kirkpatrick et al., 2015). At Greville Bay the scaly fabric has formed with phyllosilicates composed purely of muscovite and chlorite. Formation of these fabrics can occur therefore when the grain size has been reduced through brittle fracture, there is a high percentage of phyllosilicates that are weak compared to the host material, the phyllosilicates show velocity strengthening behaviour, and high fluid pressures exist. In these conditions multiple slip surfaces can accommodate deformation through continual reorganization of active surfaces (Tarling and Rowe, 2015).

By examining phyllosilicate-rich fault zones this study has shown how various deformation mechanisms can operate in conjunction with one another to weaken faults. Deformation mechanisms, in particular pressure solution, can be activated through brittle fracture, and deactivated through fault zone healing. Phyllosilicate-rich fault zones are consistently weaker than traditional strength profiles would predict.

REFERENCES

Abad, I., Murphy, J.B., Nieto, F., Gutiérrez-Alonso, G., 2010. Diagenesis to metamorphism transition in an episutural basin: the late Paleozoic St. Mary's Basin, Nova Scotia, Canada. *Canadian Journal of Earth Sciences* 47, 121–135.

Agar, S.M., Prior, D.J., Behrmann, J.H., 1989. Back-scattered electron imagery of the tectonic fabrics of some fine-grained sediments : Implications for fabric nomenclature and deformation processes. *Geology* 17, 901–904.

Anderson, E.M., 1905. The Dynamics of Faulting. *Transactions of the Edinburgh Geological Society* 8, 387–402.

Ardell, A.J., Christie, J.M., McCormick, J.W., 1974. Dislocation images in quartz and the determination of Burgers vectors. *Philosophical Magazine* 29, 1399–1411.

Ashby, M.., Verrall, R.., 1973. Diffusion-accommodated flow and superplasticity. *Acta Metallurgica* 21, 149–163.

Bailey, S.W., 1988. Chlorites: Structures and Crystal Chemistry, in: Bailey, S.W. (Ed.), Volume 19: Hydrous Phyllosilicates (exclusive of Micas). Mineralogical Society of America, Madison, Wisconsin, USA, pp. 347–404.

Beeler, N.M., Tullis, T.E., Blanpied, M.L., Weeks, J.D., 1996. Frictional behavior of large displacement experimental faults. *Journal of Geophysical Research* 101, 8697.

Behnsen, J., Faulkner, D.R., 2012. The effect of mineralogy and effective normal stress on frictional strength of sheet silicates. *Journal of Structural Geology* 42, 49–61.

Berthé, D., Choukroune, P., Jegouzo, P., 1979. Orthogneiss, mylonite and non coaxial deformation of granites: the example of the South Armorican Shear Zone. *Journal of Structural Geology* 1, 31–42.

Bleibinhaus, F., Hole, J.A., Ryberg, T., Fuis, G.S., 2007. Structure of the California Coast Ranges and San Andreas Fault at SAFOD from seismic waveform inversion and reflection imaging. *Journal of Geophysical Research: Solid Earth* 112, 1–15.

Borg, I.Y., Heard, H.C., 1969. Mechanical twinning and slip in experimentally deformed plagioclases. *Contributions to Mineralogy and Petrology* 23, 128–135.

Bos, B., Spiers, C.J., 2001. Experimental investigation into the microstructural and mechanical evolution of phyllosilicate-bearing fault rock under conditions favouring pressure solution. *Journal of Structural Geology* 23, 1187–1202.

Bos, B., Spiers, C.J., 2002. Frictional-viscous flow of phyllosilicate-bearing fault rock: Microphysical model and implications for crustal strength profiles. *Journal of Geophysical Research* 107.

Boullier, A.M., Gueguen, Y., 1975. SP-Mylonites: Origin of some mylonites by superplastic flow. *Contributions to Mineralogy and Petrology* 50, 93–104.

Bradbury, K.K., Barton, D.C., Solum, J.G., Draper, S.D., Evans, J.P., 2007. Mineralogic and textural analyses of drill cuttings from the San Andreas Fault Observatory at Depth (SAFOD) boreholes: Initial interpretations of fault zone composition and constraints on geologic models. *Geosphere* 3, 299–318.

Bradbury, K.K., Evans, J.P., Chester, J.S., Chester, F.M., Kirschner, D.L., 2011. Lithology and internal structure of the San Andreas fault at depth based on characterization of Phase 3 whole-rock core in the San Andreas Fault Observatory at Depth (SAFOD) borehole. *Earth and Planetary Science Letters* 310, 131–144.

Brune, J.N., Henyey, T.L., Roy, R.F., 1969. Heat flow, stress, and rate of slip along the San Andreas Fault, California. *Journal of Geophysical Research* 74, 3821–3827.

Byerlee, J., 1978. Friction of rocks. *Pure and Applied Geophysics* 116, 615–626.

Caine, J.S., Evans, J.P., Forster, C.B., 1996. Fault zone architechture and permeability structure. *Geology* 24, 1025–1028.

Çakir, Z., Ergintav, S., Özener, H., Dogan, U., Akoglu, A.M., Meghraoui, M., Reilinger, R., 2012. Onset of aseismic creep on major strike-slip faults. *Geology* 40, 1115–1118.

Calder, J.H., 1998. The Carboniferous evolution of Nova Scotia. *Geological Society, London, Special Publications* 143, 261–302.

Carpenter, B.M., Marone, C., Saffer, D.M., 2009. Frictional behavior of materials in the 3D SAFOD volume. *Geophysical Research Letters* 36, 1–5.

Carpenter, B.M., Marone, C., Saffer, D.M., 2011. Weakness of the San Andreas Fault revealed by samples from the active fault zone. *Nature Geoscience* 4, 251–254.

Carter, C.B., Kohlstedt, D.L., 1981. Electron irradiation damage in natural quartz grains. *Physics and Chemistry of Minerals* 7, 110–116.

Cathelineau, M., 1988. Cation site occupancy in chlorites and illites as a function of temperature. *Clay Minerals* 23, 471–485.

Chandler, F.W., Sullivan, R.W., Currie, K.L., 1987. The age of the Springdale Group, western Newfoundland, and correlative rocks—evidence for a Llandovery overlap

assemblage in the Canadian Appalachians. *Transactions of the Royal Society of Edinburgh: Earth Sciences* 78, 41–49.

Chen, Y., Sammis, C.G., 2003. Asperity models for earthquakes. *Bulletin of the Seismological Society of America* 93, 1792–1802.

Chester, F.M., Chester, J.S., 1998. Ultracataclasite structure and friction processes of the Punchbowl fault, San Andreas system, California. *Tectonophysics* 295, 199–221.

Chester, F.M., Logan, J.M., 1986. Implications for mechanical properties of brittle faults from observations of the Punchbowl Fault Zone, California. *Pure and Applied Geophysics* 124, 79–106.

Coble, R.L., 1963. A Model for Boundary Diffusion Controlled Creep in Polycrystalline Materials. *Journal of Applied Physics* 34, 1679–1682.

Collettini, C., Niemeijer, A., Viti, C., Marone, C., 2009. Fault zone fabric and fault weakness. *Nature* 462, 907–910.

Curtis, C.D., Hughes, C.R., Whiteman, J.A., Whittle, C.K., 1985. Compositional Variation within Some Sedimentary Chlorites and Some Comments on Their Origin. *Mineralogical Magazine* 49, 375–386.

Dalla, T.M., Livi, K.J.T., Frey, M., 1996. Chlorite textures and compositions from high-pressure/ low-temperature metashales and metagraywackes, Franciscan Complex, Diablo Range, California, USA. *European Journal of Mineralogy* 8, 825–846.

Di Toro, G., Han, R., Hirose, T., De Paola, N., Nielsen, S., Mizoguchi, K., Ferri, F., Cocco, M., Shimamoto, T., 2011. Fault lubrication during earthquakes. *Nature* 471, 494–498.

Di Toro, G., Mittempergher, S., Ferri, F., Mitchell, T.M., Pennacchioni, G., 2012. The contribution of structural geology, experimental rock deformation and numerical modelling to an improved understanding of the seismic cycle. Preface to the Special Volume "Physico-chemical processes in seismic faults." *Journal of Structural Geology* 38, 3–10.

Doan, M.-L., Gary, G., 2009. Rock pulverization at high strain rate near the San Andreas fault. *Nature Geoscience* 2, 709–712.

Donohoe, H.V.J., Wallace, P.I., 1982. Geological Map of the Cobequid Highlands. Colchester Cumberland and Pictou counties. *Nova Scotia Department of Energy and Mines* Map 82-06.

Douglas, L.A., 1989. Vermiculites, in: Dixon, J.B., Weed, S.B. (Eds.), Minerals in Soil Environments. Soil Science Society of America Book Series, Soil Science Society of America, Madison, WI, pp. 625–674.

Durling, P., Marillier, F., 1993. Tectonic setting of Middle Devonian to Lower Carboniferous rocks in the Magdalen Basin. *Atlantic Geology* 29, 199–217.

Ellsworth, W.L., Malin, P.E., 2011. Deep rock damage in the San Andreas Fault revealed by P- and S-type fault-zone-guided waves. *Geological Society, London, Special Publications* 359, 39–53.

Fagereng, Å., 2013. On stress and strain in a continuous-discontinuous shear zone undergoing simple shear and volume loss. *Journal of Structural Geology* 50, 44–53.

Fagereng, Å., Cooper, A.F., 2010. The metamorphic history of rocks buried, accreted and exhumed in an accretionary prism: An example from the Otago Schist, New Zealand. *Journal of Metamorphic Geology* 28, 935–954.

Fagereng, Å., Sibson, R.H., 2010. Mélange rheology and seismic style. *Geology* 38, 751–754.

Faulkner, D.R., Jackson, C.A.L., Lunn, R.J., Schlische, R.W., Shipton, Z.K., Wibberley, C.A.J., Withjack, M.O., 2010. A review of recent developments concerning the structure, mechanics and fluid flow properties of fault zones. *Journal of Structural Geology* 32, 1557–1575.

Faulkner, D.R., Lewis, A.C., Rutter, E.H., 2003. On the internal structure and mechanics of large strike-slip fault zones: Field observations of the Carboneras fault in southeastern Spain. *Tectonophysics* 367, 235–251.

Faulkner, D.R., Mitchell, T.M., Rutter, E.H., Cembrano, J., 2008. On the structure and mechanical properties of large strike-slip faults. *Geological Society, London, Special Publications* 299, 139–150.

Fenton, C.R., Webb, R.H., Pearthree, P.A., Cerling, T.E., Poreda, R.J., 2001. Displacement rates on the Toroweap and Hurricane faults: Implications for Quaternary downcutting in the Grand Canyon, Arizona. *Geology* 29, 1035–1038.

Frank, F.C., Read, W.T., 1950. Multiplication processes for slow moving dislocations. *Physical Review* 79, 722–723.

French, M.E., Kitajima, H., Chester, J.S., Chester, F.M., Hirose, T., 2014. Displacement and dynamic weakening processes in smectite-rich gouge from the Central Deforming Zone of the San Andreas Fault. *Journal of Geophysical Research: Solid Earth* 119, 1777–1802.

Frey, M., Robinson, D., 1999. Low Temperature Metamorphism. Blackwell Science, Cambridge.

Frimmel, H.E., 1997. Chlorite Thermometry in the Witwatersrand Basin: Constraints on the Paleoproterozoic Geotherm in the Kaapvaal Craton, South Africa. *The Journal of Geology* 105, 601–616.

Gibbons, W., Doig, R., Gordon, T., Murphy, B., Reynolds, P., White, J.C., 1996. Mylonite to megabreccia: Tracking fault events within a transcurrent terrane boundary in Nova Scotia, Canada. *Geology* 24, 411–414.

Gifkins, R.C., 1976. Grain-boundary sliding and its accommodation during creep and superplasticity. *Metallurgical Transactions* 7A, 1225–1232.

Gleason, G.C., Tullis, J., 1995. A flow law for dislocation creep of quartz aggregates determined with the molten salt cell. *Tectonophysics* 247, 1–23.

Gratier, J.P., Guiguet, R., Renard, F., Jenatton, L., Bernard, D., 2009. A pressure solution creep law for quartz from indentation experiments. *Journal of Geophysical Research* 114, 1–16.

Gratier, J.P., Renard, F., Labaume, P., 1999. How pressure solution creep and fracturing processes interact in the upper crust to make it behave in both a brittle and viscous manner. *Journal of Structural Geology* 21, 1189–1197.

Gratier, J.P., Richard, J., Renard, F., Mittempergher, S., Doan, M.L., Di Toro, G., Hadizadeh, J., Boullier, a. M., 2011. Aseismic sliding of active faults by pressure solution creep: Evidence from the San Andreas fault observatory at Depth. *Geology* 39, 1131–1134.

Griggs, D., 1967. Hydrolytic weakening of quartz and other silicates. *Geophysical Journal of the Royal Astronomical Society* 14, 19–31.

Hadizadeh, J., Mittempergher, S., Gratier, J.P., Renard, F., Di Toro, G., Richard, J., Babaie, H.A., 2012. A microstructural study of fault rocks from the SAFOD: Implications for the deformation mechanisms and strength of the creeping segment of the San Andreas Fault. *Journal of Structural Geology* 42, 246–260.

Hamilton, M.A., Murphy, J.B., 2004. Tectonic significance of a Llanvirn age for the Dunn Point volcanic rocks, Avalon terrane, Nova Scotia, Canada: Implications for the evolution of the Iapetus and Rheic Oceans. *Tectonophysics* 379, 199–209.

Hardebeck, J.L., Michael, A.J., 2004. Stress orientations at intermediate angles to the San Andreas Fault, California. *Journal of Geophysical Research: Solid Earth: Solid Earth* 109, 1–16.

Herring, C., 1950. Diffusional viscosity of a polycrystalline solid. *Journal of Applied Physics* 21, 437–445.

Hibbard, J.P., Van Staal, C.R., Rankin, D.W., Williams, H., 2006. Lithotectonic map of the Appalachian Orogen, Canada-United States of America. *Geological Survey of Canada* Map 2096A,.

Hickman, S., Zoback, M., 2004. Stress orientations and magnitudes in the SAFOD pilot hole. *Geophysical Research Letters* 31, 13–16.

Hickman, S.H., Evans, B., 1995. Kinetics of pressure solution at halite-silica interfaces and intergranular clay films. *Journal of Geophysical Research* 100, 13113.

Hillier, S., Velde, B., 1991. Octahedral Occupancy and the Chemical Composition of Diagenetic (Low-Temperature) Chlorites. *Clay Minerals* 26, 149–168.

Hiraga, T., Miyazaki, T., Yoshida, H., Zimmerman, M.E., 2013. Comparison of microstructures in superplastically deformed synthetic materials and natural mylonites: Mineral aggregation via grain boundary sliding. *Geology* 41, 959–962.

Hirth, G., Tullis, J., 1992. Dislocation creep regimes in quartz aggregates. *Journal of Structural Geology* 14, 145–159.

Hirth, J.P., Lothe, J., 1982. Theory of Dislocations, 2nd ed. Wiley-Interscience, New York.

Holdsworth, R.E., van Diggelen, E.W.E., Spiers, C.J., de Bresser, J.H.P., Walker, R.J., Bowen, L., 2011. Fault rocks from the SAFOD core samples: Implications for weakening at shallow depths along the San Andreas Fault, California. *Journal of Structural Geology* 33, 132–144.

Hubbert, M.K., Rubey, W.W., 1959. Role of fluid pressure in mechanics of overthrust faulting: I. Mechanics of fluid-filled porous solids and its application to overthrust faulting. *Bulletin of the Geological Society of America* 70, 115–166.

Hutchinson, D.R., Klitgord, K.D., Lee, M.W., Trehu, A.M., 1988. U.S. Geological Survey deep seismic reflection profile across the Gulf of Maine. *GSA Bulletin* 100, 172–184.

Ikari, M.J., Marone, C., Saffer, D.M., 2011a. On the relation between fault strength and frictional stability. *Geology* 39, 83–86.

Ikari, M.J., Niemeijer, A.R., Marone, C., 2011b. The role of fault zone fabric and lithification state on frictional strength, constitutive behavior, and deformation microstructure. *Journal of Geophysical Research: Solid Earth* 116, 1–25.

Ikari, M.J., Saffer, D.M., Marone, C., 2009. Frictional and hydrologic properties of clay-rich fault gouge. *Journal of Geophysical Research: Solid Earth* 114, 1–18.

Imber, J., Holdsworth, R.E., Smith, S.A.F., Jefferies, S.P., Collettini, C., 2008. Frictional-viscous flow, seismicity and the geology of weak faults: a review and future directions. *Geological Society, London, Special Publications* 299, 151–173.

Ingamells, C.O., 1980. Microprobe Column. *Geostandards Newsletter* 4, 139.

Ingamells, C.O., Engels, J.C., 1976. Preparation, analysis, and sampling constants for a biotite, in: National Bureau of Standards Special Publication 422. pp. 401–419.

Inoue, A., Meunier, A., Patrier-Mas, P., Rigault, C., Beaufort, D., Vieillard, P., 2009. Application of chemical geothermometry to low-temperature trioctahedral chlorites. *Clays and Clay Minerals* 57, 371–382.

Janssen, C., Kanitpanyacharoen, W., Wenk, H.R., Wirth, R., Morales, L., Rybacki, E., Kienast, M., Dresen, G., 2012. Clay fabrics in SAFOD core samples. *Journal of Structural Geology* 43, 118–127.

Jaoul, O., Tullis, J., Kronenberg, A., 1984. The effect of varying water contents on the creep behaviour of Heavitree quartzite. *Journal of Geophysical Research* 89, 4298–4312.

Jarosewich, E., Nelen, J.A., Norberg, J.A., 1980a. Reference Samples for Electron Microprobe Analysis. *Geostandards Newsletter* 4, 43–47.

Jarosewich, E., Nelen, J.A., Norberg, J.A., 1980b. Corrections. *Geostandards Newsletter* 4, 257–258.

Jefferies, S.P., Holdsworth, R.E., Wibberley, C. a J., Shimamoto, T., Spiers, C.J., Niemeijer, a. R., Lloyd, G.E., 2006. The nature and importance of phyllonite development in crustal-scale fault cores: An example from the Median Tectonic Line, Japan. *Journal of Structural Geology* 28, 220–235.

Kameda, J., Shimizu, M., Ujiie, K., Hirose, T., Ikari, M., Mori, J., Oohashi, K., Kimura, G., 2015. Pelagic smectite as an important factor in tsunamigenic slip along the Japan Trench. *Geology* 43, 155–158.

Karato, S., 2012. Deformation of Earth Materials. Cambridge University Press, Cambridge.

Keen, C.E., Kay, W.A., Keppie, D., Marillier, F., Pe-Piper, G., Waldron, J.W.F., 1991. Deep seismic reflection data from the Bay of Fundy and Gulf of Maine: tectonic implications for the northern Appalachians. *Canadian Journal of Earth Sciences* 28, 1096–1111.

Kekulawala, K.R.S.S., Paterson, M.S., Boland, J.N., 1978. Hydrolytic weakening in quartz. *Tectonophysics* 46, T1–T6.

Keppie, J.D., 1982. The Minas Geofracture, in: Major Structural Zones of the Canadian Appalachians. Geological Association of Canada Special Paper. pp. 263–280.

Keppie, J.D., 2000. Digital Version of Nova Scotia Department of Natural Resources Map ME 2000-1, Geological Map of the Province of Nova Scotia. *Department of Natural Resources* scale1:500 000.

Keppie, J.D., Dostal, J., Murphy, J.B., Cousens, B.L., 1997. Palaeozoic within-plate volcanic rocks in Nova Scotia (Canada) reinterpreted; isotopic constraints on magmatic source and palaeocontinental reconstructions. *Geological Magazine* 134, 425–447.

Kim, W.Y., 2013. Induced seismicity associated with fluid injection into a deep well in Youngstown, Ohio. *Journal of Geophysical Research: Solid Earth* 118, 3506–3518.

Kirkpatrick, J.D., Rowe, C.D., 2013. Disappearing ink: How pseudotachylytes are lost from the rock record. *Journal of Structural Geology* 52, 183–198.

Kirkpatrick, J.D., Rowe, C.D., Ujiie, K., Moore, J.C., Regalla, C., Remitti, F., Toy, V., Kameda, J., Bose, S., Chester, F.M., 2015. Structure and lithology of the Japan Trench subduction plate boundary fault. *Tectonics* 34, 53–69.

Kisch, H.J., 1991. Illite crystallinity: recommendations on sample preparation, X-ray diffraction settings, and interlaboratory samples. *Journal of Metamorphic Geology* 9, 665–670.

Kisch, H.J., Arkai, P., Brime, C., 2004. On the calibration of the illite Kubler index (illite "crystallinity"). *Schweizerische Mineralogische und Petrographische Mitteilungen* 84, 323–331.

Knipe, R.J., 1989. Deformation mechanisms — recognition from natural tectonites. *Journal of Structural Geology* 11, 127–146.

Kohlstedt, D.L., Evans, B., Mackwell, S.J., 1995. Strength of the lithosphere: Constraints imposed by laboratory experiments. *Journal of Geophysical Research: Solid Earth* 100, 17587–17602.

Kranz, R.L., 1980. The effects of confining pressure and stress difference on static fatigue of granite. *Journal of Geophysical Research* 85, 1854–1866.

Kretz, R., 1983. Symbols for rock-forming minerals. *American Mineralogist* 68, 277–279.

Kronenberg, A.K., Kirby, S.H., Pinkston, J., 1990. Basal slip and mechanical anisotropy of biotite. *Journal of Geophysical Research* 95, 19,257 – 19,278.

Kronenberg, A.K., Tullis, J., 1984. Flow strengths of quartz aggregates: Grain size and pressure effects due to hydrolytic weakening. *Journal of Geophysical Research* 89, 4281.

Kübler, B., 1984. Les indicateurs des transformations physiques et chimiques dans la diagenese, temperature et calorimetrie, in: Lagoche, M. (Ed.), Termometrie et Barometrie Geologiques. Soc. Francais Mineralogie et Cristallographie, Paris, pp. 489–596.

Labaume, P., Maltman, A.J., Bolton, A., Tessier, D., Ogawa, Y., Takizawa, S., 1997. Scaly Fabrics in Sheared Clays from the Décollement Zone of the Barbados Accretionary Prism. *Proceedings of the Ocean Drilling Program, Scientific Results* 156.

Lachenbruch, A.H., 1980. Frictional heating, fluid pressure, and the resistance to fault motion. *Journal of Geophysical Research* 85, 6097.

Lachenbruch, A.H., Sass, J.H., 1980. Heat flow and energetics of the San Andreas fault zone. *Journal of Geophysical Research* 85, 6185–6222.

Landing, E., 1996. Avalon: Insular continent by the latest Precambrian. *Geological Society of America Special Papers* 304, 29–63.

Langdon, T.G., 2006. Grain boundary sliding revisited: Developments in sliding over four decades. *Journal of Materials Science* 41, 597–609.

Lockner, D.A., Beeler, N.M., 2002. Rock failure and earthquakes, in: Lee, W.H.K., Kanamori, H., Jennings, P.C., Kisslinger, C. (Eds.), International Handbook of Earthquake and Engineering Seismology. International Geophysics, pp. 505–537.

Lockner, D.A., Morrow, C., Moore, D., Hickman, S., 2011. Low strength of deep San Andreas fault gouge from SAFOD core. *Nature* 472, 82–85.

Logan, J.M., Dengo, C.A., Higgs, N.G., Wang, Z.Z., 1992. Fabrics of Experimental Fault Zones: Their Development and Relationship to Mechanical Behavior, in: Evans, B., Wong, T.F. (Eds.), Fault Mechanics and Transport Properties of Rocks. International Geophysics, pp. 33–67.

Luan, F.C., Paterson, M.S., 1992. Preparation and deformation of synthetic aggregates of quartz. *Journal of Geophysical Research* 97, 301.

Lundberg, N., Moore, J.C., 1986. Macroscopic structural features in Deep Sea Drilling Project cores from forearc regions. *Geological Society of America Memoirs* 166, 13–44.

MacInnes, E.A., 2005. Structural and Kinematic Evolution of a Segment of the Minas Fault System, Nova Scotia, Canada. Ph.D. Thesis, University of New Brunswick.

MacInnes, E.A., White, J.C., 2004. Geometric and kinematic analysis of a transpression terrane boundary: Minas fault system, Nova Scotia, Canada. *Geological Society, London, Special Publications* 224, 201–214.

Manga, M., 1998. Advective heat transport by low-temperature discharge in the Oregon Cascades. *Geology* 26, 799–802.

Mares, V.M., Kronenberg, A.K., 1993. Experimental deformation of muscovite. *Journal of Structural Geology* 15, 1061–1075.

Martel, A.T., Gibling, M.R., 1996. Stratigraphy and tectonic history of the Devonian to Lower Carboniferous Horton Bluff Formation, Nova Scotia. *Atlantic Geology* 32, 13–38.

Massonne, H.-J., Szpurka, Z., 1997. Thermodynamic properties of white micas on the basis of high-pressure experiments in the systems K2O-MgO-Al2O3-SiO2-H2O and K2O-FeO-Al2O3-SiO2-H2O. *Lithos* 41, 229–250.

Mawer, C.K., White, J.C., 1987. Sense of displacement on the Cobequid–Chedabucto fault system, Nova Scotia, Canada. *Canadian Journal of Earth Sciences* 24, 217–223.

McLaren, A.C., Cook, R.F., Hyde, S.T., Tobin, R.C., 1983. The mechanisms of the formation and growth of water bubbles and associated dislocation loops in synthetic quarz. *Physics and Chemistry of Minerals.* 9, 79–94.

Mitchell, T.M., Faulkner, D.R., 2009. The nature and origin of off-fault damage surrounding strike-slip fault zones with a wide range of displacements: A field study from the Atacama fault system, northern Chile. *Journal of Structural Geology* 31, 802–816.

Mittempergher, S., Di Toro, G., Gratier, J.P., Hadizadeh, J., Smith, S.A.F., Spiess, R., 2011. Evidence of transient increases of fluid pressure in SAFOD phase III cores. *Geophysical Research Letters* 38, 4–9.

Moore, D.E., 2014. Comparative mineral chemistry and textures of SAFOD fault gouge and damage-zone rocks. *Journal of Structural Geology* 68, 82–96.

Moore, D.E., Rymer, M.J., 2007. Talc-bearing serpentinite and the creeping section of the San Andreas fault. *Nature* 448, 795–797.

Moore, D.M., Reynolds, R.C., 1997. X-Ray Diffraction and the Identification and Analysis of Clay Minerals, 2nd ed. Oxford University Press.

Moore, J.C., Roeske, S., Cowan, D.S., Lundberg, N., Gonzales, E., Schoonmaker, J., Lucas, S.E., 1986. Scaly fabrics from deep sea drilling project cores from forearcs. *Geological Society of America Memoirs* 166, 55–74.

Mount, V.S., Suppe, J., 1987. State of stress near the San Andreas fault: Implications for wrench tectonics. *Geology* 15, 1143–1146.

Mount, V.S., Suppe, J., 1992. Present-day stress orientations adjacent to active strike-slip faults: California and Sumatra. *Journal of Geophysical Research* 97, 11995.

Murphy, J.B., 2003. Late Palaeozoic formation and development of the St Marys Basin, mainland Nova Scotia, Canada: a prolonged record of intracontinental strike-slip deformation during the assembly of Pangaea. *Geological Society, London, Special Publications* 210, 185–196.

Murphy, J.B., Collins, A.S., 2008. 40Ar-39Ar white mica ages reveal Neoproterozoic/Paleozoic provenance and an Alleghanian overprint in coeval Upper Ordovician-Lower Devonian rocks of Meguma and Avalonia. *Tectonophysics* 461, 265–276.

Murphy, J.B., Fernández-Suárez, J., Keppie, J.D., Jeffries, T.E., 2004. Contiguous rather than discrete Paleozoic histories for the Avalon and Meguma terranes based on detrital zircon data. *Geology* 32, 585–588.

Murphy, J.B., Keppie, J.D., 1998. Late Devonian palinspastic reconstruction of the Avalon-Meguma terrane boundary: implications for terrane accretion and basin development in the Appalachian orogen. *Tectonophysics* 284, 221–231.

Murphy, J.B., Keppie, J.D., Nance, R.D., 1999. Fault reactivation within Avalonia: Plate margin to continental interior deformation. *Tectonophysics* 305, 183–204.

Murphy, J.B., Nance, D.R., Keppie, J.D., 2002. Discussion and reply : West African proximity of the Avalon terrane in the latest Precambrian. *Geological Society of America Bulletin* 114, 1049–1051.

Murphy, J.B., Rice, R.J., Stokes, T.R., Keppie, D.F., 1995. The St Mary's basin, central mainland Nova Scotia: late Paleozoic basin formation and deformation along the Avalon-Meguma terrane boundary, Canadian Appalachians, in: Hibbard, J.P., Van Staal, C.R., Cawood, P. (Eds.), New Perspectives in the Caledonian-Appalachian Orogen. Geological Association of Canada Special Paper, pp. 409–420.

Murphy, J.B., Waldron, J.W.F., Kontak, D.J., Pe-Piper, G., Piper, D.J.W., 2011. Minas Fault Zone: Late Paleozoic history of an intra-continental orogenic transform fault in the Canadian Appalachians. *Journal of Structural Geology* 33, 312–328.

Nabarro, F.R.N., 1948. Report of a Conference on the Strength of Solids, in: Physical Society, London. p. 75.

New Brunswick Department of Energy and Resources, 2000. Bedrock Geology of New Brunswick. *Minerals and Energy Division* Map NR-1.

Niemeijer, A.R., Spiers, C.J., 2005. Influence of phyllosilicates on fault strength in the brittle-ductile transition: insights from rock analogue experiments. *Geological Society, London, Special Publications* 245, 303–327.

Noda, H., Lapusta, N., 2013. Stable creeping fault segments can become destructive as a result of dynamic weakening. *Nature* 493, 518–21.

Orowan, E., 1934. Zur Kristallplastizität II: Die dynamische Auffassung der Kristallplasticität. *Zeitschrift für Physik* 89, 614–633.

Passchier, C.W., Trouw, R.A.J., 2005. Microtectonics, 2nd ed. Springer, Berlin.

Paterson, M.S., 1958. Experimental Deformation and Faulting in Wombeyan Marble. *Bulletin of the Geological Society of America* 69, 465–476.

Paterson, M.S., 1989. The interaction of water with quartz and its influence in dislocation flow - an overview, in: Karato, S., Toriumi, M. (Eds.), Rheology of Solids and of the Earth. Oxford University Press, London, pp. 107–142.

Paterson, M.S., 2013. Materials Science for Structural Geology. Springer, New York.

Paterson, M.S., Wong, T.F., 2005. Experimental Rock Deformation - The Brittle Field. Springer-Verlag, Heidelberg.

Peierls, R., 1940. The size of a dislocation. *Proceedings of the Physical Society* 52, 34–37.

Pe-Piper, G., Cormier, R.F., Piper, D.J.W., 1989. The age and significance of Carboniferous plutons of the western Cobequid Highlands, Nova Scotia. *Canadian Journal of Earth Sciences* 26, 1297–1307.

Pe-Piper, G., Jansa, L.F., 1999. Pre-Mesozoic basement rocks offshore Nova Scotia, Canada: New constraints on the accretion history of the Meguma terrane. *Bulletin of the Geological Society of America* 111, 1773–1791.

Pe-Piper, G., Piper, D.J.W., 2002. A synopsis of the geology of the Cobequid Highlands. *Atlantic Geology* 38, 145–160.

Pe-Piper, G., Piper, D.J.W., 2005. Bedrock geology map of the Cape Chignecto area, Cobequid Highlands, Nova Scotia. *Nova Scotia Department of Natural Resources* Open File, scale 1:50 000.

Poppe, L.J., Paskevich, V.F., Hathaway, J.C., Blackwood, D.S., 2001. A Laboratory Manual for X-Ray Powder Diffraction. *U. S. Geological Survey Open-File Report 01-041* 88.

Potel, S., Mählmann, R.F., Stern, W.B., Mullis, J., Frey, M., 2006. Very low-grade metamorphic evolution of pelitic rocks under high-pressure/low-temperature conditions, NW New Caledonia (SW Pacific). *Journal of Petrology* 47, 991–1015.

Prior, D.J., Behrmann, J.H., 1990. Thrust-related mudstone fabrics from the Barbados Forearc: A backscattered scanning electron microscope study. *Journal of Geophysical Research* 95, 9055.

Raleigh, C.B., Healy, J.H., Bredehoeft, J.D., 1976. An experiment in earthquake control at Rangely, Colorado. *Science* 191, 1230–1237.

Reches, Z., Dewers, T.A., 2005. Gouge formation by dynamic pulverization during earthquake rupture. *Earth and Planetary Science Letters* 235, 361–374.

Renard, F., Gratier, J.P., Jamtveit, B., 2000. Kinetics of crack-sealing, intergranular pressure solution, and compaction around active faults. *Journal of Structural Geology* 22, 1395–1407.

Renard, F., Ortoleva, P., Gratier, J.P., 1997. Pressure solution in sandstones: influence of clays and dependence on temperature and stress. *Tectonophysics* 280, 257–266.

Renard, F., Park, A., Ortoleva, P., Gratier, J.P., 1999. An integrated model for transitional pressure solution in sandstones. *Tectonophysics* 312, 97–115.

Rice, J.R., 1992. Fault stress states, pore pressure distributions, and the weakness of the San Andreas fault, in: Evans, B., Wong, T.F. (Eds.), Fault Mechanics and Transport Properties of Rocks. Academic Press, San Diego, pp. 475–504.

Richard, J., Gratier, J., Doan, M.L., Boullier, A., Renard, F., 2014. Rock and mineral transformations in a fault zone leading to permanent creep: Interactions between brittle and viscous mechanisms in the San Andreas Fault. *Journal of Geophysical Research* 119, 8132–8153.

Rosen, P., Werner, C., Fielding, E., Hensley, S., Buckley, S., Vincent, P., 1998. Aseismic creep along the San Andreas Fault northwest of Parkfield, CA measured by radar interferometry. *Geophysical Research Letters*.

Rowe, C.D., Meneghini, F., Moore, J.C., 2011. Textural record of the seismic cycle: strain-rate variation in an ancient subduction thrust. *Geological Society, London, Special Publications* 359, 77–95.

Rutter, E.H., 1974. The influence of temperature, strain rate, and intrastitial water in the experimental deformation of calcite rocks. *Tectonophysics* 22, 311–334.

Rutter, E.H., 1983. Pressure solution in nature, theory and experiment. *Journal of the Geological Society* 140, 725–740.

Rutter, E.H., 1986. On the nomenclature of mode of failure transitions in rocks. *Tectonophysics* 122, 381–387.

Rutter, E.H., Hackston, A.J., Yeatman, E., Brodie, K.H., Mecklenburgh, J., May, S.E., 2013. Reduction of friction on geological faults by weak-phase smearing. *Journal of Structural Geology* 51, 52–60.

Rutter, E.H., Maddock, R.H., Hall, S.H., White, S.H., 1986. Comparative microstructures of natural and experimentally produced clay-bearing fault gouges. *Pure and Applied Geophysics* 124, 3–30.

Rutter, E.H., Mainprice, D.H., 1978. The effect of water on stress relaxation of faulted and unfaulted sandstone. *Pure and Applied Geophysics* 116, 634–654.

Rutter, E.H., Wanten, P.H., 2000. Experimental Study of the Compaction of Phyllosilicate-Bearing Sand at Elevated Temperature and with Controlled Pore Water Pressure. *Journal of Sedimentary Research* 70, 107–116.

Ryan, R.J., Boehner, R.C., 1990. Cumberland Basin Geology Map, Apple River and Cape Chignecto. *Nova Scotia Department of Natural Resources* DP ME 32,.

Saffer, D.M., Bekins, B.A., Hickman, S., 2003. Topographically driven groundwater flow and the San Andreas heat flow paradox revisited. *Journal of Geophysical Research* 108, 1–14.

SAFOD, 2010. The core atlas (version 4) available from http://www.earthscope.org/es_doc/data/safod/Core%20Photo%20Atlas%20v4.pdf.

Sass, J.H., Lachenbruch, A.H., Moses, T.H., Morgan, P., 1992. Heat flow from a scientific research well at Cajon Pass, California. *Journal of Geophysical Research* 97, 5017–5030.

Sass, J.H., Williams, C.F., Lachenbruch, A.H., Galanis, S.P., Grubb, F.V., 1997. Thermal regime of the San Andreas Fault near Parkfield, California. *Journal of Geophysical Research* 102, 27,575–27,585.

Schleicher, A.M., van der Pluijm, B.A., Warr, L.N., 2010. Nanocoatings of clay and creep of the San Andreas fault at Parkfield, California. *Geology* 38, 667–670.

Schleicher, A.M., Warr, L.N., van der Pluijm, B.A., 2009. On the origin of mixed-layered clay minerals from the San Andreas Fault at 2.5-3 km vertical depth (SAFOD drillhole at Parkfield, California). *Contributions to Mineralogy and Petrology* 157, 173–187.

Scholz, C.H., 2000. Evidence for a strong San Andreas fault. *Geology* 28, 163–166.

Scholz, C.H., 2006. The strength of the San Andreas Fault: A critical analysis, in: Abercrombie, R., McGarr, A., Kanamori, H., Di Toro, G. (Eds.), Earthquakes: Radiated Energy and the Physics of Faulting. American Geophysical Union, Washington, DC, pp. 301–312.

Schoonmaker, J., 1986. Clay mineralogy and diagenesis of sediments from deformation zones in the Barbados accretionary wedge (Deep Sea Drilling Project Leg 78A). *Geological Society of America Memoirs* 166, 105–116.

Sibson, R.H., 1974. Frictional constraints on thrust, wrench and normal faults. *Nature* 249, 542–544.

Sibson, R.H., 1977. Fault rocks and fault mechanisms. *Journal of the Geological Society* 133, 191–213.

Sibson, R.H., 1982. Fault zone model, heat flow, and the depth distribution of earthquakes in the continental crust of the United States. *Bulletin of the Seismological Society of America* 72, 151–163.

Sibson, R.H., 1983. Continental fault structure and the shallow earthquake source. *Journal of the Geological Society* 140, 741–767.

Sibson, R.H., 1989. Earthquake faulting as a structural process. *Journal of Structural Geology* 11, 1–14.

Sibson, R.H., 1992. Implications of fault-valve behaviour for rupture nucleation and recurrence. *Tectonophysics* 211, 283–293.

Solum, J.G., Hickman, S.H., Lockner, D.A., Moore, D.E., van Der Pluijm, B.A., Schleicher, A.M., Evans, J.P., 2006. Mineralogical characterization of protolith and fault rocks from the SAFOD Main Hole. *Geophysical Research Letters* 33, 1–5.

Stipp, M., Stünitz, H., Heilbronner, R., Schmid, S.M., 2002. The eastern Tonale fault zone: A "natural laboratory" for crystal plastic deformation of quartz over a temperature range from 250 to 700 °C. *Journal of Structural Geology* 24, 1861–1884.

Streitz, R., Sherburne, R., 1980. Studies of the San Andreas Fault Zone in Northern California. California Division of Mines and Geology, Sacremento.

Suppe, J., 2014. Fluid overpressures and strength of the sedimentary upper crust. *Journal of Structural Geology* 69, 481–492.

Tarling, M.S., Rowe, C.D., 2015. Shear strain distribution in scaly fabrics. *Submitted*.

Tembe, S., Lockner, D., Wong, T.F., 2009. Constraints on the stress state of the San Andreas Fault with analysis based on core and cuttings from San Andreas Fault Observatory at Depth (SAFOD) drilling phases 1 and 2. *Journal of Geophysical Research: Solid Earth* 114, 1–21.

Tembe, S., Lockner, D.A., Wong, T.F., 2010. Effect of clay content and mineralogy on frictional sliding behavior of simulated gouges: Binary and ternary mixtures of quartz, illite, and montmorillonite. *Journal of Geophysical Research: Solid Earth* 115, 1–22.

Tesei, T., Collettini, C., Carpenter, B.M., Viti, C., Marone, C., 2012. Frictional strength and healing behavior of phyllosilicate-rich faults. *Journal of Geophysical Research: Solid Earth* 117, 1–13.

Titus, S.J., DeMets, C., Tikoff, B., 2006. Thirty-five-year creep rates for the creeping segment of the San Andreas fault and the effects of the 2004 Parkfield earthquake: Constraints from alignment arrays, continuous global positioning system, and creepmeters. *Bulletin of the Seismological Society of America* 96, 250–268.

Townend, J., Zoback, M.D., 2000. How faulting keeps the crust strong. *Geology* 28, 399–402.

Tullis, J., Yund, R.A., 1989. Hydrolytic weakening of quartz aggregates: The effects of water and pressure on recovery. *Geophysical Research Letters* 16, 1343–1346.

Van Staal, C.R., Whalen, J.B., Valverde-Vaquero, P., Zagorevski, A., Rogers, N., 2009. Pre-Carboniferous, episodic accretion-related, orogenesis along the Laurentian margin of the northern Appalachians. *Geological Society, London, Special Publications* 327, 271–316.

Vannucchi, P., Maltman, A., Bettelli, G., Clennell, B., 2003. On the nature of scaly fabric and scaly clay. *Journal of Structural Geology* 25, 673–688.

Vidal, O., Parra, T., 2000. Exhumation paths of high-pressure metapelites obtained from local equilibria for chlorite-phengite assemblages. *Geological Journal* 35, 139–161.

Waldron, J.W.F., Piper, D.J.W., Pe-Piper, G., 1989. Deformation of the Cape Chignecto Pluton, Cobequid Highlands, Nova Scotia: thrusting at the Meguma-Avalon boundary. *Atlantic Geology* 25, 51–62.

Wang, C.Y., 2011. High pore pressure, or its absence, in the San Andreas fault. *Geology* 39, 1047–1050.

Warr, L.N., Rice, A.H.N., 1994. Interlaboratory standardization and calibration of day mineral crystallinity and crystallite size data. *Journal of Metamorphic Geology* 12, 141–152.

Webb, G.W., 1969. Paleozoic wrench faults in the Canadian Appalachians, in: Kay, M. (Ed.), North Atlantic Geology and Continental Drift. American Association of Petroleum Geologists, pp. 745–786.

Weertman, J., 1957. Steady-state creep of crystals. *Journal of Applied Physics* 28, 1185–1189.

Wheeler, J., 1992. Importance of pressure solution and coble creep in the deformation of polymineralic rocks. *Journal of Geophysical Research* 97, 4579–4586.

White, J.C., 1982. Quartz deformation and the recognition of recrystallization regimes in the Flinton Group conglomerates, Ontario. *Canadian Journal of Earth Sciences* 19, 81–93.

White, J.C., 2004. Instability and localization of deformation in lower crust granulites, Minas fault zone, Nova Scotia, Canada. *Geological Society, London, Special Publications* 224, 25–37.

White, J.C., 2012. Paradoxical pseudotachylyte - Fault melt outside the seismogenic zone. *Journal of Structural Geology* 38, 11–20.

White, J.C., White, S.H., 1983. Semi-brittle deformation within the Alpine fault zone, New Zealand. *Journal of Structural Geology* 5, 579–589.

White, R.W., 1966. Ultramafic inclusions in basaltic rocks from Hawaii. *Contributions to Mineralogy and Petrology* 12, 245–314.

White, S.H., 1977. Geological significance of recovery and recrystallization processes in quartz. *Tectonophysics* 39, 143–170.

White, S.H., Burrows, S.E., Carreras, J., Shaw, N.D., Humphreys, F.J., 1980. On mylonites in ductile shear zones. *Journal of Structural Geology* 2, 175–187.

Wibberley, C.A.J., Yielding, G., Di Toro, G., 2008. Recent advances in the understanding of fault zone internal structure: a review. *Geological Society, London, Special Publications* 299, 5–33.

Wiersberg, T., Erzinger, J., 2008. Origin and spatial distribution of gas at seismogenic depths of the San Andreas Fault from drill-mud gas analysis. *Applied Geochemistry* 23, 1675–1690.

Wiewióra, A., Weiss, Z., 1990. Crystallochemical Classifications of Phyllosilicates Based on the Unified System of Projection of Chemical Composition: II. The Chlorite Group. *Clay Minerals* 25, 83–92.

Williams, C.F., Grubb, F. V., Galanis, S.P., 2004. Heat flow in the SAFOD pilot hole and implications for the strength of the San Andreas Fault. *Geophysical Research Letters* 31, 22–25.

Williams, H., 1979. Appalachian Orogen in Canada. *Canadian Journal of Earth Sciences* 16, 792–807.

Williams, H., 1995. Geology of the Appalachian-Caledonian Orogen in Canada and Greenland. Energy, Mines and Resources Canada : Geological Survey of Canada, Ottawa, Canada.

Wilson, B., Dewers, T., Reches, Z., Brune, J.N., 2005. Particle size and energetics of gouge from earthquake rupture zones. *Nature* 434, 749–752.

Xue, L., Li, H.B., Brodsky, E.E., Xu, Z., Kano, Y., Wang, H., Mori, J.J., Si, J., Pei, J., Zhang, W., Yang, G., Sun, Z., Huang, Y., 2013. Continuous Permeability Measurements Record Healing Inside the Wenchuan Earthquake Fault Zone. *Science* 340, 1555–1559.

Yuan, F., Prakash, V., Tullis, T., 2011. Origin of pulverized rocks during earthquake fault rupture. *Journal of Geophysical Research: Solid Earth* 116, 1–18.

Zang, W., Fyfe, W.S., 1995. Chloritization of the hydrothermally altered bedrock at the Igarape Bahia gold deposit, Carajas, Brazil. *Mineralium Deposita* 30, 30–38.

Zoback, M., Hickman, S., Ellsworth, W., 2010. Scientific Drilling Into the San Andreas Fault Zone. *Eos, Transactions American Geophysical Union* 91, 197.

Zoback, M.D., 2010. Scientific Drilling.

Zoback, M.D., Zoback, M.L., Mount, V.S., Suppe, J., Eaton, J.P., Healy, J.H., Oppenheimer, D., Reasenberg, P., Jones, L., Raleigh, C.B., Wong, I.G., Scotti, O., Wentworth, C., 1987. New evidence on the state of stress of the San Andreas fault system. *Science* 238, 1105–1111.

APPENDIX 1: ELECTRON MICROPROBE RESULTS

Major element chemical compositions of individually selected chlorites and phengites were obtained using a JEOL JXA-733 Electron Microprobe with four 2-crystal spectrometers housed at the Microscopy and Microanalysis facility at the University of New Brunswick. Standards used were jadeite (Na), clinopyroxene (Si, Ca), olivine (Mg), bytownite (Al), orthoclase (K), ilmenite (Ti), hematite (Fe), and bustamite (Mn). The microprobe was operated using an accelerating voltage of 15kV, and 30nA of current intensity. The measured intensity ratios for Al, Si, and Fe were recalibrated (post-acquisition) to a biotite standard.

This Appendix presents additional details on the standards and the raw results from each analysis.

Standards Used

Biotite:

The biotite standard (LP6) is from a pyroxenite mass from the Okangan Highlands of Washington State. A full characterization of the standard can be found in Ingamells and Engels (1976).

Jadeite:

The Jadeite standard is from San Benito, California.

Butamite:

The Bustamite is from ASTIMEX Scientific Limited, standard number MINM25-53.

Clinopyroxene:

The clinopyroxene standard, Clinopyroxene 5-118, is the same as the Pennsylvania State University pyroxene PSU Px-1 analyzed by Art Chodos, at the California Institute of Technology. A full revision of the results may be found in Ingamells (1980).

Olivine:

The olivine standard, Olivine 174.1, is from the Kamoolda Stream Lherzolite, Kauai, Hawaii. It is the same as that analyzed by White (1966).

Bytownite:

The Bytownite standard, Plgbyt, is from a gabbro sill at Crystal Bay, Minnesota. Analyses are found in Borg and Heard (1969).

Orthoclase:

The orthoclase standard, PSU Or-1A, is from the Pennsylvania State University Orthoclase. Analyses are found in Ingamells (1980).

Ilmenite:

The ilmenite standard, USNM 96189, is from the Ilmen Mountains, Miask, Russia. Analyses are found in Jarosewich et al. (1980a, 1980b).

Hematite:

The hematite standard, U.C. #8093, is from the University of California Berkeley.

Raw Results from Chlorite Analyses

Raw results from electron microprobe of chlorite are included here. Results highlighted in red were not used in the results or calculations presented in section 3.4, as the results did not fit the crystal chemistry of chlorite. Compositions are normalized to 28 oxygens.

Table A-1.1: Chlorite analyses from sample NJP-04-05.

	NJP-04-05 CHLORITE																
Pt#	86	87	88	89	90	91	92	93	94	95	96	97	98	99	100	101	102
SiO2	34.46	30.26	27.89	24.67	24.96	28.34	25.65	25.8	26	29.48	19.49	32.62	31.99	29.58	28.23	25.5	28.72
TiO2	0.0118	1.5801	0.0277	0.4103	0.1173	0.0957	0.0223	0.021	0.055	0.0937	0.0675	0.3205	0.0761	0.1973	0.1474	0.1352	0.2428
Al2O3	20.02	24.84	25.25	24.28	22.87	26.04	24.35	23.99	26.08	27.1	22.42	27.02	28.07	26.25	25.79	24.56	26.25
FeO	25.14	23.97	30.32	28.41	31.35	29.54	30.52	29.73	27.37	24.81	27.38	23.51	25.82	27.62	29.73	29.12	26.83
MnO	0.1021	0.2177	0.1774	0.2872	0.0826	0.4414	0.1323	0.1269	0.2293	0.1499	0.1169	0.3287	0.2933	0.1499	0.1599	0.3337	0.196
MgO	9.71	6.9	10.16	10.71	6.6	9.1	11.14	11.17	10.48	10.17	8.17	11.98	10.74	7.84	8.74	7.81	10.69
CaO	0.0406	0.1288	0.0699	0.0625	0.0645	0.0618	0.0491	0.0578	0.0513	0.0521	0.0505	0.1487	0.0819	0.1298	0.1564	0.0579	0.1089
Na2O	0.0257	0.1843	0.0329	0.0446	0.0522	0.0644	0.0006	0.0047	0.093	0.1783	0.1291	0.1293	0.1654	0.1835	0.0974	0.1383	0.2666
K2O	0.016	1.9952	0.3009	0.3871	0.7258	0.5416	0.0126	0.0183	0.8881	1.3924	1.1386	1.0269	1.0923	1.579	0.9497	1.1189	1.0361
Total	89.54	90.07	94.24	89.26	86.83	94.23	91.88	90.92	91.24	93.43	78.98	97.09	98.32	93.54	94	88.78	94.34
X(mm)	52.5298	52.325	52.2618	52.3205	52.574	52.3233	52.5338	52.538	52.7703	52.4343	52.3685	52.6298	52.411	52.4855	52.5345	52.6783	52.2733
Y(mm)	60.5419	61.6039	58.3536	58.6351	58.6426	59.6531	60.5429	60.5241	61.3626	61.7319	62.4091	62.9599	63.5774	63.9036	65.2161	65.4511	65.8444
Si	6.740	5.931	5.472	5.156	5.435	5.519	5.236	5.299	5.238	5.620	4.682	5.882	5.762	5.712	5.523	5.350	5.512
Al iv	1.260	2.069	2.528	2.844	2.565	2.481	2.764	2.701	2.762	2.380	3.318	2.118	2.238	2.288	2.477	2.650	2.488
Al vi	3.460	3.832	3.364	3.172	3.367	3.572	3.115	3.131	3.493	3.824	3.127	3.740	3.836	3.809	3.552	3.500	3.537
Ti	0.002	0.233	0.004	0.064	0.019	0.014	0.003	0.003	0.008	0.013	0.012	0.043	0.010	0.029	0.022	0.021	0.035
Cr	0.000	0.000	0.000	0.000	0.000	0.000	0.000	0.000	0.000	0.000	0.000	0.000	0.000	0.000	0.000	0.000	0.000
Fe3+	1.219	0.969	0.424	0.196	0.361	0.542	0.195	0.237	0.290	0.623	0.000	0.813	0.749	0.659	0.490	0.329	0.455
Fe2+	2.893	2.961	4.550	4.770	5.348	4.269	5.015	4.869	4.322	3.333	5.717	2.732	3.141	3.802	4.374	4.781	3.851
Mn	0.017	0.036	0.029	0.051	0.015	0.073	0.023	0.022	0.039	0.024	0.024	0.050	0.045	0.025	0.026	0.059	0.032
Mg	2.831	2.016	2.971	3.337	2.142	2.642	3.390	3.420	3.147	2.890	2.926	3.220	2.884	2.257	2.549	2.443	3.058
Ca	0.009	0.027	0.015	0.014	0.015	0.013	0.011	0.013	0.011	0.011	0.013	0.029	0.016	0.027	0.033	0.013	0.022
Na	0.019	0.140	0.025	0.036	0.044	0.049	0.000	0.004	0.073	0.132	0.120	0.090	0.116	0.137	0.074	0.113	0.198
K	0.008	0.998	0.151	0.206	0.403	0.269	0.007	0.010	0.456	0.677	0.698	0.472	0.502	0.778	0.474	0.599	0.507
OH*	16.000	16.000	16.000	16.000	16.000	16.000	16.000	16.000	16.000	16.000	16.000	16.000	16.000	16.000	16.000	16.000	16.000
Total	34.458	35.214	35.534	35.846	35.716	35.442	35.759	35.708	35.839	35.530	36.637	35.192	35.297	35.521	35.593	35.858	35.696
Oxidized	no	no	yes	yes	yes	yes	yes	yes	yes	no	yes	no	no	no	yes	yes	yes
Fe/Fe+Mg	0.592	0.661	0.626	0.598	0.727	0.646	0.606	0.599	0.594	0.578	0.661	0.524	0.574	0.664	0.656	0.677	0.585

Table A-1.2: Chlorite analyses from sample NJP-07-01A (*1/2*).

	NJP-07-01A Chlorite																					
Pt#	1	2	3	4	5	6	7	8	9	10	11	12	13	14	15	16	17	18	19	20	21	22
SiO2	22.98	22.96	23.27	22.80	19.21	23.22	23.18	23.19	23.41	23.05	23.87	23.18	23.22	23.29	22.83	23.04	22.84	23.04	23.14	23.21	23.24	23.43
TiO2	0.06	0.05	0.04	0.05	0.03	0.05	0.04	0.03	0.03	0.03	0.03	0.05	0.05	0.05	0.05	0.04	0.05	0.05	0.04	0.05	0.06	0.05
Al2O3	23.05	23.40	23.18	22.61	20.90	23.32	23.39	22.95	22.83	22.83	22.88	22.47	22.84	23.10	23.01	23.15	23.24	23.25	23.32	23.00	23.14	22.83
FeO	31.85	31.84	32.25	32.45	31.05	32.38	32.01	31.83	31.52	31.71	30.46	31.98	32.10	32.06	32.18	31.97	32.15	32.21	32.31	32.50	32.24	32.25
MnO	0.30	0.31	0.22	0.26	0.25	0.32	0.18	0.19	0.20	0.25	0.16	0.19	0.26	0.25	0.23	0.33	0.15	0.28	0.36	0.36	0.26	0.26
MgO	8.88	8.98	9.01	8.75	8.28	8.89	8.57	8.67	8.67	8.97	8.47	8.82	8.95	8.89	8.98	9.07	8.66	8.82	8.90	9.03	8.90	9.11
CaO	0.05	0.06	0.07	0.04	0.08	0.03	0.06	0.05	0.08	0.06	0.07	0.05	0.04	0.03	0.03	0.02	0.05	0.02	0.01	0.01	0.02	0.02
Na2O	0.02	0.03	0.01	0.01	0.05	0.01	0.02	0.02	0.03	0.00	0.04	0.01	0.02	0.00	0.00	0.02	0.01	0.00	0.01	0.03	0.00	0.00
K2O	0.01	0.02	0.00	0.00	0.12	0.00	0.05	0.05	0.03	0.00	0.24	0.00	0.00	0.02	0.00	0.00	0.01	0.00	0.00	0.00	0.00	0.00
Total	87.21	87.66	88.05	86.97	79.98	88.22	87.49	86.96	86.80	86.90	86.22	86.76	87.48	87.69	87.31	87.63	87.16	87.67	88.09	88.19	87.86	87.94
X(mm)	20.68	20.61	20.61	20.64	20.60	20.56	20.57	20.61	20.63	20.64	20.62	20.63	20.56	20.54	20.58	20.51	20.53	20.50	20.50	20.64	20.59	20.47
Y(mm)	51.68	51.38	51.15	51.01	50.89	50.81	50.77	50.65	50.53	50.51	50.50	50.44	50.43	50.39	50.34	50.25	50.15	49.80	49.53	49.38	48.03	48.03
Si	5.06	5.03	5.07	5.06	4.66	5.06	5.08	5.11	5.15	5.09	5.25	5.13	5.10	5.09	5.03	5.05	5.04	5.05	5.05	5.07	5.08	5.11
Al iv	2.94	2.97	2.93	2.94	3.34	2.94	2.92	2.89	2.85	2.91	2.75	2.87	2.90	2.91	2.97	2.95	2.96	2.95	2.95	2.93	2.92	2.89
Al vi	3.05	3.07	3.04	2.98	2.70	3.05	3.13	3.08	3.10	3.04	3.20	3.00	3.02	3.06	3.02	3.03	3.08	3.06	3.05	2.99	3.05	3.00
Ti	0.01	0.01	0.01	0.01	0.01	0.01	0.01	0.00	0.01	0.01	0.01	0.01	0.01	0.01	0.01	0.01	0.01	0.01	0.01	0.01	0.01	0.01
Cr	0.00	0.00	0.00	0.00	0.00	0.00	0.00	0.00	0.00	0.00	0.00	0.00	0.00	0.00	0.00	0.00	0.00	0.00	0.00	0.00	0.00	0.00
Fe3+	0.06	0.05	0.07	0.03	0.00	0.07	0.11	0.10	0.13	0.07	0.21	0.08	0.07	0.09	0.04	0.05	0.07	0.07	0.06	0.03	0.08	0.07
Fe2+	5.80	5.78	5.81	6.00	6.59	5.83	5.75	5.76	5.67	5.78	5.38	5.84	5.83	5.77	5.90	5.81	5.86	5.83	5.83	5.90	5.81	5.82
Mn	0.06	0.06	0.04	0.05	0.05	0.06	0.03	0.04	0.04	0.05	0.03	0.04	0.05	0.05	0.04	0.06	0.03	0.05	0.07	0.07	0.05	0.05
Mg	2.91	2.93	2.93	2.89	2.99	2.89	2.80	2.85	2.85	2.95	2.77	2.91	2.93	2.90	2.95	2.96	2.85	2.88	2.89	2.94	2.90	2.96
Ca	0.01	0.01	0.02	0.01	0.02	0.01	0.01	0.01	0.02	0.01	0.02	0.01	0.01	0.01	0.01	0.00	0.01	0.00	0.00	0.00	0.00	0.01
Na	0.02	0.03	0.01	0.01	0.05	0.00	0.01	0.02	0.02	0.00	0.03	0.01	0.02	0.00	0.00	0.02	0.01	0.00	0.01	0.03	0.00	0.00
K	0.01	0.01	0.00	0.00	0.07	0.00	0.03	0.03	0.02	0.00	0.13	0.00	0.00	0.01	0.00	0.00	0.00	0.00	0.00	0.00	0.00	0.00
OH*	16.000	16.000	16.000	16.000	16.000	16.000	16.000	16.000	16.000	16.000	16.000	16.000	16.000	16.000	16.000	16.000	16.000	16.000	16.000	16.000	16.000	16.000
Total	35.931	35.947	35.921	35.968	36.479	35.918	35.879	35.891	35.849	35.910	35.793	35.900	35.923	35.890	35.956	35.944	35.918	35.912	35.926	35.969	35.901	35.912
Oxidized	yes	yes	yes	yes	yes	yes	yes	yes	yes	yes	yes	yes	yes	yes	yes	yes	yes	yes	yes	yes	yes	yes
Fe/Fe+Mg	0.668	0.665	0.668	0.675	0.688	0.671	0.677	0.673	0.671	0.665	0.669	0.670	0.668	0.669	0.668	0.664	0.676	0.672	0.671	0.669	0.670	0.665

Table A-1.3: Continued: Chlorite analyses from sample NJP-07-01A (*2/2*).

Pt#	23	24	25	26	27	28	29	30	31	32	33	34	35	36	37	38	39	40	41	42	43	44
SiO2	23.59	23.34	23.23	23.12	23.49	23.67	23.18	23.36	23.84	23.21	23.72	23.55	24.13	23.93	24.53	22.28	23.34	23.34	25.20	23.21	23.40	23.72
TiO2	0.05	0.05	0.05	0.06	0.04	0.04	0.05	0.05	0.04	0.04	0.05	0.04	0.09	0.07	0.05	0.06	0.11	0.04	0.05	0.04	0.08	0.06
Al2O3	23.07	22.92	22.95	23.20	23.36	23.32	23.51	23.57	23.29	23.49	22.85	23.24	22.86	23.46	23.91	23.12	23.16	23.41	23.10	23.45	23.25	23.84
FeO	31.87	32.32	32.23	32.30	32.56	32.34	32.66	32.41	32.26	32.03	32.23	32.53	32.31	31.85	29.72	31.99	32.05	31.80	30.90	32.34	31.90	31.27
MnO	0.24	0.26	0.25	0.32	0.23	0.20	0.27	0.27	0.25	0.42	0.22	0.25	0.17	0.27	0.20	0.16	0.29	0.37	0.22	0.29	0.34	0.23
MgO	9.04	8.87	8.90	8.89	8.83	9.09	8.85	8.94	9.22	8.97	9.17	8.93	9.08	9.29	8.43	8.53	9.01	8.90	8.94	8.92	9.10	9.22
CaO	0.06	0.06	0.04	0.03	0.04	0.04	0.05	0.02	0.06	0.04	0.08	0.05	0.06	0.07	0.12	0.04	0.03	0.05	0.15	0.03	0.03	0.07
Na2O	0.01	0.00	0.00	0.00	0.00	0.00	0.00	0.00	0.00	0.01	0.03	0.01	0.02	0.00	0.09	0.01	0.01	0.03	0.10	0.01	0.02	0.02
K2O	0.08	0.00	0.00	0.00	0.00	0.00	0.00	0.00	0.00	0.00	0.00	0.00	0.00	0.00	0.43	0.00	0.00	0.01	0.02	0.00	0.02	0.02
Total	88.02	87.82	87.65	87.91	88.56	88.71	88.58	88.62	88.96	88.22	88.35	88.60	88.73	88.93	87.49	86.18	88.00	87.94	88.69	88.30	88.15	88.44
X(mm)	19.98	19.95	19.53	19.57	19.43	19.23	19.51	18.90	18.86	19.04	17.97	17.69	17.42	17.42	17.36	15.94	16.21	15.56	15.30	19.62	19.10	18.50
Y(mm)	48.08	48.07	47.79	47.59	47.18	47.16	46.87	46.75	46.39	46.23	46.38	46.07	45.77	45.60	45.44	39.65	39.38	39.01	38.44	28.08	52.05	52.74
Si	5.13	5.11	5.09	5.06	5.09	5.11	5.03	5.06	5.13	5.05	5.15	5.10	5.20	5.13	5.26	4.98	5.08	5.08	5.36	5.05	5.09	5.10
Al iv	2.87	2.89	2.91	2.94	2.91	2.89	2.97	2.94	2.87	2.95	2.85	2.90	2.80	2.87	2.74	3.02	2.92	2.92	2.64	2.95	2.91	2.90
Al vi	3.05	3.02	3.03	3.04	3.07	3.06	3.06	3.08	3.04	3.08	3.00	3.04	3.02	3.08	3.36	3.07	3.04	3.10	3.18	3.07	3.05	3.16
Ti	0.01	0.01	0.01	0.01	0.01	0.01	0.01	0.01	0.01	0.01	0.01	0.01	0.01	0.01	0.01	0.01	0.02	0.01	0.01	0.01	0.01	0.01
Cr	0.00	0.00	0.00	0.00	0.00	0.00	0.00	0.00	0.00	0.00	0.00	0.00	0.00	0.00	0.00	0.00	0.00	0.00	0.00	0.00	0.00	0.00
Fe3+	0.10	0.08	0.07	0.06	0.09	0.10	0.06	0.08	0.10	0.07	0.08	0.09	0.14	0.13	0.28	0.04	0.09	0.10	0.28	0.07	0.08	0.15
Fe2+	5.70	5.83	5.83	5.84	5.81	5.74	5.87	5.78	5.70	5.75	5.76	5.81	5.69	5.59	5.05	5.94	5.75	5.69	5.21	5.81	5.71	5.48
Mn	0.04	0.05	0.05	0.06	0.04	0.04	0.05	0.05	0.05	0.08	0.04	0.05	0.03	0.05	0.04	0.03	0.05	0.07	0.04	0.05	0.06	0.04
Mg	2.93	2.89	2.91	2.90	2.85	2.93	2.86	2.88	2.96	2.91	2.97	2.88	2.92	2.97	2.70	2.84	2.93	2.89	2.83	2.89	2.95	2.95
Ca	0.01	0.01	0.01	0.01	0.01	0.01	0.01	0.00	0.01	0.01	0.02	0.01	0.01	0.02	0.03	0.01	0.01	0.01	0.03	0.01	0.01	0.02
Na	0.01	0.00	0.00	0.00	0.00	0.00	0.00	0.00	0.00	0.01	0.02	0.01	0.01	0.00	0.08	0.01	0.01	0.02	0.08	0.01	0.01	0.01
K	0.05	0.00	0.00	0.00	0.00	0.00	0.00	0.00	0.00	0.00	0.00	0.00	0.00	0.00	0.23	0.00	0.00	0.00	0.01	0.00	0.01	0.01
OH*	16.000	16.000	16.000	16.000	16.000	16.000	16.000	16.000	16.000	16.000	16.000	16.000	16.000	16.000	16.000	16.000	16.000	16.000	16.000	16.000	16.000	16.000
Total	35.902	35.899	35.907	35.921	35.884	35.877	35.926	35.895	35.871	35.909	35.904	35.898	35.835	35.841	35.771	35.958	35.894	35.886	35.682	35.919	35.906	35.827
Oxidized	yes	yes	yes	yes	yes	yes	yes	yes	yes	yes	yes	yes	yes	yes	yes	yes	yes	yes	yes	yes	yes	yes
Fe/Fe+Mg	0.664	0.672	0.670	0.671	0.674	0.666	0.674	0.670	0.663	0.667	0.664	0.671	0.666	0.658	0.664	0.678	0.666	0.667	0.660	0.670	0.663	0.655

Table A-1.4: Chlorite analyses from sample NJP-07-02.

	NJP-07-02 CHLORITES																					
Pt#	1	3	4	6	8	10	11	12	14	16	18	19	22	24	26	27	29	30	32	33	35	37
SiO2	26.71	26.1	26.12	25.36	26.91	26.47	26.47	24.99	25.8	24.34	25.93	26.65	27.43	27.58	26.35	26.52	26.19	26.89	24.29	25.11	29.02	23.55
TiO2	0.2233	0.1814	0.104	0.1825	0.4066	0.1181	0.0746	0.1923	0.0901	0.0819	0.1156	0.0808	0.1006	0.1117	0.0963	0.1287	0.2507	0.1397	0.042	0.0713	0.4233	0.1079
Al2O3	23.35	22.75	23.4	22.81	23.11	24.83	22.88	22.21	23.05	23.1	23.32	24.3	24.63	24.51	22.44	23.53	23.26	22.75	22.24	23.09	23.66	23.23
FeO	23.78	25.41	24.24	24.68	23.3	23.28	25.52	24.88	25.29	25.16	23.63	23.53	22.05	22.97	24.5	24.38	24.42	24.52	26.39	26.82	22.06	25.03
MnO	0.1289	0.1786	0.1954	0.1887	0.1798	0.163	0.1745	0.1658	0.1679	0.1794	0.191	0.1717	0.1781	0.2021	0.1998	0.134	0.1661	0.1807	0.1151	0.1444	0.1754	0.1854
MgO	14.29	14.75	15.46	14.67	13.72	14.41	14.24	13.44	15.83	15.7	15.9	15.54	13.27	14.1	14.89	16.26	15.02	15.73	14.15	14.66	13.25	14.97
CaO	0.1031	0.0712	0.2895	0.0681	0.0753	0.0516	0.1972	0.1037	0.0497	0.0389	0.1108	0.0763	0.2846	0.0878	0.0802	0.0457	0.1533	0.0727	0.2212	0.2488	0.4018	0.0619
Na2O	0.4006	2.0965	1.4173	0.9453	0.9097	1.527	1.1679	0	0.8627	0.6748	1.0353	0	0.0084	0.5747	0.4787	2.9022	0	0	0.1808	0	1.4414	0.7716
K2O	1.0471	0.6237	0.4294	0.6044	1.7871	0.6516	0.0756	0.9189	0.1753	0.0976	0.4026	0.351	1.1194	0.9635	0.294	0.4802	0.3426	0.5903	0.0245	0.0048	0.569	0.0751
Total	90.03	92.16	91.65	89.51	90.4	91.51	90.8	86.9	91.31	89.37	90.62	90.7	89.08	91.09	89.32	94.38	89.81	90.87	87.65	90.15	91	87.97
X(mm)	35.3435	35.251	35.2185	35.1575	35.008	34.7198	34.5648	34.559	30.2393	30.4435	30.4685	30.423	30.4685	30.479	30.3525	30.265	30.1595	29.4243	29.3725	29.4848	30.4065	30.4448
Y(mm)	12.1471	12.7126	12.7539	12.8041	12.9289	13.1626	13.5884	13.7254	6.8741	7.2659	7.5469	7.8821	5.1866	5.2089	5.2729	5.4051	5.7239	9.9446	10.3319	10.4631	15.9151	16.0771
Si	5.392	5.096	5.140	5.156	5.383	5.195	5.321	5.306	5.147	4.975	5.166	5.317	5.501	5.441	5.393	4.974	5.147	4.975	5.166	5.317	5.501	5.441
Al iv	2.608	2.904	2.860	2.844	2.617	2.805	2.679	2.694	2.853	3.025	2.834	2.683	2.499	2.559	2.607	3.026	2.853	3.025	2.834	2.683	2.499	2.559
Al vi	2.996	2.514	2.687	2.718	2.931	3.046	2.808	2.892	2.644	2.622	2.732	3.058	3.393	3.206	2.834	2.414	2.644	2.622	2.732	3.058	3.393	3.206
Ti	0.034	0.027	0.015	0.028	0.061	0.017	0.011	0.031	0.014	0.013	0.017	0.012	0.015	0.017	0.015	0.018	0.014	0.013	0.017	0.012	0.015	0.017
Cr	0.000	0.000	0.000	0.000	0.000	0.000	0.000	0.000	0.000	0.000	0.000	0.000	0.000	0.000	0.000	0.000	0.000	0.000	0.000	0.000	0.000	0.000
Fe3+	0.060	0.000	0.000	0.000	0.000	0.000	0.000	0.031	0.000	0.000	0.000	0.179	0.378	0.166	0.022	0.000	0.000	0.000	0.000	0.179	0.378	0.166
Fe2+	3.955	4.615	4.271	4.408	3.992	3.962	4.389	4.387	4.425	4.561	4.138	3.746	3.321	3.624	4.172	4.466	4.425	4.561	4.138	3.746	3.321	3.624
Mn	0.022	0.030	0.033	0.033	0.030	0.027	0.030	0.030	0.028	0.031	0.032	0.029	0.030	0.034	0.035	0.021	0.028	0.031	0.032	0.029	0.030	0.034
Mg	4.300	4.293	4.535	4.447	4.091	4.216	4.267	4.254	4.707	4.784	4.722	4.621	3.967	4.147	4.543	4.546	4.707	4.784	4.722	4.621	3.967	4.147
Ca	0.022	0.015	0.061	0.015	0.016	0.011	0.042	0.024	0.011	0.009	0.024	0.016	0.061	0.019	0.018	0.009	0.011	0.009	0.024	0.016	0.061	0.019
Na	0.314	1.587	1.082	0.745	0.706	1.162	0.910	0.000	0.667	0.535	0.800	0.000	0.007	0.440	0.380	2.111	0.667	0.535	0.800	0.000	0.007	0.440
K	0.539	0.311	0.216	0.314	0.912	0.326	0.039	0.498	0.089	0.051	0.205	0.179	0.573	0.485	0.153	0.230	0.089	0.051	0.205	0.179	0.573	0.485
OH*	16.000	16.000	16.000	16.000	16.000	16.000	16.000	16.000	16.000	16.000	16.000	16.000	16.000	16.000	16.000	16.000	16.000	16.000	16.000	16.000	16.000	16.000
Total	36.242	37.390	36.900	36.706	36.739	36.767	36.497	36.146	36.586	36.605	36.670	35.841	35.744	36.136	36.170	37.816	36.586	36.605	36.670	35.841	35.744	36.136
Oxidized	yes	yes	yes	yes	yes	yes	yes	yes	yes	yes	yes	yes	yes	yes	yes	yes	yes	yes	yes	yes	yes	yes
Fe/Fe+Mg	0.483	0.518	0.485	0.498	0.494	0.485	0.507	0.509	0.485	0.488	0.467	0.459	0.482	0.478	0.480	0.496	0.485	0.488	0.467	0.459	0.482	0.478

Table A-1.5: Chlorite analyses from sample NJP-07-01.

	NJP-07-01 CHLORITE																		
Pt#	39	40	43	45	49	51	52	54	56	58	60	62	63	65	66	67	68	69	70
SiO2	22.66	23.35	32.54	23.54	23.05	23.09	24.65	23.4	23.03	22.94	23.21	24.57	23.29	24.47	23.52	29.03	22.38	22.35	22.26
TiO2	0.063	0.0569	0.0432	0.0698	0.1732	0.0634	0.1192	0.0595	0.0546	0.0568	0.0499	0.052	0.0491	0.0539	0.0494	0.0531	0.055	0.0593	0.047
Al2O3	23.32	23.66	21.56	24.31	23.62	23.85	24.37	23.87	23.9	23.48	23.98	23.66	23.81	23.23	23.66	22.97	23.46	23.75	23.66
FeO	33.52	33.18	30.98	35.15	35.18	35.4	33.09	34.33	35.51	35.45	35.18	33.55	35.64	34.86	35.32	30.59	35.29	35.73	35.91
MnO	0.2411	0.2645	0.2425	0.1835	0.3112	0.3033	0.2477	0.1989	0.178	0.3001	0.2894	0.1663	0.2693	0.2859	0.2521	0.2497	0.2256	0.2825	0.2563
MgO	8.73	7.65	7.42	8.18	7.7	8.56	7.2	8.28	8.53	7.79	8.05	7.17	8.36	8.23	7.8	6.88	7.89	8.43	6.91
CaO	0.0278	0.0387	0.2045	0.0307	0.0162	0.0307	0.0297	0.0275	0.0284	0.0456	0.0402	0.0851	0.0419	0.0231	0.0448	0.5025	0.0432	0.0246	0.0139
Na2O	0.7269	0.1062	1.4428	0	1.4545	0	0	0	0.9173	1.0066	0.6458	0.3017	1.3608	0	0	0.5087	1.7314	0.0176	0.5619
K2O	0	0.165	0.0137	0.0444	0.077	0	0.6009	0.2501	0.0538	0	0	0.2475	0	0	0	0.0711	0.0065	0.0051	0
Total	89.29	88.47	94.45	91.52	91.59	91.3	90.3	90.41	92.2	91.06	91.44	89.81	92.82	91.14	90.65	90.85	91.09	90.65	89.62
X(mm)	34.8683	34.9825	34.96	34.849	34.8	34.8488	34.6393	34.8568	34.0525	33.8513	30.3863	30.3155	30.309	30.059	30.1038	30.1723	29.662	29.5645	29.5373
Y(mm)	32.3604	32.6141	32.8291	33.0534	33.1744	33.2851	34.0116	35.0599	39.1374	39.8051	50.4304	50.1011	49.1849	48.5994	48.4729	48.1444	47.8761	48.0506	47.8636
Si	4.868	5.080	6.279	4.990	4.819	4.922	5.207	5.013	4.802	4.855	4.901	5.238	4.803	5.188	5.046	5.888	4.689	4.808	4.838
Al iv	3.132	2.920	1.721	3.010	3.181	3.078	2.793	2.987	3.198	3.145	3.099	2.762	3.197	2.812	2.954	2.112	3.311	3.192	3.162
Al vi	2.851	3.169	3.287	3.069	2.780	2.926	3.319	3.050	2.781	2.815	2.932	3.223	2.728	3.006	3.036	3.468	2.667	2.860	2.961
Ti	0.010	0.009	0.006	0.011	0.027	0.010	0.019	0.010	0.009	0.009	0.008	0.008	0.008	0.009	0.008	0.008	0.009	0.010	0.008
Cr	0.000	0.000	0.000	0.000	0.000	0.000	0.000	0.000	0.000	0.000	0.000	0.000	0.000	0.000	0.000	0.000	0.000	0.000	0.000
Fe3+	0.000	0.106	0.633	0.039	0.000	0.000	0.236	0.014	0.000	0.000	0.000	0.175	0.000	0.116	0.054	0.658	0.000	0.000	0.000
Fe2+	6.238	5.931	4.366	6.192	6.510	6.367	5.610	6.137	6.496	6.551	6.369	5.806	6.528	6.065	6.284	4.531	6.695	6.564	6.689
Mn	0.044	0.049	0.040	0.033	0.055	0.055	0.044	0.036	0.031	0.054	0.052	0.030	0.047	0.051	0.046	0.043	0.040	0.051	0.047
Mg	2.796	2.481	2.134	2.585	2.400	2.720	2.267	2.644	2.651	2.458	2.534	2.279	2.570	2.601	2.495	2.080	2.464	2.703	2.239
Ca	0.006	0.009	0.042	0.007	0.004	0.007	0.007	0.006	0.006	0.010	0.009	0.019	0.009	0.005	0.010	0.109	0.010	0.006	0.003
Na	0.606	0.090	1.080	0.000	1.179	0.000	0.000	0.000	0.742	0.826	0.529	0.249	1.088	0.000	0.000	0.400	1.407	0.015	0.474
K	0.000	0.092	0.007	0.024	0.041	0.000	0.324	0.137	0.029	0.000	0.000	0.135	0.000	0.000	0.000	0.037	0.003	0.003	0.000
OH*	16.000	16.000	16.000	16.000	16.000	16.000	16.000	16.000	16.000	16.000	16.000	16.000	16.000	16.000	16.000	16.000	16.000	16.000	16.000
Total	36.551	35.936	35.595	35.960	36.996	36.084	35.827	36.034	36.744	36.723	36.433	35.925	36.978	35.854	35.933	35.334	37.295	36.211	36.421
Oxidized	yes	yes	no	yes	yes	yes	yes	yes	yes	yes	yes	yes	yes	yes	yes	no	yes	yes	yes
Fe/Fe+Mg	0.691	0.709	0.701	0.707	0.731	0.701	0.721	0.699	0.710	0.727	0.715	0.724	0.718	0.704	0.718	0.714	0.731	0.708	0.749

Raw Results From Phengite Analyses

Phengites were analyzed from four samples from the S-C bearing phyllite and the folded carbonaceous phyllite. No samples were analyzed from the north bounding fault as the intensely reduced grain size made clean (*i.e.* uncontaminated) analyses impossible. Analyses are normalized to 11 oxygens under the assumption that all iron is ferrous. All analyses showing MnO % + TiO_2 % greater than 0.5% were rejected (red) due to probable contamination (Vidal and Parra, 2000). These analyses are not included in the results or calculations presented in section 3.4.

Table A-1.6: Phengite analyses from sample NJP-08-02.

	NJP-08-02 Phengite					
Pt#	103	110	115	120	121	122
SiO2	43.73	50.17	45.75	55.54	44.43	38.81
TiO2	0.2024	0.6084	0.31	3.26	0.236	0.311
Al2O3	30.57	29.72	36.56	24.2	29.51	28.77
FeO	5.47	3.59	1.9476	2.8027	7.96	14.76
MnO	0.0362	0.0472	0	0.0169	0.0221	0.0398
MgO	1.6978	1.0651	0.8315	1.0778	3.18	4.86
CaO	0.0805	0.0501	0.1602	0.1105	0.0505	0.0387
Na2O	0.389	0.711	0.7521	0.838	0.4563	0.2338
K2O	9.45	8.36	9.14	5.09	6.26	5.35
Total	91.62	94.32	95.45	92.93	92.1	93.17
X(mm)	34.9478	34.5585	34.9033	35.0975	35.1233	35.1618
Y(mm)	65.9159	66.7451	70.6141	71.8499	71.8986	72.0659
Si	3.09	3.35	3.03	3.66	3.11	2.80
Ti	0.01	0.03	0.02	0.16	0.01	0.02
Al	2.55	2.34	2.85	1.88	2.43	2.45
Fe	0.32	0.20	0.11	0.15	0.47	0.89
Mn	0.00	0.00	0.00	0.00	0.00	0.00
Mg	0.18	0.11	0.08	0.11	0.33	0.52
Ca	0.01	0.00	0.01	0.01	0.00	0.00
Na	0.05	0.09	0.10	0.11	0.06	0.03
K	0.85	0.71	0.77	0.43	0.56	0.49
H	2.00	2.00	2.00	2.00	2.00	2.00

Table A-1.7: Phengite analyses from sample NJP-07-02.

	NJP-07-02 PHENGITE															
Pt#	2	5	7	9	13	15	17	20	21	23	25	28	31	34	36	38
SiO2	34.88	45.56	41.13	44.25	43.5	45.35	45.7	45.12	46.84	45.73	46.88	45.73	45.43	42.24	43.56	43.17
TiO2	1.2848	0.3887	0.9697	0.5237	0.4143	0.2048	0.3449	0.4378	0.2939	0.4128	0.423	0.365	0.6227	0.853	0.3887	0.4524
Al2O3	20.36	35.85	33.46	34.88	34.77	35.69	36.4	34.92	36.87	36.61	35.94	36.44	35.58	34.19	34.94	35.87
FeO	18.83	4.31	4.99	2.3203	4.98	3.27	3.83	3.88	2.0642	2.2305	2.4554	3.11	4.6	2.7843	3.2	2.5205
MnO	0.1165	0.0281	0.013	0.0323	0.0096	0.0082	0.0171	0.0021	0.013	0.0287	0.0014	0.0376	0.0504	0	0.0226	0
MgO	10.53	1.8526	2.8373	0.7692	2.5442	1.3707	1.4611	1.221	0.5152	0	0.6459	1.2317	2.3091	0.6205	1.6361	0.8055
CaO	0.0646	0.0681	0.0386	0.0555	0.0536	0.0039	0.0552	0.0663	0.0068	0.0554	0.0488	0.0317	0.1383	0.0189	0.0253	0.0245
Na2O	0.5279	0.9124	1.2558	1.775	1.8961	0	6.02	0.0376	0	0.1797	0.736	0.7587	1.105	1.5413	0.4666	0
K2O	7.04	8.35	8.65	9.59	8.32	9.28	8.99	8.74	9.74	9.54	9.82	9.21	8.44	9.38	8.89	9.3
Total	93.62	97.31	93.34	94.2	96.48	95.17	102.83	94.42	96.34	94.79	96.95	96.91	98.27	91.62	93.13	92.15
X(mm)	35.3028	35.2125	35.0485	34.9213	34.573	30.323	30.4768	30.4085	30.4683	30.4993	30.4365	30.2198	29.4038	30.332	30.455	30.423
Y(mm)	12.6686	12.7539	12.8806	13.0876	13.7254	6.8959	7.4114	7.8616	5.1674	5.1941	5.2336	5.5911	10.0721	15.8934	15.9301	16.3871
Si	2.66	2.99	2.86	3.01	2.91	3.03	2.90	3.04	3.07	3.05	3.07	3.00	2.96	2.96	2.98	2.97
Ti	0.07	0.02	0.05	0.03	0.02	0.01	0.02	0.02	0.01	0.02	0.02	0.02	0.03	0.04	0.02	0.02
Al	1.83	2.77	2.74	2.79	2.74	2.81	2.72	2.77	2.84	2.88	2.77	2.82	2.74	2.82	2.82	2.91
Fe	1.20	0.24	0.29	0.13	0.28	0.18	0.20	0.22	0.11	0.12	0.13	0.17	0.25	0.16	0.18	0.15
Mn	0.01	0.00	0.00	0.00	0.00	0.00	0.00	0.00	0.00	0.00	0.00	0.00	0.00	0.00	0.00	0.00
Mg	1.20	0.18	0.29	0.08	0.25	0.14	0.14	0.12	0.05	0.00	0.06	0.12	0.22	0.06	0.17	0.08
Ca	0.01	0.00	0.00	0.00	0.00	0.00	0.00	0.00	0.00	0.00	0.00	0.00	0.01	0.00	0.00	0.00
Na	0.08	0.12	0.17	0.23	0.25	0.00	0.74	0.00	0.00	0.02	0.09	0.10	0.14	0.21	0.06	0.00
K	0.68	0.70	0.77	0.83	0.71	0.79	0.73	0.75	0.81	0.81	0.82	0.77	0.70	0.84	0.78	0.82
H	2.00	2.00	2.00	2.00	2.00	2.00	2.00	2.00	2.00	2.00	2.00	2.00	2.00	2.00	2.00	2.00

Table A-1.8: Phengite analyses from sample NJP-07-01.

	NJP-07-01 PHENGITE												
Pt#	41	42	44	46	47	48	50	53	55	57	59	61	64
SiO2	45.04	45.27	48.09	46.2	44.92	46.19	46.39	47.79	46.83	45.87	50.67	46.64	46.52
TiO2	0.1883	0.2072	0.1575	0.2279	0.2283	0.2215	0.2386	0.2241	0.2229	0.2259	0.1798	1.1593	0.2288
Al2O3	37.4	36.91	35.1	38.1	37.27	37.68	38.41	37.46	37.53	37.74	35.3	36.37	37.72
FeO	1.722	1.8517	2.9254	1.5654	4.18	1.9832	1.4676	1.2943	1.8144	1.6115	1.6374	2.3681	1.1634
MnO	0.0151	0.0137	0	0.0274	0.0096	0.0144	0.0103	0	0	0	0	0	0
MgO	0	0	0	0	0.2437	0.0383	0.3021	0.0968	0	0	0	0.4363	0
CaO	0.0253	0	0.5861	0.0262	0.0192	0.0117	0.0332	0.1946	0.0549	0.0064	0.0661	0.8848	0.1215
Na2O	1.4937	0	3.29	0.722	1.1168	0.3107	2.5802	2.4292	0.5796	1.7101	3.37	0.6822	0
K2O	9.27	9.38	7.68	9.33	8.75	9.37	9.5	8.97	8.94	9.54	8.58	9.3	9.53
Total	95.15	93.63	97.83	96.2	96.74	95.81	98.93	98.46	95.97	96.7	99.81	97.84	95.28
X(mm)	34.9525	34.9228	34.8523	34.8828	34.8643	34.868	34.821	34.677	34.8485	33.9708	33.92	30.346	29.9895
Y(mm)	32.6834	32.7501	32.9564	33.0819	33.1266	33.1549	33.2394	34.6516	35.1186	39.1809	39.8349	50.6984	48.7464
Si	3.00	3.04	3.12	3.02	2.97	3.04	2.98	3.06	3.06	3.01	3.20	3.03	3.06
Ti	0.01	0.01	0.01	0.01	0.01	0.01	0.01	0.01	0.01	0.01	0.01	0.06	0.01
Al	2.93	2.92	2.68	2.94	2.90	2.92	2.91	2.83	2.89	2.91	2.63	2.78	2.92
Fe	0.10	0.10	0.16	0.09	0.23	0.11	0.08	0.07	0.10	0.09	0.09	0.13	0.06
Mn	0.00	0.00	0.00	0.00	0.00	0.00	0.00	0.00	0.00	0.00	0.00	0.00	0.00
Mg	0.00	0.00	0.00	0.00	0.02	0.00	0.03	0.01	0.00	0.00	0.00	0.04	0.00
Ca	0.00	0.00	0.04	0.00	0.00	0.00	0.00	0.01	0.00	0.00	0.00	0.06	0.01
Na	0.19	0.00	0.41	0.09	0.14	0.04	0.32	0.30	0.07	0.22	0.41	0.09	0.00
K	0.79	0.80	0.64	0.78	0.74	0.79	0.78	0.73	0.75	0.80	0.69	0.77	0.80
H	2.00	2.00	2.00	2.00	2.00	2.00	2.00	2.00	2.00	2.00	2.00	2.00	2.00

Table A-1.9: Phengite analyses from sample NJP-07-01A.

	NJP-07-01A PHENGITE														
Pt#	71	72	73	74	75	76	77	78	79	80	81	82	83	84	85
SiO2	46.07	46.5	45.57	45.69	53.02	50.95	44.76	50.42	70.54	45.59	46.5	46.81	47.33	45.53	46.35
TiO2	0.1892	0.2155	0.1914	0.2052	0.1916	0.0974	0.2212	0.2144	0.1746	0.2111	0.1976	0.1122	0.1514	0.129	0.1069
Al2O3	38.23	38.21	36.14	37.92	30.63	32.94	37.56	33.63	21.32	37	38.56	39.21	38.81	38.81	38.8
FeO	1.0387	1.0426	1.1296	1.1345	1.5728	0.9139	1.3006	1.0794	0.9491	0.9019	0.9053	1.3325	1.2791	1.2785	0.9989
MnO	0.0208	0	0.0107	0.0094	0.002	0.0269	0.0268	0	0.0061	0.0141	0	0.002	0	0.0155	0.0243
MgO	0.4352	0.455	0.486	0.449	0.4563	0.4114	0.4321	0.3416	0.3119	0.3762	0.3749	0.437	0.398	0.3681	0.4186
CaO	0.0408	0.0479	0.5056	0.063	1.475	2.3295	0.0322	0.6627	0.0469	0.0707	0.1371	0.0484	0.0698	0.0805	0.0529
Na2O	0.9693	0.9757	1.4583	1.0332	2.3168	3.53	0.9372	2.0016	0.5205	1.0439	1.1521	1.0444	1.118	1.0824	1.1245
K2O	9.22	9.17	8.36	8.97	6.17	5.96	9.31	7.57	5.29	9.3	9	9.02	8.84	8.99	9.16
Total	96.22	96.61	93.85	95.48	95.84	97.17	94.57	95.92	99.16	94.51	96.83	98.02	98	96.3	97.04
X(mm)	60.7408	60.6835	60.7228	60.871	61.1108	61.2075	61.4038	61.4178	61.4283	52.8275	53.6065	52.9518	52.8625	52.9683	52.9345
Y(mm)	34.0311	34.4171	34.1124	33.6611	33.1059	33.0084	32.5324	32.3286	32.1726	29.7784	30.2096	30.0026	30.0206	30.1999	29.2746
Si	3.01	3.02	3.05	3.01	3.43	3.27	2.99	3.27	4.21	3.03	3.01	3.00	3.03	2.97	3.00
Ti	0.01	0.01	0.01	0.01	0.01	0.00	0.01	0.01	0.01	0.01	0.01	0.01	0.01	0.01	0.01
Al	2.94	2.93	2.85	2.94	2.33	2.49	2.95	2.57	1.50	2.90	2.94	2.96	2.93	2.99	2.96
Fe	0.06	0.06	0.06	0.06	0.08	0.05	0.07	0.06	0.05	0.05	0.05	0.07	0.07	0.07	0.05
Mn	0.00	0.00	0.00	0.00	0.00	0.00	0.00	0.00	0.00	0.00	0.00	0.00	0.00	0.00	0.00
Mg	0.04	0.04	0.05	0.04	0.04	0.04	0.04	0.03	0.03	0.04	0.04	0.04	0.04	0.04	0.04
Ca	0.00	0.00	0.04	0.00	0.10	0.16	0.00	0.05	0.00	0.01	0.01	0.00	0.00	0.01	0.00
Na	0.12	0.12	0.19	0.13	0.29	0.44	0.12	0.25	0.06	0.13	0.14	0.13	0.14	0.14	0.14
K	0.77	0.76	0.71	0.75	0.51	0.49	0.79	0.63	0.40	0.79	0.74	0.74	0.72	0.75	0.76
H	2.00	2.00	2.00	2.00	2.00	2.00	2.00	2.00	2.00	2.00	2.00	2.00	2.00	2.00	2.00

APPENDIX 2: THIN SECTION SCANS

TEM Thin Sections and Slot Locations for the Minas Fault Zone

Representative thin section scans and slot locations for TEM analysis. If more than 1 thin section was cut for the sample a representative scan is shown with the number of scans at the end in italic (*e.g. 1/3*).

Figure A-2.1: Representative polished thin section scan with location of TEM slots for sample NJP-04-05 (*1/3*).

Figure A-2.2: Polished thin section scan with location of TEM slots for sample NJP-07-01.

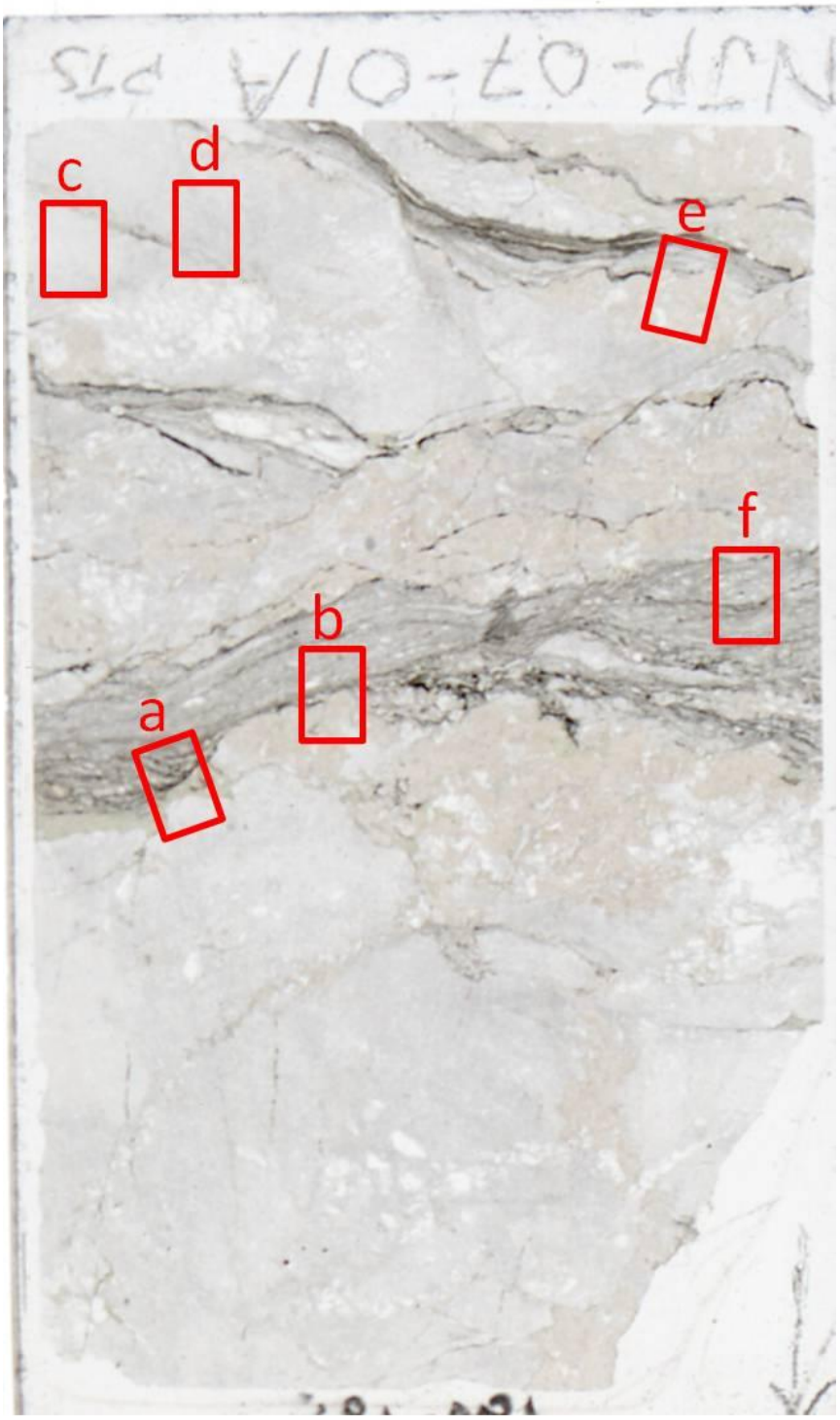

Figure A-2.3: Polished thin section scan with location of TEM slots for sample NJP-07-01A.

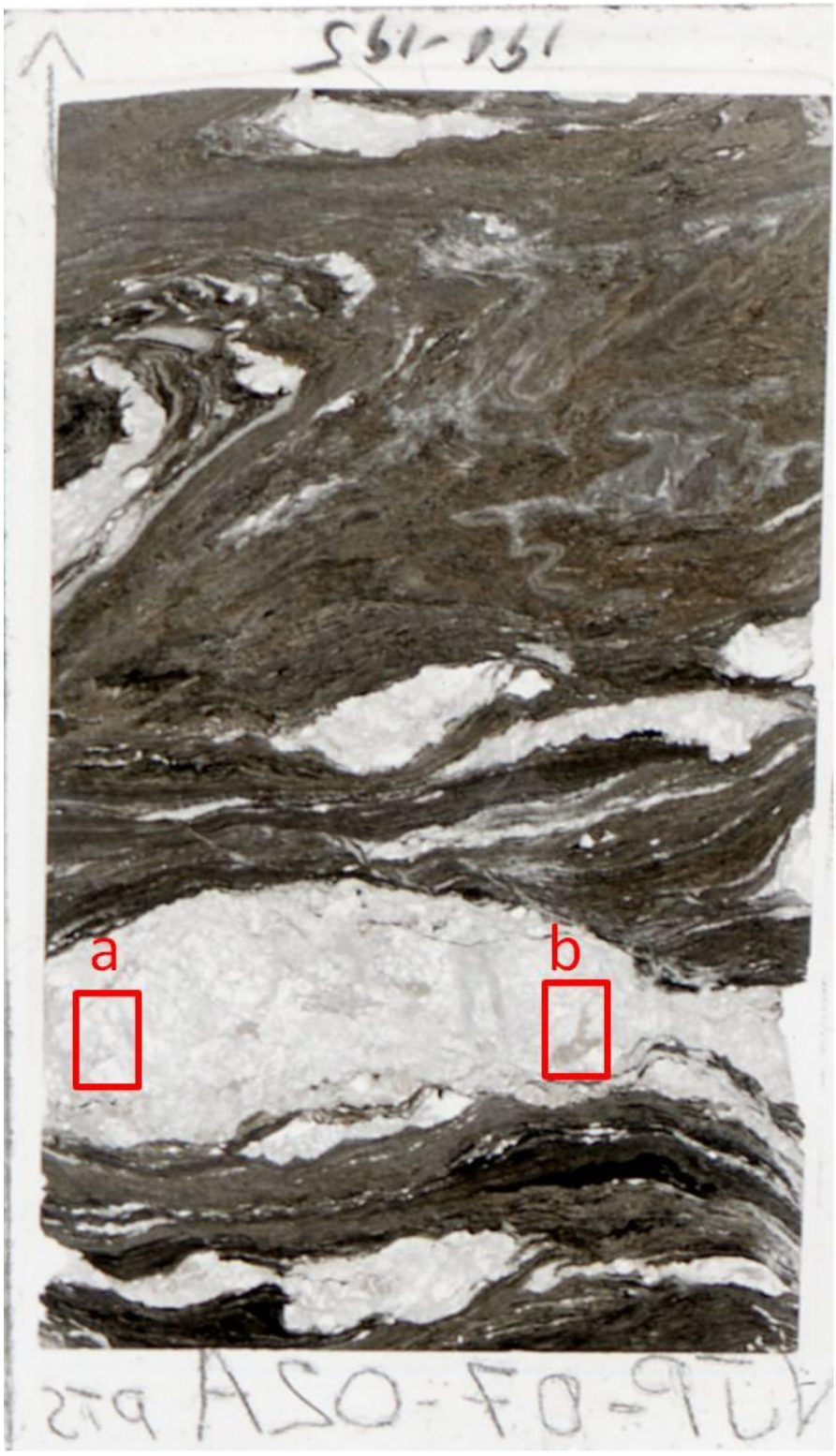

Figure A-2.4: Polished thin section scan with location of TEM slots for sample NJP-07-02A.

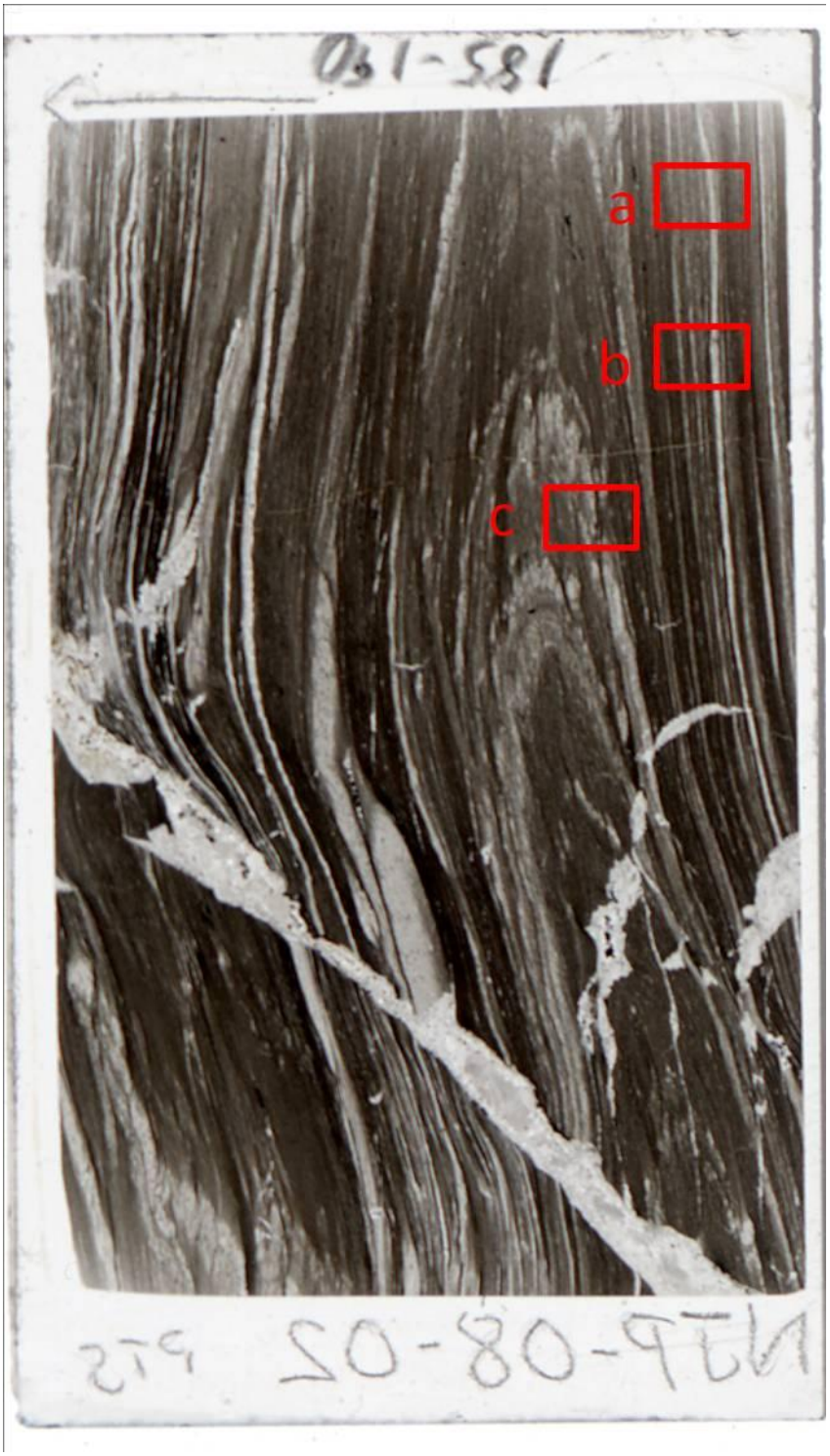

Figure A-2.5: Polished thin section scan with location of TEM slots for sample NJP-08-02.

Polished and Large Format Thin Sections for the Minas Fault Zone

Representative polished thin section scans for samples not prepared for TEM. If more than 1 thin section was cut for the sample a representative scan is shown with the number of scans at the end in italic (*e.g. 1/3*).

Figure A-2.6: Representative polished thin section scan for sample NJP-08-03 (*1/3*).

Figure A-2.7: Polished thin section scan for sample NJP-08-04.

Figure A-2.8: Scan of large format thin section for sample NJP-00-01.

Figure A-2.9: Scan of large format thin section for sample NJP-04-05.

Figure A-2.10: Scan of large format thin section for sample NJP-07-01A.

Figure A-2.11: Scan of large format thin section for sample NJP-07-02.

Figure A-2.12: Scan of large format thin section for sample NJP-08-04.

Thin Sections and Core Samples for the San Andreas Fault Observatory at Depth

Core segments, location of samples, and thin section scans for the San Andreas Fault Observatory at Depth project. Red lines indicate section of core received from the SAFOD project for this study. For a full visual of all the core retrieved from phase 3 of the SAFOD project, please refer to the SAFOD core atlas (SAFOD, 2010).

E14:

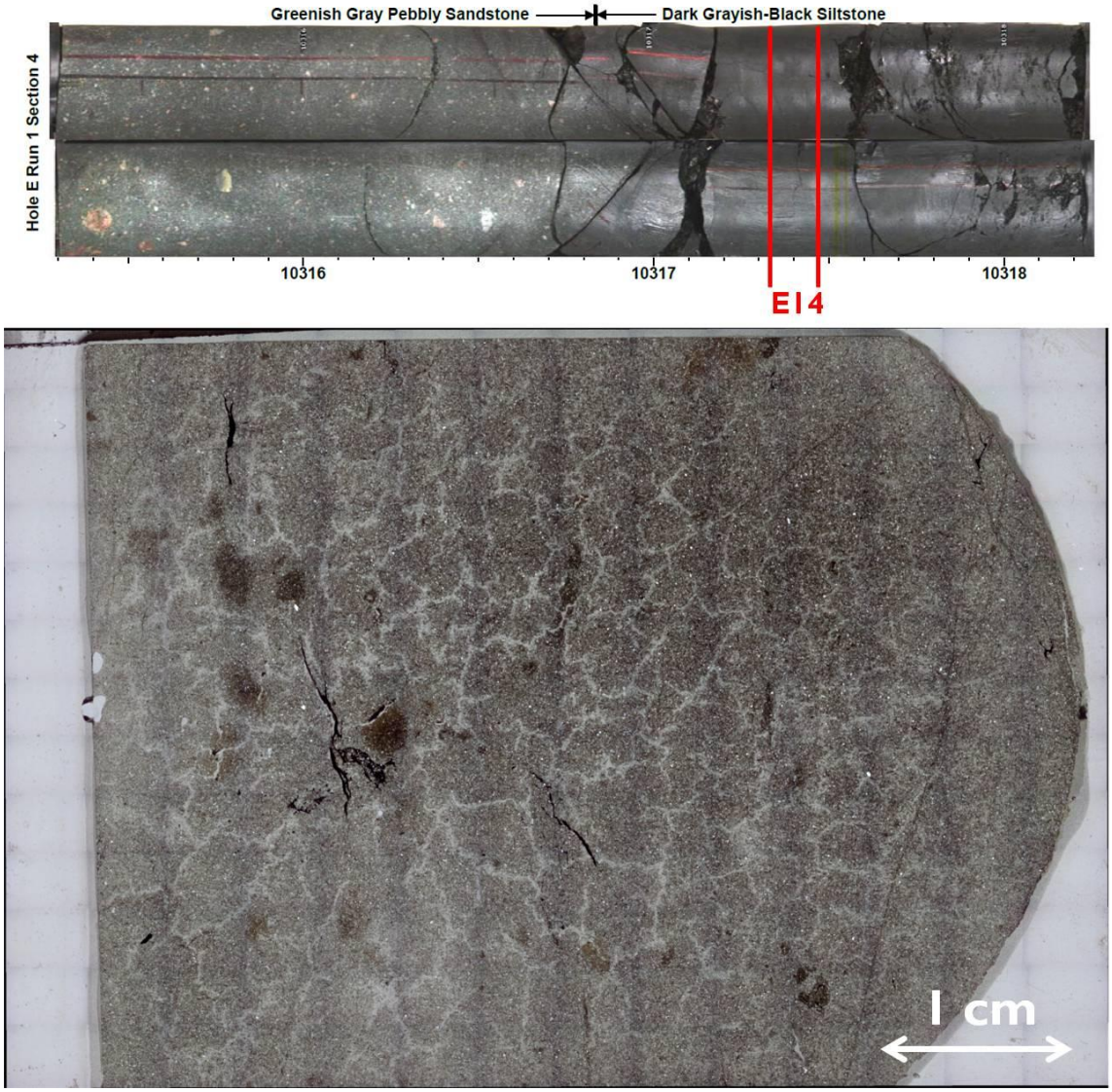

Figure A-2.13: Core segment and thin section scan for SAFOD E-14.

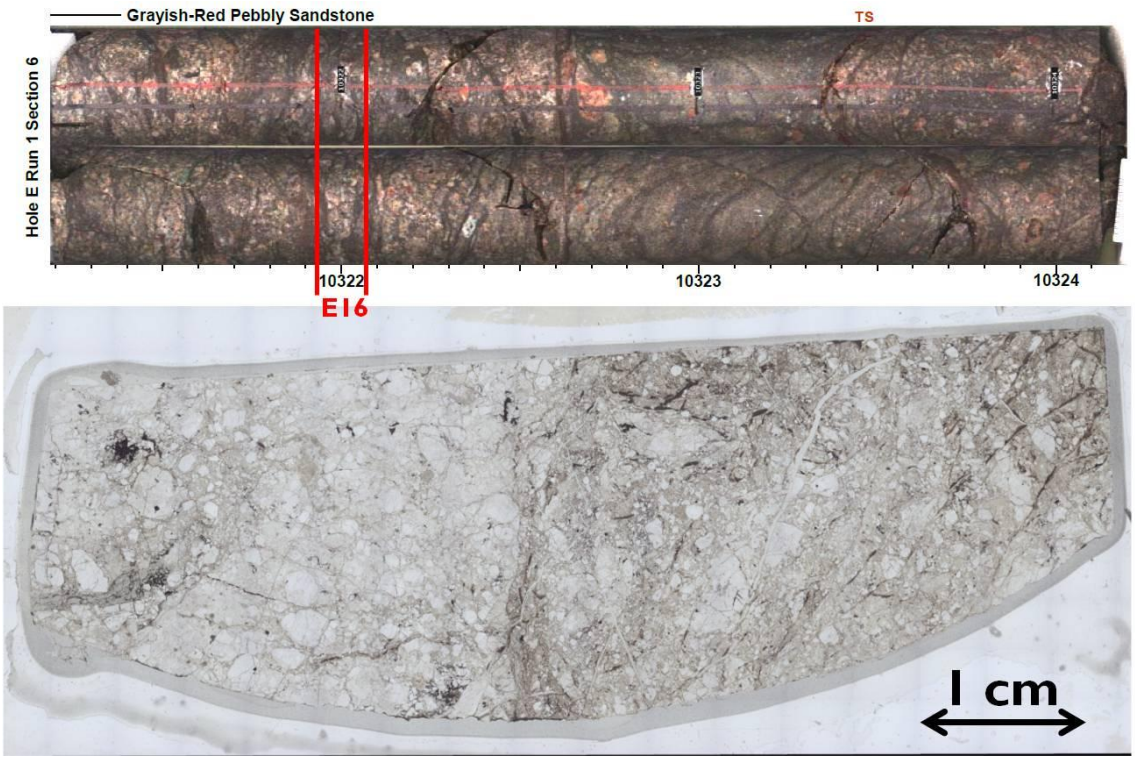

Figure A-2.14: Core segment and thin section scan for SAFOD E-16.

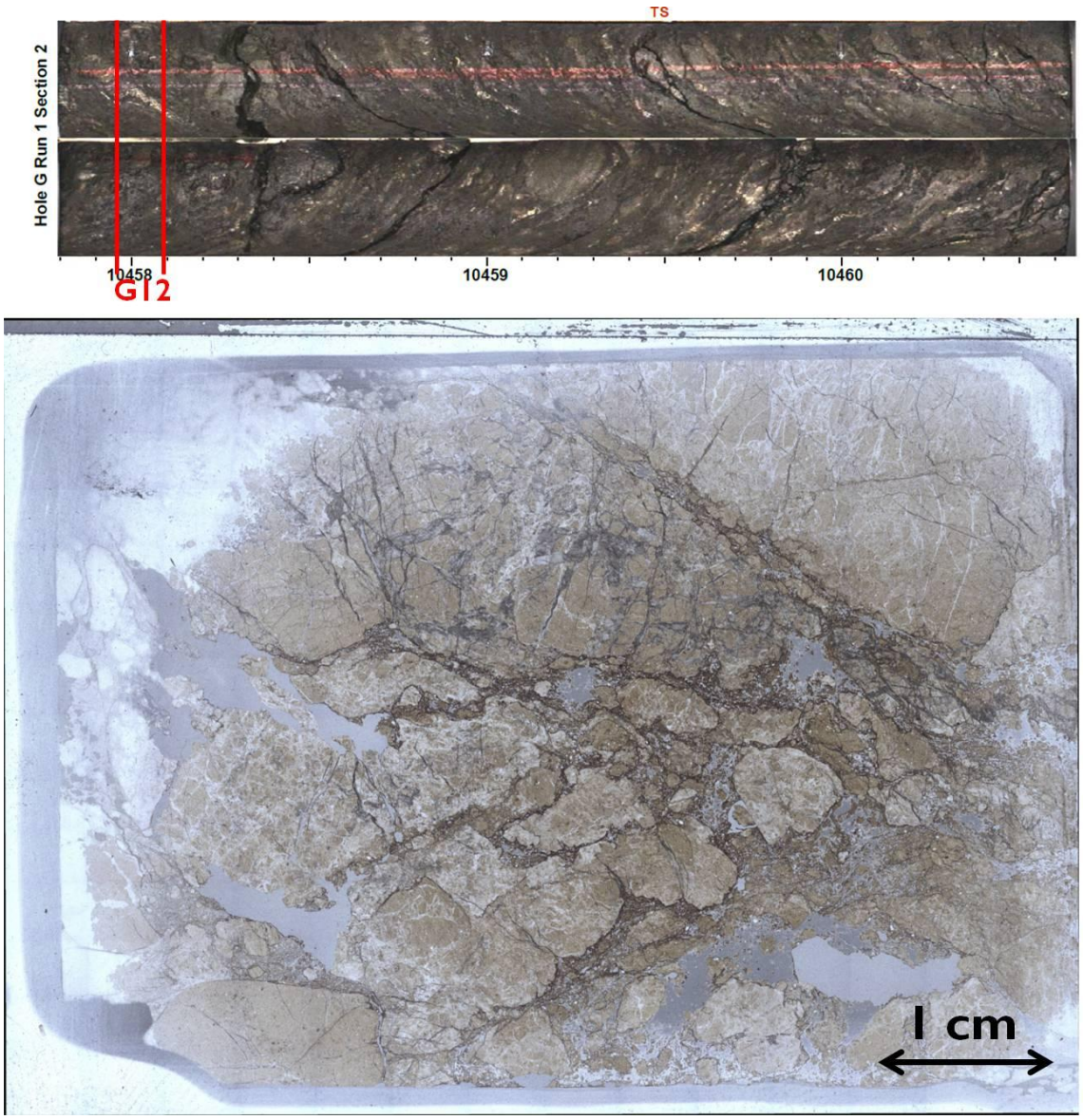

Figure A-2.15: Core segment and thin section scan for SAFOD G-12.

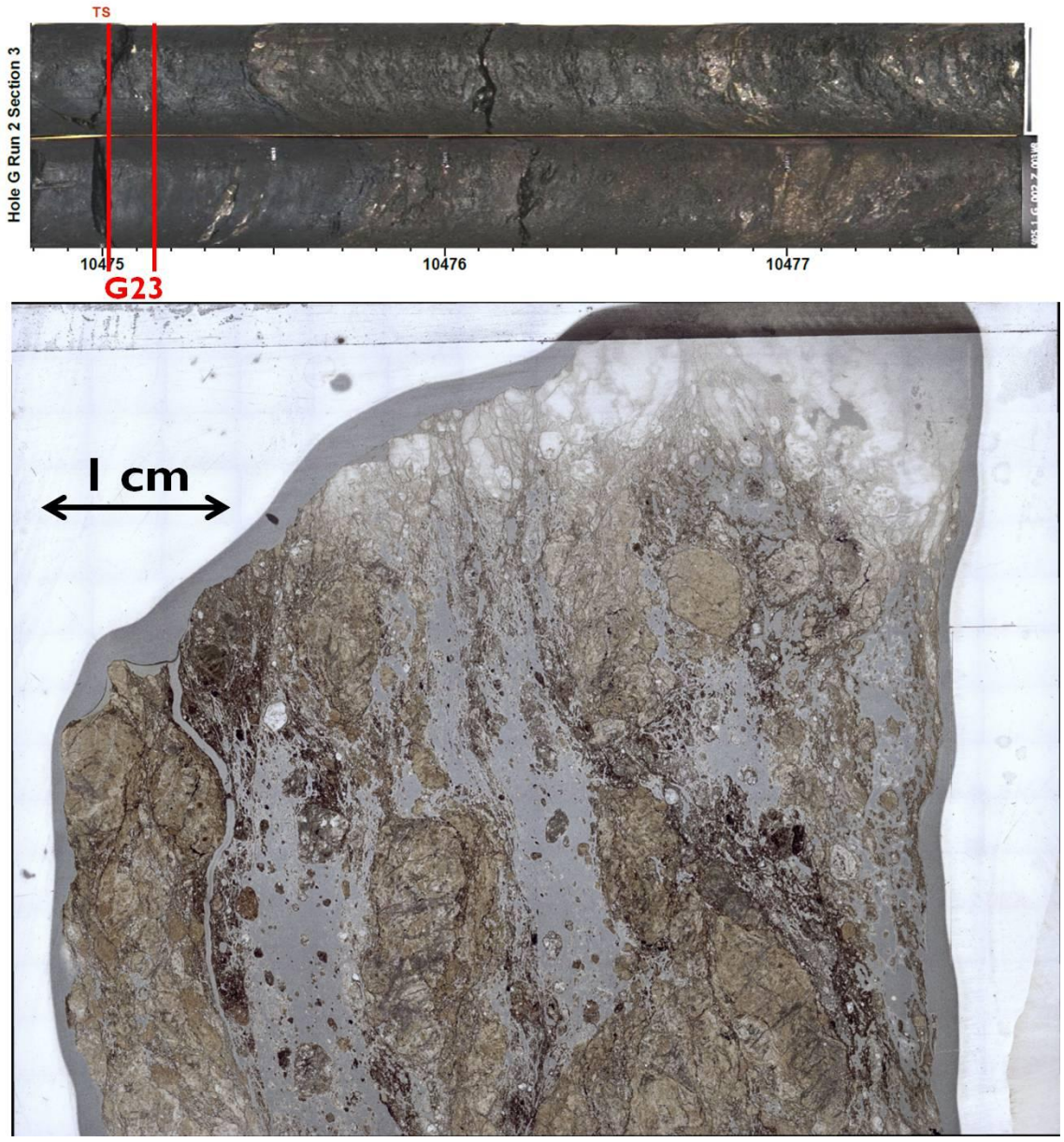

Figure A-2.16: Core segment and thin section scan for SAFOD G-23.

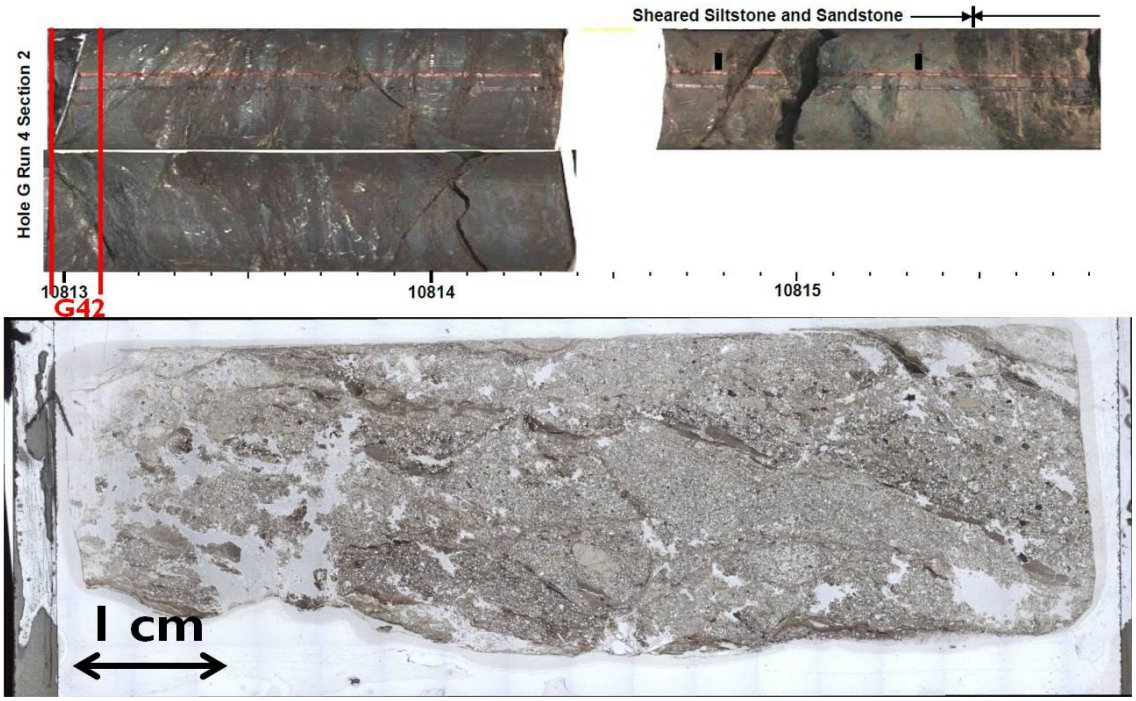

Figure A-2.17: Core segment and thin section scan for SAFOD G-42.

APPENDIX 3: XRD DATA FROM THE MINAS FAULT ZONE

Plots of Oriented Cay Aggregates from the Minas fault zone

Oriented clay aggregates were prepared from a variety of samples from the Minas fault zone to determine phyllosilicate compositions. Samples were analyzed All analyses show simple mixtures of chlorite and muscovite.

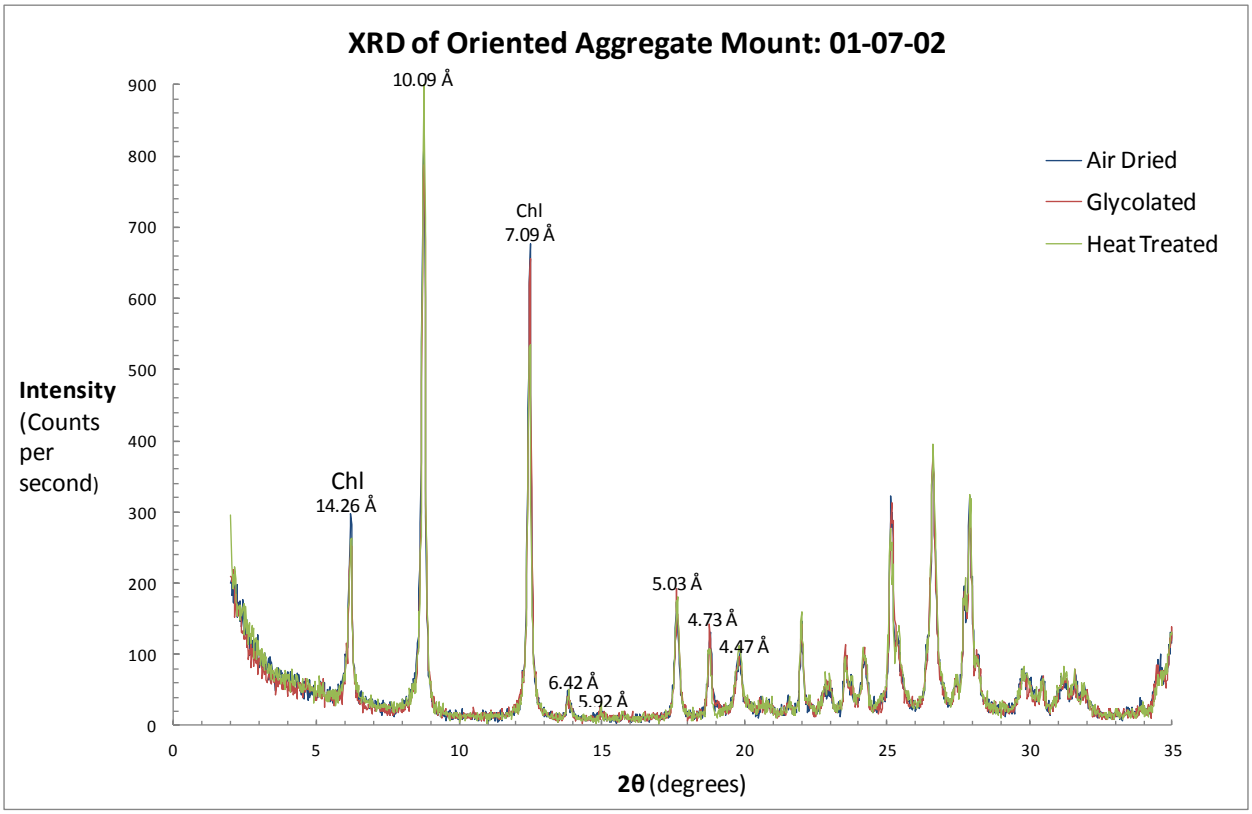

Figure A-3.1: XRD of oriented aggregate mount for sample 01-07-02.

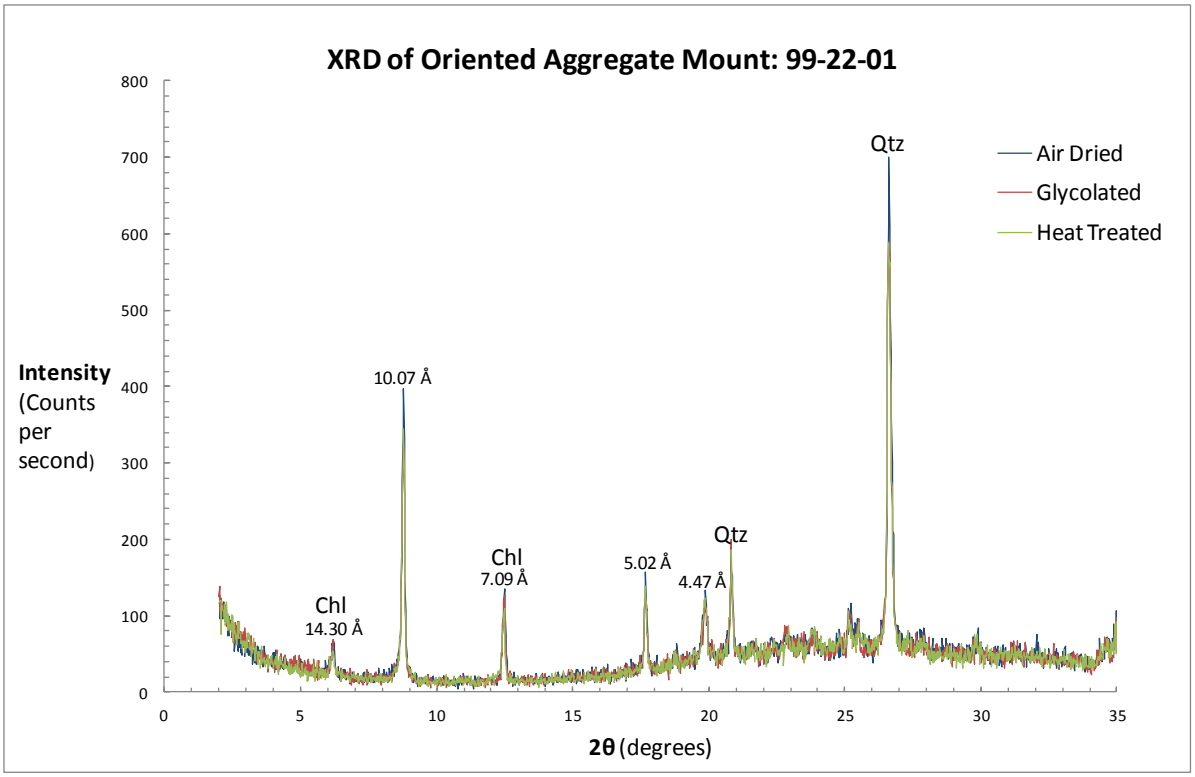

Figure A-3.2: XRD of oriented aggregate mount for sample 01-07-02.

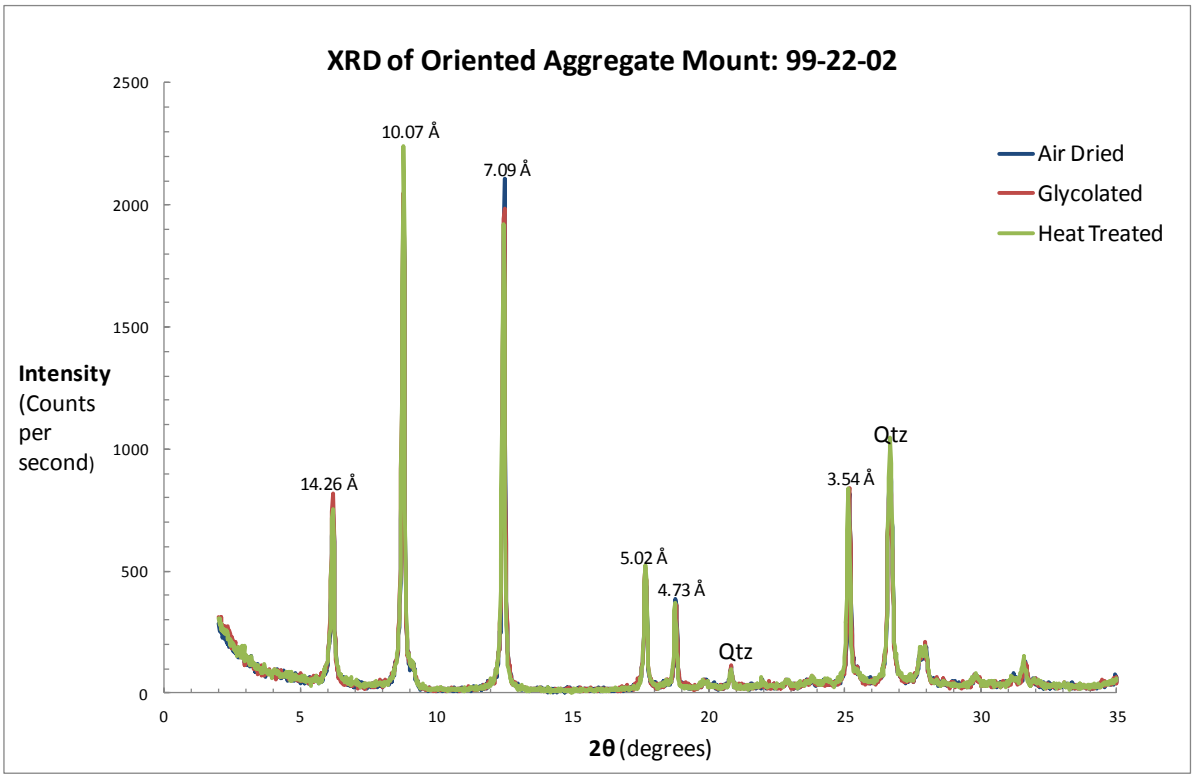

Figure A-3.3: XRD of oriented aggregate mount for sample 99-22-02.

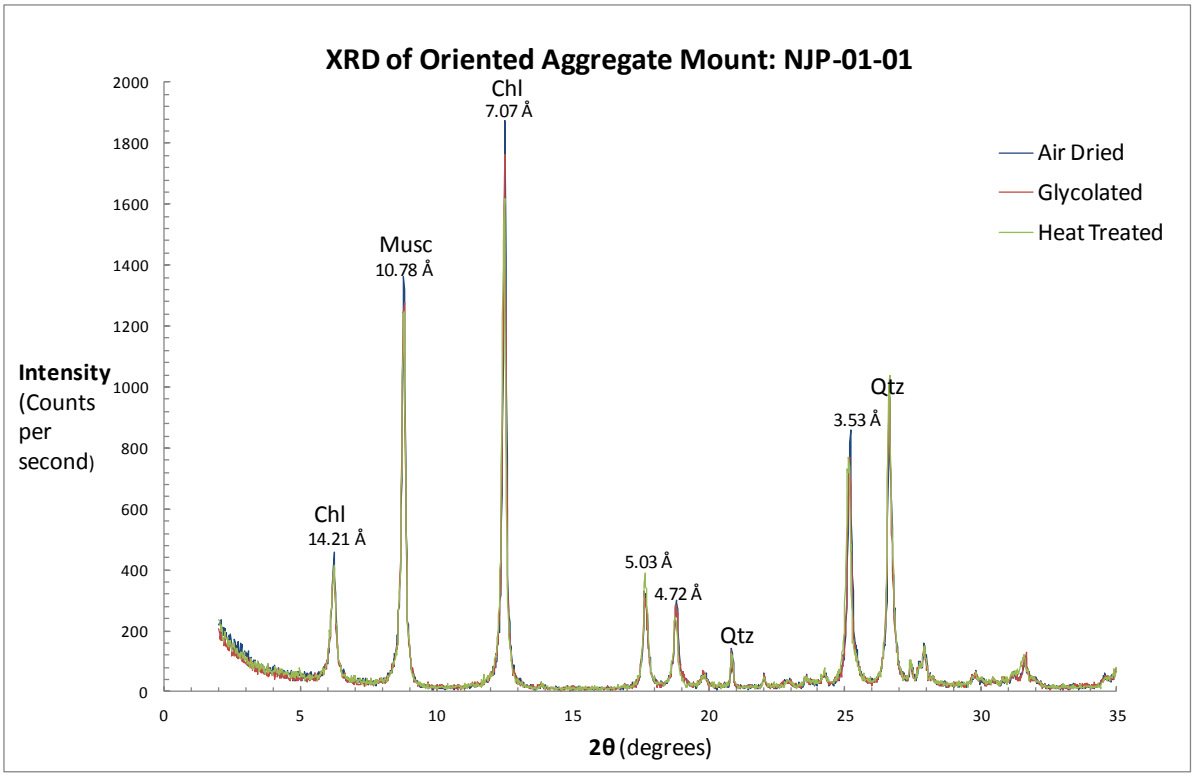

Figure A-3.4: XRD of oriented aggregate mount for sample NJP-01-01.

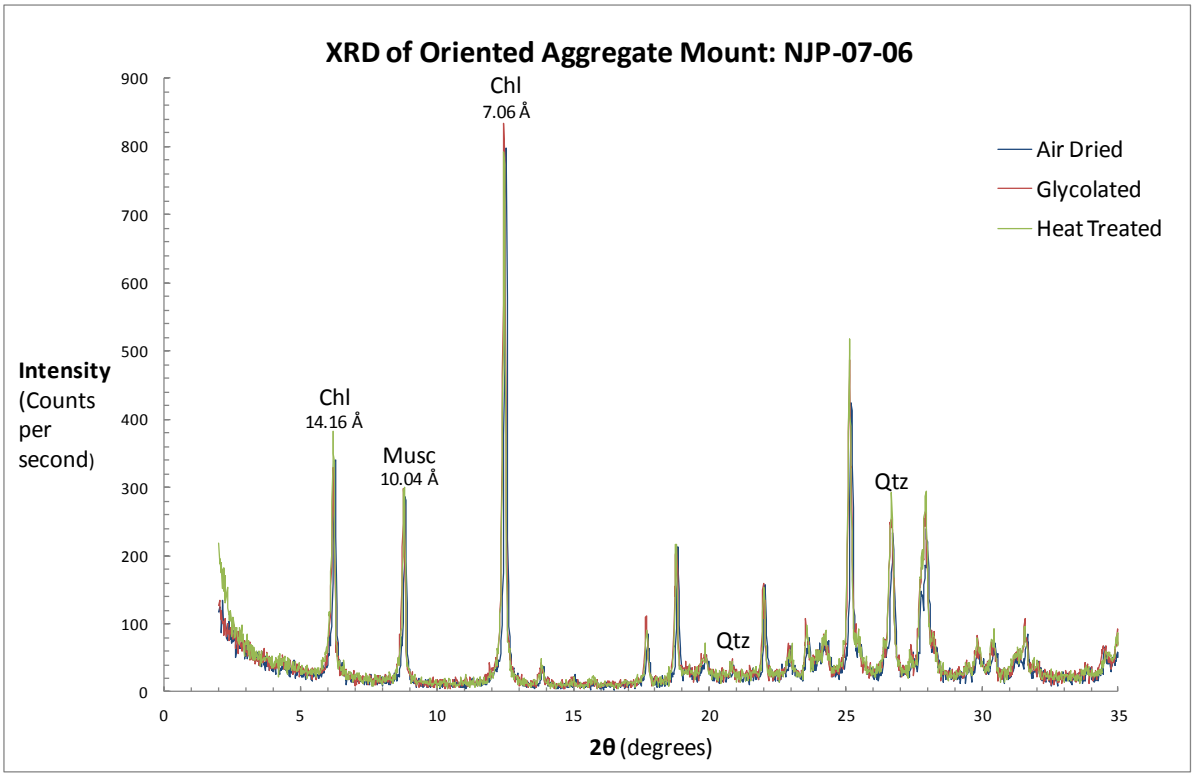

Figure A-3.5: XRD of oriented aggregate mount for sample NJP-07-06.

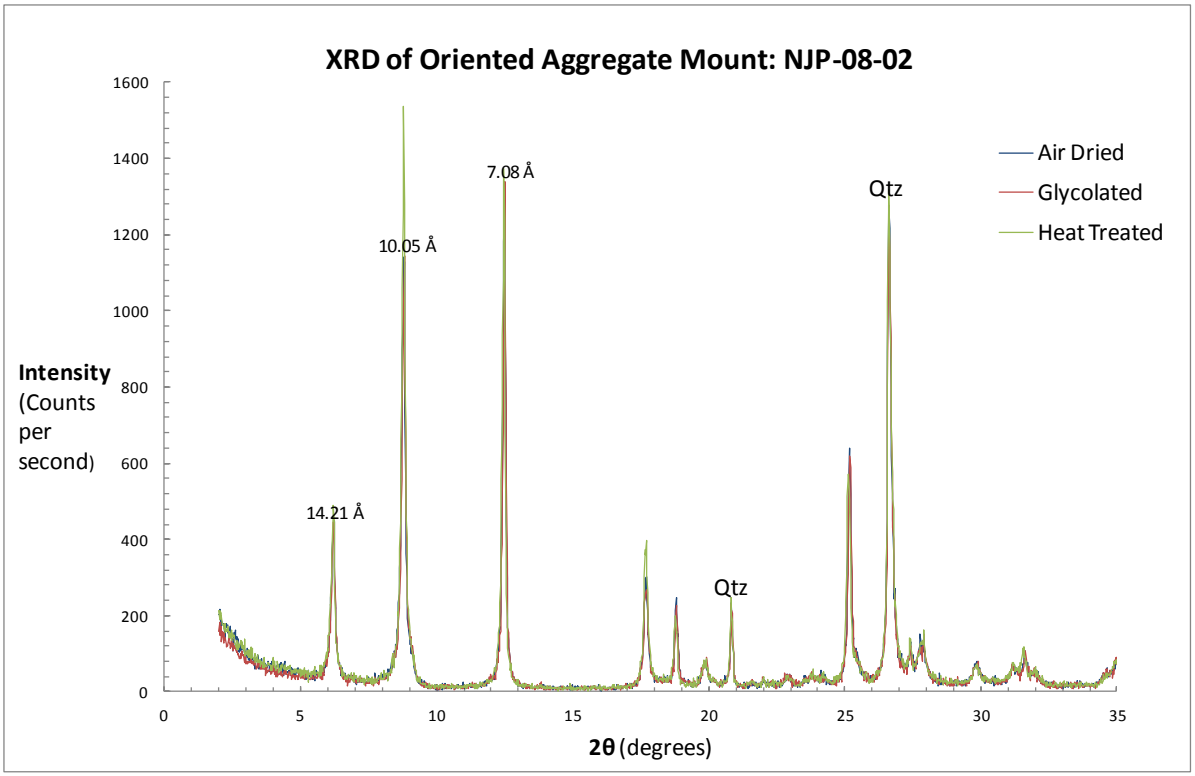

Figure A-3.6: XRD of oriented aggregate mount for sample NJP-08-02.

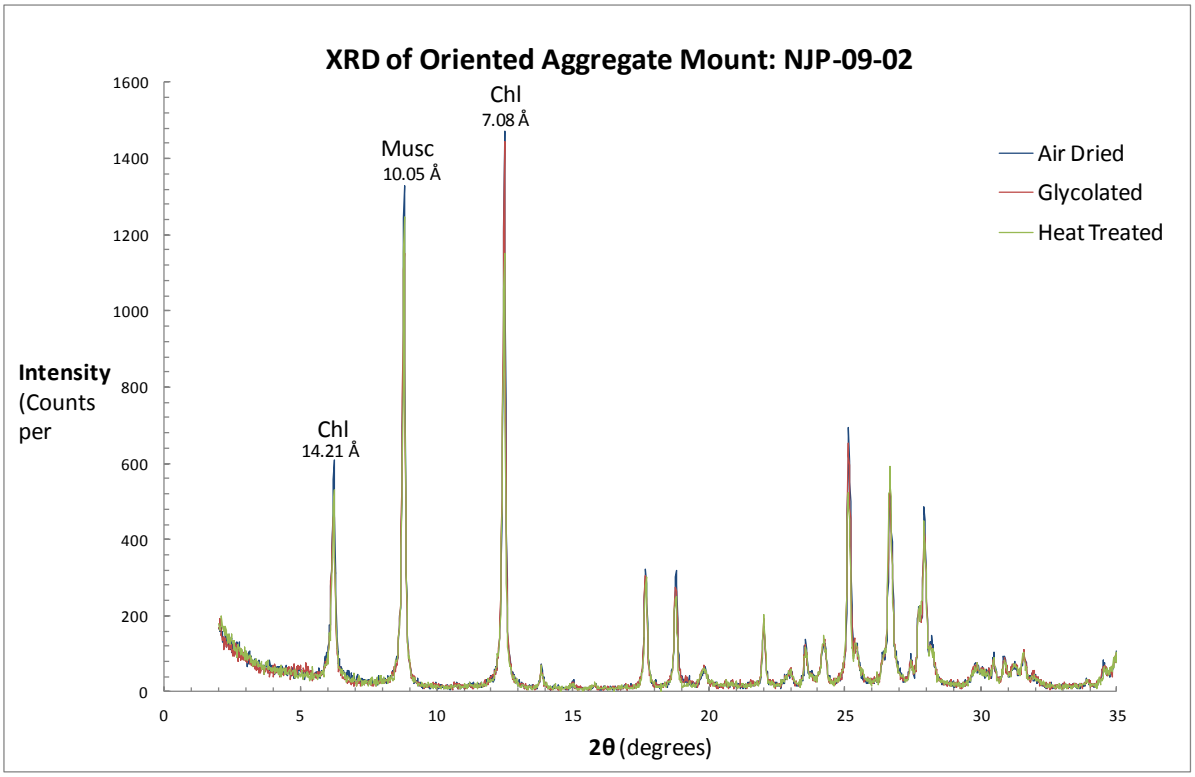

Figure A-3.7: XRD of oriented aggregate mount for sample NJP-09-02.

Raw Data from Crystallinity Measurements:

Table A-3.1: Raw data from chlorite and illite crystallinity measurements. Results shaded in blue represent the lower grade units while results shaded in purple have been grouped as higher grade. (**IC(001)** illite crystallinity from (001) reflection; **ChC(002)** chlorite crystallinity measurement from (002) reflection; **MinIll(001)** Location of illite in 2θ at lower bound for full width of half maxima; **MaxIll(001)** Location of illite in 2θ at upper bound for full width of half maxima; **MAXILL(counts)** Intensity of illite peak in counts per second; **MAXILL(loc)** Location of illite peak (2θ); **MinChl(002)** Location of chlorite in 2θ at lower bound for full width of half maxima; **MaxChl(002)** Location of chlorite in 2θ at lower bound for full width of half maxima; **MAXILL(counts)** Intensity of chlorite peak in counts per second; **MAXCHL(loc)** Location of illite peak (2θ)).

	IC(001)	ChC(002)	MinIll(001)	Max Ill(001)	MAX ILL (counts)	MAXILL (loc)	MinChl(002)	MaxChl(002)	MAXCHL (counts)	MAXILL (loc)
01--07-02	0.14	0.13	8.67	8.81	808	8.76	12.4	12.53	665	12.48
NJP-01-01	0.15	0.16	8.72	8.87	1338	8.78	12.43	12.59	1856	12.5
NJP-08-02	0.15	0.14	8.7	8.85	1118	8.78	12.41	12.55	1266	12.48
S258-GB2-Dark	0.14	0.13	8.78	8.92	696	8.86	12.48	12.61	27	12.54
99--22-01	0.1	0.12	8.73	8.83	382	8.78	12.42	12.54	121	12.48
99--22-02	0.11	0.1	8.72	8.83	1978	8.78	12.42	12.52	2092	12.48
NJP-07-06	0.12	0.11	8.77	8.89	276	8.82	12.47	12.58	786	12.54
NJP-09-02	0.11	0.11	8.74	8.85	1309	8.8	12.43	12.54	1458	12.48
S258-GB18	0.11	0.12	8.72	8.83	658	8.78	12.4	12.52	752	12.46
S258-GB24	0.11	0.11	8.72	8.83	222	8.78	12.4	12.51	1030	12.48
S258-GB2-Light	0.1	0.11	8.74	8.84	159	8.78	12.43	12.54	16	12.48

CURRICULUM VITAE

Education

B.Sc. Honours Geology with Distinction *University of British Columbia* 2012

Thesis: "The Role of Calcite on the Mechanical Strength, Fracture Geometry and Fracture Distribution of Limestone-Dolomite Composites"

Publications

Phillips, N.J., and White, J.C., 2014, Minas Fault Zone, Nova Scotia, Canada: Geometry, kinematics and processes associated with localization in a mature transpressional fault zone. GAC-MAC Field Trip Guidebook B2, Fredericton, NB, pp. 1-39.

Conference Presentations

Phillips, N.J., and White, J.C., 2014, Faulted Phyllites: Examining the variability in clay morphologies within an exhumed fault zone. Geological Society of America Abstracts with Programs, v. 46, no. 6, Vancouver, BC – **Poster**

Gordon Research Conference – Rock Deformation, Andover, NH **–** August 2014**- Poster**

Phillips, N.J., and White, J.C., 2014, How phyllosilicate-rich fault zones creep: An arguement for pressure solution accommodated creep over frictional sliding. GAC-MAC Annual Meeting, Fredericton, May - **Talk**

Phillips, N.J., and White, J.C., 2013, Seismic Suppression vs. Seismic Expression: Evidence from the Minas Fault Zone, Nova Scotia, Canada. Geological Society of America Abstracts with Programs, v. 45, no. 7, Denver CO – **Poster**

Awards

Wright Scholarship for Academic Achievement *UNB*, Fredericton, NB 2014

APEG-BC Award for Promise in Geology *UBC*, Vancouver, BC 2012

DuMoulin Black Award in Geological Sciences *UBC*, Vancouver, BC 2012

Dr. A. C. Skerl Memorial Scholarship in Geology *UBC*, Vancouver, BC 2011 & 2012

Thomas and Marguerite MacKay Memorial Scholarship *UBC*, Vancouver, BC 2011

Shell Canada Prize for Excellence at Field School *UBC*, Vancouver, BC 2009